Hydrogen Isotope Productions in Sn + Sn Collisions with Radioactive Beams at 270 MeV/nucleon

By

Masanori Kaneko

A dissertation

submitted to
Department of Physics, Kyoto University
in partial fulfillment of the requirements
for the degree of

Science — Doctor of Philosophy

January, 2022

Abstract

The density dependence of the symmetry energy is important for elucidating the property of the isospin-asymmetric nuclear matter with a wide range of densities, which plays a key role in understanding astrophysical phenomena, such as core-collapse supernovae and binary neutron-star mergers. In the vicinity of and lower than the nuclear saturation density, both experimental and theoretical work have placed a consistent constraint on the symmetry energy, while it is not well constrained at suprasaturation densities. At a terrestrial laboratory, the high-density matter can be probed experimentally only by means of heavy-ion collisions at intermediate energies. Although there have been some attempts to investigate isospin-sensitive observables in nuclear collisions between stable nuclei, the interpretation of the results is not robust due to large uncertainties of the experimental data and a strong model dependence in theoretical predictions. Therefore, a systematic measurement focusing on the isospin degrees of freedom in a wider range of isospin asymmetries has been desired. To provide reliable information on the density dependence of the symmetry energy by such a new experiment, we measured nuclear collisions of radioactive tin (Sn) isotope beams with stable Sn targets at the Radioactive Isotope Beam Factory in RIKEN.

In this dissertation, we present experimental results on the hydrogen-isotopes production in central collisions of neutron-rich ^{132}Sn + ^{124}Sn and neutron-deficient ^{108}Sn + ^{112}Sn systems at an incident energy of 270 MeV/nucleon. The differential yields $\mathrm{d}^2N/\mathrm{d}p_T\,\mathrm{d}y_0$ in the phase space of transverse momentum p_T vs. scaled rapidity y_0 were measured for protons, deuterons, and tritons detected within the azimuthal-angle range of $-30^\circ \leq \phi \leq 20^\circ$ and with laboratory momenta greater than 100, 200, and 300 MeV/c, respectively. The rapidity distributions $\mathrm{d}N/\mathrm{d}y_0$ of hydrogen isotopes were obtained by integrating the measured phase spaces along the p_T axis. In the forward rapidity domain, the neutron-rich Sn+Sn system produces more tritons and less protons compared to the neutron-deficient one, simply due to the difference of the isospin asymmetry in the two systems. A slight forward-backward asymmetry in the $\mathrm{d}N/\mathrm{d}y_0$ distributions is observed depending on the neutron content in respective hydrogen isotopes, which is indicative of the isospin-asymmetry difference between projectile and target nuclei in the measured Sn + Sn systems.

The experimental results were compared with the antisymmetrized molecular dynamics (AMD) model predictions. To investigate the symmetry-energy dependence, we carried out calculations with two assumptions of the symmetry energy characterized by its slope parameter of $L = 46$ MeV and $L = 108$ MeV. By tuning the in-medium nucleon-nucleon scattering cross-sections and the phase space for a formation of light clusters with mass numbers $A = 2$ and $A = 3$ within the AMD, the experimental rapidity distributions can be reasonably reproduced by the model. To discuss the isospin dynamics during the dynamical phase of collisions, we constructed isospin-sensitive observables, *i.e.*, deuteron-to-proton (d/p) and triton-to-proton (t/p) double spectral ratios. The values of the d/p and t/p double ratios at midrapidity agree with the system neutron-number ratio and the squared ratio, respectively. This fact implies that the modification of the neutron-to-proton density in the participant matter, which is induced by the density dependence of the symmetry energy, may not differ greatly between the two systems, despite the different isospin asymmetries of the systems. Hence a weak or moderate symmetry energy at high densities is

expected. The rapidity dependence of the double ratio in the rapidity range of $0 \leq y_0 \leq 0.7$ can be parametrized in a similar way for both d/p and t/p, indicating the partial isospin mixing between the two colliding nuclei. In comparison with the AMD calculation which shows a strong symmetry-energy dependence of the t/p double ratio, the experimental data in the midrapidity domain favors the calculation using the symmetry energy with a slope parameter of $L = 46\,\mathrm{MeV}$ rather than $L = 108\,\mathrm{MeV}$.

Contents

1 Thesis Overview **1**

2 Nuclear Symmetry Energy and Heavy-Ion Collisions **3**
2.1 Nuclear Equation of State . . . 3
2.2 Isospin-symmetric matter EOS . . . 5
2.3 Isospin-Asymmetric Nuclear Matter EOS and the Nuclear Symmetry Energy . . . 9
2.4 Heavy-Ion Collisions as a Probe of the High-Density Symmetry Energy . . . 11
2.5 Cluster Productions and Correlations in Heavy-Ion Collisions . . . 19
2.6 SπRIT Experimental Project . . . 24
2.7 Thesis Objective . . . 25

3 Experiment **27**
3.1 Radioactive Isotope Beam Factory . . . 27
3.1.1 Production of radioactive Sn beams . . . 28
3.1.2 In-flight fragment separator: BigRIPS . . . 30
3.1.3 Detector systems in BigRIPS . . . 35
3.2 Detectors for Heavy-Ion Collision Products . . . 38
3.2.1 SAMURAI magnet . . . 39
3.2.2 SπRIT time projection chamber . . . 40
3.2.3 Multiplicity trigger detector . . . 47
3.2.4 Forward veto counter for peripheral collisions: KATANA . . . 49
3.2.5 Active veto array . . . 51
3.2.6 Ancillary detectors . . . 51
3.3 Electronic Circuits . . . 55
3.3.1 Data acquisition system . . . 55
3.3.2 Trigger logic . . . 57
3.4 Summary of Experimental Conditions and Accumulated Data . . . 60

4 Data Analysis **63**
4.1 RI Beam Identification by BigRIPS . . . 64
4.1.1 Analysis of PPAC . . . 64
4.1.2 Analysis of plastic counters . . . 68
4.1.3 Analysis of MUSIC . . . 71
4.1.4 Reconstruction of the mass-to-charge ratio A/Q . . . 71
4.1.5 Beam isotope identification in Z vs. A/Q . . . 74

4.2 Beam Position and Energy on the Sn Target . . . 77
4.2.1 BDC Analysis . . . 77
4.2.2 Beam projection under magnetic field . . . 79
4.3 Event Reconstruction by the SπRIT TPC . . . 82
4.4 Selection of the On-target Events . . . 89
4.4.1 Selection of vertices reconstructed on target . . . 89
4.4.2 Correlation requirement between TPC and BDC . . . 90
4.5 Measurement of Reaction Cross Section . . . 93
4.6 Selection of Central Collisions . . . 96
4.7 Particle Identification in the SπRIT TPC . . . 99
4.7.1 Empirical fits on PID spectra in different emission angles . . . 99
4.7.2 Selection of hydrogen isotopes . . . 100
4.7.3 Differential yield of selected hydrogen isotopes . . . 106
4.8 Spectrum Corrections . . . 110
4.8.1 Monte Carlo embedding technique . . . 110
4.8.2 Procedure for unfolding . . . 111
4.8.3 Correction for energy loss in Sn target . . . 114
4.8.4 High-p_T contribution . . . 115
4.9 Evaluation of Systematic Uncertainties . . . 117
4.9.1 Treatment of each systematic uncertainty . . . 118
4.9.2 Total systematic uncertainties . . . 119

5 Results **123**

6 Discussion **131**
6.1 Discussion on the dN/dy_0 Distributions of Hydrogen Isotopes . . . 131
6.2 Discussion on the Single Cluster/Proton Ratios . . . 136
6.3 Discussion on the Double Cluster/Proton Ratios . . . 138
6.3.1 Observation in the experimental double ratio . . . 138
6.3.2 Symmetry energy investigation based on AMD . . . 139
6.3.3 Parameter dependence in the double ratios . . . 140

7 Concluding Remarks **141**

Acknowledgements **143**

A Kinematics **145**
A.1 Kinematic Variables . . . 145
A.2 Coordinate Systems . . . 147

B Supplementals for the AMD Calculation **149**
B.1 Formulation of the AMD . . . 149
B.2 Skyrme Mean-Field Parametrization . . . 152
B.3 Correction for Zero-Point Ocillation Energy . . . 152
B.4 Connection of the Nonrelativistic Calculation to the Relativistic World . . . 154

C Data Set **157**

D Table of Hydrogen Yields and Relative Yields **159**

E Supplemental Figures in the Systematic Uncertainty Evaluation **173**

List of Figures

2.1 Average binding energy vs. number density for the isopin symmetric matter ($\delta = 0$) and the pure neutron matter ($\delta = 1$). 4
2.2 Beam-energy dependence of the K^+ yield in Au + Au collisions relative to that in C + C collisions. 6
2.3 Beam-energy excitation function of the transverse flow F (left) and that of the elliptic flow $\langle \cos 2\phi \rangle$ (right) in Au + Au collisions. 8
2.4 Constraints of the average pressure P vs. normalized density ρ/ρ_0 for the isospin symmetric matter. 8
2.5 Density dependence of the symmetry energy from Skyrme interactions with different parameter sets. 10
2.6 Isospin asymmetry vs. baryon density in central collisions of ^{132}Sn + ^{124}Sn at incident energy of 400 MeV/nucleon, an impact parameter of 1 fm, and the reaction time of $t = 20\,\mathrm{fm}/c$. 12
2.7 Time evolutions of the neutron-to-proton ratio at $\rho/\rho_0 > 1$ (left) and that of the ratio between pion-like states (right) in $b = 1$ fm of central ^{132}Sn + ^{124}Sn collisions at incident energies of 200, 400, and 1000 MeV/nucleon. 13
2.8 Beam-energy dependence of the π^-/π^+ ratio in central ^{197}Au + ^{197}Au collisions. 15
2.9 System-N/Z dependence of the π^-/π^+ ratio in central collisions of ^{40}Ca + ^{40}Ca, ^{96}Ru + ^{96}Ru, ^{96}Zr + ^{96}Zr, and ^{197}Au + ^{197}Au systems at 400 MeV/nucleon. . . . 15
2.10 ASY-EOS results on the elliptic flows of neutrons to that of charged particles from semi-central ^{197}Au + ^{197}Au collisions at 400 MeV/nucleon. 17
2.11 Time evolutions of the triton multiplicity (top), the ^{3}He multiplicity (middle), and the $t/^3$He ratio (bottom) in central Au + Au collisions at 400 MeV/nucleon. . 18
2.12 Excitation function of the $t/^3$He ratio compared with the UrQMD calculations. . 18
2.13 Proton occupancies in central collisions of ^{129}Xe + $^{\mathrm{nat}}$Sn, ^{129}Xe + CsI, and ^{197}Au + ^{197}Au systems at intermediate energies. 19
2.14 Neutron-proton dynamics in central ($b = 0$–1 fm) ^{132}Sn + ^{124} Sn collisions at 300 MeV/nucleon by calculations of the AMD and JAM. 21
2.15 The π^-/π^+ yield ratio and relevant ratios based on the theoretical calculations with different options: with and without cluster correlations for different stiffness of the symmetry energy by the AMD + JAM calculation, and the single JAM calculation. 22
2.16 Spectra of $(N/Z)_{\mathrm{gas}}$ as a function of kinetic energy per nucleon in central ^{132}Sn + ^{124}Sn collisions at 300 MeV/nucleon by the AMD with cluster correlations. . . . 23

3.1 The bird's eye view of the RIBF. 28

3.2 Beam acceleration modes in the RIBF. . . . 29
3.3 The schematic view of the BigRIPS fragment separator. . . . 30
3.4 Schematic drawing of the 240×150 mm PPAC detector. . . . 36
3.5 Schematic drawing of the MUSIC detector. . . . 37
3.6 Illustration of the SAMURAI experimental area. . . . 38
3.7 Photograph of the SAMURAI experimental area. . . . 39
3.8 Basics of the SπRIT TPC operation. . . . 40
3.9 θ_{yaw} vs. θ_{pitch} distribution for the ^{132}Sn + ^{124}Sn reactions. . . . 41
3.10 Exploded view of the SπRIT TPC. . . . 43
3.11 Photographs of the field cage attached on the bottom of the rigid top plate (left) and that off from the top plate (right). . . . 43
3.12 A photograph of the three wire planes and one edge of the pad plane. . . . 44
3.13 Simulated electron drift lines near the wire planes. . . . 45
3.14 Photographs of the target mechanism. . . . 46
3.15 Overall structure of the GET readout system and a photograph of one AsAd board mounted on the SπRIT TPC. . . . 47
3.16 Schematical drawing of the experimental setup from the top, showing two walls of the MTD, KATANA veto counters, and the active area of the SπRIT TPC. . . . 48
3.17 Simulated MTD performance for ^{112}Sn + ^{124}Sn reactions at 270 MeV/nucleon. . . . 49
3.18 Photograph of the KATANA detectors at donwstream of the SπRIT TPC. . . . 50
3.19 KATANA veto performance evaluated with projectile fragments of ^{132}Xe + CsI reactions at 300 MeV/nucleon. . . . 50
3.20 Photograph of the active veto array mounted on a housing frange. . . . 51
3.21 Photographs of the SBT (left) and the beam pipe with counters installed (right). . . . 52
3.22 Experimental setup upstream from the SπRIT TPC. . . . 52
3.23 Schematic drawing and a photograph of the BDC. . . . 53
3.24 Photograph of the NeuLAND demonstrator with charged-particle veto counters. . . . 54
3.25 Trigger Box diagram. . . . 57
3.26 DAQ trigger diagram with the simplified description of the GTO module. . . . 58
3.27 Diagrams of the Fast trigger, Fast clear, and the array of G&D generators for an open/close of the gating grid. . . . 59

4.1 TDC spectra of the X1 signal of the F3–1A PPAC. . . . 64
4.2 T_{sum} spectra of the F3–1 PPAC. . . . 65
4.3 PPAC hit efficiencies as a function of run number in the measurement with the ^{108}Sn beam setting (top) and that with the ^{112}Sn beam setting (bottom). . . . 66
4.4 Conceptual illustration of the time-walk effect. . . . 68
4.5 TDC spectra as a function of charge measured by the left PMT attached to F3 plastic with and without the slewing correction. . . . 69
4.6 Elapsed time dependence of the peak of TOF_{37} for ^{108}Sn and ^{112}Sn isotopes. . . . 70
4.7 TOF spectra with (red) and without (blue) slewing correction for the two beam settings. . . . 70
4.8 Preliminary PID spectra of the geometrical mean of the MUSIC ADC vs. TOF_{37}, used for selecting events of a certain RI of interests. . . . 71

4.9 β_{35}–β_{57} correlation, which is fitted by a linear function $\beta_{35} = p_0 + p_1\beta_{57}$. 73
4.10 A/Q spectra reconstructed by different procedures. 73
4.11 Two-dimensional Z vs. A/Q spectra obtained by analyzing the data of the beam-line detectors installed in the BigRIPS, for four kinds of RI beam settings: (a) ^{108}Sn, (b) ^{112}Sn, (c) ^{124}Sn, and (d) ^{132}Sn isotopes. 75
4.12 TDC distributions and STC functions of the two BDCs. 78
4.13 Conceptual illustration of the trajectory reconstruction in the x–z plane within a single BDC. 78
4.14 Conceptual drawings of the beam propagation under the SAMURAI magnetic field. 79
4.15 Phase space of incident Sn beams projected onto the plane of Sn targets. 81
4.16 Sn beam energy per nucleon at the midpoint of the target. 81
4.17 Example of the template fit on multiple pulses in a signle pad. 82
4.18 Top view of a track reconstruction from hit clusters made in x and z directions. . 84
4.19 Event viewers from top and side of the TPC, representing the highest ADC values in each pixel. 85
4.20 Vertex position distribution along the beam axis. 86
4.21 Position correlations between reconstructed vertices vs. incident beams projected onto the vertex-z plane. 87
4.22 Probability distributions for the gating grid fully-opened events and for the fast-closed events in the ^{132}Sn + ^{124}Sn runs. 88
4.23 Vertex z-position distribution as a function of run number for the ^{108}Sn + ^{112}Sn system (top) and that for the ^{132}Sn + ^{124}Sn system (bottom). 89
4.24 Track multiplicity distribution as a function of vertex z position in the ^{132}Sn beam runs. 90
4.25 The xy profiles of the vertices at the z-position peak at the target with and without higher multiplicity requirement of $M_c \geq 50$, with top and bottom rows for the ^{108}Sn and the ^{132}Sn beam runs, respectively. 91
4.26 Residual distributions between the vertex reconstructed by the TPC and the beam position extrapolated by the BDC for on-target events in the ^{108}Sn + ^{112}Sn system (top) and those in the ^{132}Sn + ^{124}Sn system (bottom). 92
4.27 The triggerable reaction cross section ($\sigma_{\text{Triggerable}}$) as a function of run number for the ^{108}Sn + ^{112}Sn system (top) and that for the ^{132}Sn + ^{124}Sn system (bottom). 95
4.28 Probability distributions of the charged-particle multiplicity detected in the SπRIT TPC for Sn + Sn systems. 97
4.29 Response function of the scaled impact parameter (b_0) with a particular charged particle multiplicity (M_c). 98
4.30 PID spectra for the central ^{132}Sn + ^{124}Sn collisions in certain emission angles. . . 101
4.31 Same as Fig. 4.30 but for the central ^{108}Sn + ^{112}Sn collisions. 102
4.32 Particle mass spectra in the rigidity range of 900 MeV/$c \leq p/q \leq$ 1000 MeV/c with/without the emission-angle calibration for the two systems. 103
4.33 Rigidity-sliced mass spectra along with the triple Gaussian fits on three peaks. . . 104
4.34 Two-dimensional mass vs. magnetic rigidity spectra for the two systems. 105

4.35 Uncorrected differential yields in the p_T vs. y_0 phase space for protons (left), deuterons (middle), and tritons (right) emitted in central collisions of the ^{132}Sn + ^{124}Sn system (top) and ^{108}Sn + ^{112}Sn system (bottom). . . . 107
4.36 Uncorrected dN_{raw}/dy_0 spectra for protons (left), deuterons (middle), and tritons (right) emitted in central collisions of the ^{132}Sn + ^{124}Sn system (filled markers) and ^{108}Sn + ^{112}Sn system (open markers). . . . 108
4.37 Contamination rate as functions of p_T vs. y_0 for protons (left), deuterons (middle), and tritons (right) in central collisions of ^{132}Sn + ^{124}Sn (top) and ^{108}Sn + ^{112}Sn (bottom) systems. . . . 108
4.38 Overall contamination rate as a function of scaled rapidity for protons (left), deuterons (middle), and tritons (right) emitted in central collisions of the ^{132}Sn + ^{124}Sn system (filled markers) and ^{108}Sn + ^{112}Sn system (open markers). . . . 109
4.40 Same as Fig. 4.39 but the simulated tracks are not weighted (always $w = 1$). . . . 112
4.41 Raw dN/dy_0 spectra of hydrogen isotopes in the two Sn + Sn systems (black circles) and those obtained in each iterative correction process (red, green, blue markers). . . . 113
4.42 Efficiency functions as a function of p_T-y_0 phase space for protons (left), deuterons (middle), and tritons (right) in central collisions of ^{132}Sn + ^{124}Sn (top) and ^{108}Sn + ^{112}Sn (bottom) systems. . . . 114
4.43 The momentum-loss rate of hydrogen isotopes in the 280 mg/cm^2-thick solid ^{124}Sn as a function of initial momentum for different polar angles θ in the laboratory frame. . . . 115
4.44 The effect of the ΔE_{target} correction in the phase space. . . . 116

5.1 The differential yields $d^2N/dp_T dy_0$ of hydrogen isotopes in central ($b_0 < 0.15$) collisions of ^{132}Sn + ^{124}Sn and ^{108}Sn + ^{112}Sn systems at 270 MeV/nucleon. . . . 124
5.2 Invariant yields of hydrogen isotopes in central collisions of the ^{132}Sn + ^{124}Sn system (top) and the ^{108}Sn + ^{112}Sn system (bottom). . . . 125
5.3 dN/dy_0 distributions of hydrogen isotopes in central ($b_0 < 0.15$) collisions of ^{132}Sn + ^{124}Sn and ^{108}Sn + ^{112}Sn systems at 270 MeV/nucleon. . . . 126
5.4 Spectral ratios of the dN/dy_0 distribution over the y_0-axis-inverted one for protons (red), deuterons (green), and tritons (blue) in the ^{132}Sn + ^{124}Sn (left) and the ^{108}Sn + ^{112}Sn (right) reactions. . . . 127
5.5 Single cluster-to-proton relative yields as a function of scaled rapidity in the two Sn + Sn systems. . . . 129
5.6 Double ratios of the cluster-to-proton relative yield in the ^{132}Sn + ^{124}Sn system over that in the ^{108}Sn + ^{112}Sn system. . . . 129

6.1 Rapidity distributions of (a) protons, (b) deuterons, and (c) tritons in central collisions of ^{132}Sn + ^{124}Sn system, and those for ^{108}Sn + ^{112}Sn system (d-f), compared with the AMD calculations. . . . 133
6.2 dN/dy_0 spectra of $Z = 1, 2$ isotopes in the ^{132}Sn + ^{124}Sn system calculated with the four assumptions of NN cross sections and the asy-soft parametrization. . . . 134

6.3 Single and double spectral ratios for d/p and t/p compared to the AMD calculations with the asy-soft and asy-stiff symmetry energies. 137
6.4 The systematic investigation on the parameter dependence in the cluster-to-proton double spectral ratios. 140

A.1 Illustrations of the experimental setup with the description of the coordinate systems. 147

E.1 Systematic variations derived from the data set. 174
E.2 Systematic variations derived from the minimum multiplicity threshold. 175
E.3 Systematic variations derived from the d_{POCA} threshold. 176
E.4 Systematic variations derived from the n_{Cluster} threshold. 177
E.5 Systematic variations derived from the ϕ angle cut. 178
E.6 Systematic variations derived from the PID gate. 179
E.7 Systematic variations derived from the probability assignment. 180
E.8 Systematic variations derived from the $\Delta E_{\mathrm{target}}$ correction. 181

List of Tables

2.1 A set of Sn + Sn reactions measured in the first series of the SπRIT experiments. 24

3.1 List of the primary and secondary beams in the SπRIT experiment. 29
3.2 List of parameter configurations of the BigRIPS for different measurements. . . . 31
3.3 Relevant parameters of the SπRIT TPC. 41
3.4 The property of each wire. 44
3.5 Relevant parameters of the BDC in the present experiment. 53
3.6 The list of the electronics modules for the data acquisition. 56
3.7 List of the start-and-end time of the experiments, the stored file IDs, and the statistics of the collected data. 60
3.8 Trigger configurations in the regular run and the minimum bias runs. 61

4.1 Overall hit efficiency for each PPAC during the measurement using ^{108}Sn and ^{112}Sn beams. 66
4.2 Overall beam-trajectory reconstruction efficiency in each focal plane. 67
4.3 Parameters used for the $B\rho$ calculation. 68
4.4 Energy deposits of RI beams in each region of the MUSIC, calculated by the LISE++. 72
4.5 Overall A/Q reconstruction efficiency. 74
4.6 Parameters of two-dimensional normal distribution fitted to the Sn isotope peaks in the Z vs. A/Q spectra. 75
4.7 Summary of the event statistics with respect to the RI beam identifications. 76
4.8 List of material considered in the beam propagation. 80
4.9 Properties of beam profiles on target. 80
4.10 Mean and root-mean-square values of the per-nucleon kinetic-energy distributions of incident Sn beams projected on the midpoint of the target. 81
4.11 Gaussian fit results on the on-target peak in the vertex z-position distribution and the number of events selected as on-target Sn+Sn reactions. 90
4.12 Gaussian fit results on the vertex–beam position residuals. 92
4.13 Triggerable reaction cross section $\sigma_{\text{Triggerable}}$ for four systems with several factors used for the calculations. 94
4.14 Charged-particle-multiplicity threshold for selecting the most central ($b_0 \leq 0.15$) event samples. 97
4.15 Maximum impact parameters calculated by several theoretical model parametrizations of the total reaction cross section. 98
4.16 Summary of the gate conditions for hydrogen isotopes. 106

4.17 Overall efficiency of hydrogen isotopes in each reaction system. 114
4.18 List of items considered in evaluating the systematic uncertainties. 117
4.19 The scaled impact parameter b_0 variations with respect to the minimum charged-particle multiplicity requirement for selecting central collision events. 118
4.20 Systematic uncertainties in the $\mathrm{d}N/\mathrm{d}y_0$ spectra stemming from each variation. . 120
4.21 List of systematic uncertainties in the single and double cluster-to-proton spectral ratios. 121

5.1 Hydrogen isotope yields integrated for the positive scaled rapidity region ($y_0 \geq 0$). 128

6.1 Integrated yields and root-mean-square (RMS) values of the $\mathrm{d}N/\mathrm{d}y_0$ distributions of $Z = 1, 2$ isotopes for different scenarios of the NN cross section. 135
6.2 Parameters used in the modifications for the bound phase space of $A = 2, 3$ light clusters. 135

B.1 Total binding energies (MeV) of light cluster nuclei in different options of the AMD. 154

C.1 List of the regular runs used in this work. 158

D.1 Data table of the proton $\mathrm{d}N/\mathrm{d}y_0$ distribution in central ($b_0 < 0.15$) collisions of the ^{132}Sn + ^{124}Sn system at 270 MeV/nucleon. 160
D.2 Data table of the deuteron $\mathrm{d}N/\mathrm{d}y_0$ distribution in central ($b_0 < 0.15$) collisions of the ^{132}Sn + ^{124}Sn system at 270 MeV/nucleon. 161
D.3 Data table of the triton $\mathrm{d}N/\mathrm{d}y_0$ distribution in central ($b_0 < 0.15$) collisions of the ^{132}Sn + ^{124}Sn system at 270 MeV/nucleon. 162
D.4 Data table of the proton $\mathrm{d}N/\mathrm{d}y_0$ distribution in central ($b_0 < 0.15$) collisions of the ^{108}Sn + ^{112}Sn system at 270 MeV/nucleon. 163
D.5 Data table of the deuteron $\mathrm{d}N/\mathrm{d}y_0$ distribution in central ($b_0 < 0.15$) collisions of the ^{108}Sn + ^{112}Sn system at 270 MeV/nucleon. 164
D.6 Data table of the triton $\mathrm{d}N/\mathrm{d}y_0$ ditribution in central ($b_0 < 0.15$) collisions of the ^{108}Sn + ^{112}Sn system at 270 MeV/nucleon. 165
D.7 Data table of the deuteron-to-proton (d/p) relative yield in central collisions of the ^{132}Sn + ^{124}Sn system at 270 MeV/nucleon. 166
D.8 Data table of the triton-to-proton (t/p) relative yield in central collisions of the ^{132}Sn + ^{124}Sn system at 270 MeV/nucleon. 167
D.9 Data table of the deuteron-to-proton (d/p) relative yield in central collisions of the ^{108}Sn + ^{112}Sn system at 270 MeV/nucleon. 168
D.10 Data table of the triton-to-proton (t/p) relative yield in central collisions of the ^{108}Sn + ^{112}Sn system at 270 MeV/nucleon. 169
D.11 Data table of the deuteron-to-proton double spectral ratio $DR_{d/p}$. 170
D.12 Data table of the triton-to-proton double spectral ratio $DR_{t/p}$. 171

1 Thesis Overview

An atomic nucleus is one of the most fascinating quantum-mechanical objects composed of two kinds of fermions, namely, neutrons and protons (or nucleons as a general term). It is a strongly correlated self-confining system governed by the strong force and the Coulomb force, of which various and unique properties have been established. The knowledge of nuclei is useful to reveal not merely the fundamental of matter but also the fact of explosive astronomical phenomena that occurred somewhere in the universe.

Big news was brought by the LIGO–Virgo Collaborations in 2017. That was the detection of the gravitational wave and the subsequent electromagnetic counterparts from the binary neutron-star merger [1–5]. By analyzing the gravitational wave, the tidal deformability associated with the pressure of the neutron-star matter was constrained. Furthermore, the characteristic signal of the kilonova, which is the evidence of heavy-element productions, was observed in the visible light spectrum [6–9]. This observation implies that the ejecta of a neutron-star merger could be a promising site of the rapid neutron capture process. For modeling a neutron star, *i.e.*, for elucidating the property of the nuclear matter with a wide range of densities and neutron-proton asymmetries, we turn to the nuclear equation of state (EOS). A dominant uncertainty in the EOS of the isospin-asymmetric matter comes from the density-dependent symmetry energy, which is the energy difference between the neutron matter and the isospin symmetric matter. Particularly at suprasaturation densities, a lack of experimental data and divergent theoretical predictions are a bottleneck to constrain the symmetry energy.

To explore the EOS of the high-density nuclear matter, heavy-ion collisions at intermediate energies have been measured since momentary densities up to 2–3 times the nuclear saturation density is attained in the central region of the compressing system. While the π^-/π^+ relative yield [10] and the elliptic-flow ratio between neutrons and charged particles [11, 12] have been proposed and used to probe the high-density symmetry energy, the interpretation of the data depends on theoretical models and physical parameters in calculations [13–16]. Previously, nuclear

collisions were measured for stable nuclei with wide ranges of masses and energies, which were not fully suited for examining the isospin-asymmetry dependence of the EOS. Therefore, we systematically measured ^{132}Sn + ^{124}Sn, ^{124}Sn + ^{112}Sn, ^{112}Sn + ^{124}Sn, and ^{108}Sn + ^{112}Sn collisions at an incident energy of 270 MeV/nucleon, aiming to construct quantities highly sensitive to the isospin asymmetry degrees of freedom. The maximum density with this beam energy is less than twice the saturation density, which approximately corresponds to the outer core of neutron stars.

This dissertation describes the rapidity distributions of hydrogen isotopes emitted in head-on (central) collisions of the neutron-rich ^{132}Sn + ^{124}Sn system and the neutron-deficient ^{108}Sn + ^{112}Sn system. As an isospin sensitive observable, the deuteron-to-proton (d/p) and triton-to-proton (t/p) double spectral ratios were constructed. In the rapidity dependence of the double ratios, a partial isospin mixing between colliding nuclei was observed. The experimental data are compared with the AMD calculation [17–20] to discuss the isospin dynamics. Although model parameters needed to be tuned in the AMD for reproducing the experimental distributions, it was found not to strongly influence the conclusion of this dissertation. In comparison with the AMD calculations, the experimental t/p double ratio in the midrapidity domain favors the calculation with the symmetry-energy slope parameter of $L = 46$ MeV rather than $L = 108$ MeV.

Organization of this dissertation

This dissertation begins with reviewing the past-to-present investigations on the high-density symmetry energy via heavy-ion collisions and a short overview of this work in Chap. 2, which is followed by a detailed description of the experimental equipment in Chap. 3. We will then describe the procedure of the data analysis for transported RI beams and that for charged particles produced in Sn + Sn collisions in Chap. 4. The obtained experimental results are provided in Chap. 5. In Chap. 6, the isospin dynamics in the measured Sn + Sn collisions and the effect of the high-density symmetry energy are discussed based on the comparison with the AMD predictions. Finally in Chap. 7 we conclude the dissertation.

Main contribution of the author

Relevant to this dissertation, the author M. K. has participated in and worked with the SπRIT (SAMURAI Pion Reconstruction and Ion-Tracker) Collaboration which has been devoted to a detailed examination of the density-dependent nuclear symmetry energy from radioactive-heavy-ion collision experiments. The main contribution of the author is as follows.

- The technical development and construction of the multiplicity trigger detector, the performance evaluation based on simulations, and the data analysis [21, 22].
- The data analysis on ^{108,112}Sn isotope beam particles with detectors in the BigRIPS.
- The data analysis on hydrogen isotope productions in central Sn + Sn collisions.
- The publication of the letter: "Rapidity distributions of $Z = 1$ isotopes and the nuclear symmetry energy from Sn + Sn collisions with radioactive beams at 270 MeV/nucleon" [23] as a first author.

2

Nuclear Symmetry Energy and Heavy-Ion Collisions

2.1 Nuclear Equation of State

The nuclear equation of state (EOS) is one of the most fundamental properties of nuclear matter, which describes the relationship between thermodynamic variables such as energy, pressure, temperature, density, and isospin asymmetry, *i.e.*, the relative neutron-to-proton abundance. The EOS is relevant to not only properties of atomic nuclei such as structure, mass, resonant excitation [24] but also the space-time evolution of dynamic nuclear reactions [25]. Analogous to nuclei, various characteristics of neutron stars are also associated with the nuclear EOS, *e.g.*, the internal structure, mass-radius relationship, cooling mechanism, and the tidal deformability probed by binary neutron-star mergers [26]. The determination of the nuclear EOS is one of the main goals of nuclear physics.

The EOS of the infinite nuclear matter at zero temperature can be empirically expressed as a Tailor series expansion of the binding energy per nucleon $\epsilon(\rho, \delta)$ [27]:

$$\epsilon(\rho, \delta) = \epsilon_0(\rho) + \mathcal{S}(\rho)\delta^2 + O\left(\delta^4\right). \tag{2.1}$$

Here the variables $\rho \equiv \rho_n + \rho_p$ and $\delta \equiv (\rho_n - \rho_p)/\rho$ are the number density of nucleons and the isospin asymmetry of the system, respectively, with the neutron density ρ_n and the proton density ρ_p. The first term $\epsilon_0(\rho)$ is the binding energy of the isospin symmetric matter, followed by terms representing the extra energy generated in the isospin asymmetric system. The second-order coefficient $\mathcal{S}(\rho)$ is the so-called nuclear symmetry energy. Figure 2.1 presents the EOS of the isospin symmetric matter ($\delta = 0$) and that of the pure neutron matter ($\delta = 1$) based on effective-field

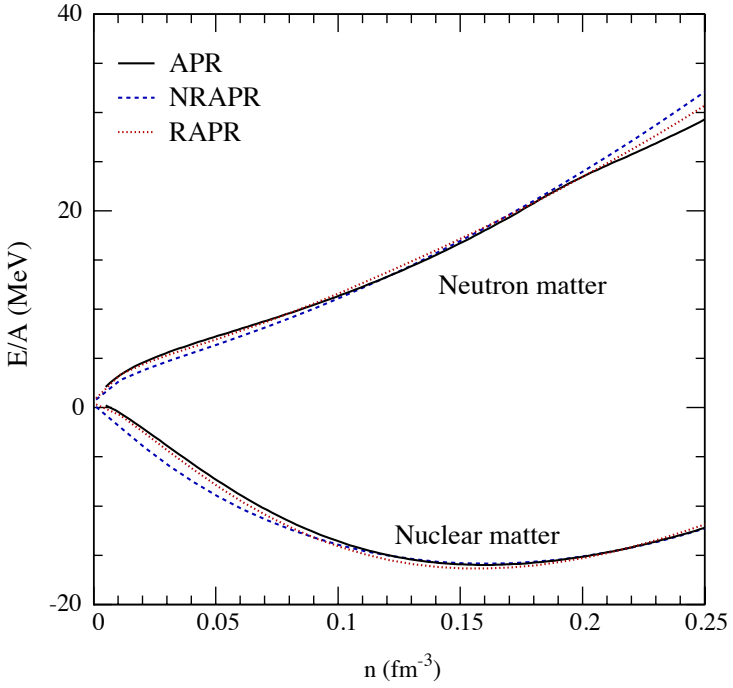

Figure 2.1: Average binding energy vs. number density for the isospin symmetric matter ($\delta = 0$) and the pure neutron matter ($\delta = 1$). The black-solid curves show the EOS derived from the variational microscopic calculations of Akmal, Pandharipande, and Ravenhall (APR). The blue-dashed curves (NRAPR) indicate the EOS given by a potential model using the non-relativistic Skyrme-like effective Hamiltonian density. The Skyrme parameters are determined by fitting the EOS to that of APR, and the spin-orbit interaction is additionally adjusted based on the experimental charge radii and binding energies of ^{40}Ca, ^{90}Zr, and ^{208}Pb. The red-dotted curves (RAPR) are obtained by the fit of the field-theoretical approach to the APR EOS. Adapted from Ref. [28].

theories [28]. The EOS of the isospin symmetric matter has a stability point at nuclear saturation density $\rho_0 \simeq 0.16\,\mathrm{fm}^{-3}$ with the average energy of $\epsilon_0(\rho = \rho_0) \simeq -16\,\mathrm{MeV}$. The odd-order δ terms in Eq. 2.1 are forbidden under the assumption of the charge symmetry in the nuclear force, meaning that the nuclear EOS is invariant with respect to the exchange of neutrons and protons. The higher-order δ terms are basically expected to have a minor contribution to the binding energy of the system [29]. Within the variational calculation using the realistic two-nucleon interaction and the phenomenological three-nucleon force, the coefficient of the δ^4 term was found to be practically zero at saturation density and the order of 1 MeV at suprasaturation densities [30]. Thus the nuclear EOS is often approximated as $\epsilon(\rho, \delta) = \epsilon_0(\rho) + \mathcal{S}(\rho)\delta^2$, by neglecting the higher-order δ terms. However, in some cases, the higher-order δ terms are expected to have a non-negligible impact, for example, in determining the core-crust transition density of neutron stars [31, 32] and the number of bound nuclei in the nuclear landscape [33].

The density dependence of the EOS is often associated with a "stiffness" or a "softness" of the nuclear matter. If the nuclear matter gains energy rapidly with an increase of density, it means that a high pressure[1] is induced at high density and the system is hard to be compressed. In such case, the EOS is called as "stiff". Conversely, when the energy increases loosely or decreases with an increase of density, the EOS is called as "soft".

[1]The pressure of the nuclear matter is given by $P(\rho, \delta) = \rho^2\, \partial\epsilon(\rho, \delta)/\partial\rho$. The pressure as a function of density and isospin asymmetry can be treated as an alternative expression of Eq. 2.1.

2.2 Isospin-symmetric matter EOS

In this section, the current understanding of the isospin-symmetric matter EOS, given as $\epsilon(\rho, \delta = 0) = \epsilon_0(\rho)$ in Eq. 2.1, is reviewed. The density dependence of the $\epsilon_0(\rho)$ can be often characterized by a Tailor series expansion near the nuclear saturation density ρ_0, which is written as:

$$\epsilon_0(\rho) = \epsilon_0(\rho_0) + \frac{K_0}{2!}x^2 + O\left(x^3\right), \tag{2.2}$$

with $x \equiv (\rho - \rho_0)/3\rho_0$. Note that the first-order coefficient in the right-hand side should be zero since the $\epsilon_0(\rho)$ takes the minimum value at $\rho = \rho_0$. The second-order coefficient K_0 represents the incompressibility of the isospin symmetric matter at ρ_0, expressed as:

$$K_0 = 9\rho_0^2\left(\frac{\partial^2\epsilon_0(\rho)}{\partial\rho^2}\right)_{\rho=\rho_0}. \tag{2.3}$$

Isoscalar giant monopole resonance It is well known that the incompressibility is relevant to the isoscalar giant monopole resonance (ISGMR), the so-called "breathing mode" in nuclei, see Ref. [24] as a review. By comparisons of microscopic calculations with the ISGMR energies measured for several nuclei such as ^{16}O, ^{40}Ca, ^{90}Zr, ^{116}Sn, ^{144}Sm, and ^{208}Pb, the K_0 have been moderately constrained, *e.g.*, $K_0 = (210 \pm 30)$ MeV [34], (231 ± 5) MeV [35], and (240 ± 20) MeV [36]. However, a precise determination of K_0 seems to require an extensive understanding of the nuclear interaction, since the relation between K_0 and the ISGMR energy is determined based on an effective force and depends on the model assumption [37]. In Ref. [38], it is shown that the ISGMR energy of ^{208}Pb correlates with both the isoscalar effective mass[2] and the slope coefficient of the symmetry energy, which are still uncertain factors in the EOS. On the other hand, a toy calculation without microscopic model assumptions resulted in a slightly stiffer constraint of $250 < K_0 < 315$ MeV, and it was indicated that the surface diffuseness of vibrating nuclei plays an important role in the deduction of K_0 [39]. Accurate knowledge on the relevant factors is necessary to determine K_0 from the ISGMR energy with less systematic uncertainties.

Subthreshold kaon production in heavy-ion collisions In the density domain above the saturation one, the subthreshold production of K^+ mesons in heavy-ion collisions has been proposed and used to probe the symmetric-matter EOS [40–46]. It is expected that kaons serve as a clean probe of nuclear matter since they interact with nucleons much weakly compared to pions and cannot be reabsorbed due to strangeness conservation. At incident energies below the production threshold[3], kaons are predominantly produced in the early compression phase of collisions, where many violent baryon-induced reactions occur and deficit energy is likely to be supplemented. In fact, microscopic transport calculations predicted that the average baryon density at coordinates where kaons are originally produced is around 1.5 times the saturation density, in the case of central Au + Au collisions at 0.8 GeV/nucleon [42]. Therefore, the K^+ yield reflects the degree of compression in heavy-ion collisions, *i.e.*, a soft EOS will lead to more compression of the system

[2]The isoscalar effective mass is the nucleon effective mass in the isospin-symmetric matter at saturation density.

[3]An elementary process of K^+ productions, $NN \to N\Lambda K^+$, has a threshold energy of $E_{\rm lab} = 1.58$ GeV.

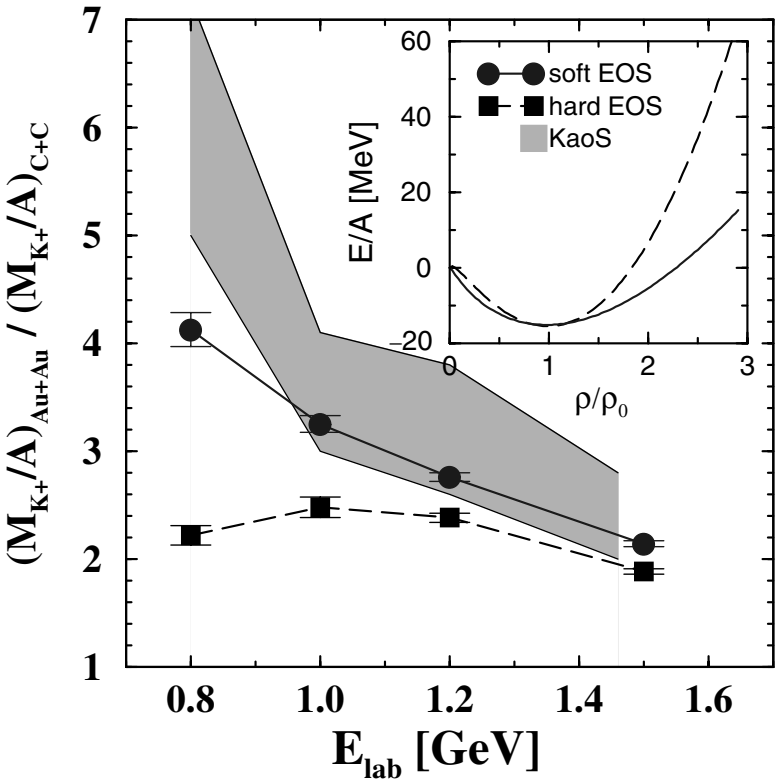

Figure 2.2: Beam-energy dependence of the K^+ yield in Au + Au collisions relative to that in C + C collisions. The experimental data by the KaoS Collaboration (shaded area) is compared with the transport calculations using the two specific stiffnesses of the EOS. The right top panel shows the symmetric-matter EOS adopted in the calculation, where the soft EOS has an incompressibility of $K_0 = 200$ MeV while the stiff one has $K_0 = 380$ MeV. Adapted from Ref. [42].

reaching a higher density and a larger K^+ yield, and vice versa [40, 42]. Figure 2.2 presents the excitation function of the K^+ yield in central Au + Au collisions relative to that in C + C collisions at incident energies below the K^+ production threshold. The experimental data favors the calculation with a soft EOS using $K_0 = 200$ MeV rather than a hard one using $K_0 = 380$ MeV [42, 43]. The K^+ ratio was found to be well robust against uncertain factors in calculations, such as kaon production channels [42], effective fields adopted to calculations [45], the kaon-nucleon potential, the cross-section $\Delta N \rightarrow NK^+\Lambda$, and the in-medium lifetime of the Δ state [46].

Collective flows in heavy-ion collisions Because the kaon production becomes insensitive to the nuclear EOS as an incident beam energy increases beyond the subthreshold energy [40], collective flows have been used to constrain the EOS at suprasaturation and much higher densities [25, 47–50]. In non-central heavy-ion collisions, the overlapping region (participant[4]) of colliding nuclei forms an almond-shaped high-density matter, which induces an azimuthal anisotropy in particle emissions with respect to the reaction plane orientation[5]. One of the quantities that characterize the anisotropy is the transverse flow. It is a measure of the sideways deflection of spectator nucleons

[4]In heavy-ion collisions at an incident energy higher than 100 MeV/nucleon, the geometrical overlap between a projectile nucleus and a target nucleus produces a violently reacting high-density matter, called as "participant", and the other parts of nuclei keep going without changing the original velocity, called as "spectator".

[5]A reaction plane is spanned by the beam-momentum vector and the impact-parameter vector.

within the reaction plane, due to the pressure of the adjacent compressed participant matter. The transverse flow is usually defined as [25]:

$$F = \left.\frac{\mathrm{d}\langle p_x/A\rangle}{\mathrm{d}(y/y_{\mathrm{c.m.}})}\right|_{y/y_{\mathrm{c.m.}}=1}, \tag{2.4}$$

where $\langle p_x/A\rangle$ represents the mean transverse momentum per nucleon, y and $y_{\mathrm{c.m.}}$ are the rapidity of particles and the center-of-mass rapidity in the laboratory frame. A larger value of F is expected for a higher incompressibility. In addition to the transverse flow, the anisotropy is quantified by the Fourier coefficients of the azimuthal angle distribution of particles,

$$\frac{\mathrm{d}N}{\mathrm{d}\phi} \propto 1 + 2v_1\cos\big(\phi\big) + 2v_2\cos\big(2\phi\big) + \cdots, \tag{2.5}$$

where ϕ means the azimuthal angle of detected particles relative to the reaction plane orientation. The coefficients $v_1 = \langle\cos\big(\phi\big)\rangle$ and $v_2 = \langle\cos\big(2\phi\big)\rangle$ are referred to as the directed flow and the elliptic flow, respectively. In particular, the elliptic flow provides a measure of the in-plane to out-of-plane emission rate. A negative v_2 indicates that more particles are emitted out of plane ($\phi \approx 90°$ or $\phi \approx 270°$) than in plane ($\phi \approx 0°$ or $\phi \approx 180°$). In non-central collisions at lower incident energies, a negative v_2 can be expected in the midrapidity domain because the spectator matter is still close to the participant matter that starts to expand after the compression, and tends to interfere with the in-plane emission perpendicular to the beam axis. A higher incompressibility will lead a faster expansion of the participant matter and more interference with spectator nucleons, resulting in a larger negative value of v_2.

Figure 2.3 presents the beam-energy excitation functions of collective flows in Au+Au collisions measured by four independent experiments compared with the microscopic transport calculation. The left panel shows the transverse flow calculated using $Z = 1, 2$ particles while the right one shows the elliptic flow of protons at midrapidity. As expected, the transport calculations predict larger values of F and negative v_2 with the assumption of a higher incompressibility, *i.e.*, a stiffer EOS. By comparing the calculation with the experimental data, the lower and upper bounds of the incompressibility were deduced as $K_0 = 167$ MeV and 380 MeV, respectively, in the density range of $2 \leq \rho/\rho_0 \leq 5$ [25]. Recently, collective flows of light charged particles in Au + Au collisions at incident energies of 0.4–1.5 GeV/nucleon were measured by the FOPI Collaboration. By analyzing this FOPI flow data, the incompressibility has been constrained to be a moderately soft EOS. For example, $K_0 = 200$ MeV was favored rather than $K_0 = 380$ MeV from the deuteron elliptic flow [48] and from the directed flow using $Z = 1, 2$ particles [47]. Further analyses provided the constraint of $K_0 = (190 \pm 30)$ MeV in the density range up to $3\rho_0$ using the elliptic flow of protons [49] and $K_0 = (220 \pm 40)$ MeV using the rapidity-dependent elliptic flows of protons and deuterons [50], each of which is consistent with the already placed limitations.

As described up to here, one may say that the EOS of the isospin symmetric matter have been constrained to some extent in a wide range of densities, as shown in Fig. 2.4. However, the density dependence of the isospin-asymmetric matter EOS requires more discussion particularly in the high-density domain, as we see in the following sections.

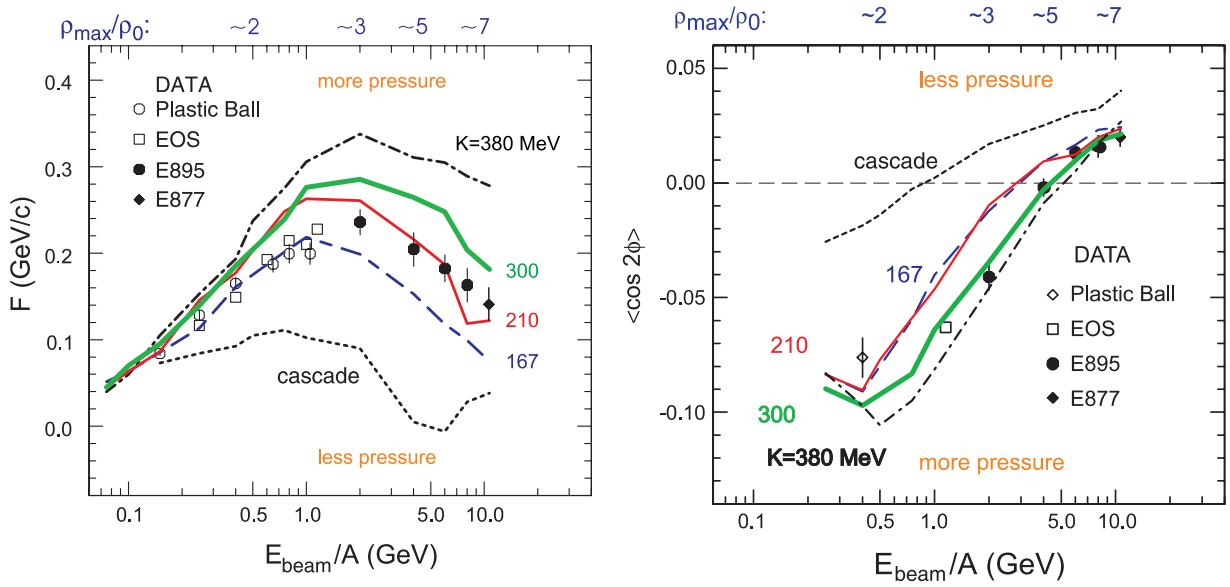

Figure 2.3: Beam-energy excitation function of the transverse flow F (left) and that of the elliptic flow $\langle \cos 2\phi \rangle$ (right) in Au + Au collisions. The transverse flow is constructed for light charged particles including hydrogen and helium isotopes. The elliptic flow is constructed for protons at midrapidity. Adapted from Ref. [25].

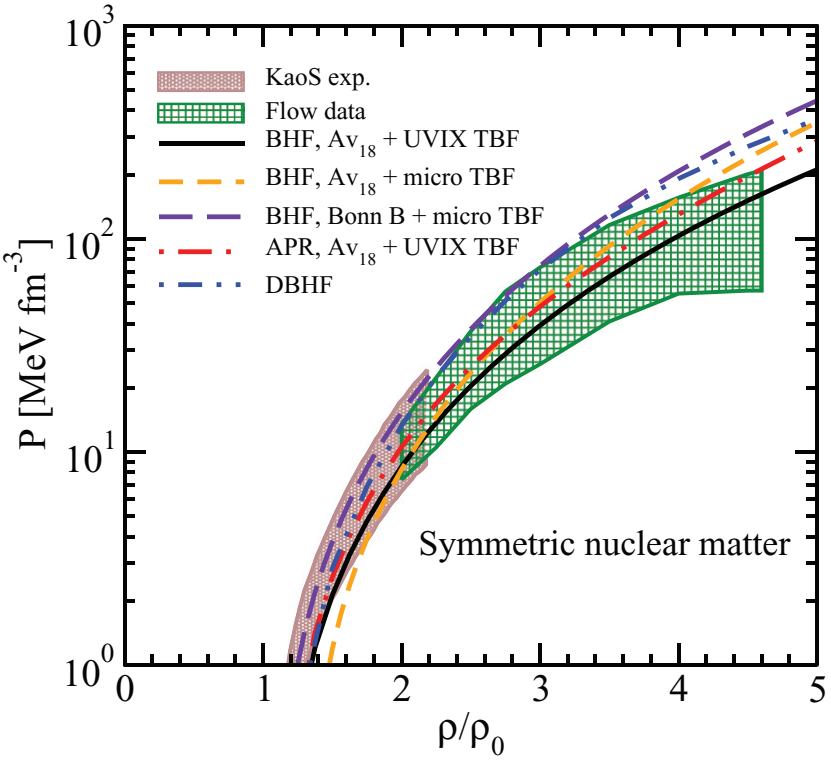

Figure 2.4: Constraints of the average pressure P vs. normalized density ρ/ρ_0 for the isospin symmetric matter. The constraints from the kaon ratio and collective flows are drawn by the brown filled area denoted by "KaoS exp." and the green grid-shaped area denoted by "Flow data", respectively. Adapted from Ref. [51].

2.3 Isospin-Asymmetric Nuclear Matter EOS and the Nuclear Symmetry Energy

The isospin asymmetry dependence of the nuclear EOS is characterized mainly by the nuclear symmetry energy $\mathcal{S}(\rho)$, the density dependence of which plays a crucial role in understanding diverse properties in neutron-rich nuclei as well as neutron stars [52, 53]. The $\mathcal{S}(\rho)$ is given as a second-order derivative of the $\epsilon(\rho,\delta)$ at $\delta = 0$. It is also equivalent to the energy difference between the pure neutron matter ($\delta = 1$) and the isospin symmetric matter ($\delta = 0$), if one ignores the higher-order δ terms in Eq. 2.1, given as:

$$\mathcal{S}(\rho) \equiv \frac{1}{2}\left(\frac{\partial^2\epsilon(\rho,\delta)}{\partial\delta^2}\right)_{\delta=0} \approx \epsilon(\rho,1) - \epsilon(\rho,0). \tag{2.6}$$

Similarly to Eq. 2.2, the property of the density dependence of the symmetry energy can be parametrized by a Tailor series expansion near the saturation density,

$$\mathcal{S}(\rho) = J + Lx + \frac{1}{2}K_{\rm sym}x^2 + \cdots, \tag{2.7}$$

with $x = (\rho - \rho_0)/3\rho_0$ and typical denotations of the coefficients in the expansion,

$$J \equiv \mathcal{S}(\rho_0), \tag{2.8}$$

$$L \equiv 3\rho_0\left(\frac{\partial\mathcal{S}(\rho)}{\partial\rho}\right)_{\rho=\rho_0} = \frac{3P_{\rm sym}}{\rho_0}, \tag{2.9}$$

$$K_{\rm sym} \equiv 9\rho_0^2\left(\frac{\partial^2\mathcal{S}(\rho)}{\partial\rho^2}\right)_{\rho=\rho_0}. \tag{2.10}$$

Especially the symmetry-energy slope parameter denoted by L is associated with the pressure difference between the neutron matter and the isospin-symmetric matter at saturation density, *i.e.*, $P_{\rm sym} \approx P(\rho_0,1) - P(\rho_0,0)$. The curvature parameter $K_{\rm sym}$ represents the extra incompressibility of the neutron matter compared to the symmetric matter, which can be connected with a new incompressibility[6] of the isospin-asymmetric matter as $K_\tau \approx K_{\rm sym} - 6L$ [54]. The relevant parameters J, L, and $K_{\rm sym}$ can be probed by various properties observed in nuclei with a wide range of isospin asymmetries, *e.g.*, nuclear masses from a liquid-drop model [55], isovector resonances of nuclei [24], isovector skins [56], excitation energies to isobaric analogue states [57], and so on. Also, heavy-ion collisions are predicted to provide a sensitive probe of the density dependence of the symmetry energy. In the colliding nuclei, the symmetry energy induces an isovector potential which exerts an antiphase pressure on neutrons and protons, and therefore, subsequently emitted particles can be a messenger of the symmetry energy. As a promising observable in heavy-ion collisions, the neutron-to-proton relative yield [58], the isospin diffusion [59, 60], mirror-nuclei ratios of ^{3}H/^{3}He or ^{7}Li/^{7}Be [61–63], the charged pion ratio π^-/π^+ [10, 64, 65], and collective

[6] K_τ is the symmetry term of the incompressibility, $K_A = K_0 + K_\tau\delta^2$, with the infinite-matter incompressibility K_A which can be deduced by a systematic investigation of the ISGMR energies of nuclei.

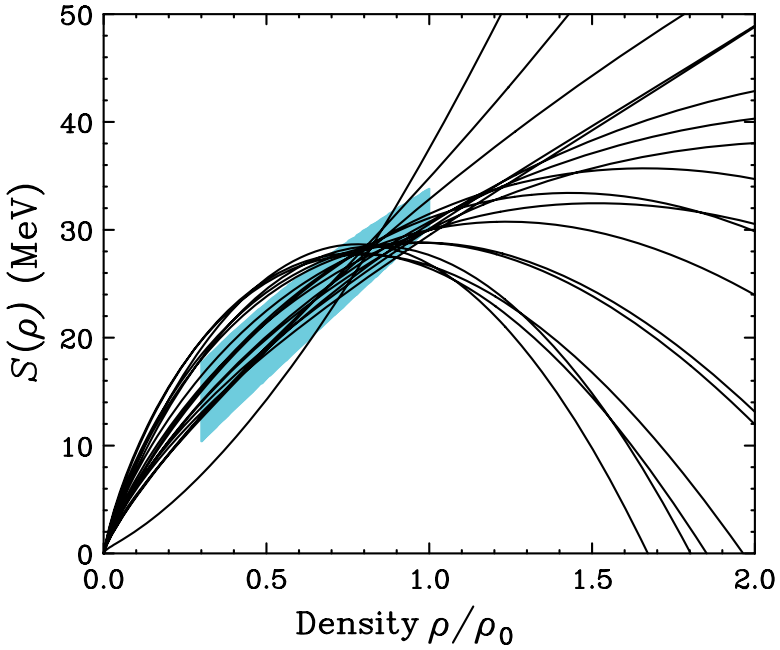

Figure 2.5: Density dependence of the symmetry energy from Skyrme interactions with different parameter sets. The shaded region is the experimental constraint in the density range of $0.3 \leq \rho/\rho_0 \leq 1.0$, which was deduced by a χ^2 analysis for both the neutron-to-proton energy spectra [58] and the isospin transport ratios [59] from ^{124,112}Sn + ^{124,112}Sn collisions at 50 MeV/nucleon. Adapted from Ref. [69].

flow observables [11, 12, 48, 66–68] have been measured at an incident energy of tens or hundreds MeV/nucleon. By these various probes, a many-sided survey on the density-dependent symmetry energy has been made particularly since radioactive beam facilities started their operations. In addition, astrophysical probes became available thanks to developments of worldwide observatories. The present era is thus the most suited to approach the density dependence of the symmetry energy from diverse physics research of terrestrial experiments, astronomical observations, and theories.

Our understanding of the density dependence of the symmetry energy has been advanced mainly at normal and subsaturation densities, *e.g.*, see a number of data samples in Refs. [39, 69–73] and references therein. One of the work provided $J = (31.7 \pm 3.2)$ MeV and $L = (58.7 \pm 28.1)$ MeV as averages of the data samples [72]. On the other hand, the symmetry energy at suprasaturation densities is not yet consistently constrained, as highlighted in Fig. 2.5. The shown curves are provided by the Skyrme interactions with 18 different parameter sets, by which the experimental binding energy difference between ^{132}Sn and ^{100}Sn is reasonably reproduced [74]. The theoretical curves are also consistent with the constraint obtained from the low-energy heavy-ion collision data [58, 59]. As seen in Fig. 2.5, a variety of scenarios of the density-dependent symmetry energy is possible, even if the given calculations consistently reproduce the data on subsaturation densities. A direct probe of the high-density matter is necessary to constrain the symmetry energy at high densities stringently. The only terrestrial means to explore nuclear matter at suprasaturation densities is heavy-ion collisions, the current understandings on which will be reviewed in the following section.

2.4 Heavy-Ion Collisions as a Probe of the High-Density Symmetry Energy

Overview

As is described in the previous section, heavy-ion collisions provide a unique probe to investigate the property of the high-density nuclear matter. In collisions of heavy nuclei with similar mass numbers at incident energies from several hundreds MeV/nucleon to a few GeV/nucleon, *i.e.*, intermediate energies, the overlapping participant region is compressed in the early phase of the reaction, and the density in the central part of the system may reach approximately twice the saturation density in a short time scale of $t \approx 20\,\mathrm{fm}/c$. The compressed state quickly starts to expand due to an absence of the external pressure. In the expanding system, the interactions between particles become weaker, and eventually, the system disintegrates into various particles such as free nucleons, mesons, light clusters, and heavy fragment nuclei. The overall reaction process depends on the initial conditions (such as a projectile-target combination, an incident energy, and an impact parameter), the macroscopic property of the EOS, and the microscopic property such as two-nucleon (NN) collision cross sections and many-body correlations in a nuclear medium. As for theoretical approaches to heavy-ion collisions, transport theories have been developed to simulate the complex space-time evolution from beginning to end of the reaction and to extract physics information from experimental observables. Commonly used frameworks are the Boltzmann-Uehling-Uhlenbeck (BUU) approach and the quantum molecular dynamics (QMD) approach, see, *e.g.*, Ref. [75] for specifications of each model. A transport theory solves the single-particle motions with the following ingredients: a density- and momentum-dependent mean-field potential, NN collisions, and initializations of projectile and target nuclei. In the mean-field approximation, the density-dependent symmetry energy is associated with the isovector part of the single-nucleon potential and with the isoscalar effective mass, according to the Hugenholtz-Van Hove theorem [76].

In the high-density matter formed in heavy-ion collisions, which is normally neutron rich as heavy nuclei are, the symmetry-energy potential induces a repulsive force acting on neutrons and an attractive force acting on protons. Such the effect on the neutron-proton dynamics in the early phase of the reaction is expected to somewhat remain in the finally emitted particles. However, the isospin asymmetry realized in the colliding system is not so large, *i.e.*, $\delta_{\mathrm{sys}} \approx 0.2$ at most for collisions of stable nuclei, and thus the effect can be hidden by the isoscalar effect. To enhance the isovector contributions and to cancel the isoscalar ones, relative observables constructed from the set of isospin multiplets should be effective. More specifically, the neutron-to-proton relative yield [77–81], the neutron-to-proton transverse [82–84] and elliptic flows [85, 86], the triton-to-^{3}He relative yield [78, 80, 87, 88] and transverse flow [89], π^-/π^+ [18, 78, 83, 90–96], K^0/K^+ [91], and Σ^-/Σ^+ ratios [97] have been predicted to be sensitive to the high-density behavior of the symmetry energy. To obtain such promising observables, the FOPI and ASY-EOS Collaborations conducted heavy-ion collision experiments at GSI facility [10–12, 48, 62]. They measured neutrons and charged particles from central and semi-central collisions with wide ranges of system masses (from ^{40}Ca + ^{40}Ca as the lightest system to ^{197}Au + ^{197}Au as the heaviest one) and incident energies

(E_{beam} = 0.09–1.5 GeV/nucleon for Au + Au reactions). The representative probes measured in ^{197}Au + ^{197}Au reactions, such as the π^-/π^+ relative yield, the neutron-to-charged particles elliptic flow, and the triton-to-^{3}He relative yield, have been referred the most for investigating the symmetry energy at suprasaturation densities, which will be reviewed in the followings.

Symmetry-energy effect in heavy-ion collision dynamics

Effect on the isospin asymmetry vs. baryon density Before introducing the specific observables, we describe how the symmetry energy affects the dynamics of heavy-ion collisions. Within the isospin-dependent BUU transport calculation, it was predicted that the high-density behavior of the symmetry energy has an impact on the determination of the isospin asymmetry–density correlation in heavy-ion collisions [83, 84]. In the calculation, two forms of the symmetry energy having different trends at high densities, given in the left-top panel of Fig. 2.6, were used. The right panel of Fig. 2.6 presents the average isospin asymmetry as a function of baryon density over the whole space of compressing matter in central ^{132}Sn + ^{124}Sn collisions at 400 MeV/nucleon. The isospin asymmetry at high densities becomes smaller in the calculation with a stiff symmetry energy (E^a_{sym}) than with a soft one (E^b_{sym}). The same trend is observed in a simple model of neutron stars shown in the inset. This is because the stiff symmetry energy repels more neutrons from and attracts more protons into the high-density region than the soft one. Additionally, due to the conservation of the total isospin of the system, the opposite trend is observed in the low-density region. As is described here, the initial δ–ρ correlation of the system evolves depending on the stiffness of the symmetry energy.

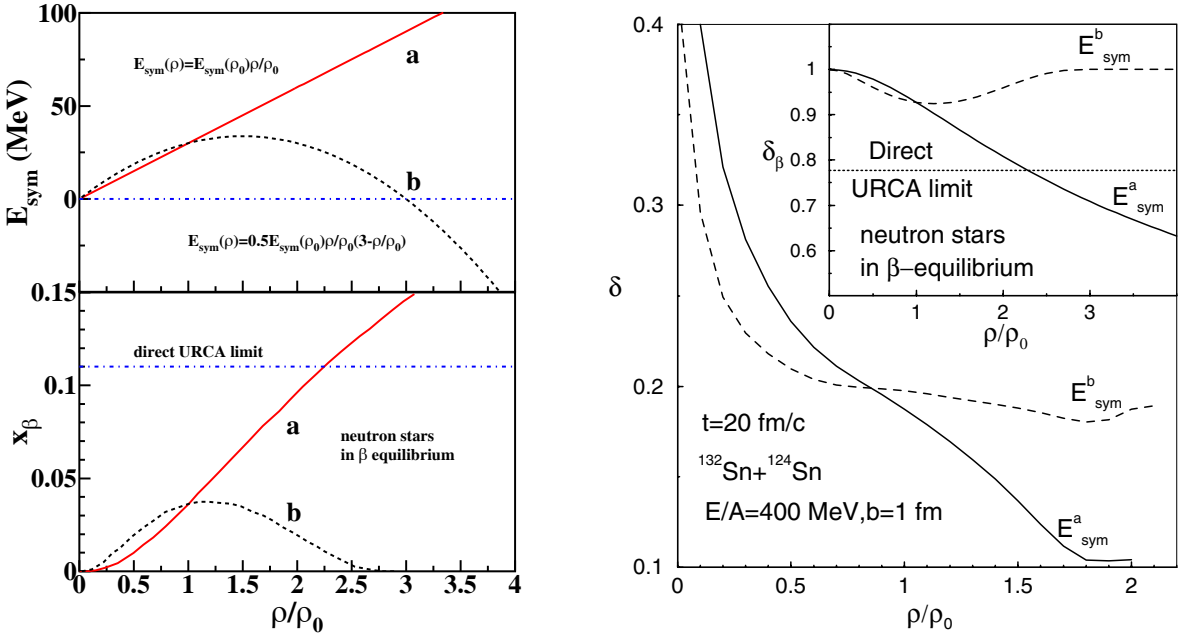

Figure 2.6: Left: the nuclear symmetry energy as a function of baryon density (top) and the corresponding proton fraction x_β in neutron stars at β equilibrium (bottom). Adapted from Ref. [93]. Right: the isospin asymmetry vs. baryon density in central collisions of ^{132}Sn + ^{124}Sn at incident energy of 400 MeV/nucleon, an impact parameter of 1 fm, and the reaction time of $t = 20\,\text{fm}/c$. Adapted from Ref. [83]. Denotations of **a** and **b** in the left panel and those of E^a_{sym} and E^b_{sym} in the right panel represent a stiff symmetry energy and a soft one, respectively.

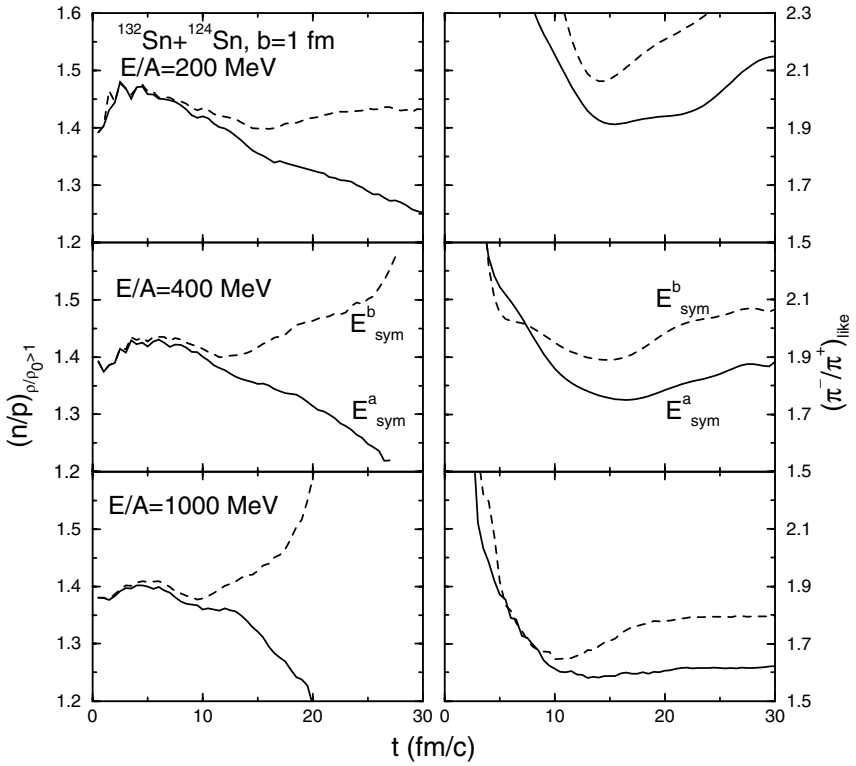

Figure 2.7: Time evolutions of the neutron-to-proton ratio at $\rho/\rho_0 > 1$ (left) and those of the ratio between pion-like states (right) in $b = 1$ fm of central ^{132}Sn + ^{124}Sn collisions at incident energies of 200, 400, and 1000 MeV/nucleon. Adapted from Ref. [83].

Time evolution of the isospin asymmetry at high densities The left panel of Fig. 2.7 presents the time evolutions of the neutron-to-proton multiplicity ratio at high densities of $\rho/\rho_0 > 1$, denoted by $(n/p)_{\rho/\rho_0>1}$, in central ^{132}Sn + ^{124}Sn collisions at 200, 400, and 1000 MeV/nucleon. Similarly to the high-density behavior of the δ–ρ correlation, the $(n/p)_{\rho/\rho_0>1}$ becomes smaller with the stiff symmetry energy compared to the soft one. Such the neutron-proton dynamics in the high-density region is an essential key to probe the high-density behavior of the symmetry energy. However, it could be difficult to precisely measure the multiplicity and/or momentum of neutrons due to a problem of the low detection efficiency. In contrast, the use of charged pions produced at subthreshold energies has an advantage for probing the neutron-proton dynamics at high densities in terms of both the detection efficiency and the production process, as described in the following.

π^-/π^+ ratio in heavy-ion collisions at intermediate energies

Production channel of pions and the time evolution of the π^-/π^+ Below 2 GeV/nucleon of incident energy, pions are predominantly produced through the decay of $\Delta(1232)$ resonances [83] which are produced via NN collisions in the early compression phase of reactions. The specific channels that contribute largely to the final yield of charged pions are,

$$n + n \rightarrow \Delta^- + p, \qquad \Delta^- \rightarrow n + \pi^-, \tag{2.11}$$

$$p + p \rightarrow \Delta^{++} + n, \qquad \Delta^{++} \rightarrow p + \pi^+. \tag{2.12}$$

Consequently, the yields of negatively and positively charged pions in subthreshold energies are expected to correlate with the multiplicities of neutrons and protons in the high-density region, respectively. This expectation was demonstrated by investigating the time evolution of the ratio of pion-like states, as shown in the right panel of Fig. 2.7. Here the pion-like state includes free pions plus effective pions in the Δ resonance, and the ratio can be given as:

$$(\pi^-/\pi^+)_{\text{like}} \equiv \frac{\pi^- + \Delta^- + \frac{1}{3}\Delta^0}{\pi^+ + \Delta^{++} + \frac{1}{3}\Delta^+}. \tag{2.13}$$

This quantity naturally becomes the final π^-/π^+ ratio through a quick decay of the Δ resonance ($\tau_\Delta \simeq 1.6\,\text{fm}/c$ of lifetime in vacuum) as the reaction time elapses until NN collisions don't newly occur. As shown in Fig. 2.7, the symmetry-energy dependence seen in the $(\pi^-/\pi^+)_{\text{like}}$ is similar to that in the $(n/p)_{\rho/\rho_0>1}$, which indicates that the π^-/π^+ ratio is a sensitive probe of the high-density neutron-proton dynamics determined by the density-dependent symmetry energy.

Symmetry energy from the π^-/π^+ ratio The FOPI Collaboration measured charged pions from central collisions of mass-symmetric systems such as ^{40}Ca + ^{40}Ca, ^{96}Ru + ^{96}Ru, ^{96}Zr + ^{96}Zr, and ^{197}Au + ^{197}Au at intermediate energies [10]. Figures 2.8 and 2.9 compare the experimental π^-/π^+ excitation functions with two independent transport calculations: the isospin-dependent BUU model (IBUU04) [13] and the improved isospin-dependent QMD model (ImIQMD) [14]. As seen in the figures, the dependence of the π^-/π^+ ratio on the symmetry-energy stiffness shows a completely opposite trend for the two models. The opposite tendency between different models was also observed in other models [91, 98, 99]. Furthermore, within the pBUU model calculation, the sensitivity to the high-density symmetry energy was not confirmed in the π^-/π^+ yield ratio [99]. Instead, the center-of-mass kinetic energy ($E_{\text{c.m.}}$) distribution of charged pions was proposed to be measured, because the high-energy tail in the $E_{\text{c.m.}}$ distribution of the π^-/π^+ ratio and the difference of mean kinetic energy between π^- and π^+ were found to be sensitive to the high-density symmetry energy. A consistent conclusion on the π^-/π^+ ratio is still not attained.

The discrepancy among different transport models could arise due to the different bases of each model and unknown physical inputs relevant to the in-medium properties of nucleons, pions, and Δ resonance states. Various factors that potentially influence the π^-/π^+ ratio have been investigated, *e.g.*, the pion-nucleon s-wave and p-wave interactions [100], the in-medium baryon-baryon cross sections [101, 102], the in-medium pion potential [103–106], the in-medium lifetime [107] and potential [108] of the $\Delta(1232)$ resonance, the Pauli blocking [109] and the threshold effect [110] in the processes of $NN \leftrightarrow N\Delta$ and $\Delta \rightarrow N\pi$, the nucleon-nucleon short-range correlation [102, 111], the energy conservation in the two-body collision [112], and cluster correlations [18, 94]. In addition, the transport model evaluation project is running to understand the origin of the difference among models by simple calculations with the same initialization [75, 113–115].

To mitigate the theoretical uncertainties arising from the different bases among the models for pions, it has also been desired to construct a double π^-/π^+ ratio between reactions containing the same charge but different isospin asymmetries [92, 95, 96]. Very recently, the SπRIT Collaboration reported results on charged pions emitted in central collisions of ^{132}Sn + ^{124}Sn, ^{112}Sn + ^{124}Sn, and ^{108}Sn + ^{112}Sn systems at 270 MeV/nucleon [64, 65]. Seven transport calculations without adjusting input parameters specifically for the SπRIT data were compared with both single and double

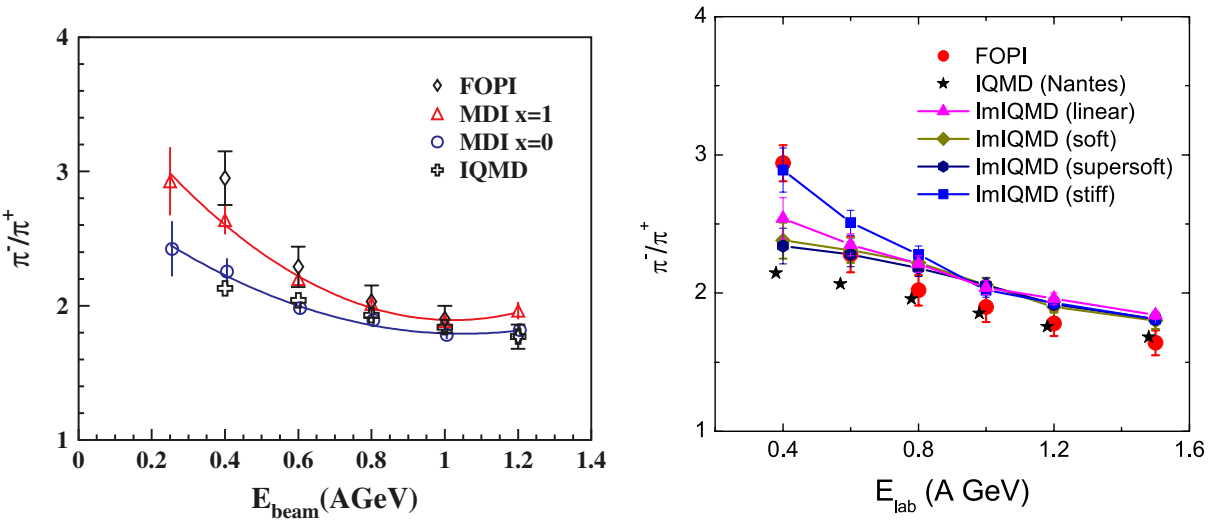

(a) IBUU04 calculations [13] (b) ImIQMD calculations [14]

Figure 2.8: Beam-energy dependence of the π^-/π^+ ratio in central ^{197}Au + ^{197}Au collisions. The experimental data measured by the FOPI Collaboration is compared with theoretical predictions. In the IBUU04 model, the stiffness of the symmetry energy is parametrized by the parameter x, where $x = 1$ corresponds to a soft density dependence and $x = 0$ to a stiff one [13]. The IBUU04 calculation predicts higher π^-/π^+ ratio with the softer symmetry energy. On the other hand, the ImIQMD calculation predicts the opposite symmetry-energy dependence at 0.4–0.8 AGeV of incident energy, which almost dissapears at $E_{lab} \geq 1$ AGeV.

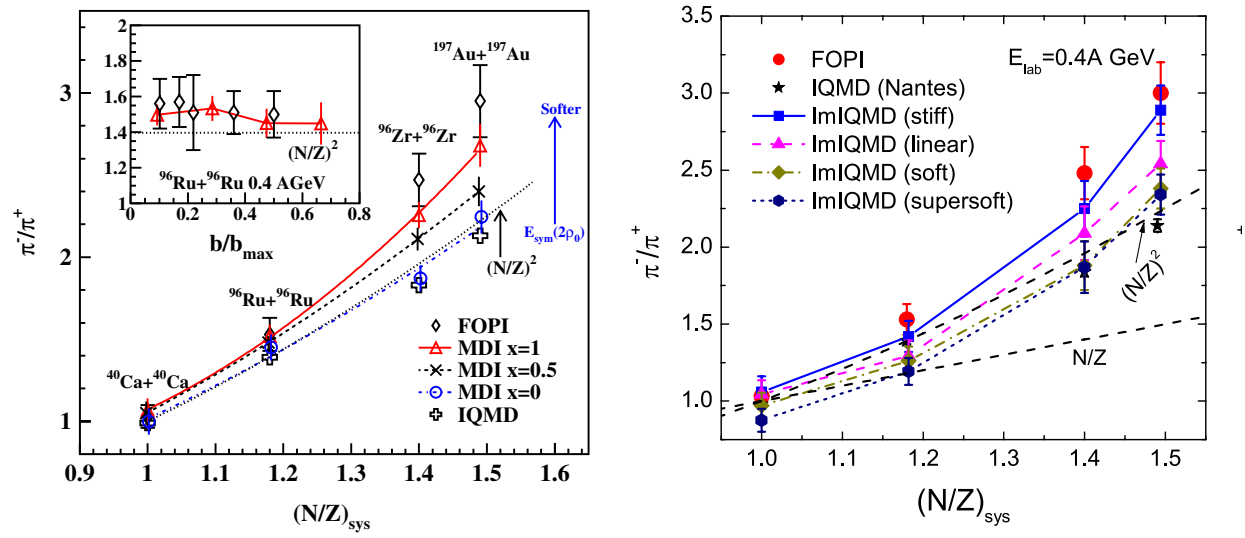

(a) IBUU04 calculations [13] (b) ImIQMD calculations [14]

Figure 2.9: System-N/Z dependence of the π^-/π^+ ratio in central collisions of ^{40}Ca + ^{40}Ca, ^{96}Ru + ^{96}Ru, ^{96}Zr + ^{96}Zr, and ^{197}Au + ^{197}Au systems at 400 MeV/nucleon. The experimental data measured by the FOPI Collaboration is compared with theoretical calculations which predict opposite dependences on the high-density symmetry energy. The inset in the left panel presents the impact-parameter dependence of the π^-/π^+ ratio in ^{96}Ru + ^{96}Ru collisions at 0.4 AGeV.

π^-/π^+ yield ratios, and the results were found to be model dependent beyond the experimental uncertainties [64]. After adjusting some of the in-medium properties on the Δ resonance states within the dcQMD model for reproducing the experimental total pion multiplicities and mean kinetic energies, the π^-/π^+ spectral ratios at high-p_T region were analyzed by the model, which deduced the slope parameter as $42 < L < 117$ MeV [65]. It is mandatory to improve model descriptions for confirming the sensitivity to the high-density symmetry energy and for accurately probing it.

Elliptic flows of neutrons and charged particles

The relative and/or differential collective flows between neutrons and protons have been also predicted as a good probe of the density-dependent symmetry energy [82–86]. The FOPI-LAND Collaboration measured elliptic flows of free neutrons (v_2^n), free protons (v_2^p), and hydrogen isotopes (v_2^h) in semi-central ^{197}Au + ^{197}Au collisions at 400 MeV/nucleon [11, 48, 116, 117]. These data were analyzed with the ultra-relativistic QMD (UrQMD) transport model in several studies, each of which deduced the slope parameter of $L = (83 \pm 26)$ MeV from the v_2^n/v_2^h ratio [11], $L = (85 \pm 25)$ MeV from the ratios and differences for v_2^n vs. v_2^p and for v_2^n vs. v_2^h [118], and $L = (43 \pm 20)$ MeV from the v_2^p [119]. Whereas, a slightly stiff symmetry energy of $L = (127 \pm 57)$ MeV was obtained based on the Tübingen QMD model [15], implying a model dependence in the flow parameters. As a successor of the FOPI-LAND, the ASY-EOS Collaboration measured the elliptic flows of neutrons and charged particles ($v_2^{\rm ch}$) from the same system and energy with improved statistics [12]. Figure 2.10 presents the comparison of the transverse-velocity-dependent $v_2^n/v_2^{\rm ch}$ ratio with the UrQMD calculation in the left panel and the density dependence of the symmetry energy corresponding to the deduced slope parameter of $L = (72 \pm 13)$ MeV [12] in the right panel. Although the statistics of flow parameters were improved, the ASY-EOS experiment suffered from technical issues, *e.g.*, the timing correction in the neutron detector and insufficient separation power of charged particles. To obtain a more reliable conclusion on the flow parameters relevant to the density-dependent symmetry energy, a future experiment at FAIR facility is planned, and of course, the understanding of the parameter dependence in calculations is required.

The model parameter dependence in the elliptic flow has been investigated similarly to pion observables [11, 15, 16, 102, 118, 120, 121]. Within the Tübingen QMD model used in Ref. [15], for example, it was shown that the v_2^n vs. v_2^p observables depend rather weakly on model parameters such as the incompressibility of the nuclear matter, the width of the nucleon wave function, and the optical potential, compared to the good sensitivity to the high-density symmetry energy. Among various factors, the in-medium two-nucleon cross section (σ_{NN}^*) seems to have been frequently discussed, partly because of the observation of a strong correlation between collective flows and the nuclear stopping[7] which is highly sensitive to the σ_{NN}^* [47, 122]. In the end, there was a concerning observation that the calculations used in the flow studies overestimated the yield of protons and underestimated those of deuterons, tritons, and helium isotopes by about a factor of 2–3 [11, 12], which may be a non-negligible issue in describing the heavy-ion collision dynamics, as explained in the later section.

[7]The nuclear stopping is a degree of energy loss induced mainly by two-nucleon collisions, which can be quantified by the longitudinal-to-transverse energy rate of emitted particles.

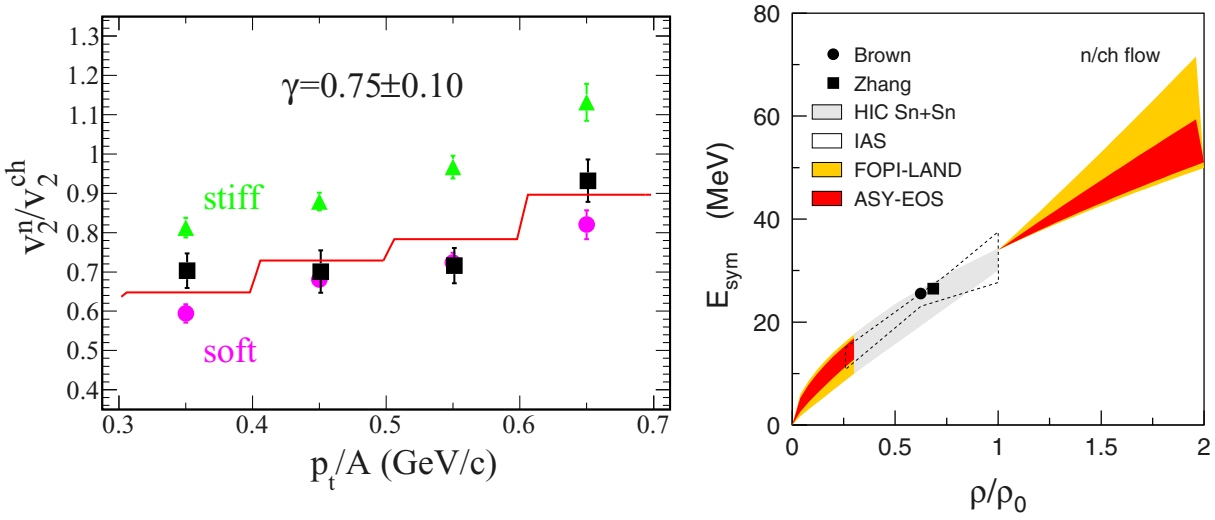

Figure 2.10: Left: the comparison of the elliptic-flow ratio between neutrons and charged particles (v_2^n/v_2^{ch}) in semi-central Au + Au collisions at 400 MeV/nucleon with the UrQMD transport model calculations. The v_2^{ch} is constructed from the all recorded charged particles due to an insufficient separation power. The parametrization of the symmetry energy is given by $E_{\mathrm{sym}}^{\mathrm{pot}}(\rho) = 22\,\mathrm{MeV}\cdot(\rho/\rho_0)^{\gamma}$, with $\gamma = 1.5$ corresponding to a stiff symmetry energy and $\gamma = 0.5$ corresponding to a soft one. The red line is an interpolation of the calculated v_2^n/v_2^{ch} indicating $\gamma = 0.75$ as presented in the figure. Right: constraints of the symmetry energy deduced from elliptic flow observables. The yellow and red envelopes indicate the result of the FOPI-LAND experiment ($L = (83 \pm 26)$ MeV [11]) and that of the ASY-EOS one ($L = (72 \pm 13)$ MeV [12]). Adapted from Ref. [12].

Triton-to-^{3}He ratio

The $t/^3$He relative observables have been predicted as a good probe of the high-density symmetry energy [78, 87–89, 123] since the $t/^3$He is expected to behave as similar as the n/p ratio. In Ref. [63], the $t/^3$He yield ratio in central collisions of ^{40}Ca + ^{40}Ca, ^{96}Ru + ^{96}Ru, ^{96}Zr + ^{96}Zr, and ^{197}Au + ^{197}Au systems reported by the FOPI Collaboration were compared with the UrQMD predictions. Thirteen types of the Skyrme interactions were adopted in the calculations, in which the L parameter ranges from 5.75 up to 161.05 MeV and the J and K_0 parameters were kept within 32–38 MeV and 230–255 MeV, respectively. As shown in Fig. 2.11, the calculation indicates that the triton multiplicity is sensitive to the symmetry-energy stiffness while ^{3}He multiplicity is almost independent of it, possibly due to the competition between the symmetry energy and the Coulomb force. Figure 2.12 compares the excitation functions of the $t/^3$He ratio with the theoretical predictions. The experimental data in the beam energy domain higher than 250 MeV/nucleon are well reproduced by the MSL0 ($L = 60$ MeV) and the Ska35s25 ($L = 98.89$ MeV) parametrizations, which correspond to a moderately soft to linear density dependence of the symmetry energy. However, the all calculated results cannot reproduce the decreasing trend of the $t/^3$He ratio in the lower beam energy domain. In addition, even if the $t/^3$He ratio from central ^{197}Au + ^{197}Au collisions at 400 MeV/nucleon can be reproduced, the theoretical calculation underestimates the experimental yield of tritons and that of ^{3}He by a factor of 3, as shown in the upper and middle panels of Fig. 2.11. A similar discrepancy has been observed in the Tübingen QMD model calculation used for the flow analysis as described in the previous section. To obtain a reliable conclusion on the symmetry-energy stiffness via the measurement of the $t/^3$He ratio, theoretical progress on the cluster production mechanism is necessary.

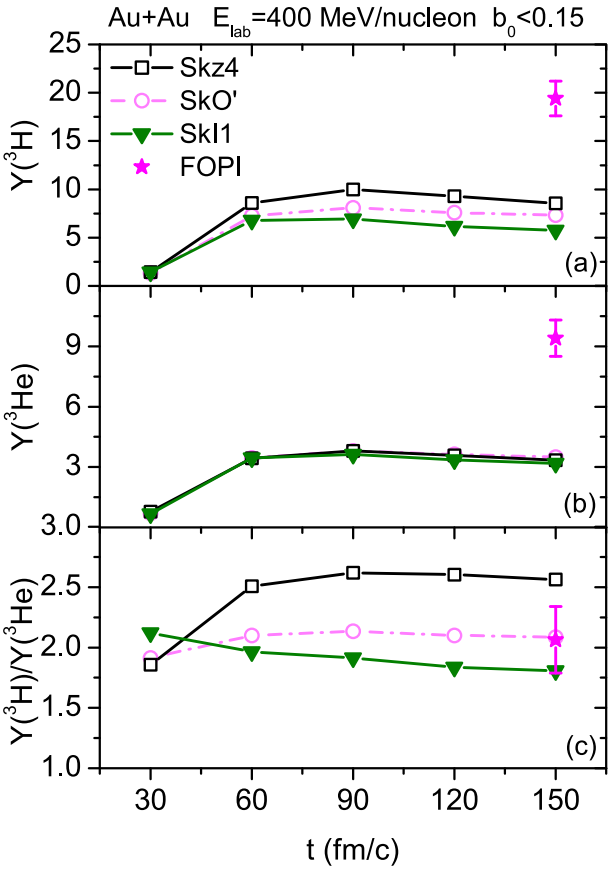

Figure 2.11: Time evolutions of the triton multiplicity (top), the ^{3}He multiplicity (middle), and the $t/^3$He ratio (bottom) in central Au + Au collisions at 400 MeV/nucleon. The clusters are identified using the isospin-dependent minimum spanning tree algorithm, see the later section. The FOPI data (magenta stars) are added at $t = 150\,\mathrm{fm}/c$ of reaction time to compare with the final yields in the calculation. Adapted from Ref. [63].

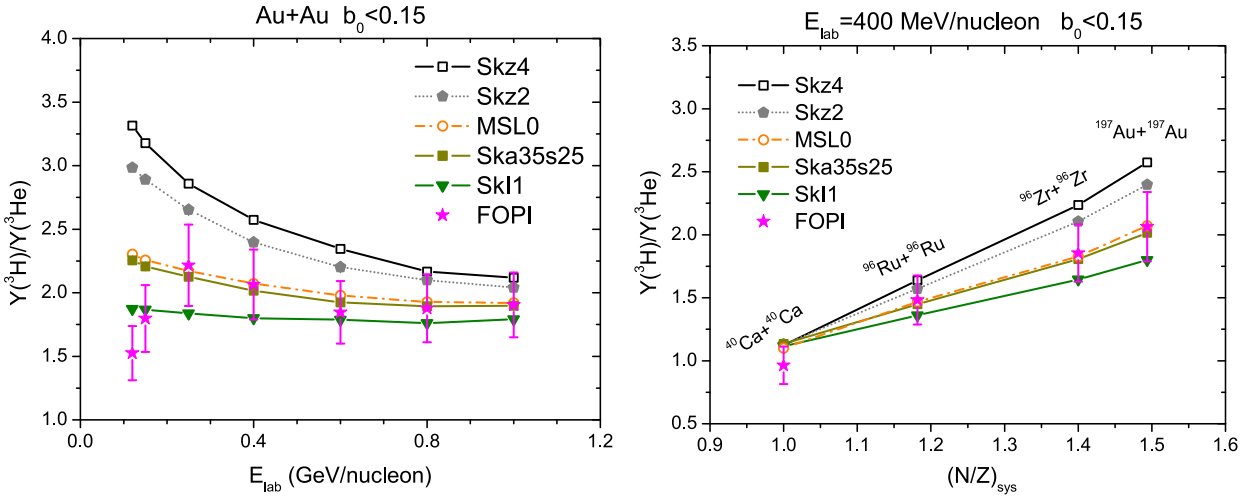

Figure 2.12: Beam-energy dependence of the $t/^3$He ratio in central Au + Au collisions (left) and the system-N/Z dependence of the $t/^3$He ratio in central collisions of four systems at $E_{\mathrm{lab}} = 400\,\mathrm{MeV}$/nucleon (right), compared with the UrQMD calculations. The corresponding L values of the shown Skyrme parametrizations are, Skz4(5.75), Skz2(16.81), MSL0(60.00), Ska35s25(98.89), and SkI1(161.05) in MeV unit, see the reference in detail. Adapted from Ref. [63].

2.5 Cluster Productions and Correlations in Heavy-Ion Collisions

As described in the previous section, theoretical interpretations on heavy-ion collision observables, especially on the π^-/π^+ ratio, have been suffered from a strong model dependence. Another concern is that transport calculations employed for those studies considerably fail to reproduce the experimental yields of $Z = 1, 2$ isotopes. Most of transport models calculate only the motion of single particles (baryons and mesons) in the mean field but not that of composite particles, which could be related to the issue. A possible solution is to explicitly take cluster correlations into account in the dynamical phase of collisions, which has been also shown to have a strong impact on the collision dynamics and final observables of heavy-ion collisions [18–20, 94, 124–126]. In this section, the experimental and theoretical results on clusters in heavy-ion collisions are reviewed.

Abundant bound clusters produced in heavy-ion collisions The intermediate energy domain is much higher than a typical nuclear binding energy of ~ 8 MeV per nucleon. However, this never means that the collision system would totally disintegrate into free nucleons. In fact, the experimental results from the FOPI and INDRA Collaborations [62, 127, 128] show that most of nucleons are emitted as bound clusters, as presented in Fig. 2.13. In the case of central ^{197}Au+^{197}Au collisions at 250 MeV/nucleon, the yields of free protons and neutrons are 33.7 ± 1.7 [62] and 97.9 ± 8.2 [127], each of which corresponds to about 21% and 41% of the total number of protons and neutrons in the system, respectively. Including the ^{197}Au + ^{197}Au system at the highest energy

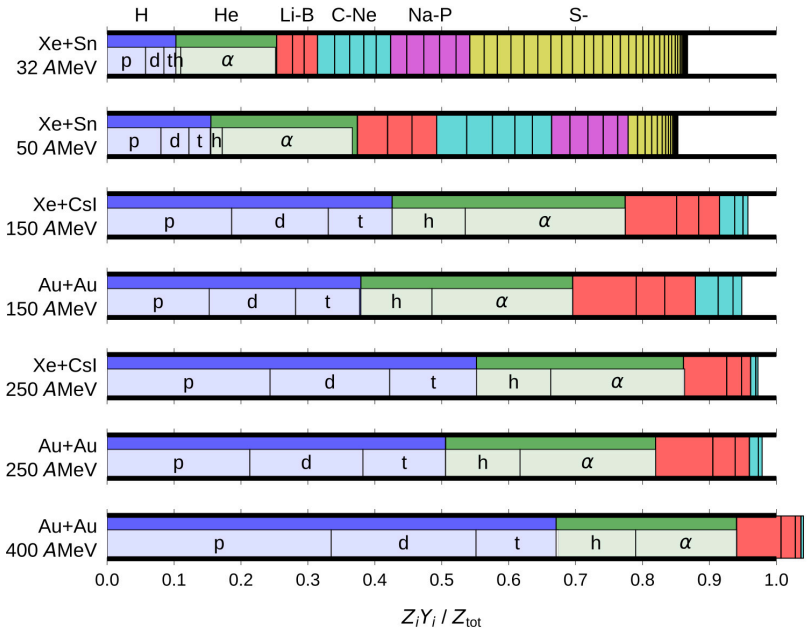

Figure 2.13: Proton occupancies in central collisions of ^{129}Xe + ^{nat}Sn [128], ^{129}Xe + CsI, and ^{197}Au + ^{197}Au [62] systems at intermediate energies. Charge fractions $Z_i Y_i / Z_{tot}$ are presented for experimentally identified particles, with Z_i and Y_i being the proton number and the yield of particle species i, respectively, and the $Z_{tot} = Z_{projectile} + Z_{target}$ represents the total charge in the reaction system. Adapted from Ref. [124].

of 400 MeV/nucleon shown in the figure, more than half of protons in the collision system are emitted as bound clusters. In Ref. [62], it is suggested that the clustered proton fraction stays above 10% up to 4 GeV/nucleon of incident energy, more than two orders of magnitude higher than typical nuclear binding energies. A simple question now arises; how do the light clusters and heavy fragment nuclei emerge in the expanding system, or, what is the cluster production mechanism that must explain their abundant yields? Such the expansion and fragmentation mechanism is also a fundamental property of nuclear matter, which can be related to, *e.g.*, the nuclear liquid-gas phase transition [129]. In the following, we describe the treatment of clusters in transport calculations.

Typical procedure for cluster productions As a theoretical approach to a cluster formation, the phase-space coalescence prescription is usually adopted to recognize clusters from the nucleons phase-space distribution calculated by a transport model. In this prescription, a number of nucleons can form a cluster if their relative distances in coordinate and momentum space are smaller than a set of given coalescence parameters. In brief, after calculating the time evolution of the reaction with a transport model until the moment when particles rarely interact with each other, *i.e.*, freeze-out[8], clusters are formed if propagated nucleons satisfy the conditions of $\Delta r \leq R_c$ and $\Delta p \leq P_c$. The coalescence parameters can be determined based on the fragment charge distribution [11], where the binding energy and/or the isospin dependence of the parameters can be also considered [130]. Since some of clusters may be excited states and/or short-lived ones, their de-excitation processes will be properly treated with a statistical decay code. Within this procedure, many-body correlations are not explicitly considered during the dynamical phase of the reaction, except for ones induced by the mean-field propagation and NN collisions. Therefore, the overestimation of the yield of protons and the underestimation of those of light cluster particles with $A \leq 4$ observed in many studies [11, 12, 63, 88, 127, 131] indicate that many-body correlations, which can enhance a clusterization process, are important degrees of freedom in the collision dynamics.

Explicit consideration of cluster correlations in transport calculations The cluster degrees of freedom can naturally emerge everywhere in a nuclear many-body system. For example, an appearance of the alpha-cluster structure in excited states of nuclei has been predicted and observed [132, 133], and an existence of the alpha cluster on the neutron skin was evidenced by quasi-free alpha knockout reactions [134]. Additionally, recent theoretical studies indicate that in-medium formations and continuum correlations of light clusters with $A \leq 4$ have impacts on the nuclear EOS, and on its application to astrophysical simulations [72, 135–140]. In heavy-ion collision simulations, some transport models explicitly consider cluster correlations in the dynamical phase of collisions [18–20, 94, 124–126, 141–143], see, *e.g.*, Ref. [124] as a review. In Ref. [19], cluster correlations were explicitly taken into account within the AMD transport model so that light clusters are formed in the final states of two-nucleon collisions, and then correlated clusters are propagated according to the equation of motion until the next collision process. A cluster state can be broken mainly by two-nucleon collisions and by the mean-field effect during the propagation. A cluster-cluster binding process, *e.g.*, $t + \alpha \rightarrow {}^7\mathrm{Li}$, is also introduced as a stochastic process. As a result of such the extension, the calculation consistently reproduced the experimental fragment

[8] In the intermediate energy domain, the freeze-out time is typically taken as approximately 100–300 fm/c of the reaction time. Usually it is determined so that final fragment yields hardly depend on the choice of the freeze-out time.

charge distribution in central ^{197}Au + ^{197}Au collisions at 150 and 250 MeV/nucleon. Additionally, the calculation of Xe + Sn at 50 MeV/nucleon with cluster correlations predicted a strong transverse expansion of the compressed matter, *i.e.*, a strong nuclear stopping, compared to without them, which reasonably reproduced the experimental data. As described here, cluster correlations have a drastic impact both on the reaction dynamics and on the final observables. In the following, an impact of cluster correlations in the collision dynamics relevant to the symmetry-energy effect within the framework of the AMD model will be described.

Dynamical effect of cluster correlations relevant to the symmetry-energy effect As described in Sect. 2.4, the high-density behavior of the symmetry energy affects the neutron-proton dynamics in the matter formed in the early phase of heavy-ion collisions. In Ref. [18, 94], the impacts of cluster correlations on the neutron-proton dynamics as well as on the π^-/π^+ ratio are investigated by combining the AMD with the jet AA microscopic (JAM) transport models. Central ^{132}Sn+^{124}Sn collisions at an incident energy of 300 MeV/nucleon and an impact parameter of b = 0–1 fm were calculated with/without cluster correlations for the two cases of symmetry energies: soft and stiff corresponding to L = 46 MeV and 108 MeV, respectively. The density profiles of neutrons and protons in the central part of the colliding system are shown in the upper panels of Fig. 2.14. Obviously, the calculations with cluster correlations lead to more compression of the system than without them. This is likely because cluster correlations localize nucleons within a limited space and widen the Pauli-allowed region where other nucleons can get into. The bottom panels of

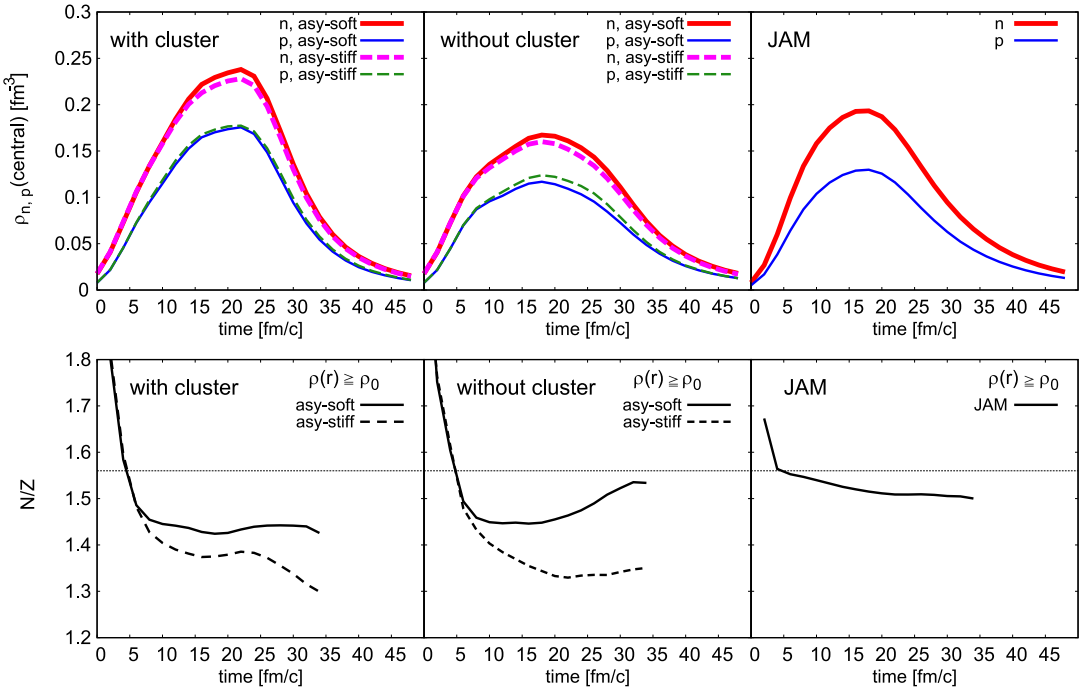

Figure 2.14: Neutron-proton dynamics in central (b = 0–1 fm) ^{132}Sn +^{124} Sn collisions at 300 MeV/nucleon by calculations of the AMD and JAM. Above: neutron and proton densities in the central part of the system within a radius of 2 fm. Bottom: the N/Z ratios in the high density region of $\rho(\boldsymbol{r}) \geq \rho_0$. The left and middle panels present the results from AMD + JAM calculations with cluster correlations turned on and off, respectively. The right panels show the results from JAM calcualtions without the mean field. Adapted from Ref. [94].

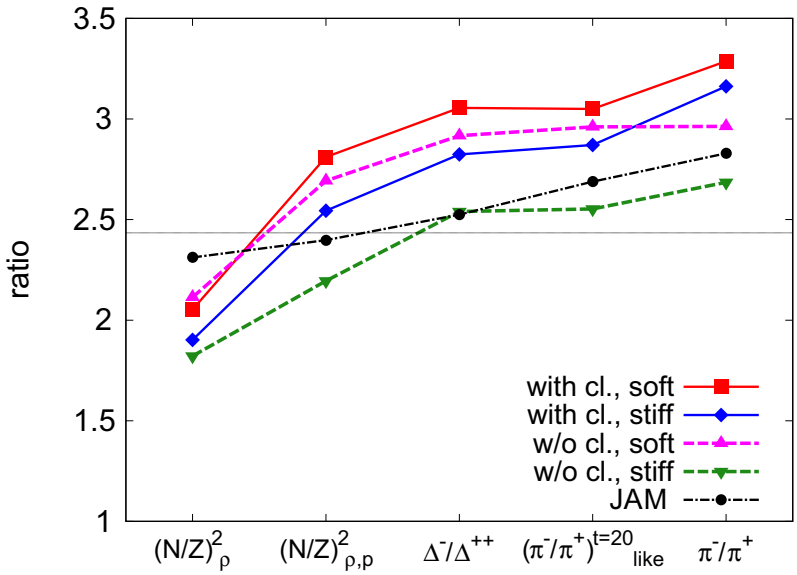

Figure 2.15: The π^-/π^+ yield ratio and relevant ratios based on the theoretical calculations with different options: the AMD + JAM calculation with and without cluster correlations for different stiffness of the symmetry energy, and the single JAM calculation. Adapted from Ref. [94].

Fig. 2.14 present the time evolutions of neutron-to-proton ratios (N/Z) at $\rho \geq \rho_0$. The symmetry-energy effect is evident similarly to the left panels of Fig. 2.7. An important observation is that the N/Z gap between different symmetry energies with cluster correlations is smaller than that without them. This is understandable since a similar number of neutrons and protons in correlated clusters propagates together so that the N/Z is not largely modified.

Effect on final observables Figure 2.15 presents the final π^-/π^+ ratio in central ^{132}Sn + ^{124}Sn collisions at 300 MeV/nucleon together with isospin-relevant ratios expected to be related to the π^-/π^+ ratio. As we do not describe the intermediate observables in the figure in detail, see Ref. [18] for values in each column. What should be noted is that the difference in the final π^-/π^+ ratio between the soft and stiff symmetry energies is smaller with cluster correlations than that without them. This observation may stem from the fact that the high-density N/Z ratio in calculations with cluster correlations is weakly sensitive to the symmetry energy compared to without them, as seen in the bottom panels of Fig. 2.14. Moreover, the dependence of the final π^-/π^+ ratio on the cluster correlations is almost comparable to that on the symmetry-energy stiffness.

In Ref. [125], the sensitivity to the symmetry energy in the $(N/Z)_{\rm gas} = \sum_{A=1}^{4} M_n / \sum_{A=1}^{4} M_p$ was also observed, with M_n and M_p being the number of neutrons and protons contained in light particles from nucleons to alphas, respectively. Figure 2.16 presents the kinetic energy distributions of the final $(N/Z)_{\rm gas}$ in central ^{132}Sn + ^{124}Sn collisions at 300 MeV/nucleon. In calculations with the stiff symmetry energy of $L = 108$ MeV, a higher $(N/Z)_{\rm gas}$ ratio in the high kinetic energy region is predicted compared to that with the soft one of $L = 46$ MeV, and vice versa. This trend is similar to the dynamical effect of the density-dependent symmetry energy in the early compression phase of collisions, *i.e.*, the stiffer symmetry energy will accelerate neutrons and decelerate protons more than the soft one. This observation indicates that the dynamical effect in the early phase is likely to be preserved because cluster correlations make particles in the expansion phase quickly

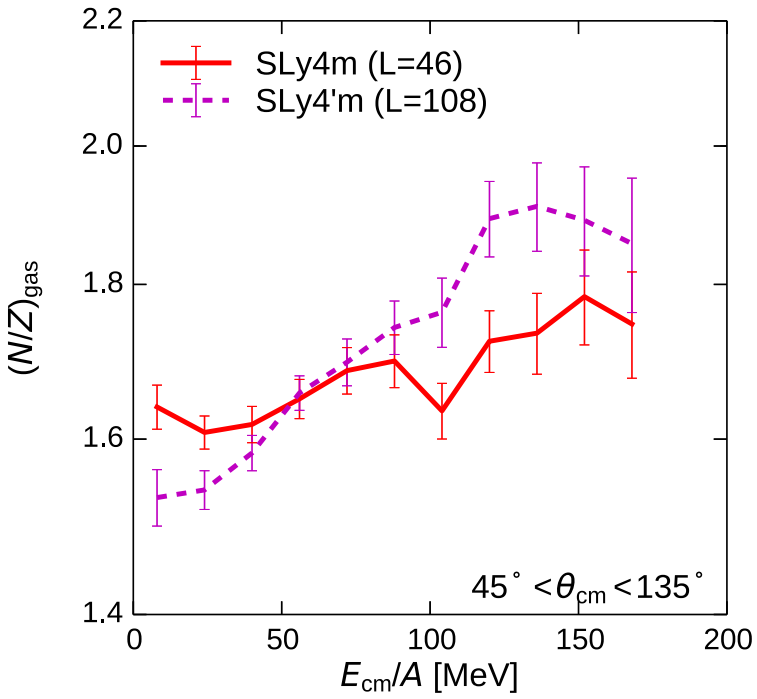

Figure 2.16: Spectra of $(N/Z)_{\rm gas}$ as a function of kinetic energy per nucleon in central ^{132}Sn + ^{124}Sn collisions at 300 MeV/nucleon by the AMD with cluster correlations. Here light particles with mass numbers $1 \leq A \leq 4$ emitted perpendicular to the beam axis in the center of mass frame ($45° < \theta_{\rm cm} < 135°$) are summed to construct the $(N/Z)_{\rm gas}$ ratio. Adapted from Ref. [125].

stop interacting with each other and not be strongly modified. In fact, such the symmetry-energy dependence was not observed in the final $(N/Z)_{\rm gas}$ ratio without cluster correlations [125], even though the dependence is evidently seen in the early phase as presented in the bottom-middle panel of Fig.2.14. This is because the interaction between particles continues for a long time in the expansion phase without cluster correlations so that the dynamics is too modified to preserve the information in the early phase. Therefore, it is important to understand properties of cluster correlations well for confirming the sensitivity to the high-density behavior of the symmetry energy in heavy-ion collision observables. Recently, a more detailed study on the suppression of cluster correlations depending on the phase-space density was provided [20]. The refined AMD model successfully described the experimental data on the fragment-charge-dependent nuclear stopping and the cluster yield distribution in Xe + CsI reactions at 250 MeV/nucleon.

As described up to here, explicitly considering the cluster degrees of freedom as many-body correlations in the dynamical phase is important not only for understanding the entire collision dynamics but also for obtaining reliable information on the density-dependent symmetry energy. To constrain a strength of correlations, we need to understand the sensitive observables comprehensively, *e.g.*, yields and momentum distributions of particles from nucleons to clusters, and the degree of nuclear stopping. Investigating a two (or more) particle correlation function may be also good to know the property of cluster correlations [144, 145].

2.6 SπRIT Experimental Project

In the previous studies based on the FOPI data, it was difficult to clearly distinguish dependencies on mass, charge, and isospin asymmetry of the system. For example, the N/Z dependence of the π^-/π^+ ratio in Fig. 2.9 and that of the $t/^3$He ratio in Fig. 2.12 can contain the charge and mass dependence as well. And besides, low statistics and the inefficiency of the low-p_T region were issues for the charged pion measurement [10].

To stringently constrain the density dependence of the symmetry energy particularly at suprasaturation densities, the SπRIT Collaboration proposed a systematic measurement of isospin-asymmetric Sn + Sn collisions utilizing unstable beams at Radioactive Isotope Beam Factory (RIBF) in RIKEN. By constructing relative and/or differential observables between two Sn+Sn systems with different isospin asymmetry, the isoscalar and Coulomb effects as well as systematic uncertainties can be canceled out, and the isovector effect driven by the symmetry energy can be enhanced. In addition, Sn isotopes have the proton magic number of $Z = 50$, and therefore, high-purity and high-intensity radioactive Sn beams in both neutron-rich and neutron-deficient sides are available at RIBF. As a central collision with a small cross section is our main focus for probing the high-density matter, such high-quality radioactive beams will be conducive to reducing the statistical uncertainty. To measure yields and momenta of light charged particles including π^- and π^+ with a high efficiency and a wide acceptance, a large volume time projection chamber (TPC) has been developed together with ancillary trigger detectors. The whole detection system was commissioned outside the magnet in October 2015 with ^{79}Se beams impinging on an Al target, and inside the magnet at the beginning of April 2016 with ^{132}Sn beams on a natural Sn target.

In the spring of 2016, the first series of experiments was conducted at RIBF. As tabulated in Table 2.1, four kinds of Sn + Sn reactions at an incident beam energy of about 270 MeV/nucleon were measured. Neutron-rich ^{132}Sn and neutron-deficient ^{108}Sn radioactive isotope beams allowed us to survey Sn+Sn systems with the broadest range of isospin asymmetries ever ($\delta_{\rm sys} = 0.09$–0.22), which has been impossible so far by the use of stable Sn beams (with mass numbers $A = 112$–124). In addition, the ^{132}Sn + ^{124}Sn is the most isospin asymmetric system out of measured in the intermediate energy domain. In this dissertation, we focus on the data taken in the two reactions: the neutron-rich ^{132}Sn + ^{124}Sn system and the neutron-deficient ^{108}Sn + ^{112}Sn system.

Table 2.1: A set of Sn + Sn reactions measured in the first series of the SπRIT experiments.

Proposal No.	System	$(N/Z)_{\rm system}$	Note
NP1312-SAMURAI22	^{108}Sn + ^{112}Sn	1.2	Neutron deficient
	^{112}Sn + ^{124}Sn	1.36	Interm. asymmetry
NP1306-SAMURAI15	^{132}Sn + ^{124}Sn	1.56	Neutron rich
	^{124}Sn + ^{112}Sn	1.36	Interm. asymmetry

2.7 Thesis Objective

The primary motivation of this work is to probe the high-density symmetry energy by the systematic measurement of Sn + Sn reactions with a wide range of isospin asymmetries. As described in this introductory chapter, a detailed understanding of the collision dynamics and its relation to final observables within a transport theory are inevitable to extract reliable physics information from experimental observables in heavy-ion collisions. Among various physical properties, many-body correlations that introduce a formation and disintegration of clusters seem to have a strong impact on the collision dynamics. It has been predicted that cluster correlations studied within the AMD transport calculation play an important role in the reproduction of the experimental data but modify the sensitivity to the symmetry energy [18–20, 94, 125]. Thus, it is better to first go over a global character of reactions including the production of clusters and to subsequently investigate the specific symmetry energy effects in the experimental observable. In the present work, we will focus on rapidity distributions ($\mathrm{d}N/\mathrm{d}y$) of hydrogen isotopes: protons, deuterons, and tritons for grasping a global property in heavy-ion collisions and for discussing the isospin dynamics. First of all, hydrogen isotopes are predicted to carry information on the high-density symmetry energy [63, 87, 125]. The $\mathrm{d}N/\mathrm{d}y$ distribution has been widely used to discuss the degree of nuclear stopping [47, 62, 146–149] which quantifies the kinetic energy transfer from a longitudinal (beam-axis) to a transverse direction. From the microscopic point of view, it is associated with important parameters in the model calculation such as cluster correlations [19, 20, 125] and in-medium two-nucleon scattering cross sections [146, 148, 150, 151]. The $\mathrm{d}N/\mathrm{d}y$ distribution is also informative for investigating the isospin degrees of freedom in collisions. In Refs. [147, 150, 152], the isospin equilibration in the collision system was examined by constructing the ratio of $\mathrm{d}N/\mathrm{d}y$ distributions between projectile-target flipped reactions, *e.g.*, ^{96}Zr + ^{96}Ru vs. ^{96}Ru + ^{96}Zr, or constructing the so-called isospin tracer observable [150]. Such the isospin observable of the $\mathrm{d}N/\mathrm{d}y$ spectral ratio has been also discussed in relevant to the density-dependent symmetry energy [147, 149, 153]. For these reasons, the rapidity distributions of hydrogen isotopes are useful for understanding the property of heavy-ion reactions in both terms of the EOS (as a mean-field potential in a transport model) and a microscopic character such as the in-medium σ_{NN}.

The strategy of the present work is as follows. The measured $\mathrm{d}N/\mathrm{d}y$ distributions of hydrogen isotopes in central collisions of the ^{132}Sn + ^{124}Sn and ^{108}Sn + ^{112}Sn systems are analyzed by the AMD transport calculation which was refined to explicitly consider cluster correlations in the dynamical phase of reactions [17–20]. As necessary, parameters in calculations will be tuned to reproduce the experimental $\mathrm{d}N/\mathrm{d}y$ distributions as reasonably as possible. The isospin dynamics in the reactions is discussed using the deuteron-to-proton (d/p) and triton-to-proton (t/p) single and double spectral ratios. The behavior of the cluster-to-proton ratios is expected to relate with that of neutrons if one postulates the isoscaling property [59, 154] observed in the lower incident energy domain. Thus, the cluster-to-proton ratio can be a measure of the population of neutrons along the rapidity (beam) axis, which can be affected by the symmetry energy. In the end, we discuss the symmetry-energy effect in the d/p and t/p double spectral ratios by comparing the AMD calculations with carefully considering the effect from parameter adjustments.

3 Experiment

In this chapter, we describe a technical detail relevant to the SπRIT experiment: the RIBF complex (Sect. 3.1), the detection system for reaction products from Sn + Sn collisions (Sect. 3.2), and the electronics for the data acquisition system and the trigger system (Sect. 3.3). The summary of the accumulated data is provided in Sect. 3.4.

3.1 Radioactive Isotope Beam Factory

The Radioactive Isotope Beam Factory (RIBF) [155, 156] in RIKEN is a cyclotron accelerator facility, which provides high-intensity RI beams at a kinetic energy around 200–300 MeV/nucleon. The advent of a variety of fast RI beams has enabled us to explore properties of unstable nuclei far from the stability line in the nuclear chart, see, *e.g.*, reviews [157–159].

The schematical layout of the RIBF is depicted in Fig. 3.1. The accelerator complex of the RIBF consists of three injectors (RILAC, RILAC2, AVF) and four ring cyclotrons (RRC, fRC, IRC, SRC). With the cyclotrons cascade, heavy ions ranging from (polarized) deuteron to uranium can be accelerated up to more than 70% of the light speed. RI beams are produced via fragmentation or fission of heavy ions and separated by the in-flight superconducting fragment separator BigRIPS. In the downstream ends, powerful equipment for different purposes are installed, *e.g.*, the ZeroDegree Spectrometer (ZDS) for forward-angle ejectiles, a large-acceptance and a multi-particle spectrometer (SAMURAI: Superconducting Analyzer for MUlti-particles from RAdioIsotope beams), a high-momentum-resolution spectrometer (SHARAQ), and the Rare-RI ring for a precise RI mass measurement. The SπRIT experiment was carried out at the SAMURAI area to measure charged particles and neutrons from Sn + Sn collisions, making the best use of the large acceptance and high analyzing power for multi-particles.

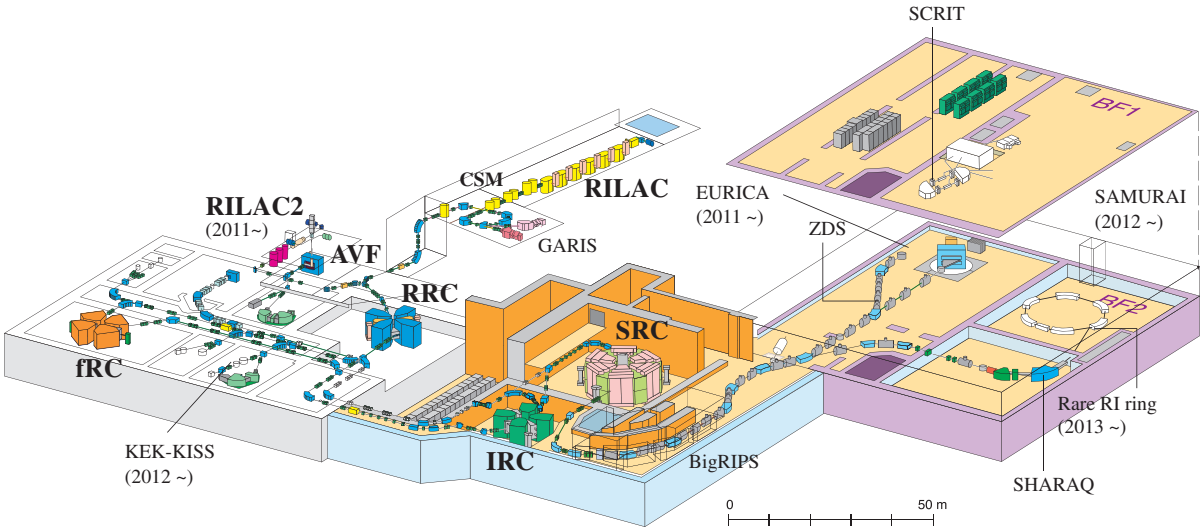

Figure 3.1: The bird's eye view of the RIBF. Adapted from Ref. [156].

3.1.1 Production of radioactive Sn beams

The ^{108}Sn and ^{132}Sn isotope beams used in the present work were produced as secondary products of projectile fragmentation of ^{124}Xe and fission of ^{238}U, respectively, where the ^{124}Xe and ^{238}U isotopes were accelerated as primary beams, as described in the following.

Acceleration of primary beams At the RIBF, three acceleration modes are available depending on beam nuclides, as shown in Fig. 3.2. In the present experiment, the "fixed-energy mode" was employed for accelerating uranium and xenon ions. In this mode, $^{238}U^{+35}$ or $^{124}Xe^{+25}$ ions are extracted by the RIKEN superconducting electron cyclotron resonance ion source (SC-ECRIS) using a 28 GHz gyrotron [160, 161]. Extracted ions are accelerated by the latter linac injector, RIKEN Heavy-ion Linac 2 (RILAC2) [162], up to an energy of 670 keV/nucleon, and subsequently, injected to downstream cyclotrons. Three room-temperature cyclotrons: RRC, fRC, IRC, and the superconducting ring cyclotron (SRC) are operated in cascade [163]. The intermediate cyclotron fRC is sandwiched by two charge strippers (ST3, ST4). The stripper ST3 utilizes helium gas [164] and the ST4 utilizes a rotating graphite disk [165]. The two-strippers operation allows accelerated ion beams to be fully stripped[1]. The final kinetic energy of the primary ^{238}U and ^{124}Xe beams is 345 MeV/nucleon.

In-flight productions of Sn isotope beams The RIBF uses projectile fragmentation and fission of heavy nuclei to produce a variety of RI beams with a wide range of neutron richness [166, 167]. In the projectile fragmentation reaction, both neutron- and proton-rich nuclei are produced as a fragmentation residue with a lighter mass than the projectile [168–170]. A characteristic of the projectile fragmentation is that the residue has almost the same velocity as the projectile, *i.e.*, a

[1]In general, heavy-ion beams extracted from an ion source have orbital electrons. In order to efficiently accelerate heavy ions up to high energies, those electrons should be stripped. Here a fully stripped ion means that the the every orbital electrons are stripped from the nucleus.

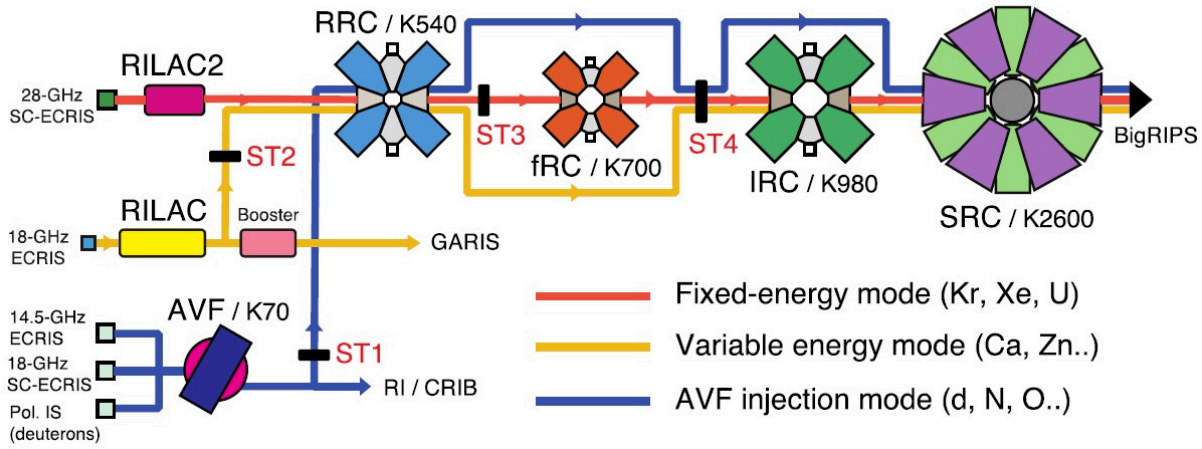

Figure 3.2: Beam acceleration modes in the RIBF. Adapted from Ref. [163].

small emittance of secondary beams. On the other hand, the in-flight fission of uranium is expected to be more advantageous in producing neutron-rich nuclei with medium-heavy mass compared to the projectile fragmentation [171–174]. However, because of the fission kinematics, a fission fragment has typically larger fluctuations in momentum and in angle. Therefore, the downstream spectrometer for separating and analyzing the secondary RI beams requires a large angle and momentum acceptance. The design of the BigRIPS fragment separator is optimized for the in-flight fission of 345 MeV/nucleon of ^{238}U isotopes as well as the projectile fragmentation reaction of medium-mass nuclei such as ^{124}Xe, as described in the next section.

In the present experiment, the neutron-rich ^{132}Sn and ^{124}Sn isotopes were produced via the in-flight fission of ^{238}U beams while the neutron-deficient ^{112}Sn and ^{108}Sn isotopes were produced via the projectile fragmentation of the ^{124}Xe beams. The beryllium production targets were installed at the entrance of the BigRIPS, see Fig. 3.3. The target thickness was 4 mm for ^{132}Sn productions but 0.1 mm for productions of the other isotopes: ^{124}Sn, ^{112}Sn, and ^{108}Sn. In addition to the tin isotope beams, cocktail beams of light charged particles at 100 MeV and 300 MeV were also produced for the purpose of the detector calibration. Table 3.1 lists the configuration of secondary beam productions.

Table 3.1: List of the primary and secondary beams in the SπRIT experiment.

Secondary beam	^{132}Sn	^{124}Sn	^{112}Sn	^{108}Sn	Z = 1–3
Primary beam	^{238}U	^{238}U	^{124}Xe	^{124}Xe	^{238}U
Beam kinetic energy	fixed 345 MeV/nucleon				
Be production target	4 mm	0.1 mm	0.1 mm	0.1 mm	5 mm

3.1.2 In-flight fragment separator: BigRIPS

The projectile fragmentation reaction and the in-flight fission of uranium yield various kinds of RIs. In principle, possibly every isotope species with a lighter mass than the projectile can be produced, hence a need for separating the isotope of interest. The BigRIPS fragment separator [175] is designed for an in-flight separation and identification of RI beams with a two-stage structure. The schematic view of the BigRIPS is presented in Fig. 3.3. The BigRIPS consists of seven focal planes (F1–F7), six room-temperature dipole magnets (D1–D6), and fourteen superconducting triplet quadrupole magnets located back and forth of each focal plane. The F3 and F7 foci are fully momentum achromatic planes while F1 and F5 foci are momentum dispersive planes. The ion-optical acceptance is typically characterized by ±40 mrad and ±50 mrad of the horizontal and vertical angular acceptances, respectively, and ±3% of the momentum acceptance, each of which is comparable with the kinematical spread of the uranium fission products in the energy domain of RIBF. The collection efficiency is approximately 50% of the uranium fission products, which enables us to utilize intense RI beams.

The first stage of the BigRIPS from F0 (Target in the figure) to F2 foci functions as an RI separator. At the second stage of the BigRIPS from F3 to F7 foci, beamline detectors for RI beam identifications are installed. The configurations of BigRIPS parameters during the measurements, such as bending power of the dipole magnets (D1–D6), openings of slits, presence/absence and thickness of energy degraders, are tabulated in Table 3.2. The parameters were optimized during the beam-tuning phase so that the Sn isotopes of interest were transported to the SAMURAI area as high energy and purity as possible, and so that the Sn beams impinged onto approximately center of the Sn target located inside the SAMURAI magnet.

In the followings, we describe the RI beam separation principle in the first stage ($B\rho$-ΔE-$B\rho$ method [176]), the RI beam identification principle in the second stage (TOF-$B\rho$-ΔE method [177]), and beamline detectors such as a plastic scintillation counter, a parallel-plate avalanche counter (PPAC) [178, 179], and a multi-sampling ionization chamber (MUSIC) [180].

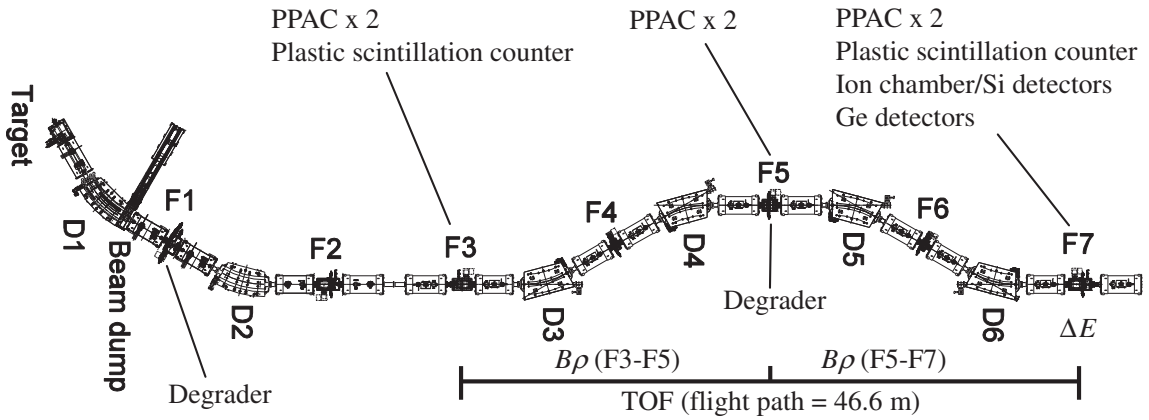

Figure 3.3: The schematic view of the BigRIPS fragment separator. Note that the "PPAC" in the figure means a double PPAC which is described later. Si and Ge detectors at F7 were not used in the present experiment. Adapted from Ref. [177].

Table 3.2: List of parameter configurations of the BigRIPS for different measurements. The slit positions of left and right can be optimized separately, where $\pm d$ mm in the "slit openings" rows means that the opening of slits is d mm in both left and right. In the magnet settings, the values of the central magnetic rigidity (magnetic field flux × curvature radius) in the unit of tesla·meter (T m) are listed. The central magnetic field values were measured by an NMR probe. During the measurement, the NMR for the D1 magnet didn't return correct values. Therefore, the designated values by the control monitor are written in the "D1" row in the table.

Isotope tuned	^{132}Sn	^{124}Sn	^{112}Sn	^{108}Sn	Z = 1–3 300 MeV	Z = 1–3 100 MeV
Aluminum degrader settings						
F1 degrader	2 mm	3 mm	1.4 mm	1.4 mm	5 mm	empty
F5 degrader	empty	empty	empty	empty	2.5 mm	empty
Slit openings (mm)						
F1 slit	±2	±8	±2	±2	±5	±5
F2 slit	±2	±1	±1	±1	±5	±6
F5 slit	±30	±12	±6	±6	±50	±100
F7 slit	±30	±5	L:+11, R:-5	L:+10, R:-4	L:+39, R:+21	L:+51, R:+9
Central magnetic rigidity in the magnet (T m)						
D1[a]	7.5605	7.3048	6.4430	6.2003	5.4339	3.0209
D2	7.1821	6.7931	6.1976	5.9584	5.4294	3.0257
D3	7.1400	6.7482	6.1379	5.9258	5.4176	2.9837[b]
D4	7.1443	6.7520	6.1416	5.9293	5.4204	2.9872
D5	7.1487	6.7550	6.1410	5.9283	5.4212	3.0030
D6	7.1421	6.7510	6.1384	5.9259	5.4197	3.0038

[a] The central magnetic rigidity values designated for the D1 magnet by the control monitor are shown.

[b] Somehow the NMR at D3 didn't work at the calibration runs using coctail of Z = 1–3 beams at 100 MeV. Therefore, the designated value is given here.

Principle of the RI beam separation: $B\rho$-ΔE-$B\rho$ method

In the first stage of the BigRIPS, RI beams are separated and purified via the two-step separation using a magnetic response of charged particles, the so-called $B\rho$-ΔE-$B\rho$ method [176], with $B\rho$ and ΔE being magnetic rigidity and energy loss, respectively.

First RI separation The first separation uses the $B\rho$ of beam particles, which is related to the mass-to-charge ratio A/Q as follows. Let us assume a nucleus with charge q and mass m is traveling under a magnetic field B with velocity v. The relativistic equation of motion is given as:

$$qvB = \frac{\gamma m v^2}{\rho}. \tag{3.1}$$

Here $\gamma = 1/\sqrt{1-\beta^2}$ is the Lorentz factor with $\beta = v/c$ and the speed of light c. The ρ represents a curvature radius of the motion. Then, the relationship between $B\rho$ and A/Q can be obtained as:

$$B\rho = \frac{\gamma m v}{q} = \frac{\gamma m_u \beta c}{e} \cdot \frac{A}{Q}, \tag{3.2}$$

with the elementary charge e and the atomic mass unit m_u. Note that the Q includes a charge state[2], *i.e.*, $Q = Z$ if the nucleus is fully stripped. In the case of the present experiment using fast RI beams of approximately 300 MeV/nucleon, it is assumable that the most of the ions are fully stripped, and $Q = Z$ unless otherwise specified in the following. According to Eq. 3.2, ion beams with the same incident angle, $\beta\gamma$, and A/Q travel the same trajectory determined by $B\rho$ in the magnetic field. Practically, an incident angle and $\beta\gamma$ are nearly equal for in-flight RI beams, and thus, a desired A/Q region can be separated by restricting the trajectory using a slit. In the BigRIPS, the slit is installed at the exit of the D1 dipole magnet. To further narrow the isotope selection, an energy degrader is combined in the second separation as follows.

Second RI separation To further separate RI beams after the first separation, the energy degrader is inserted right after the slit at F1. The empirical parametrization of energy loss in a material can be a form of $dE/dx \propto Z^2/E^{g-1}$, which provides the stopping range $\tilde{R}(A, Z, E)$ as [176]:

$$\tilde{R}(A, Z, E) \simeq k\frac{A}{Z^2}E^g + CA, \tag{3.3}$$

where E is a kinetic energy per nucleon, k, C, and g are constants depending only on a stopping material. In the case that the kinetic energy of a beam particle changed from E_1 to E_2 by the passage of a degrader with a thickness d, the following equation can be led:

$$\tilde{R}(A, Z, E_1) = d + \tilde{R}(A, Z, E_2). \tag{3.4}$$

Then, with substituting Eq. 3.3 into Eq. 3.4 and using the reduced range $R(A, Z, E) = k(A/Z^2)E^g$, the kinetic energy after the degrader can be calculated as:

$$E_2 = E_1\left(1 - \frac{d}{R(A, Z, E_1)}\right)^{1/g}. \tag{3.5}$$

[2]When a high-Z beam passes through a material, it can take along a few electrons in atoms constituting the material, *i.e.*, the so-called "charge state". If a nucleus with an atomic number of Z has n electrons in its orbit, the magnetic response of the charge state depends on the pseudo charge $Q = Z - n$.

By substituting magnetic rigidity $B\rho_1$ and $B\rho_2$ into kinetic energies E_1 and E_2,

$$\begin{aligned} B\rho_2 &= B\rho_1\left(1-\frac{d}{R(A,Z,E_1)}\right)^{1/2g}\cdot\sqrt{\frac{E_2+2m_u}{E_1+2m_u}} \\ &\simeq B\rho_1\left(1-\frac{d}{R(A,Z,E_1)}\right)^{1/2g}, \end{aligned} \tag{3.6}$$

with neglecting the right end term for a simplicity[3]. Using an approximation of $B\rho \approx \kappa A/Z\sqrt{E}$ with a constant κ, which is equivalent to $R(A,Z,E) = k\kappa^{-2g}\left(Z^{2g-2}/A^{2g-1}\right)B\rho^{2g}$, the $B\rho_2$ can be expressed as:

$$B\rho_2 = B\rho_1\left(1-\frac{d}{k\kappa^{-2g}}\frac{A^{2g-1}}{Z^{2g-2}}B\rho_1^{-2g}\right)^{1/2g}. \tag{3.7}$$

If an empirically deduced value of $g = 1.75$ for an aluminum degrader is adopted, the second RI beam separation can be achieved according to $A^{2.5}/Z^{1.5}$. At the F1 focal plane, a wedge-shaped aluminum degrader is normally installed not to disrupt the achromatic ion-optical condition.

As described up to here, the two separation methods are sensitive to A/Q and A^{2g-1}/Z^{2g-2}, which enables us to transport only objective isotopes in the desired A/Q vs. Z space to the second stage of the BigRIPS.

Principle of the RI beam identification: TOF-$B\rho$-ΔE method

Basics of the TOF-$B\rho$-ΔE method The RI cocktail beams are identified in an event-by-event basis according to the TOF-$B\rho$-ΔE method (TOF: time-of-flight) which deduces an atomic number Z and a mass-to-charge ratio A/Q of beam isotopes [177]. The physical quantities used in the TOF-$B\rho$-ΔE method are as follows:

$$\mathrm{TOF} = \frac{L}{\beta c}, \tag{3.8}$$

$$B\rho = \frac{\gamma m_u \beta c}{e}\cdot\frac{A}{Q}, \tag{3.9}$$

$$\Delta E = \int_{\Delta x}\left(-\frac{dE}{dx}\right)dx, \tag{3.10}$$

where L is a flight-path length. The mean energy loss of charged particles in a matter can be deduced based on the empirical Bethe-Bloch formula as:

$$-\left\langle\frac{dE}{dx}\right\rangle \propto \frac{Z^2}{\beta^2}\left[\ln\frac{2m_e c^2\beta^2}{I} - \ln\left(1-\beta^2\right) - \beta^2\right]. \tag{3.11}$$

Here m_e is the electron mass, and I is the mean excitation energy of atoms in the material. By solving the simultaneous equation composed of Eq. 3.8, Eq. 3.9, and Eq. 3.10, unknown variables: β, Z, and A/Q can be identified.

The magnetic rigidity $B\rho$ can be deduced based on the ion-optical transfer matrix analysis. Let (x,θ) be an expression of the optical vector of ion beams with x and θ being the distance and

[3]At intermediate energies, the right end term is not negligible for obtaining a precise value of $B\rho_2$. However, its influence can be considered to be negligibly small for discussing the isotope separation power.

angle from the optical axis, respectively. When a beam particle travels under magnetic fields of dipoles, and optical vectors changes from (x_1, θ_1) to (x_2, θ_2), the transformation of two vectors can be represented by the following ion-optical matrix equation (as a first-order approximation):

$$\begin{pmatrix} x_2 \\ \theta_2 \\ \delta \end{pmatrix} = \begin{pmatrix} (x|x) & (x|\theta) & (x|\delta) \\ (\theta|x) & (\theta|\theta) & (\theta|\delta) \\ 0 & 0 & 1 \end{pmatrix} \begin{pmatrix} x_1 \\ \theta_1 \\ \delta \end{pmatrix} \tag{3.12}$$

The $(x|x) = \partial x_2/\partial x_1|_{\theta_1=0,\delta=0}$ and so on represent the transfer matrix elements. The δ denotes the momentum dispersion of ion beams from the central rigidity $B\rho_0$, which is defined by

$$B\rho = (1+\delta)B\rho_0. \tag{3.13}$$

The Eq. 3.12 can be solved as:

$$\begin{pmatrix} \theta_1 \\ \delta \end{pmatrix} = \begin{pmatrix} (x|\theta) & (x|\delta) \\ (\theta|\theta) & (\theta|\delta) \end{pmatrix}^{-1} \cdot \left[\begin{pmatrix} x_2 \\ \theta_2 \end{pmatrix} - \begin{pmatrix} (x|x) \\ (\theta|x) \end{pmatrix} \cdot x_1 \right]. \tag{3.14}$$

Therefore, $B\rho$ of ion beams can be deduced by the two optical vectors measured at upstream and downstream of dipole magnet(s) together with the ion-optical transfer matrix. In the BigRIPS, position-sensitive detectors (such as PPAC and/or MWPC) are located at F3, F5, and F7 foci to measure the beam positions around each focus, and to reconstruct beam trajectory by their interpolations. Thanks to a wealth of experimental experiences at RIBF, the optimized ion-optical transfer matrices for the beam optics of the BigRIPS are available except for special cases such as those utilizing very heavy or very unstable isotope beams.

Practical case in the present experiment In the present experiment, the PPACs were placed at F3, F5, and F7 foci to measure the positions and angles of the beam particles. Trajectories in the F3–F5 and F5–F7 sections are reconstructed from optical vectors measured at each focal plane. The ΔE was measured by the MUSIC detector at F7 focal plane, and the TOF between F3 and F7 foci was measured by the plastic scintillation counters. In this case, several modifications are applied to the equations described above due to the energy deposit in the material at F5 focal plane. With consideration of the change of the velocity at F5 focus, Eqs. 3.8 and 3.9 are rewritten as:

$$\mathrm{TOF}_{37} = \frac{L_{35}}{\beta_{35}c} + \frac{L_{57}}{\beta_{57}c}, \tag{3.15}$$

$$\left(\frac{A}{Q}\right)_{35} = \frac{B\rho_{35}}{\beta_{35}\gamma_{35}} \cdot \frac{e}{m_u c}, \tag{3.16}$$

$$\left(\frac{A}{Q}\right)_{57} = \frac{B\rho_{57}}{\beta_{57}\gamma_{57}} \cdot \frac{e}{m_u c}, \tag{3.17}$$

where the subscripts of "35", "57", and "37" represent the quantity with respect to the F3–F5, F5–F7, and F3–F7 sections, respectively. If the A/Q value doesn't change at F5,

$$\frac{B\rho_{35}}{B\rho_{57}} = \frac{\beta_{35}\gamma_{35}}{\beta_{57}\gamma_{57}}. \tag{3.18}$$

By simultaneously solving Eqs. 3.15 and 3.18, beam velocities before and after F5 plane, β_{35} and β_{57}, can be deduced. Then, the A/Q can be obtained from Eq. 3.16 or Eq. 3.17. By rearranging Eq. 3.11, an atomic number Z can be obtained as:

$$Z = C_1\beta_{57}\sqrt{\frac{\Delta E}{\ln\frac{2m_e c^2\beta_{57}^2}{I} - \ln\left(1-\beta_{57}^2\right) - \beta_{57}^2}} + C_2. \tag{3.19}$$

Here the C_1 and C_2 are empirical coefficients.

3.1.3 Detector systems in BigRIPS

Plastic scintillation counters

Plastic scintillation counters are located at F3 and F7 foci to measure the TOF of beam isotopes. The size of the plastic is 120 mm × 100 mm in area and 0.2 mm in thickness. Scintillation photons are read by two photomultiplier tubes (PMTs) attached to both ends of the plastic. The typical operation voltage of the PMT was 1600 V. The charge and timing information of the PMT signals are recorded by the V792 charge-to-digital converter (QDC) and the V1290 multi-hit time-to-digital converter (TDC), respectively. A hit timing t can be calculated by the average of the two timings of the PMTs on the left (t_L) and right (t_R) of the plastic:

$$t = \frac{t_L + t_R}{2}. \tag{3.20}$$

Also, the TOF in the F3–F7 section can be calculated as:

$$\mathrm{TOF} = t_{\mathrm{F7}} - t_{\mathrm{F3}} + t_{\mathrm{off}}, \tag{3.21}$$

where t_{F3} and t_{F7} are timings measured at F3 and F7 foci, respectively. The t_{off} is a timing offset derived from cable delay. The QDC information was used to correct the time-walk effect, which will be described in Sect. 4.1.2. As a means of preventing the plastics from light-output deteriorations due to the irradiation of high-intensity RI beams, the position of the plastics can be shifted up and down. We moved them several times during the ^{132}Sn + ^{124}Sn and ^{124}Sn + ^{112}Sn runs based on the experiences of the first physics experiment of the ^{108}Sn + ^{112}Sn and ^{112}Sn + ^{124}Sn runs.

PPAC

The position-sensitive Parallel Plate Avalanche Counter (PPAC) [178, 179] is a gaseous detector with a delay-line readout, which was used to reconstruct beam trajectories. Figure 3.4 presents the schematic drawing of the PPAC. The PPAC consists of a cathode-anode-cathode electrode configuration, in which one cathode serves for the x-position measurement and another one for the y position. The electrodes are made by a vacuum metal deposition onto Mylar films. The cathode forms metal-deposition strips of 2.4 mm wide in a 2.55-mm pitch on the inner side of the film. The active gas was isobutane and the typical bias voltage applied between the cathode and anode was about 700–750 V. Signals induced on the strip are transmitted through the delay line toward both terminals, X1 and X2 (or Y1 and Y2). They are amplified and processed by the constant fraction

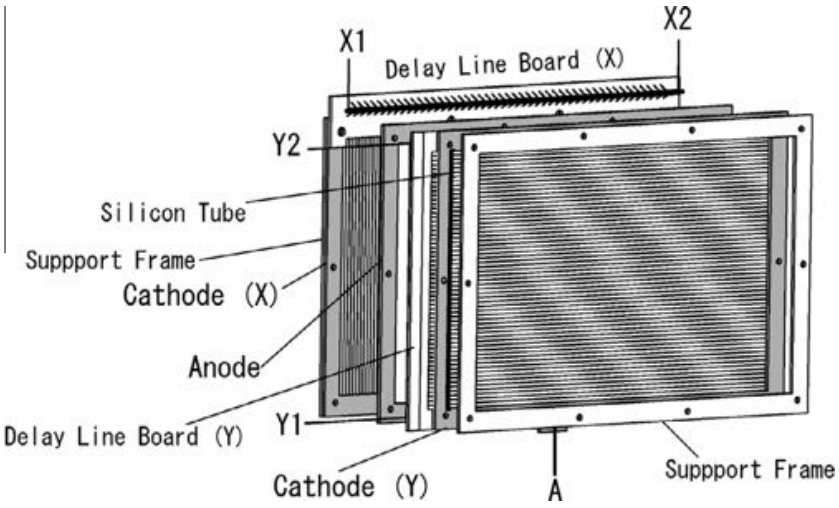

Figure 3.4: Schematic drawing of the 240×150 mm PPAC detector. Adapted from Ref. [179].

discriminator to measure delay times. The delay times of the terminals X1, X2, Y1, Y2, and a timing of a signal of the anode plane (T_{X1}, T_{X2}, T_{Y1}, T_{Y2}, and T_A, respectively) were recorded by the V1190 multi-hit TDC. The hit positions x and y can be reconstructed as:

$$x = K_x \cdot (T_{X1} - T_{X2}) + x_{\text{off}}, \tag{3.22}$$

$$y = K_y \cdot (T_{Y1} - T_{Y2}) + y_{\text{off}}, \tag{3.23}$$

with the propagation velocity in the delay line $K_{x(y)}$ (mm/ns) and the position offset x_{off} (y_{off}).

In the practical use of the PPAC in the BigRIPS, two single PPACs, A and B, are packed into a box, comprising the double PPAC. The configuration of the double PPAC is X–Y–Y–X. The double PPAC realizes high efficiency as well as redundancy in the measurement. At each focal plane, two sets of double PPACs were installed so that they sandwitch the center of the focus position, *i.e.*, four positions can be provided in maximum around the focal plane. For F3 and F7 achromatic foci, double PPACs with an active area of 150 mm (X) × 150 mm (Y) and that of 240 mm × 150 mm were used, while large acceptance 240 mm × 150 mm double PPACs were used at F5 dispersive plane to deal with a relatively wide spread of beam particles. The linear trajectory is reconstructed based on the least-square method. If we assume that the linear trajectory in the xz plane can be expressed as $x = az + b$ with x and z being the hit position and the cathode position, respectively, the least-square method gives coeffcients:

$$a = \frac{n\sum_{k=1}^{n} z_k x_k - \sum_{k=1}^{n} z_k \sum_{k=1}^{n} x_k}{n\sum_{k=1}^{n} z_k^2 - \left(\sum_{k=1}^{n} z_k\right)^2}, \qquad b = \frac{\sum_{k=1}^{n} z_k^2 \sum_{k=1}^{n} x_k - \sum_{k=1}^{n} z_k x_k \sum_{k=1}^{n} z_k}{n\sum_{k=1}^{n} z_k^2 - \left(\sum_{k=1}^{n} z_k\right)^2}, \tag{3.24}$$

where n is the number of hits in two double PPACs, four at maximum in our case. The x_k and z_k are the x position of beam particles measured by k-th PPAC and the z position of the k-th PPAC cathode, respectively. Then, the optical vector in the x-direction at a certain plane of $z = z_0$ can

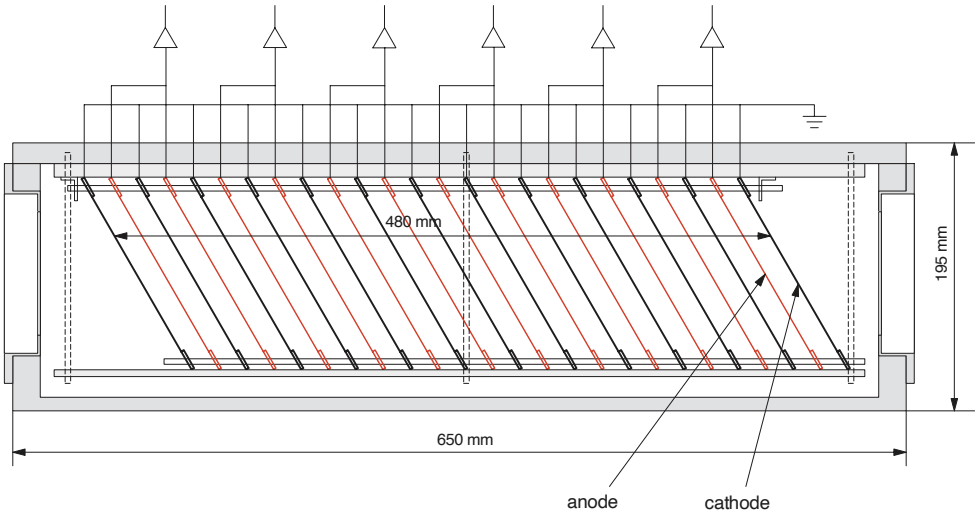

Figure 3.5: Schematic drawing of the MUSIC detector. Adapted from Ref. [180].

be interpolated as $(x_{z=z_0}, \theta_{z=z_0}) = (az_0 + b, \tan^{-1} a)$, which will be used in the ion-optical transfer matrix analysis. The optical vector in the y-direction can be obtained in a similar manner.

In the present experiment, some PPACs repeated a trip many times and had low efficiency, discussed in Sect. 4.1.1, and thus such PPACs were replaced by the alternative ones during changing the beam setting.

MUSIC

The multi-sampling ionization chamber (MUSIC) was placed at F7 to measure the energy deposit ΔE of beam particles, which is necessary to reconstruct the atomic number Z of the isotope. The schematic view of the MUSIC detector is shown in Fig. 3.5. The chamber is filled by the P10 gas – the mixture of argon and methane in composition ratios of 90% and 10%, respectively. The gas pressure was approximately 760 Torr. Twelve anode planes and thirteen cathode planes made by 4 µm-thick aluminized Mylars are staggered in 20-mm step and tilted by 30°. Signals from two anodes are summed at the preamplification stage, which provides six multi-sampling outputs in total. This is equivalent to operating a stack of plate-shaped ionization chambers and enables us to gain a high ΔE resolution for heavy-ion beams. By tilting the electrodes, electrons and positive ions generated by ionization of the gas along the beam trajectory are moved towards electrodes without going through a high charge density area created by beams. This structure thus avoids the recombinations of electrons and positive ions. The pulse heights of the amplified signals are recorded by the MADC32 ADC module. The ΔE is deduced by the geometrical mean of the obtained ADC values:

$$\Delta E = \alpha \left(\prod_{i=1}^{6} (ADC_i - c_i) \right)^{1/6} . \tag{3.25}$$

Here α is the energy calibration coefficient, ADC_i and c_i are the ADC value and baseline offset of the i-th readout channel, respectively.

3.2 Detectors for Heavy-Ion Collision Products

As described in Sect. 2.4, heavy-ion collisions at intermediate energies produce a variety of particles, *e.g.*, pions, nucleons, light clusters such as deuterons and alpha particles, and heavy fragment nuclei. In central Sn + Sn collisions at the energy domain of RIBF, it is anticipated that the number of charged particles (multiplicity) can amount to about 80, according to the data on a similar system of Xe + CsI reactions in the previous measurement [62]. In the RIBF, only a fixed-target experiment is available, and thus the emission of particles concentrates in the forward laboratory angle region. To accomplish such type of measurement, the detection system requires a high separation and identification capability for multiple particles, a high momentum resolution, and a large acceptance. Therefore we employed a large volume TPC – called as SπRIT TPC – in combination with the large-acceptance spectrometer SAMURAI to identify charged particles from Sn + Sn collisions and to determine their momenta.

Figures 3.6 and 3.7 present the illustration of the SAMURAI area and the photograph at the experiment, respectively. The SπRIT TPC was installed inside the SAMURAI chamber with being surrounded by ancillary trigger detectors. The Sn target was located just upstream of the active volume of the TPC. The neutron detector was placed at 30° of polar angle and about 7 m away from the center of the SAMURAI magnet.

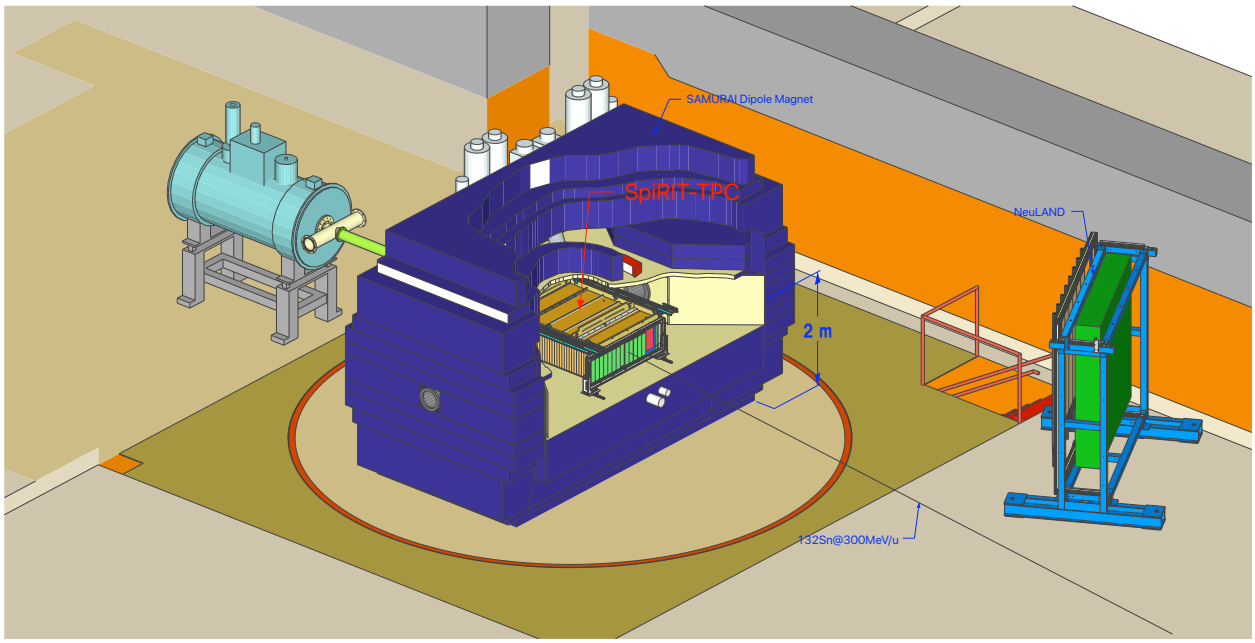

Figure 3.6: Illustration of the SAMURAI experimental area. The SAMURAI magnet is hollowed out for a visibility of the SπRIT TPC and trigger arrays. Sn beams are injected from top-left side, where the simulation-based trajectory of ^{132}Sn beams at 300 MeV/nucleon is drawn by the solid line. The Sn target is located just upstream of the active volume of the TPC.

Figure 3.7: Photograph of the SAMURAI experimental area. The SπRIT TPC and trigger arrays are lighted up inside the SAMURAI chamber. The aluminum-frame structure is used for the installation process of the TPC.

3.2.1 SAMURAI magnet

The SAMURAI magnet [181] is a superconducting dipole magnet designed to have a large kinematical acceptance for a multi-particle measurement. The magnet is an H-type dipole with superconducting coils of a diameter of 2 m and a pole gap of 880 mm. The direction of the magnetic flux is upward. Therefore positively charged particles are bent to the beam-right side[4]. Between poles, a rectangular-shaped chamber with a wide-opening exit is installed as shown in Figs. 3.6 and 3.7. The chamber has an inner height of 800 mm, about 2 m of depth, and about 5 m of opening width. The base of the SAMURAI is rotatable for applying different experimental purposes [182]. In our experiment, the SAMURAI magnet was operated in 0° setting. One reason to do so is related to the TPC design, discussed in detail in the next section. Because the TPC is designed to be rectangular and to allow beam injection along its length, it should be positioned so that the beam axis and TPC long axis are overlapped. Then for simplification of the installation procedure, the SAMURAI in 0° setting is convenient. The second reason is to allow the detection of neutrons at the beam-left side. Since most of charged particles from reactions are swept to the beam-right side by the magnet, the beam-right side tends to be contaminated for the neutron measurement. In contrast to that, the beam-left side is rather clean for the neutron measurement. In that case, the opening of the chamber is necessary for the neutron measurement in the beam-left side by setting the SAMURAI to 0°. In the present experiment, the magnetic field of 0.5 T was applied. The field strength was optimized so that low-energy charged pions are not trapped by the magnetic field because a small spiral trajectory is difficult to be reconstructed in the TPC.

[4]Here, the sight direction is taken as the direction of the beam injection.

3.2.2 SπRIT time projection chamber

The SAMURAI Pion Reconstruction and Ion-Tracker Time Projection Chamber (SπRIT TPC) [183–185] is a rectangular TPC employing a multi-wire proportional chamber with segmented charge-sensitive pad readout. It is designed to be used in conjunction with the SAMURAI dipole magnet to provide the particle identification and momenta of charged particles produced in heavy-ion collisions. In this section, a technical description of the SπRIT TPC and that of respective important components are provided. To facilitate the description, a right-handed Cartesian coordinate is defined as follows. The z axis lies along the beam axis, identical to the length direction of the SπRIT TPC. The y axis points to the upward direction, parallel to the SAMURAI magnetic field. The x axis is then defined as the beam-left direction.

A TPC enables the reconstruction of charged-particle trajectories in three-dimensional space. Figure 3.8 shows the operation principle of the SπRIT TPC. RI beams impinge on the Sn target located a few mm upstream of a field cage, emitting copious charged particles. These charged particles enter the field cage through its entrance window and ionize atoms in the P10 active gas so that electron-ion pairs are produced along the charged-particle trajectories. Ionized electrons drift in a uniform electric field built by the field cage, which is antiparallel to the magnetic field for avoiding the $\vec{E} \times \vec{B}$ effect. When electrons reach the anode wire plane situated just below the pad plane, they are accelerated enough to cause a Taunsend avalanche that typically multiplies the number of electrons by a factor of the order of 1000. Motions of the multiplied charge induce image current on the surface of the charge-sensitive cathode pads, which are amplified and digitized by the readout electronics. The distribution of charge induced on the pads provides the projection of charged-particle trajectories onto the x–z plane. The trajectory's y positions can be inferred from the time of electron's arrival multiplied by the drift velocity of electrons. Individual charged particle tracks are reconstructed by sorting, clustering, and fitting the induced signals in the three-

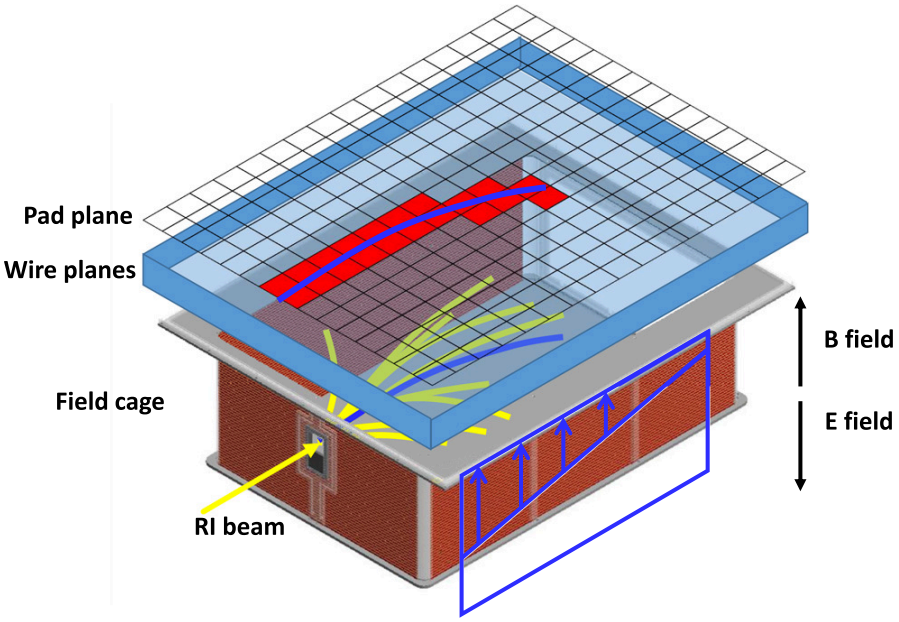

Figure 3.8: Basics of the SπRIT TPC operation. Adapted from [185].

Table 3.3: Relevant parameters of the SπRIT TPC.

Parameters			
Pad plane area	1344 mm × 864 mm	Anode voltage	∼1460 V
Pad size	12 mm × 8 mm	Gas gain	∼1000
Number of pads	12,096 (112 × 108)	ADC dynamic range	120 fC
Counter gas	90% Ar + 10% CH_4	ADC resolution	4096
Gas pressure	1 atm	Sampling rate	25 MHz
Drift distance	∼50 cm	Shaping time	117 ns
Cathode voltage	−6700 V	Track multiplicity	40–60
Electric field	∼125 V/cm	Momentum resolution	$< 2\%$ for d and t
Electron drift velocity	∼5.5 cm/μs	Identification capability	$\pi^{\pm}$, $e^{\pm}$, Z = 1–3

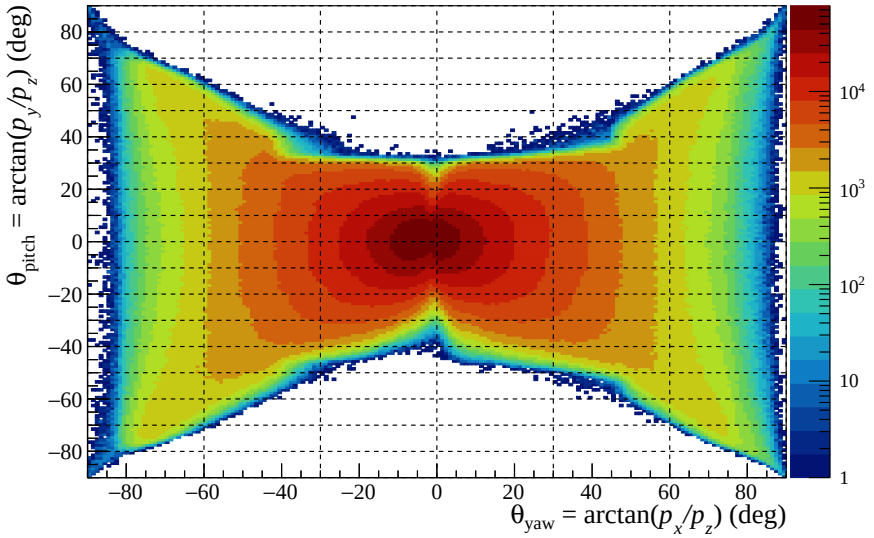

Figure 3.9: θ_{yaw} vs. θ_{pitch} distribution for the ^{132}Sn + ^{124}Sn reactions. The boundary of the distribution corresponds to the geometrical acceptance of the SπRIT TPC. The distribution is centered to a bit negative θ_{yaw} side due to the bending of the incident beams before hitting the target.

dimensional space. By analyzing the energy deposit per unit track length (dE/dx), the curvature (magnetic rigidity), and the initial emission angles of charged particles, the particle identification and momenta of the detected charged particles are provided. Typical operation parameters of the SπRIT TPC are listed in Table 3.3.

Figure 3.9 presents the measured geometrical acceptance of the SπRIT TPC based on the charged-particle tracks reconstructed in the TPC in the space of laboratory pitch and yaw angles. Note that the short tracks containing a small number of hit-clusters less than 15 are ignored here, and the detail of the analysis will be discussed in Sect. 4.3. Since the active region of the SπRIT TPC is a laterally-wide volume, a wide yaw-angle acceptance is achieved to be approximately

$|\theta_{\text{yaw}}| \leq 85°$, which is near the allowable geometrical angle limit of $\theta_{\text{yaw}} \simeq \pm 88°$ determined by the target position and the left-right edges of the pad plane. On the other hand, there are likely to be the insufficient number of hit-clusters for vertically emitted charged particles, and thus, the pitch-angle acceptance is limited to approximately $-40° < \theta_{\text{pitch}} < 30°$, while the geometrical pitch-angle limit is approximately $-87° < \theta_{\text{pitch}} < 86°$.

Figure 3.10 presents an exploded view of the SπRIT TPC. The outermost enclosures consist of the half-inch-thick aluminum plates attached to the skeleton. Both sides and downstream plates have 0.81 mm thick aluminum windows to allow charged particles to exit and to be detected by ancillary detectors surrounding the TPC enclosures. The chamber is covered by the top plate consisting of a 3/4-inch-thick aluminum plate. With the reinforcements of supporting ribs, the top plate provides the rigid mounting surface for the readout electronics on the top, and for the pad plane, the wire planes, the field cage, and the target mechanism on the bottom. The whole outer dimension of the SπRIT TPC is about 2.06 m long $(z) \times 1.50$ m wide $(x) \times 0.74$ m high (y), to be best fitted to the inner gap of the SAMURAI chamber with a margin for placing the readout electronics.

Field cage In order to measure an accurate position where charged particles traversed, the electric field in the TPC is required to be uniform. The field cage, which is used to build a uniform electric field, is therefore an important component of the TPC. As shown in Fig. 3.11, the field cage is mounted on the bottom of the top plate, making an airtightness inside the cage. The bottom of the field cage functions as a cathode electrode, which is made of a graphite-coated honeycomb aluminum plate. Since graphite has a high electron work function compared to aluminum, surface ionization by high-energy gamma rays can be suppressed. A high bias voltage of -6.7 kV is applied to the bottom cathode, forming the electric field toward the ground wire plane located before the pad plane. The side and front walls are composed of 1.575 mm-thick G10 PCBs with 6 mm-wide copper strips pasted in 10 mm pitch in the x–z direction on both sides of the board. Adjacent strips are connected in parallel by 10 MΩ registers, which causes a gradual voltage drop from the top (ground) strip to the bottom (negatively biased) one so that the uniform electric field is formed inside the cage. According to the Garfield [186] simulation, the electric-field uniformity is guaranteed inside the field cage. At the front and rear walls, the entrance and exit windows are installed, respectively. The entrance window is made of 4 µm-thick polyparaphenylene terephthalamide with 5.73 cm $(x) \times 7$ cm (y) of area, which allows charged particles from nuclear reactions on target to pass through with the minimal energy loss. The exit window employs 125 µm-thick polyamide with 80.8 cm $(x) \times 38.9$ cm (y). Aluminum strips are evaporated onto the window films and are connected with copper strips on the walls so that a seamless field cage structure is realized.

Pad plane The pad plane consists of 12 mm $(z) \times 8$ mm (x) charge-sensitive pads arranged in 112 rows $(z) \times 108$ columns (x), covering 1344 mm $(z) \times 864$ mm (x) of area in total. By constructing the centroid of signals from neighboring pads, a millimeter order of position resolution can be achieved. The pad plane lies on a printed circuit board (PCB) for concentrating electrical signals from pads. The PCB is epoxied to the bottom of the rigid top plate. The planar precision of the pad plane determined by the laser alignment system is about a level of 125 µm.

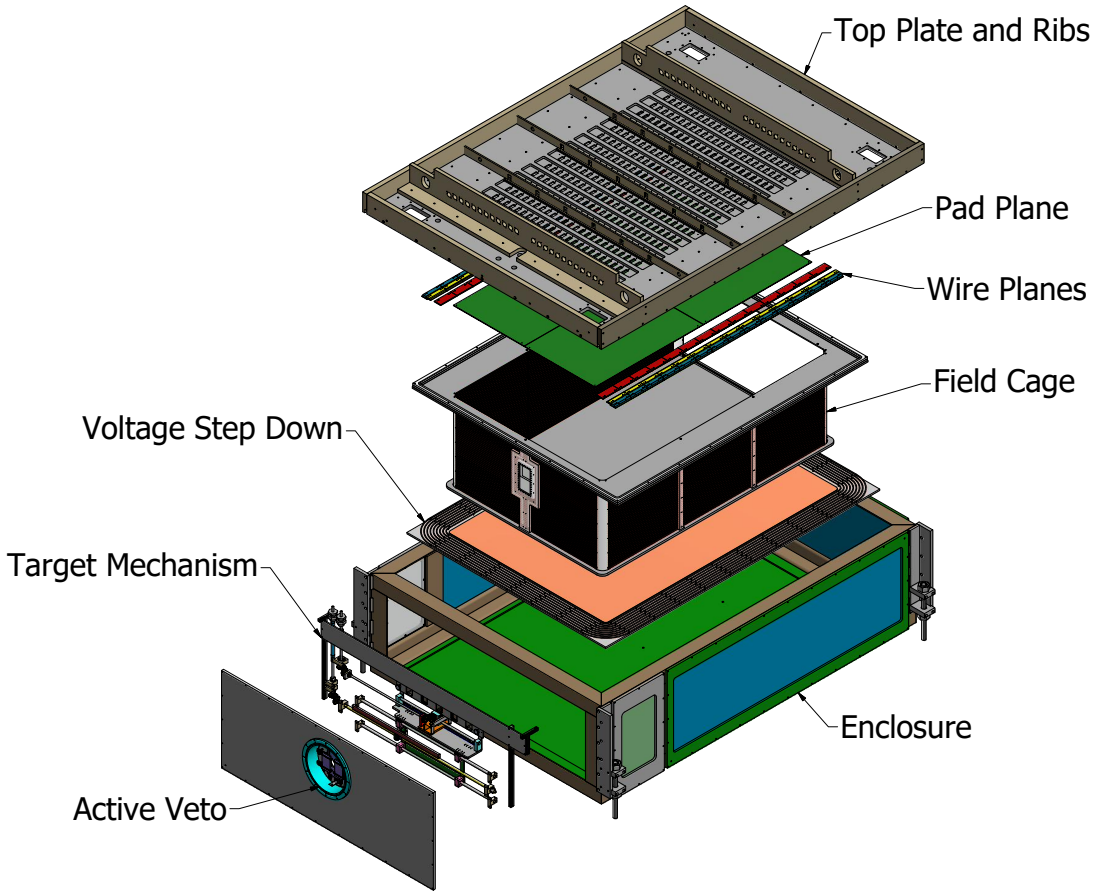

Figure 3.10: Exploded view of the SπRIT TPC. Adapted from [184].

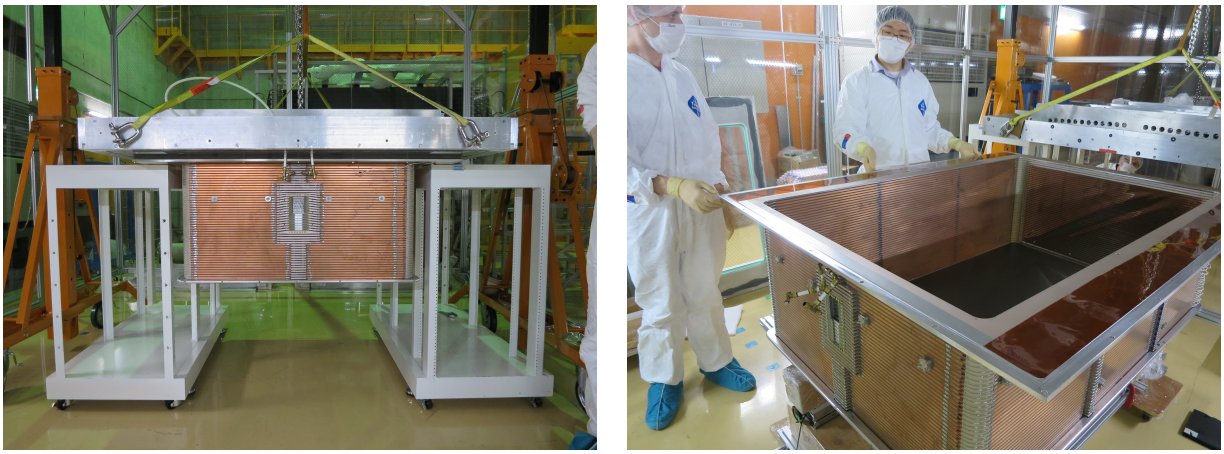

Figure 3.11: Photographs of the field cage attached on the bottom of the rigid top plate (left) and that off from the top plate (right).

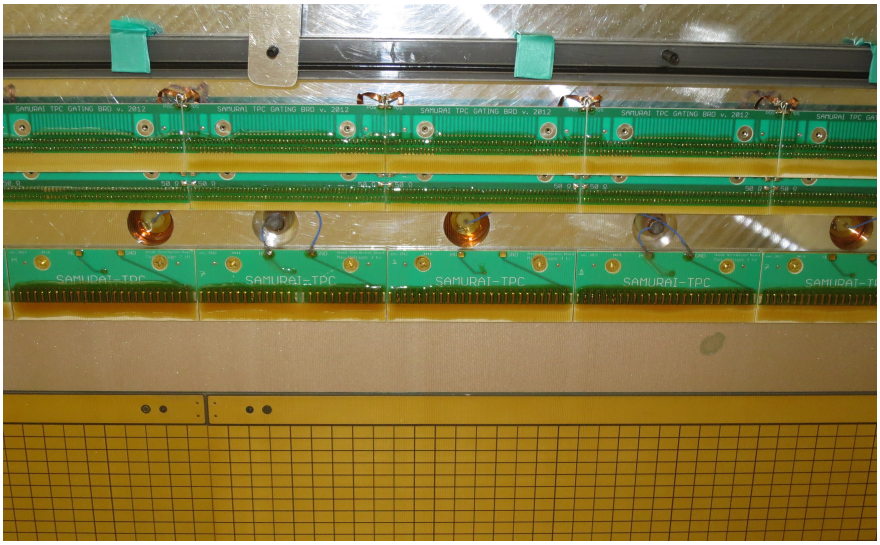

Figure 3.12: A photograph of the three wire planes and one edge of the pad plane. The top, middle, and bottom PCBs mount the gating grid wires, the ground wires, and the anode wires, respectively. Each wire is soldered on the PCB and tautened vertically in the photo (almost not seen in the photograph resolution).

Table 3.4: The property of each wire.

Plane	Material	Diameter (μm)	Pitch (mm)	Distance to pad plane (mm)	Tension (N)	No. of wires
Anode	Au-plated W	20	4	4	0.5	364
Ground	BeCu	76	1	8	1.2	1456
Gating	BeCu	76	1	14	1.2	1456

Wire planes Three wire planes: the anode wire plane, the ground wire plane, and the gating grid wire plane are mounted on the bottom of the top plate just below the pad plane, as shown in Fig. 3.12. The wires are tautened along the x-axis direction, perpendicular to the beam direction. Table 3.4 summarizes the properties of employed wires. The bias voltage applied to the anode wires was 1460 V, which corresponds to the amplification gain factor of approximately 1000 with the P10 gas at 1 atm.

Gating grid The gating grid prevents drifting electrons from invading the amplification region, which is an important function for operating the TPC under irradiations of high-intensity and/or high-stopping-power beams. Since the SπRIT TPC is placed on the beamline, unreacted RI beams enter the sensitive volume, producing a large number of electrons due to the high ionization power of heavy beam particles. If these electrons are drifted and amplified at the close of the anode wires, there would occur copious ionizations. The resultant electrons and positive ions create negatively charged polymers from a hydrocarbon or impurities in active gas, which can cause aging of the anode wires by deposition of polymers. Furthermore, the backflow of positive ions induces a space charge in the drift volume for a relatively long period since their drift velocity is slow, *i.e.*, of the order of cm/ms. The space charge distorts the electric field and consequently deteriorates the

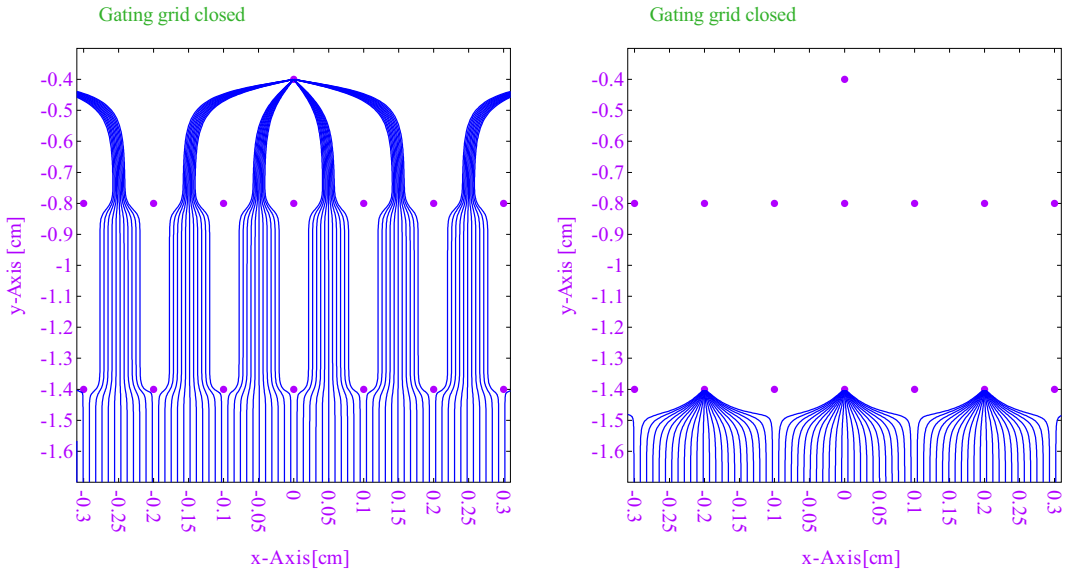

Figure 3.13: Simulated electron drift lines near the wire planes. The purple dots indicate the wire position in y-z position, not to scale the diameter. Taken from Ref. [187]. Left: With the gating grid open; Right: With the gating grid closed. The y coordinate here represents the distance from the pad plane with the anode wire at $y = -0.4\,\text{cm}$, the ground wires at $y = -0.8\,\text{cm}$, and the gating grid wires at $y = -1.4\,\text{cm}$, respectively. The x represents the position along beam direction centered at an anode wire.

position resolution of the TPC. Thus we employed the gating grid to terminate the beam-induced electrons before their amplifications.

For the SπRIT TPC, a bipolar type gating grid is employed. When it is opened, the gating grid wires are biased to a common voltage, $\boldsymbol{V_a}$, so as not to interfere with the electric field in the field cage, as shown in Fig. 3.13. In the closed state of the gating grid, the wires are alternately biased to $\boldsymbol{V_a \pm \Delta V}$ with positively and negatively biased wires serving as a terminator of electrons and positive ions, respectively. The bias voltage was determined as $(-110 \pm 70)\,\text{V}$ based on Garfield simulations with considering the magnetic field so that the electron transparency is maximized and minimized for the open and close of the gating grid, respectively. The gating grid is normally closed, keeping the TPC insensitive. When desired collision events occur, the grid should be opened as fast as possible not to enlarge the dead region of the TPC. A driver for the gating grid [187] has been developed to switch the state of the gating grid, which opens the grid within 350 ns after accepting a trigger signal. When the gating grid is opened, it also needs to be closed as soon as finishing the collection of all drifting electrons, in order to avoid the positive-ion backflows. Therefore, the width of the opening signal sent to the gating grid driver was set to 11 µs, which is nearly equivalent to the drift time spent by electrons produced at the bottom of the field cage.

Target mechanism The targets are fixed on the holding ladder made of aluminum. The ladder and its motion mechanism are shown in Fig. 3.14. The inner dimension of the target holder is 30 mm wide (x) × 40 mm high (y) so as to deal with a relatively wide profile of RI beams spreading of the order of centimeters. The ladder can be moved in x and z directions separately, whose positions are determined by potentiometers. The y position is fixed so that the target center is matched to the height of beam trajectories. The target mechanism is controlled by rotary handles which are built outside of the SπRIT TPC to change the Sn targets without opening the TPC. The handle with a

Figure 3.14: Photographs of the target mechanism. Left: The target holders (vacant) and the target motion mechanism. Right: The target mechanism mounted on the SπRIT TPC.

rod is connected with the inside structure via a feedthrough, and the rotation is converted to the motion in x and z directions by meshed gears.

During the experiment, isotopically enriched ^{112}Sn and ^{124}Sn targets with purity better than 95% were borrowed from GSI group. Their thicknesses were determined as 0.836(4) mm and 0.828(3) mm by the manufacturer based on the capacitance measurement, which corresponds to area densities of 561(2) mg/cm^2 and 608(3) mg/cm^2, respectively. They were installed into the target holder. A brick of aluminum was also installed for calibration runs using Z = 1–3 beams, to vary the incident energy of beam particles by the energy loss in the aluminum brick.

Readout electronics To read electrical signals from 12,096 pads and to record their waveforms, a readout system has been developed based on the General Electronics for TPCs (GET) [188, 189]. The left panel of Fig. 3.15 presents the overall structure of the readout system for the SπRIT TPC. The AsAd (ASIC and ADC) board contains 4 AGET (ASIC for GET) chip, an FPGA providing slow control, and a 4-channel 12-bit ADC, which is connected with the pad plane via the interface board, as shown in the right panel of Fig. 3.15. The AGET chip has 68 channels, with 64 channels to read out signals from pads and 4 channels to determine a reference of the fixed pattern noise. Each channel employs a charge-sensitive preamplifier, a shaper, a discriminator, and a 512-cell switch capacitor array for an analogue buffer. The buffered charge is digitized by the onboard ADC when the system receives a trigger. For the SπRIT TPC, one AGET chip reads 63 signals from pads, and 48 AsAd boards were installed in total. During the experiment, parameters of the AGET chip were configured as 120 fC dynamic range with a positive polarity, 117 ns of peaking time, and 25 MHz sampling rate. The discriminator signals were not used.

The data from AsAd boards are concentrated by the Concentration Board (CoBo) mounted on the Micro Telecom Computing Architecture (MicroTCA) crate which is placed outside of the SAMURAI magnet. Each CoBo handles 4 AsAd boards, which are connected by 8 m long commercial VHDCI cables. The extraction of signals from AsAd is performed in the frequency of 25 MHz, with the data being buffered in a DDRAM of the CoBo. The buffered event data is transmitted to the DAQ server through a 10 Gbps network switch of the MicroTCA carrier hub. Since one Cobo can send the data with $\sim$ 800 Mbps, we employed two MicroTCA crates to avoid

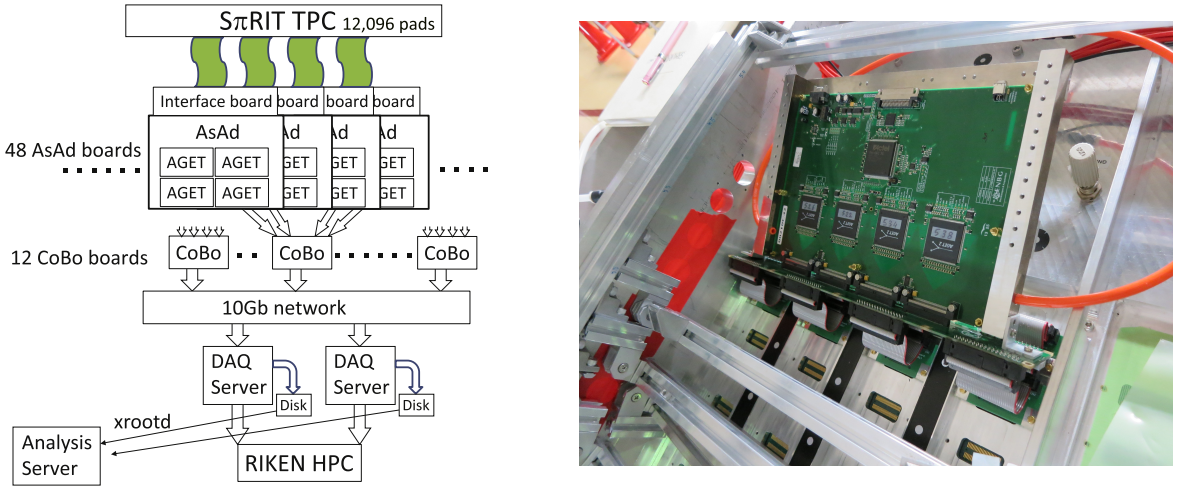

Figure 3.15: Overall structure of the GET readout system and a photograph of one AsAd board mounted on the SπRIT TPC. Left figure is adapted from Ref. [189].

the rate limitation and allocated 12 CoBo as 8 boards for one crate and 4 boards for another. The master trigger and a global clock for the system are distributed by the Multiplicity, Trigger and Time (MuTanT) module. Two servers using a RAID6 configuration storage of 52 TByte through an 8 Gbps fiber channel interface are employed as DAQ servers, which were operated by the NARVAL framework [190]. The acquired data were stored in the online server and copied to the HOKUSAI GreatWave[5] system of the RIKEN for the offline analysis.

3.2.3 Multiplicity trigger detector

The multiplicity trigger detector (MTD) [21, 22] is designed to provide a trigger signal sensitive to central collision events. It is well established that the multiplicity of particles produced in heavy-ion collisions strongly anti-correlates with the impact parameter between two colliding nuclei. Therefore the MTD measures the charged-particle multiplicity from heavy-ion collisions and generates a trigger signal only when the measured multiplicity exceeds a certain threshold value.

The MTD consists of two side-walls attached on both sides of the SπRIT TPC, as shown in Fig. 3.16. Each wall has a geometrical dimension of 1515 mm (z) × 450 mm (y) × 10 mm (x). Its z–y size is designed to cover the thin windows in the side enclosure plates of the TPC, whose area is 1461 mm (z) × 411 mm (y). The acceptance of the two walls in polar angles covers 24° to 73° in the laboratory frame, and that in the azimuthal angle is approximately 1/6 of 2π rad. The side-wall is segmented into 30 elements along z direction. Each element is composed of a plastic scintillator slab with a wavelength shifting (WLS) fiber read by a multi pixel photon counter (MPPC) which works in a magnetic field. The plastic slab has a dimension of 50 mm (z) × 450 mm (y) × 10 mm (x), which was extruded with a hole of 1.5 mm diameter along its length to insert the WLS fiber of 1 mmϕ. The use of the WLS fiber aims to deal with a relatively short attenuation

[5]The HOKUSAI GreatWave is a common use supercomputer operated in the RIKEN, which provides an online storage, a massive parallel computation, and an application-based computation system.

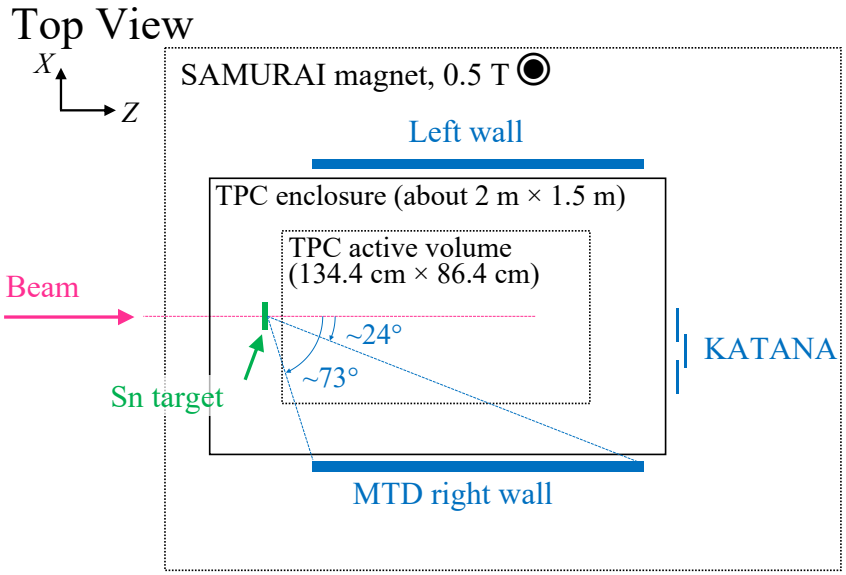

Figure 3.16: Schematical drawing of the experimental setup from the top, showing two walls of the MTD, KATANA veto counters, and the sensitive active area of the SπRIT TPC.

length of the extruded plastics and to efficiently propagate photons toward a small active area of the MPPC, where 1.3 mm × 1.3 mm of MPPC was employed. The extrusion also makes a titanium oxide coating on the plastic surface to improve the photon collection efficiency. The plastic was wrapped by a 12 µm thick aluminum foil for the shading, which was fixed by a black shrinkable tube. The detection efficiency of the single element for light charged particles at several hundred MeV/c of momentum is approximately 99%, which was evaluated by a test experiment at HIMAC using ^{132}Xe + CsI collisions at 300 MeV/nucleon [22].

Electrical signals induced by 60 MPPCs are processed by the Extended Analogue Si-pm Integrated ReadOut Chip (EASIROC) [191] based VME standard module – VME-EASIROC – which is equipped with two EASIROCs, an FPGA (Artix7) for slow control, and 12-bit peak-hold type ADC. The EASIROC has 32 channels of preamplifier-shaper-discriminator circuits and digital-to-analogue converters for adjusting the bias voltage of the MPPCs individually. In each channel, the amplified signal is divided for slow (shaping time constant τ = 175 ns) and fast (τ = 15 ns) shapers, which are followed by a voltage-holding circuit connected to the ADC and a leading-edge discriminator, respectively. The discriminated signals from the two EASIROCs (64 channels) are sent to the FPGA to count the multiplicity in the MTD (M_{MTD}) and to generate a trigger if the counted multiplicity exceeds the threshold. The multiplicity threshold is configurable through the slow control. During the experiment, the minimum multiplicity requirement of the MTD was set as $M_{\mathrm{MTD}} \geq 4$. The low-biased trigger was also tested, see Sect. 3.4. The total latency of the MTD until the generation of the trigger signal was estimated to be less than 100 ns, including the photon propagation in the plastic and fiber, the electrical signal propagation in cables (7 m in total), and the processing time in the VME-EASIROC. The deduced latency corresponds to approximately 0.5 cm of the electron drift or ~ 1% of the drift length of the SπRIT TPC.

The sensitivity of the MTD to the impact parameter is evaluated by a simulation using the GEANT4 tool-kit [192] with the UrQMD model [193] version 3.4 as a generator of the heavy-ion collision event. Generated events are ^{112}Sn + ^{124}Sn at 270 MeV/nucleon with the impact-parameter

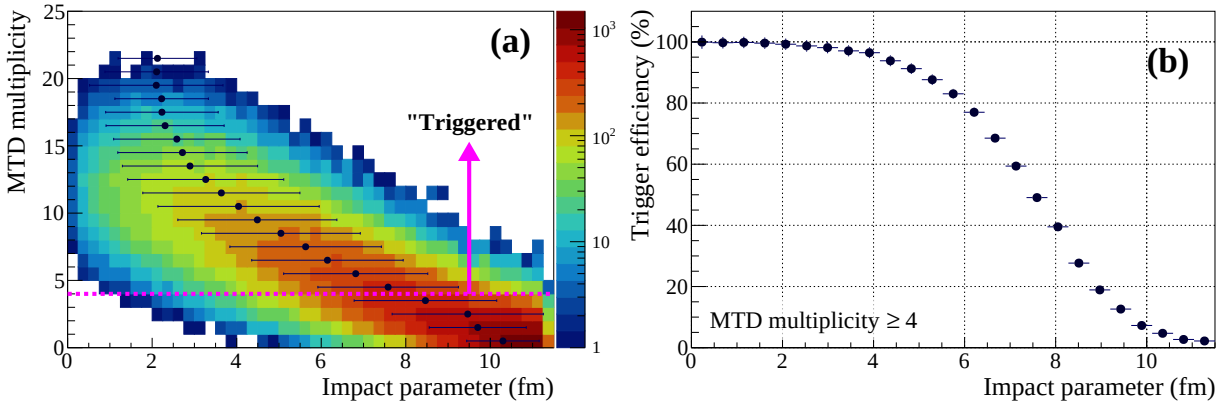

Figure 3.17: Simulated MTD performance for ^{112}Sn + ^{124}Sn reactions at 270 MeV/nucleon. (a): The correlation between the MTD multiplicity and the impact parameter. The multiplicity is counted from the number of plastics with the energy deposit higher than 200 keV of the threshold, with considering the light attenuation in the detector element. (b): The trigger efficiency as a function of impact parameter.

range of $0 \leq b \leq 11.3$ fm. Since the UrQMD model normally calculates only the nucleon dynamics, clusters are produced based on the phase-space coalescence model, with conditions of freeze-out time $t = 200\,\mathrm{fm}/c$, relative distance $r \leq 2.4$ fm, and relative momentum $p \leq 300\,\mathrm{MeV}/c$. The realistic geometries of the SπRIT TPC and the MTD under the SAMURAI magnetic field of 0.5 T are constructed by the GEANT4 libraries. Figure 3.17 presents the correlation of M_{MTD} vs. impact parameter and the trigger efficiency as a function of the impact parameter with the requirement of $M_{\mathrm{MTD}} \geq 4$. Through the simulation, the integrated trigger efficiency for $b \leq 3$ fm of central collision events is found to be greater than 99% with the higher-multiplicity requirement in the MTD of $M_{\mathrm{MTD}} \geq 4$. Similarly, the integrated suppression ratio for $b \geq 8$ fm of peripheral collision events with the same multiplicity requirement is estimated to be at least 87%.

3.2.4 Forward veto counter for peripheral collisions: KATANA

The Krakow Array for Triggering with Amplitude discrimiNAtion (KATANA) [194] consists of two parts: veto counters and a multiplicity array (not used). The KATANA veto counter measured beam-like particles to discriminate peripheral collision events accompanying high-Z residue particles and beam pileup events. It employs three thin plastic scintillators (BC-404) in dimensions of 400 mm × 100 mm × 1 mm. As shown in Fig. 3.18, the three veto counters were placed just downstream of the SπRIT TPC on the beam trajectory depending on the beam setting. The central veto counter was placed at $x = -215$ mm for the $^{132(124)}$Sn setting and $x = -246$ mm for the $^{108(112)}$Sn setting. These positions were optimized by monitoring the count rates of the veto counters with gradually increasing the magnetic flux density from 0 T to 0.5 T. WLS fibers of 1 mmϕ lie on the top and bottom edges of plastics to collect scintillation photons. The photons in the fiber are read by the MPPCs with an active area of 1 mm × 1 mm, which are equipped on both ends of the fiber. Electrical signals induced from MPPCs in the veto counters are summed for each paddle and recorded by V1730 flash ADC. The performance of the veto counter was demonstrated in the test experiment at HIMAC using projectile fragments of ^{132}Xe + CsI reactions at 300 MeV/nucleon. A high charge resolution of $\Delta Z \sim 1.6$ in FWHM for Xe ($Z = 54$) beams

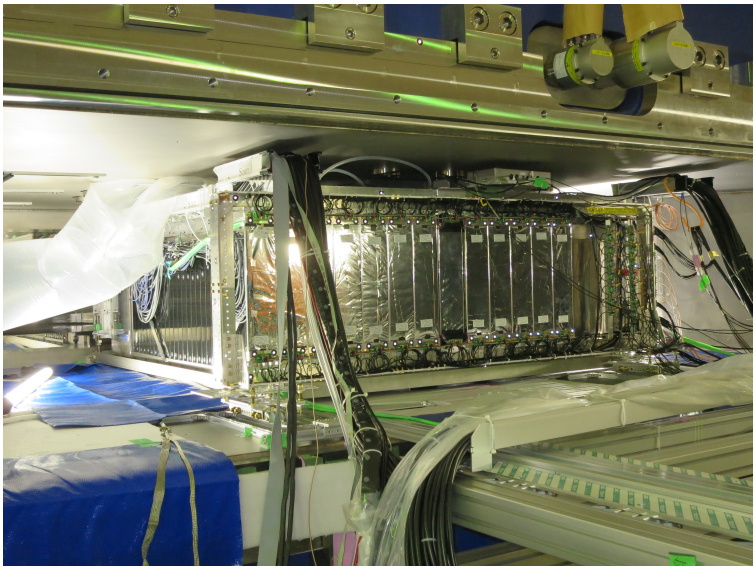

Figure 3.18: Photograph of the KATANA detectors at donwstream of the SπRIT TPC. The paddles with white labels are the multiplicity array (not used in the present work). The veto counters are installed at the center of the array, where two counters are located on left and right of the one in sight, behind the multiplicity array.

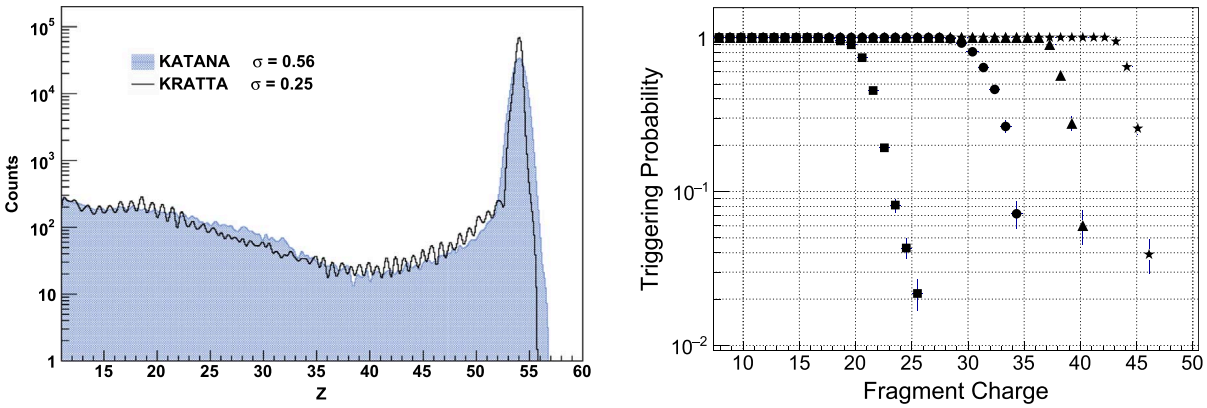

Figure 3.19: KATANA veto performance evaluated with projectile fragments of ^{132}Xe + CsI reactions at 300 MeV/nucleon. Adapted from Ref. [194]. Left: fragment-charge distribution detected in the KATANA veto counter and that in the Si–Si–CsI telescope, named KRATTA, that was used to provide the reference of charge. The charge resolution of $\Delta Z \sim 1.6$ was obtained from the Xe peak at $Z \sim 54$. Right: the triggering probability as a function of fragment charge in the KRATTA telescope. Four software thresholds based on charge detected in the KATANA veto counter were tested, showing a high discrimination power (a quick drop of the probability).

and a high discrimination power for high-Z particles were shown [194], as presented in Fig. 3.19. During the experiment, the threshold of the veto counter was set to 31 mV which corresponds to a passage of the calcium. Thus, the KATANA veto counter made a veto signal every time any one of three counters detected beam-like particles with $Z \geq 20$. The multiplicity array, which employs 12 counters to measure the forward multiplicity, didn't participate in the master trigger because its inclusion in the trigger generation allowed more active-target events inside the TPC.

3.2.5 Active veto array

The active veto array [195] was located just upstream from the target to veto off-target events. Figure 3.20 presents a photograph of the active veto array. It consists of four plastic scintillators in dimensions of 9 cm × 5 cm × 0.6 cm, each of which is directly equipped with a single MPPC. Four plastics are located to collimate beam particles, forming an empty square opened by 26 mm wide (x) × 38 mm height (y). The discriminator threshold of each MPPC signal was set to high enough to produce logic output only when the beam particles with $Z \sim 50$ hit the plastic. The inclusive OR signal of four MPPCs was used as a veto signal.

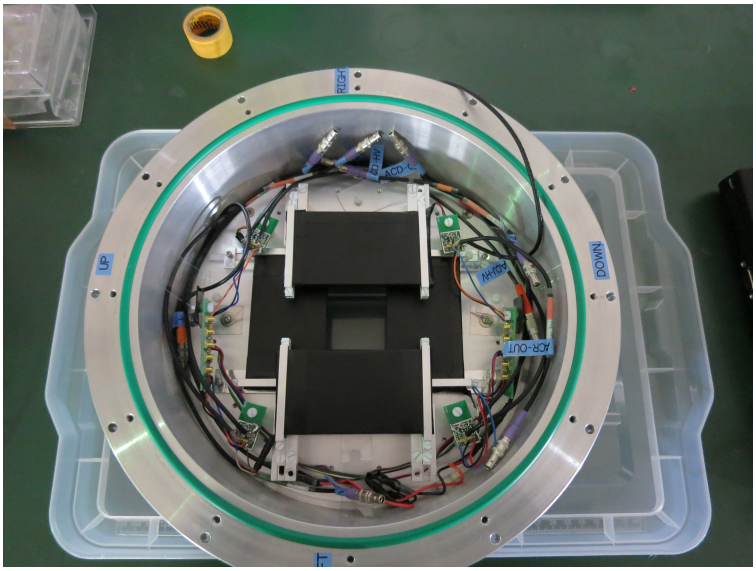

Figure 3.20: Photograph of the active veto array mounted on a housing frange. The frange was installed into the front plate of the TPC enclosure.

3.2.6 Ancillary detectors

Scintillation Beam Trigger detector

The scintillation beam trigger (SBT) served as a reference detector for a start timing. It employs a plastic scintillator in dimensions of 120 mm × 120 mm × 0.2^t mm read by two PMTs attached on both edges of the plastic. As shown in Figs. 3.21 and 3.22, two plastics together with PMTs were installed inside the beam pipe, which was positioned just downstream of the STQ25 magnet and approximately 4.3 m upstream from the Sn target. The high voltage applied to the PMTs was about 1000 V for the upstream PMTs and 1030 V for the downstream ones so that signal heights became ∼ 400 mV. The threshold of the discriminator was set to 40 mV. The coincidence of four PMTs was used as a start timing of the whole system. The time resolution of the SBT was evaluated as $\sigma_T \approx 50$ ps from the time difference between the two plastics.

Figure 3.21: Photographs of the SBT (left) and the beam pipe with counters installed (right).

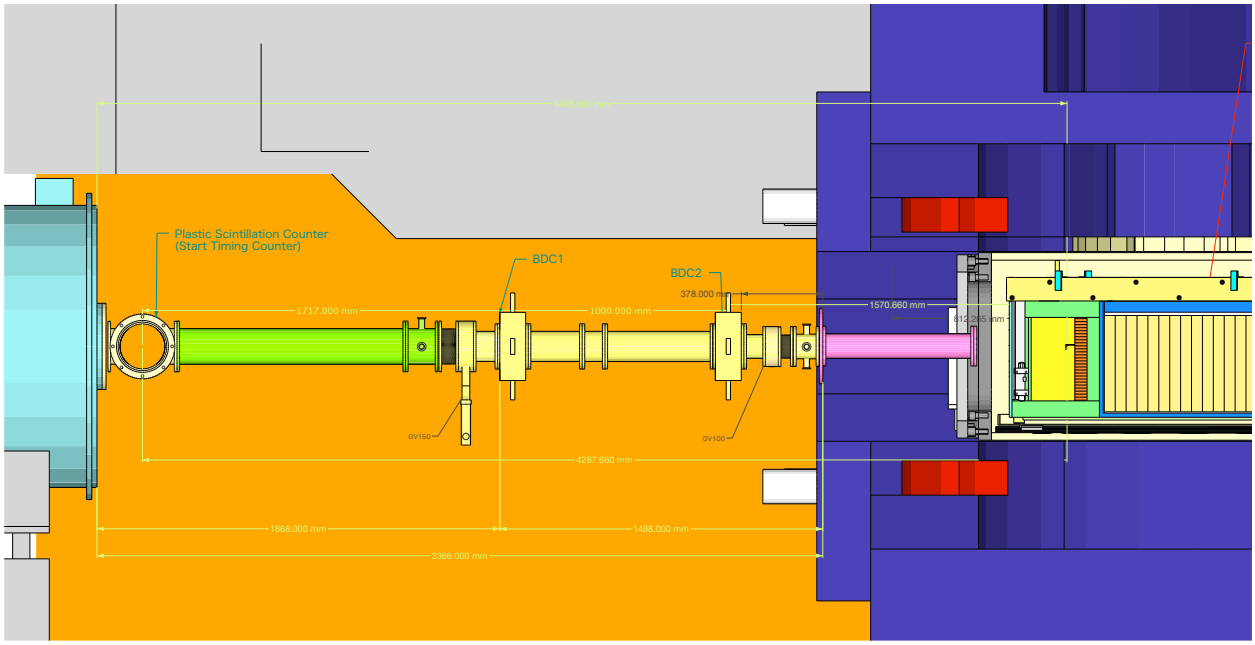

Figure 3.22: Experimental setup upstream from the SπRIT TPC. Sn beams transported from BigRIPS pass through the STQ25 (cyan), the SBT, two boxes of BDCs, a kapton film that seals a vacuum in the pipe, an entrance film of the SπRIT TPC, and then, impinge on the Sn target located a few mm in front of the field cage.

Beam Drift Chamber

Two beam drift chambers (BDCs) [196] were located upstream from the SAMURAI magnet, as shown in Fig. 3.23, to measure the trajectory of incident beams. Table 3.5 lists its specification. The BDC consists of a Walenta-type drift chamber with 2.5 mm of drift length. In the BDC, eight wire planes are boxed into a chamber that is connected directly to the beam pipe. The wires in adjacent planes (xx' or yy') are shifted by 2.5 mm to reduce a left-right ambiguity in the measurement of beam passages. Amplifier-shaper-discriminator (ASD) cards are mounted on each edge of the BDC box for reading out signals from wires with a low noise level. The LVDS outputs of the ASD cards are sent to the AMT-VME multi-hit TDC module to record timings of respective signals. For the measurement of $Z \sim 50$ beams, approximately 100 µm of position resolution and $\sim$ 96% of the total efficiency were achieved, which were evaluated in the commissioning run.

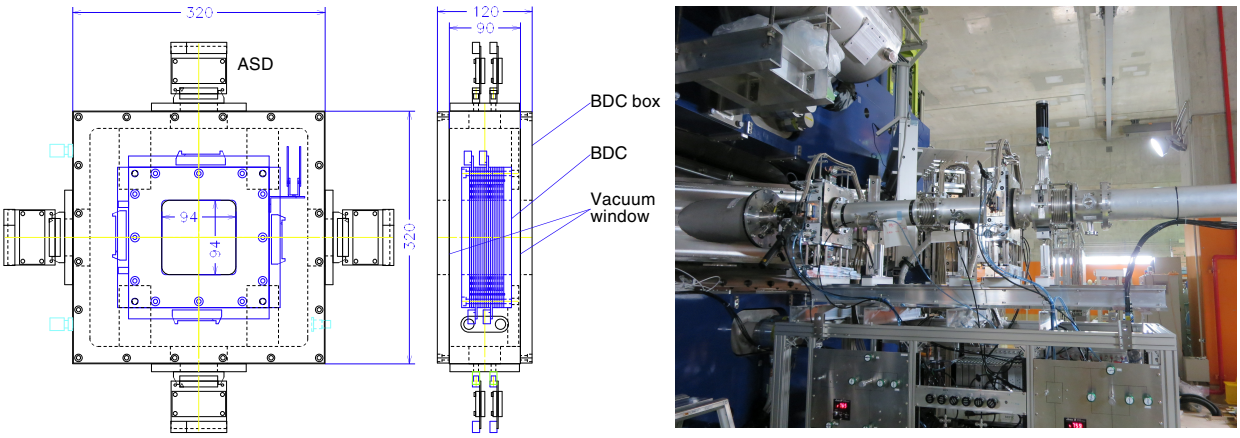

Figure 3.23: Schematic drawing and a photograph of the BDC. Left: schematic drawing of the BDC. Adapted from Ref. [196]. Right: two boxed BDCs are installed in between the beam pipes. The bottom crates are a gas handling system for the BDC and the data acquisition electronics for the BDC and SBT.

Table 3.5: Relevant parameters of the BDC in the present experiment.

Parameters			
Drift length	2.5 mm	No. of wires	16 wires/plane
Anode wire	20 µmϕ Au-W/Re	No. of channels	128 ch/chamber
Potential wire	80 µmϕ Au-Al	Operation gas	i-C_4H_{10} at 30 Torr
Configuration	$xx'yy'xx'yy'$ (8 planes)	$V_{\mathrm{pot}} = V_{\mathrm{cathode}}$	-400 V
Effective area	8 cm $\times$ 8 cm	Position resolution	$\sigma \sim 100$ µm
Cathode	8 µm^t Al-Kapton $\times$ 9	Total efficiency	$\sim$ 96%
Vacuum window	80 µm^t Kapton $\times$ 2		

Figure 3.24: Photograph of the NeuLAND demonstrator with charged-particle veto counters.

NeuLAND demonstrator

The prototype of the New Large-Area Neutron Detector (NeuLAND) – called as "NeuLAND demonstrator" [197] – was located at 30° of polar angle and about 7 m away from the center of the SAMURAI magnet, as shown before in Fig. 3.6. The NeuLAND demonstrator is a high-granularity neutron time-of-flight detector consisting of 400 plastic scintillator bars in a dimension of 5 cm × 5 cm × 250 cm, a photograph of which is presented in Fig. 3.24. Eight detector planes segmented in the horizontal or vertical direction, which are assembled from 50 plastic bars, are stacked in a depth direction with an $XYXYXYXY$ configuration. The total volume of the detector amounts to 250 cm (wide) × 250 cm (height) × 40 cm (depth). Scintillation photons in plastics are read by PMTs mounted on both ends of the bar. The electric signals from PMTs are processed by the TacQuila electronics which incorporates ASIC-based QDC and single-hit TDC elements. In front of the NeuLAND demonstrator, charged-particle veto plastic counters were installed, as shown in Fig. 3.24. The geometry of the veto plastic is 32 cm × 190 cm × 1 cm. The veto counters were marginally overlapped each other not to make gaps between them.

The multiplicity and momenta of neutrons can be obtained by analyzing the data of the NeuLAND demonstrator. A typical background signal in the neutron measurement is induced from charged particles and/or γ rays, which can be distinguished by the veto counters and the TOF spectrum of NeuLAND, respectively. In particular, a hit-clustering analysis to identify the path of neutrons and an evaluation of the detection efficiency based on simulations are further required. Because neutrons are beyond the scope of the present work, the data of the NeuLAND demonstrator is not used in this thesis. The information of neutrons will be available in the future, which will provide promising information to probe the neutron-proton dynamics in heavy-ion collisions as well as the high-density symmetry energy.

3.3 Electronic Circuits

3.3.1 Data acquisition system

The data acquisition (DAQ) system of this experiment consists of three different components: the NARVAL DAQ for reading out the GET system of the SπRIT TPC, the RIBFDAQ [198], and the KATANA DAQ, each of which works on a Linux PC. The relevant information on the DAQ system is listed in Table 3.6. Each DAQ system recorded the digitized data with a common-trigger basis, where the common trigger was distributed by the General Trigger Operator (GTO) module [199]. The trigger logic of this experiment is described in the following section.

As described in the previous section, the DAQ system for the SπRIT TPC is handled by the NARVAL framework. Although the zero-suppression mode is available, the NARVAL system was operated with the full-readout mode since the open/close of the gating grid made a spike noise in all of the TPC pads. The data were read out by first 270 sampling channels (or time buckets: Tbs) out of 512 samples, where 1 Tb corresponds to 40 ns with the sampling rate of 25 MHz. The 270 Tb (corresponding to 10.8 µs) is almost equivalent to the maximum drift time of electrons within the field cage. The data rate of this setting was approximately 7 MByte/event. In order to maximize the DAQ performance, the collected data were stored into 12 separated files in parallel. The stored data were copied to the RIKEN HPC storages for a backup and the offline analysis, leaving for partial data at the analysis server for the online analysis.

The RIBFDAQ framework enables us to operate multiple readout front-end systems, *e.g.*, a CAMAC and a VME standard, and to perform a hierarchical event building. It consists of a master event builder and several sub-DAQ systems assigned to different detectors in the slave mode. Thanks to the flexibility of the RIBFDAQ interface, not only typically used crate controllers such as the SBS-620 or the VMIVME, but also special front-end systems such as the VME-EASIROC for the MTD and the TacQuila for the NeuLAND were available as sub-DAQ systems of the RIBFDAQ. Each sub-DAQ system collects and buffers the data from readout modules until the buffer becomes full. Subsequently, the sub-DAQ system packs them into the event fragment and sends them to the master event builder via the Ethernet cables. The master event builder assembles the event fragments, and then, stores the assembled data in the storage system. As tabulated in Table 3.6, the RIBFDAQ integrates sub-DAQ systems of the BigRIPS detectors, the BDCs, the SBT, the MTD, and the NeuLAND demonstrator in the present experiment. The accumulated data are filled into a data structure called RIBF data format (RIDF), which are analyzed with the optimized analysis framework ANAROOT.

The KATANA DAQ handled the CAEN V1730 flash-ADC which reads out signals from the KATANA veto counters and those from the active veto array. Although we do not mention these data in this thesis, the data were used to investigate the stability of the part of the trigger system.

In total, fourteen independent files were stored in the experiment, which is merged in the offline analysis. The typical DAQ rate during the experiment was about 60 Hz. The dead time of the whole DAQ system was about 800 µs.

Table 3.6: The list of the electronics modules for the data acquisition.

Detector (signal)	Readout electronics	Channel #	
RIBFDAQ			DAQ slave
Plastic charge	CAEN V792	8	sva03
Plastic timing	CAEN V1290	8	sva03
PPAC	CAEN V1190	60	sva03
MUSIC	Mesytec MADC32	6	sva01
BDC	AMSC AMT-VME	256	sdaq12
NeuLAND	TacQuila	800	sdaq28
NeuLAND veto	V7XXBIGEND	16	sdaq28
MTD	VME-EASIROC	60	spdaq03
NARVAL DAQ			
SπRIT-TPC	GET system	12,096	
KATANA DAQ			
KATANA veto	CAEN V1730	3	
Active veto	CAEN V1730	4	

3.3.2 Trigger logic

In the present experiment, the master trigger for the DAQ system and the fast trigger for switching the gating grid were separately produced by an FPGA-based electronics board "Trigger Box" [194], and the NIM[6] standard modules, respectively.

The master trigger for the DAQ system was generated based on the Trigger Box, which has been developed to make it possible to configure the trigger logic circuit remotely. In the Trigger Box, a 20-channel discriminator is mounted to convert the amplified analogue signals from the KATANA array (3+12 channels) and the active veto (4 channels) into the logic signals. In addition to the KATANA array and the active veto, signals from the SBT, the MTD, and the busy signal from the readout electronics are used to generate the Trigger Box signal, as shown in Fig. 3.25. Each signal is synchronized based on the gate and delay (G&D) logic in the FPGA. The various parameters are remotely programmable via the RaspberryPi, *e.g.*, the configuration of the FPGA circuit, thresholds of discriminators, a gate width and a delay duration in the G&D logic, and the multiplicity requirement for the KATANA multiplicity array. Note that the KATANA multiplicity did not participate in the generation of Trigger Box signals since it enhanced the active target event as described in Sect. 3.2.4, meaning that the minimum multiplicity requirement was imposed only based on the MTD multiplicity. The master trigger was generated by the coincidence of the Trigger Box signal and the timing reference from the SBT, as shown in Fig. 3.26. The master trigger was sent to the GTO module which distributed the master trigger signal to each sub-DAQ system only when all of them were in readiness.

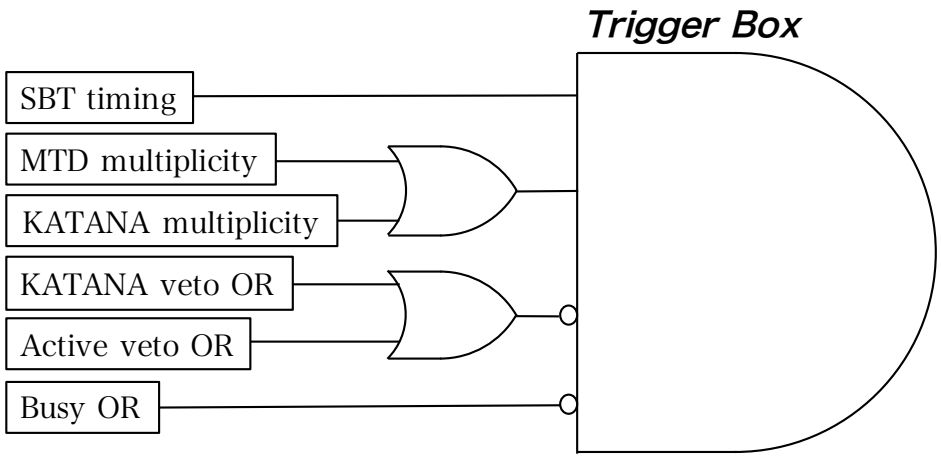

Figure 3.25: Trigger Box diagram. The "SBT timing" means the coincidence signal of four PMTs used for the SBT, which provides a reference timing for all electronics. The "MTD multiplicity" and "KATANA multiplicity" indicate trigger signals generated by the MTD and the KATANA multiplicity with the minimum multiplicity requirements, respectively. The KATANA multiplicity was not used. The "KATANA veto OR" and "Active veto OR" are inclusive OR signals of the three KATANA veto counters and the four Active veto array, respectively. The "Busy OR" is an OR signal from the readout electronics.

[6]"NIM" stands for the Nuclear Instrumentation Module, which is an electronics standard typically used in nulcear and particle physics experiments.

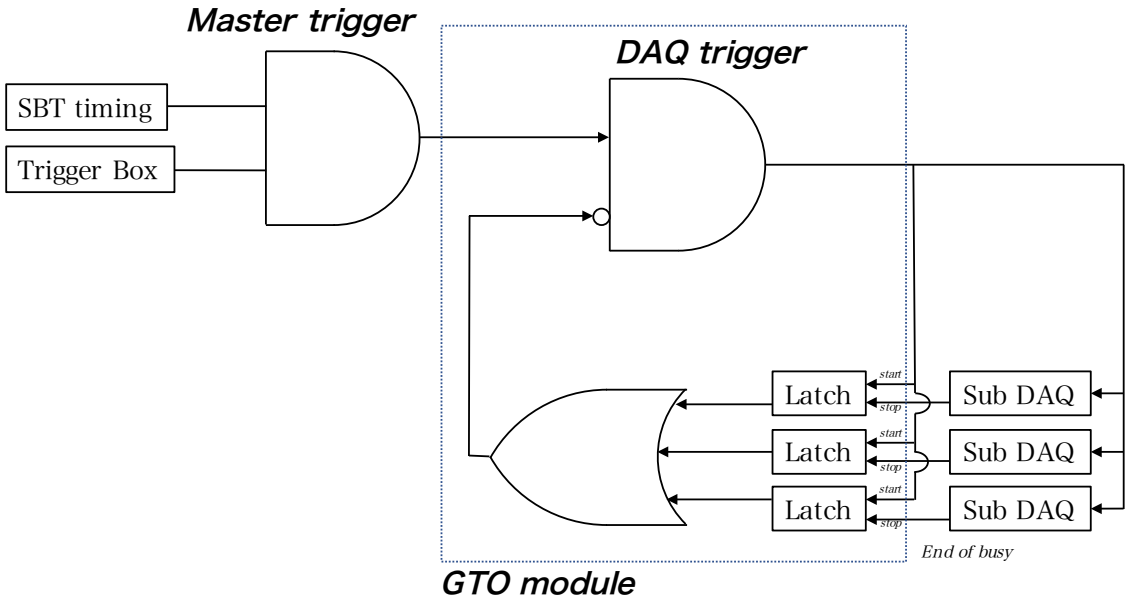

Figure 3.26: DAQ trigger diagram with the simplified description of the GTO module. The GTO module distributes the master trigger signal to each sub-DAQ system only when the inclusive OR output of latch circuits is absent.

In order to reduce the dead region of the SπRIT TPC, it is necessary to open the grid as soon as possible after the desired collision event happens. Hence the "fast trigger" signal was employed with the minimum electronics circuit. As shown in Fig. 3.27, the fast trigger was produced by the coincidence of the SBT, the MTD, the inverse of the KATANA veto, and the inverse of the busy signal. The produced fast trigger was sent to the array of the G&D generators to control the open and close of the gating grid. At the first G&D logic, the signal width is extended to 11 µs equivalent to the maximum electron's drift time in the field cage. The second G&D logic functions in a latch mode, which sends the TTL signal to open the gating grid during the input signal continues. Whenever it receives the interrupt signal, the TTL signal is stopped and the grid is closed without waiting for the electron's drift. The interrupt signal is generated by the inclusive OR of the end of the first G&D signal, the fast clear, and the delayed KATANA veto. The fast clear signal is produced when the fast trigger is generated while the Trigger Box signal is not generated. The delayed KATANA veto prevents the pileup of beam particles that arrive at the TPC before and after the detected reaction events. In this beam pileup case, the gating grid is closed but the DAQ runs, which is considered as a junk event in the offline analysis. The third G&D logic makes a 5 µs wide TTL signal to close the gating grid. The logic signals from the first and third G&D generators are also sent to the busy circuit. To process the open and close of the grid as quickly as possible, these circuits were made by the NIM modules only.

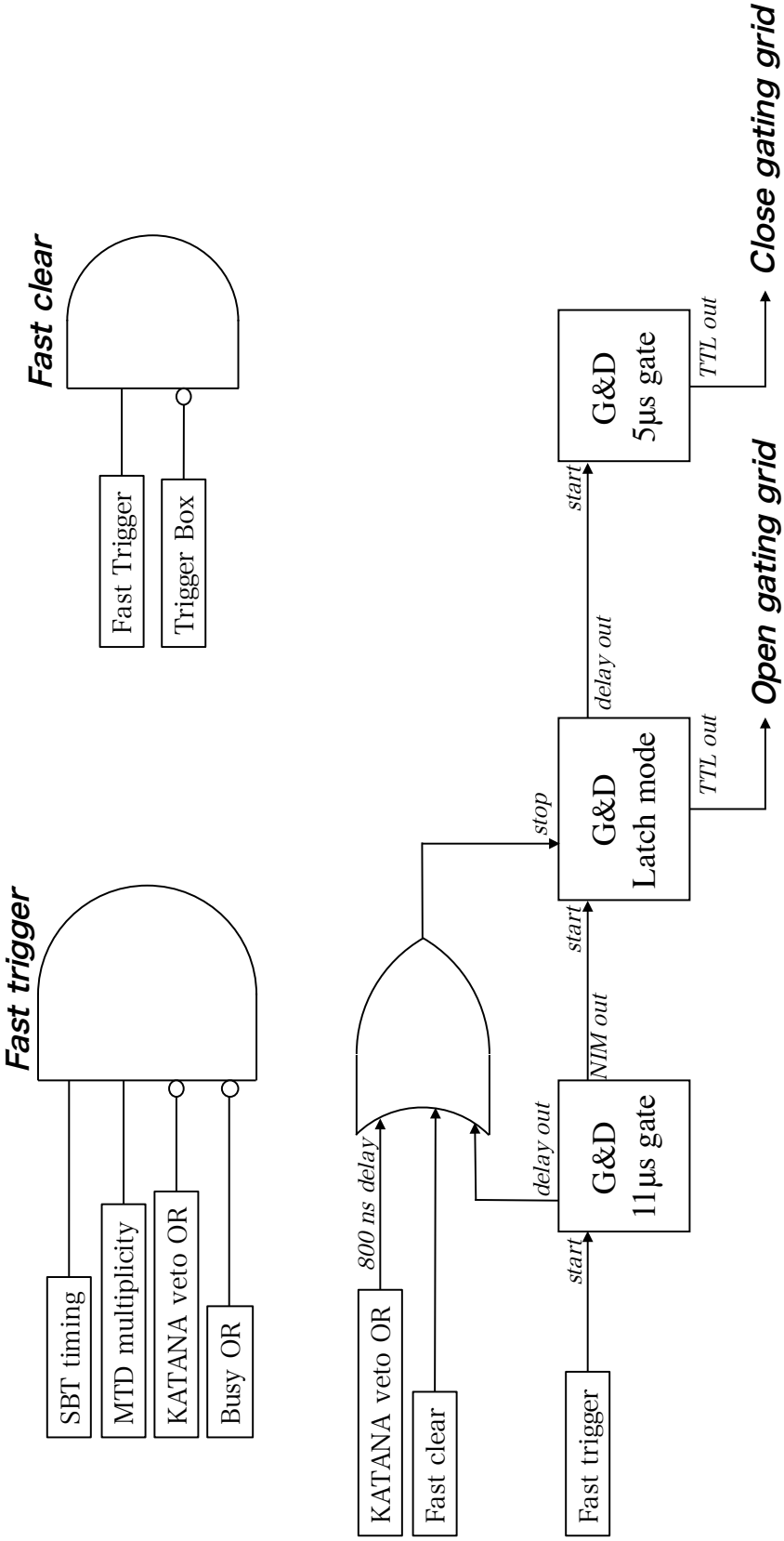

Figure 3.27: Diagrams of the Fast trigger, Fast clear, and the array of G&D generators for an open/close of the gating grid.

3.4 Summary of Experimental Conditions and Accumulated Data

This section summarizes the information on the beam time, experimental conditions optimized in the commissioning runs, and the accumulated data in the physics runs. Table 3.7 presents the timeline of the SπRIT TPC experiment.

Table 3.7: List of the start-and-end time of the experiments, the stored file IDs, and the statistics of the collected data. For the specification of the run numbers used in this work, see Appendix C.

Main system	Start time	End time	Run #	Triggered events
^{108}Sn + ^{112}Sn	April 30, 4:00	May 4, 6:40	2272 ~ 2509	6.2×10^6
^{112}Sn + ^{124}Sn	May 4, 10:10	May 6, 9:00	2542 ~ 2623	4.6×10^6
^{132}Sn + ^{124}Sn	May 26, 12:00	May 29, 16:40	2841 ~ 3039	8.9×10^6
^{124}Sn + ^{112}Sn	May 29, 20:50	May 31, 19:00	3058 ~ 3184	4.7×10^6
Z = 1–3	May 31, 23:00	June 1, 8:40	3187 ~ 3211	6.8×10^5

We accumulated the Sn + Sn collision data with changing the configuration of measurements for some purposes as follows.

Regular run As the main focus of the SπRIT experiment is central (and mid-central) collisions with a small impact parameter, the trigger condition during the regular runs was set so as to efficiently accumulate such focused events and to avoid very peripheral collisions. The multiplicity requirement of the MTD was set as $M_{\mathrm{MTD}} \geq 4$, and the discrimination threshold of the KATANA veto was 31 mV which corresponded to the residue-charge requirement of $Z \leq 20$. In the regular runs, the data were taken under 6–8 kHz of the average beam intensity and 50–60 Hz of the DAQ rate. Typically, one run corresponds to about 30 minutes of data taking. By the simulation-based study [22], it is indicated that the trigger setting in the regular run has a high sensitivity to the $b \leq 3$ fm of central Sn + Sn collisions and the impact parameter distribution of the accumulated data is centered approximately b = 3–4 fm with the almost same order of width.

Minimum bias For a purpose of investigating the trigger bias on the impact parameter selections, low and minimum biased data were also accumulated, as shown in Table 3.8. In the minimum bias runs, the threshold multiplicity of the MTD ranged from zero to three, and the discrimination threshold voltage of the KATANA veto counter varied to 70 mV and 100 mV which corresponded to the charge requirement for residues of $Z \leq 30$ and $Z \leq 40$, respectively. Several minimum bias data were taken with lowering the anode wire voltage of the SπRIT TPC so that only high-Z beam-like particles were seen in the TPC. This option was chosen

Table 3.8: Trigger configurations in the regular run and the minimum bias runs. The multiplicity threshold in the MTD (M_{MTD}), the amplitude threshold in the KATANA veto (V_{KATANA}), and the voltage setting of anode wires of the SπRIT TPC (V_{anode}) are presented.

Data type	M_{MTD}	V_{KATANA}	V_{anode}
Regular run	4	31 mV	1460 V
Minimum bias	0, 1, 2, 3	31 mV	1460 V
	0, 1	70 mV	1460 V
	0	100 mV	1460 V
	1, 3	100 mV	750 V

because one may be able to detect the reaction vertex without reconstructing multiple tracks in the TPC. In the minimum bias run, there are many events with a large impact parameter that produce only a few charged particles. In that case, the efficiency and position resolution of the vertex reconstruction by the TPC would be worse due to a low track multiplicity. Then, it becomes more inaccurate to determine the on-target event rate and the reaction cross section, which are necessary to investigate the trigger bias on the impact parameter selections. If one lowers the anode wire voltage so that only $Z \sim 50$ beams are seen, the reaction vertex can be determined by detecting the fade out of the beam trajectory. Although only the reaction that happened in the TPC can be detected by this method, it might be useful to study the reaction-position dependence of the trigger efficiency. The minimum biased data are not used in this work but used in the assessment of the trigger bias, where the trend of the trigger efficiency depending on the bias in the experiment was consistent with the simulation [22].

Empty target run The empty target data is necessary to estimate the rate of background reactions. It was taken at the end of the ^{112}Sn beam setting with the regular trigger condition.

Gating grid noise data In order to subtract the pattern noise on the TPC data induced by the opening of the gating grid, the noise data were collected without applying high voltage to the anode wires so that only the noise signal was recorded. The noise data was taken every several hours during the measurement.

Calibration run The calibration runs were taken at the end of the whole measurement using $Z = 1$–3 light ion cocktail beams at 100 MeV and 300 MeV. In addition to the empty target mode, an aluminum degrader was installed into the target frame to lower the incident energy of cocktail beams. Since the SBT plastic is too thin to detect the low-Z particles, the F8 plastic counter was used for generating the trigger signal.

4

Data Analysis

In this chapter, a detail of the data analysis will be described. The goal of the whole analysis is to obtain rapidity distributions of hydrogen isotopes emitted from central collisions of the ^{132}Sn+^{124}Sn system and the ^{108}Sn + ^{112}Sn system. In the first half of this chapter (Sect. 4.1–4.6), we focus on the data reduction based on the identification of Sn beams of interest and the selection of central collision events. The latter half will provide the analysis for charged-particle tracks reconstructed in the SπRIT TPC, such as the identification of hydrogen isotopes (Sect. 4.7), the estimation and subtraction of contaminations, the correction of the hydrogen-isotope yields based on the Monte Carlo embedding technique (Sect. 4.8), and the evaluation of the systematic uncertainties (Sect. 4.9).

4.1 RI Beam Identification by BigRIPS

In this section, the identification of RI beams based on the TOF-$B\rho$-ΔE method [177] is described mainly using the data of the two beam settings, ^{108}Sn beams and ^{112}Sn beams, for which the author was responsible. A detail of macros and parameters is uploaded on the GitHub repository [200].

4.1.1 Analysis of PPAC

In the BigRIPS, two double PPACs are installed in three focal planes: F3, F5, and F7. Each PPAC has five output signals: X1, X2, Y1, Y2, and the anode. The total number of channels amounts to sixty, which are read by the V1190 multi-hit TDC. The goal of the PPAC analysis is to obtain optical vectors (x, a) and (y, b) of beam particles at each focal plane.

Treatment of the V1190 multi-hit TDC data

Since the V1190 can record multiple beam hits within its time window in an event, the PPAC analysis begins with selecting a proper hit induced by beam particles in a correct timing. Figure 4.1 presents the TDC spectrum of the X1 signal in the F3–1A PPAC. The highest peak corresponds to the proper hit timing while the others correspond to the pileup of beams. A reference timing was defined as the mean of the highest peak component, and the hit closest to the reference was selected as the proper hit in an event. Only selected hits are used in the following analysis.

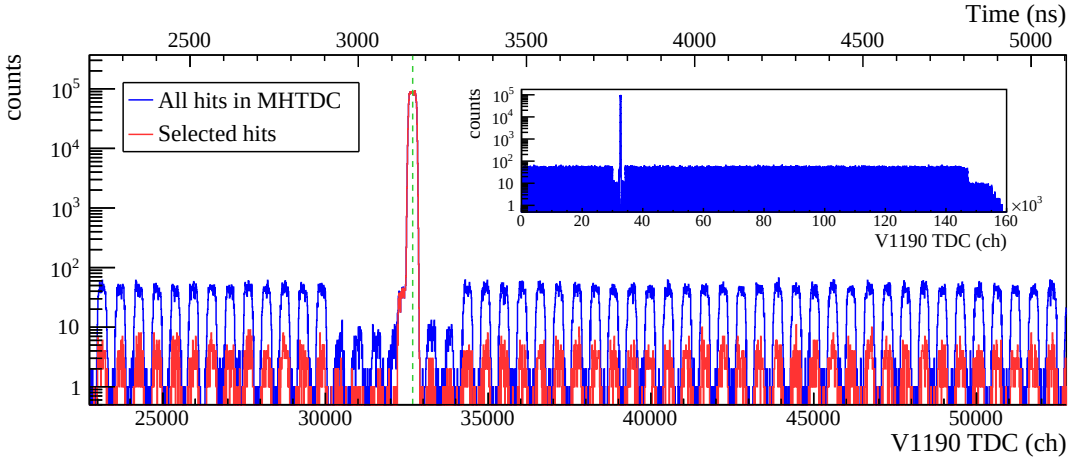

Figure 4.1: TDC spectra of the X1 signal of the F3–1A PPAC. The blue histogram shows all of recorded hits in the limited time window, while that in the full window of the V1190 (~16 μs) is shown in the inset. The red histogram are made from proper hits which are the closest to the reference timing indicated by the green-dotted line on the highest peak. An additional axis on the top side represents a time scale obtained by multiplying the TDC value by 0.09765 ns/TDC – a calibration coefficient of the high-resolution-mode V1190. It is found that the peaks including pileups are found to appear with an interval of 55 ns, equivalent to the cyclotron frequency. A few peaks around the highest one are dropped due to the hardware veto such as the KATANA.

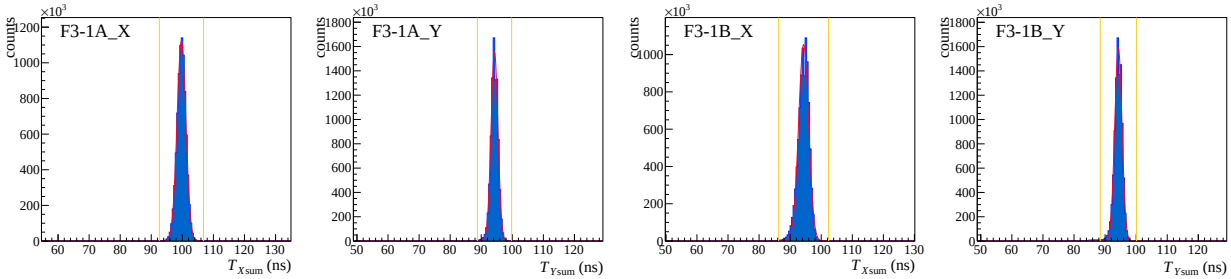

Figure 4.2: $T_{\rm sum}$ spectra of the F3–1 double PPAC. Red lines indicate Gaussian fits to the spectra. Yellow lines represent gates on the $T_{\rm sum}$.

δ-ray rejection by a $T_{\rm sum}$ gate

In the operation of the PPAC, the subtraction of events containing δ-ray-induced hits is important [179]. When the secondary electrons are produced by heavy ions traversing the PPAC, an electron and a heavy ion can make signals on different strips of the PPAC. In that case, the position measurement by Eq. 3.23 fails. To avoid such events, the sum of two delay times in one plane of the PPAC – $T_{\rm sum}$ – was gated, based on the fact that $T_{\rm sum}$ must be a constant value of the total propagation time in the delay-line circuit if the two signals are induced on a single strip. To eliminate the beam-intrinsic time fluctuation, the signal timing of the anode plane was subtracted from the delay times, which gives $T_{\rm sum}$ for the X plane ($T_{X\rm sum}$) and that for the Y plane ($T_{Y\rm sum}$) as:

$$\begin{aligned} T_{X\rm sum} &= T_{X1} - T_A + T_{X2} - T_A \\ &= T_{X1} + T_{X2} - 2T_A, \qquad (4.1) \\ T_{Y\rm sum} &= T_{Y1} + T_{Y2} - 2T_A. \qquad (4.2) \end{aligned}$$

Figure 4.2 shows typical $T_{\rm sum}$ spectra. The gate widths were defined by the results of Gaussian fits on the spectra, i.e., five standard deviations from the mean values of the fitted Gaussian functions.

PPAC efficiencies

Hit efficiency Figure 4.3 and Table 4.1 present the hit efficiencies of the PPACs during the two measurements using ^{108}Sn and ^{112}Sn beams. Here, the hit efficiency of the PPAC is defined as the ratio of the number of counts in each PPAC to the total number of events. The reconstruction of hit (position) in the PPAC should satisfy the following conditions: (1) the delay times satisfy the $T_{\rm sum}$ gate and (2) the x and y positions are reconstructed within the PPAC active area. In fact, the deficiency caused by not satisfying condition (2) was almost negligible ($< 0.01\%$) under condition (1). As shown in Fig. 4.3, some PPACs suffered low efficiencies due to many trips, which were replaced when changing the RI beam setting.

Trajectory reconstruction efficiency The linear trajectory of RI beams is reconstructed based on the least-square method (Eq. 3.24). In the present analysis, we required one hit in one double PPAC at least, out of the two double PPACs in each focal plane. Thus, the trajectory reconstruction efficiency $\epsilon_{\rm reco}$ can be evaluated as:

$$\epsilon_{\rm reco} = \{1 - (1 - \epsilon_{1A}) \times (1 - \epsilon_{1B})\} \times \{1 - (1 - \epsilon_{2A}) \times (1 - \epsilon_{2B})\}\,. \qquad (4.3)$$

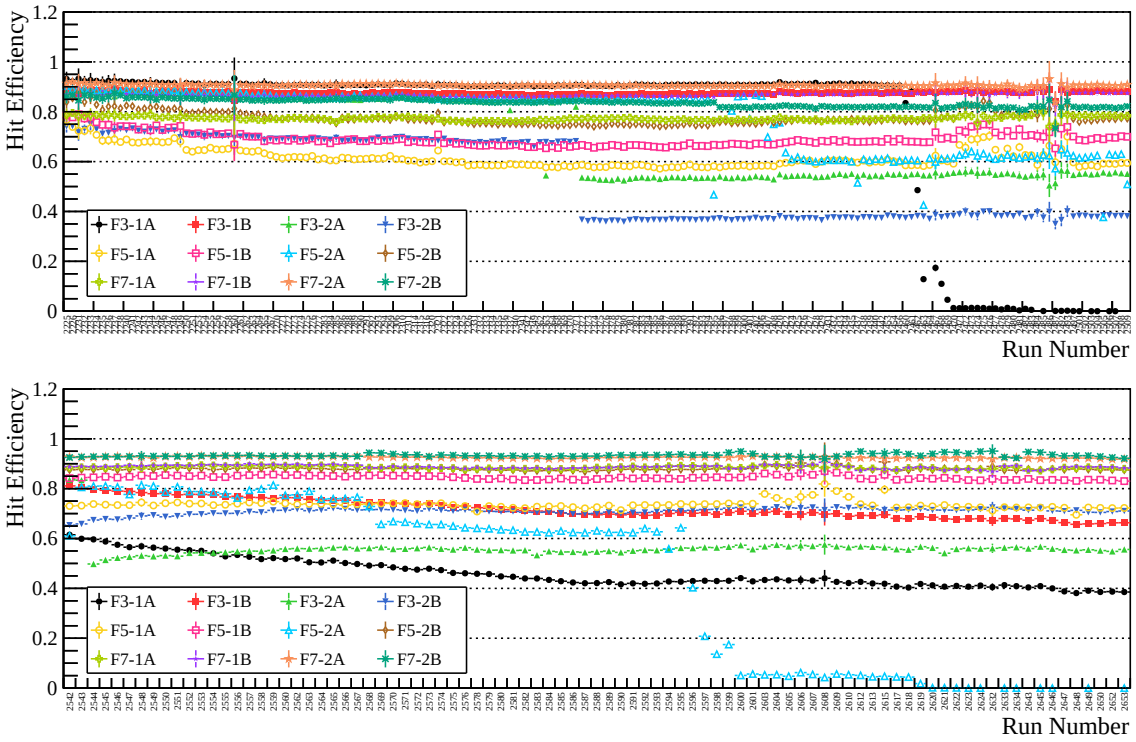

Figure 4.3: PPAC hit efficiencies as a function of run number in the measurement with the ^{108}Sn beam setting (top) and that with the ^{112}Sn beam setting (bottom). At a certain time in the measurement, some PPACs tripped many times and their efficiencies were drastically dropped.

Table 4.1: Overall hit efficiency for each PPAC during the measurements using ^{108}Sn and ^{112}Sn beams. In the "Normal ϵ_{hit}" column, hit efficiencies were obtained based on Eq. 3.23, a normal procedure. In the "Restored ϵ_{hit}" column, efficiencies were calculated including the restored position information based on Eq. 4.4.

PPAC	Normal ϵ_{hit} (%)		Restored ϵ_{hit} (%)	
	^{108}Sn	^{112}Sn	^{108}Sn	^{112}Sn
F3-1A	81.1	46.0	88.9	78.6
F3-1B	87.4	72.0	99.0	93.8
F3-2A	67.4	56.0	77.7	68.6
F3-2B	52.1	70.9	60.9	77.8
F5-1A	59.9	73.4	77.0	86.3
F5-1B	67.9	84.4	80.1	92.9
F5-2A	77.1	46.9	90.7	63.6
F5-2B	76.3	87.8	95.3	98.8
F7-1A	77.1	88.5	95.4	98.7
F7-1B	86.5	88.7	97.0	97.7
F7-2A	90.6	92.5	99.4	99.7
F7-2B	83.5	93.4	93.9	98.5

Table 4.2: Overall beam-trajectory reconstruction efficiency in each focal plane. The columns "Normal" and "Restored" have the same meaning as those in Table 4.1.

Focal plane	Normal ϵ_{reco} (%)		Restored ϵ_{reco} (%)	
	^{108}Sn	^{112}Sn	^{108}Sn	^{112}Sn
F3	80.0	76.7	88.4	90.7
F5	83.6	90.5	94.2	98.3
F7	95.6	98.4	99.4	99.9

Here, ϵ_{1A}, ϵ_{1B}, ϵ_{2A}, and ϵ_{2B} are hit efficiencies of the 1A–, 1B–, 2A–, and 2B–PPAC, respectively. The overall ϵ_{reco} are listed in Table 4.2. Lower efficiencies in the upstream focal plane F3 compared to F5 and/or F7 can be mainly attributed to a higher beam intensity in the upstream side.

Position estimation with a partial information

To compensate for the inefficiency of the PPAC, a restoration of the position information was attempted as follows. Based on the fact that the $T_{\mathrm{sum}} = T_{X1(Y1)} + T_{X2(Y2)} - 2T_A$ should be a constant, which is identical to the total delay time to propagate the whole delay line (T_{DL}), the time difference $T_{X1} - T_{X2}$ can be represented in different ways as:

$$\begin{aligned} T_{X1} - T_{X2} &= T_{\mathrm{DL}} + 2T_A - 2T_{X2} \\ &= -T_{\mathrm{DL}} - 2T_A + 2T_{X1}. \end{aligned} \tag{4.4}$$

In short, the hit position can be reconstructed from a constant $T_{\mathrm{DL}} \simeq T_{\mathrm{sum}}$, either T_{X1} or T_{X2}, and T_A. This restoration prescription was validated by checking a good correlation of $T_{X1} - T_{X2}$ obtained by the normal method and by partial information. For T_{DL}, the mean value obtained by the Gaussian fit on the T_{sum} distribution was used. By including the restored position, the position resolution in each PPAC became 0.1 mm wider, which doesn't affect the later analysis. The hit efficiencies and the trajectory reconstruction efficiencies increased as listed in the right columns of Table 4.1 and Table 4.2, respectively.

Reconstruction of magnetic rigidity $B\rho$

$B\rho$ can be calculated by solving the ion-optical transfer matrix equation (Eq. 3.12). Explicitly in the case of the F3–F5 section in the BigRIPS,

$$B\rho_{35} = \left(1 + \frac{x_5 - (x|x)x_3 - (x|a)a_3}{(x|\delta)}\right) B\rho_{0;35}, \tag{4.5}$$

where x_3 and x_5 are the measured positions at F3 and F5, respectively, and a_3 is the x component of the beam angle from the optical axis. The magnet setup values were employed as central trajectory $B\rho_{0;35}$. The first-order matrix elements $(x|x)$, $(x|a)$, and $(x|\delta)$ were obtained by COSY INFINITY [201]. The employed parameters are shown in Table 4.3.

Table 4.3: Parameters used for the $B\rho$ calculation.

Section	Central rigidity $B\rho_0$ (T m)		Transfer matrix elements		
	^{108}Sn	^{112}Sn	$(x\|x)$	$(x\|a)$ (mm/rad)	$(x\|\delta)$ (mm/%)
F3–F5	5.9203	6.136	0.917	-0.005	31.61
F5–F7	5.9243	6.1408	1.091	0.023	-34.45

4.1.2 Analysis of plastic counters

The goal of the plastic counter analysis is to obtain TOF of beam particles in the F3–F7 section. The charge information of the analogue signal from the PMT was digitized by the V792 QDC after an amplifier. The rising time of the signal was extracted and recorded by a leading-edge discriminator and the V1290 multi-hit TDC, respectively. The multi-hit TDC data were treated in the same manner as that of the PPAC analysis described above.

Slewing correction

The slewing correction is widely used to correct a pulse-height dependence in the time measurement, the so-called time-walk effect. Since a leading-edge type discriminator generates a logic signal at the moment when an analogue signal exceeds a certain threshold value, the start of the logic signal depends on the pulse height, as shown in Fig. 4.4. In the present experiment, the light-output deterioration due to the irradiation of RI beams with a strong stopping power is a main source of the pulse-height variation. The slewing method subtracts the pulse-height dependence, which is empirically parametrized by a certain function, from the measured time. In the present work, the following polynomial parametrization was used:

$$T_{\text{measure}} = T_{\text{true}} + c_0 + \frac{c_1}{\sqrt{q}}. \tag{4.6}$$

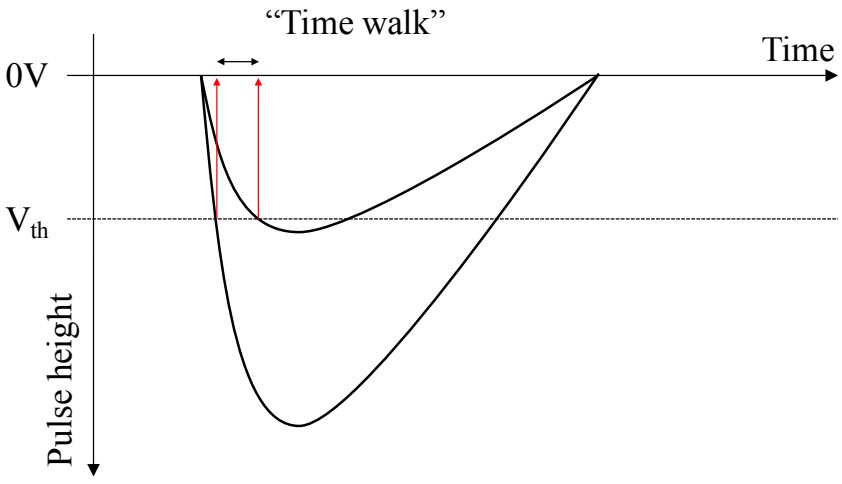

Figure 4.4: Conceptual illustration of the time-walk effect.

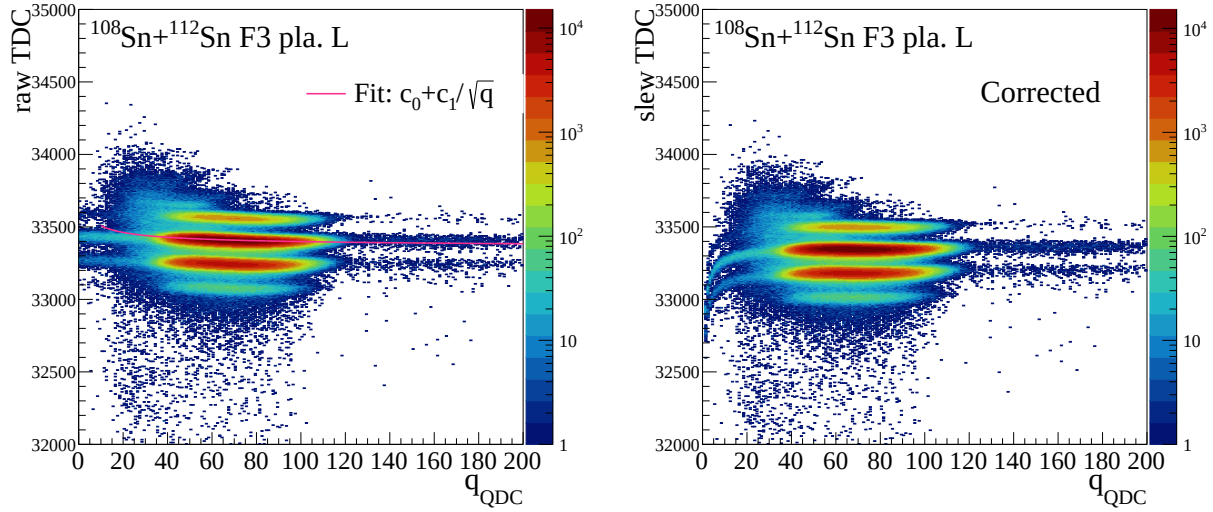

(a) Charge vs. raw TDC.

(b) Charge vs. corrected TDC.

Figure 4.5: TDC spectra as a function of charge measured by the left PMT attached to F3 plastic with and without the slewing correction. Magenta line in the left panel is the fitted polynomial on the main peak, which was used for the slewing correction. Although low q_{QDC} region corresponding to low Z of beams is strongly affected by the correction, such events will be excluded by Sn beam selections.

Here T_{true} is the correct timing independent of the pulse height, t_{measure} is the measured time, q is the charge of the signal, c_0 and c_1 are constant parameters. The T_{measure} corresponds to the measured TDC and the q is measured by the QDC with subtracting the pedestal. The constant parameters are obtained by fitting the TDC–QDC relationship by a function of $c_0 + c_1/\sqrt{q}$. Then, the corrected time T_{true} can be calculated by subtracting $c_1/\sqrt{q}$ from the measured time T_{measure}.

QDC pedestal extraction For determining the charge of signals, the pedestal value needs to be subtracted from measured QDC values. The pedestal for each QDC channel was deduced from the data accumulated with the mismatched timing of the QDC gate, where the QDC module recorded only the pedestal signal. The pedestal distributions were fitted by Gaussian functions to obtain the mean pedestal values, $\langle p_{\mathrm{QDC}} \rangle$. Then, the charge can be calculated as $q_{\mathrm{QDC}} = \mathrm{QDC} - \langle p_{\mathrm{QDC}} \rangle$.

Correlation of T_{measure} vs. q_{QDC} The left panel of Fig. 4.5 presents a correlation between q_{QDC} and TDC values measured by one of the PMT in the $^{108}\mathrm{Sn} + ^{112}\mathrm{Sn}$ data. The four high-intensity loci correspond to different isotopes with different A/Q. The most high-intensity locus corresponds to the RI of interest, ^{108}Sn, which are fitted by the function of Eq. 4.6. In the right panel of Fig. 4.5, $\mathrm{TDC} - c_1/\sqrt{q_{\mathrm{QDC}}}$ vs. q_{QDC} is shown. The dependency on charge is now corrected, showing the flat distribution as a function of q_{QDC}. The slewing correction was similarly applied for the other PMT's data.

Time of flight spectrum The TOF in the F3–F7 section was calculated according to Eq. 3.21. The time offset for each beam setting was basically obtained by the beam transport calculation code LISE++ [202]. Practically, they were optimized so that the mean A/Q values for Sn isotopes become nominal values, in the later analysis. Thanks to the slewing correction, the time variation

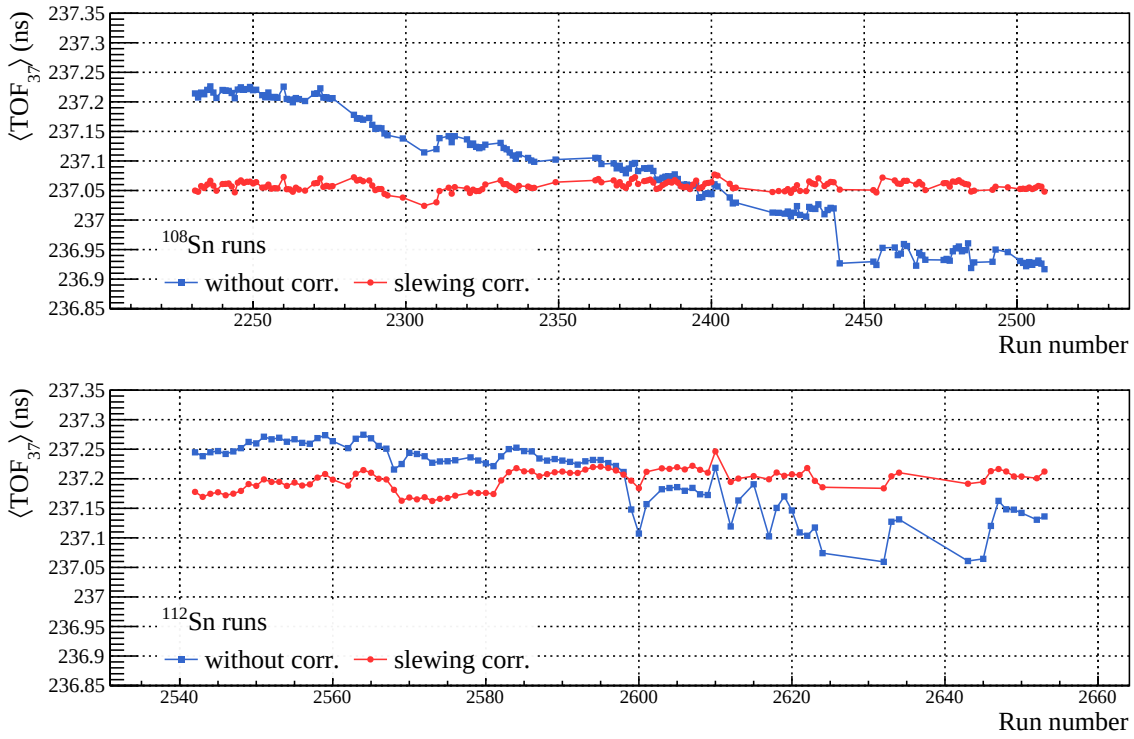

Figure 4.6: Elapsed time dependence of the peak of TOF_{37} for ^{108}Sn (top) and ^{112}Sn (bottom) isotopes, which were extracted by a Gaussian fit to each peak in the TOF_{37} spectra, see Fig. 4.7. The mean TOF_{37}, $\langle TOF_{37} \rangle$, without correction depends on the elapsed time during the measurement, because the beam intensity is higher at F3 than at F7, *i.e.*, the plastic at F3 was more irradiated than that at F7. With applying the slewing correction, the $\langle TOF_{37} \rangle$ became independent to the elapsed time.

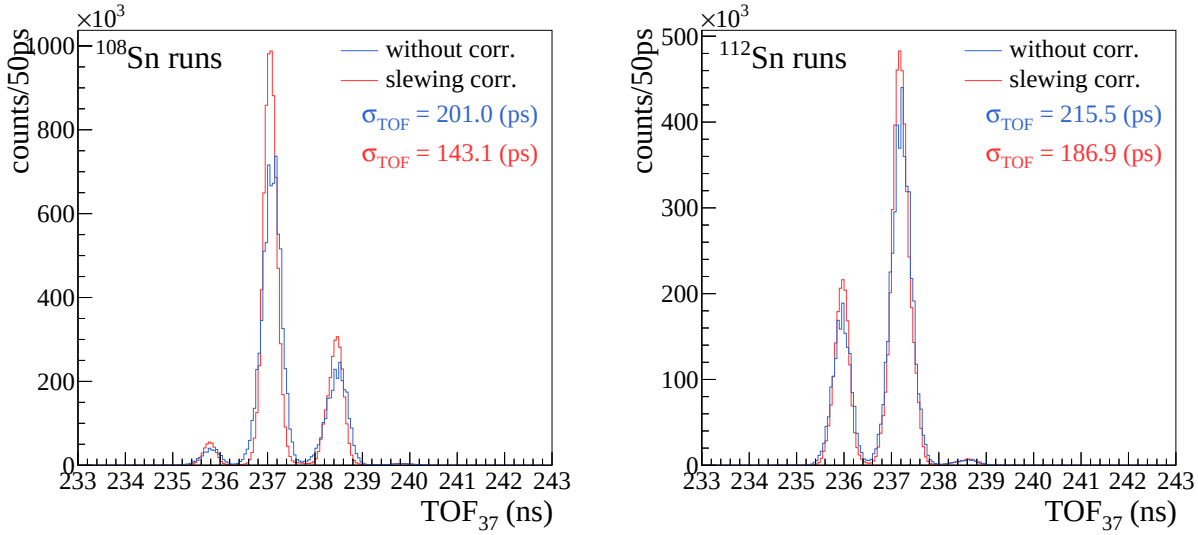

(a) TOF spectra in the ^{108}Sn runs.

(b) TOF spectra in the ^{112}Sn runs.

Figure 4.7: TOF spectra with (red) and without (blue) slewing correction for the two beam settings. The main peaks corresponding to ^{108}Sn and ^{112}Sn were fitted by Gaussian functions to evaluate the correction. The peak widths became narrower with the correction, as written in the figure.

of the TOF becomes more stabilized, as shown in Fig. 4.6. The TOF spectra with and without the slewing correction are presented in Fig. 4.7, showing an improvement of the TOF resolution.

4.1.3 Analysis of MUSIC

The goal of the MUSIC analysis is to calibrate the ADC channel into the unit of MeV based on the comparison between the ADC mean value associated with a certain isotope species and the LISE++ calculation. To select events that recorded a certain RI of interests, the preliminary particle identification (PID) spectrum was constructed, as shown in Fig. 4.8. We referred to seven isotopes in the ^{108}Sn beam runs and six isotopes in the ^{112}Sn beam runs for the calibration. Events associated with each isotope were gated by ellipsoidal cuts on the preliminary PID, and the respective channels of ADC distributions were constructed to obtain their mean values, $\langle ADC \rangle$. Table 4.4 lists the LISE++ result on the mean energy deposits ΔE_i in the i-th region of the MUSIC detector for the referred isotopes. The relationship between ΔE_i and the $\langle ADC_i \rangle$ of each selected isotope were fitted by linear function:

$$\Delta E_i = c_0 + c_1 \cdot \langle ADC_i \rangle \qquad (i = 0\text{–}5), \tag{4.7}$$

to obtain calibration parameters c_0 (MeV) and c_1 (MeV/channel). An atomic number was calculated based on Eq. 3.19 using the geometrical mean of the calibrated energy deposits.

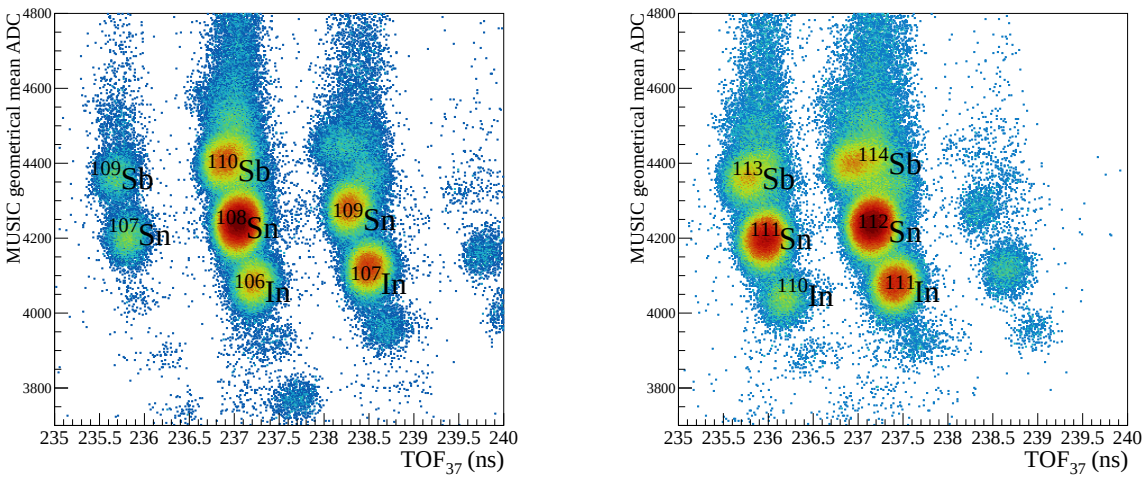

Figure 4.8: Preliminary PID spectra of the geometrical mean of the MUSIC ADC vs. TOF$_{37}$, used for selecting events of a certain RI of interests. Ellipsoidal cuts were applied for selecting RIs.

4.1.4 Reconstruction of the mass-to-charge ratio A/Q

The A/Q of beam isotopes was reconstructed based on Eqs. 3.15–3.17, and 3.18, which required a successful reconstruction of the TOF$_{37}$, $B\rho_{35}$ and $B\rho_{57}$. In the following, a restoration method that reconstructs A/Q from the TOF$_{37}$ and either $B\rho_{35}$ or $B\rho_{57}$ is described.

A/Q reconstruction from single section information As is described, the usual method reconstructing the A/Q of isotopes fails if any one of the TOF$_{37}$, $B\rho_{35}$, and $B\rho_{57}$ is not available. Here,

Table 4.4: Energy deposits of RI beams in each region of the MUSIC, calculated by the LISE++. Subscript numbers indicate the MUSIC sections from the most upstream to the downstream ones by numbers from 0 to 5.

	Energy deposit in MUSIC (MeV)					
Benchmark RI	ΔE_0	ΔE_1	ΔE_2	ΔE_3	ΔE_4	ΔE_5
^{108}Sn	68.89	68.99	69.08	69.18	69.28	69.37
^{109}Sn	69.48	69.58	69.65	69.75	69.84	69.93
^{107}Sn	68.34	68.42	68.5	68.59	68.68	68.77
^{107}In	66.78	66.86	66.96	67.05	67.12	67.22
^{106}In	66.2	66.29	66.38	66.48	66.56	66.68
^{110}Sb	71.61	71.72	71.81	71.92	72.02	72.12
^{109}Sb	71.07	71.16	71.24	71.33	71.43	71.52
^{112}Sn	68.72	68.82	68.91	69.0	69.09	69.18
^{111}Sn	68.2	68.28	68.36	68.45	68.52	68.6
^{110}In	66.08	66.16	66.26	66.34	66.43	66.52
^{111}In	66.65	66.74	66.82	66.89	66.98	67.05
^{113}Sb	70.88	70.98	71.07	71.16	71.24	71.32
^{114}Sb	71.44	71.51	71.6	71.7	71.8	71.9

an offline restoration of the A/Q in such events was attempted as follows. In the present experiment, as only two double PPACs were installed in the F5 focal plane, a change of beam velocity owing to the energy deposit was expected to be small. If we simply assume the linear relationship between two velocities upstream and downstream of the F5 plane, i.e., $\beta_{35} = b_0 + b_1 \cdot \beta_{57}$, we can deduce the β_{57} by substituting the β_{35} into Eq. 3.15:

$$\mathrm{TOF}_{37} = \frac{L_{35}}{(b_0 + b_1 \cdot \beta_{57})c} + \frac{L_{57}}{\beta_{57} c}, \tag{4.8}$$

where b_0 and b_1 are constants. Using this alternative expression, the A/Q can be reconstructed from TOF_{37} with either $B\rho_{35}$ or $B\rho_{57}$, even if the trajectory (optical vector) was reconstructed only at F3 or F7, respectively. When the ion-optical vector at the F5 plane was not available, this procedure cannot be applied since neither $B\rho_{35}$ and $B\rho_{57}$ are available.

Figure 4.9 shows the β_{35}–β_{57} relationship only using events where three optical vectors were correctly reconstructed. A linear correlation was clearly observed, indicating that the restoration procedure above may be promising. Figure 4.10 compares the A/Q spectrum obtained by the conventional procedure and those by the restoration methods. It was found that the spectrum of the A/Q reconstructed from only $B\rho_{57}$ information without $B\rho_{35}$ is comparable with the conventional one, while that with only $B\rho_{35}$ had a quite worse resolution. Therefore, this A/Q restoration was used only when the $B\rho_{35}$ is unavailable but the other $B\rho_{57}$ and TOF_{37} were available. The restoration procedure improved the A/Q reconstruction efficiencies, as summarized in Table 4.5.

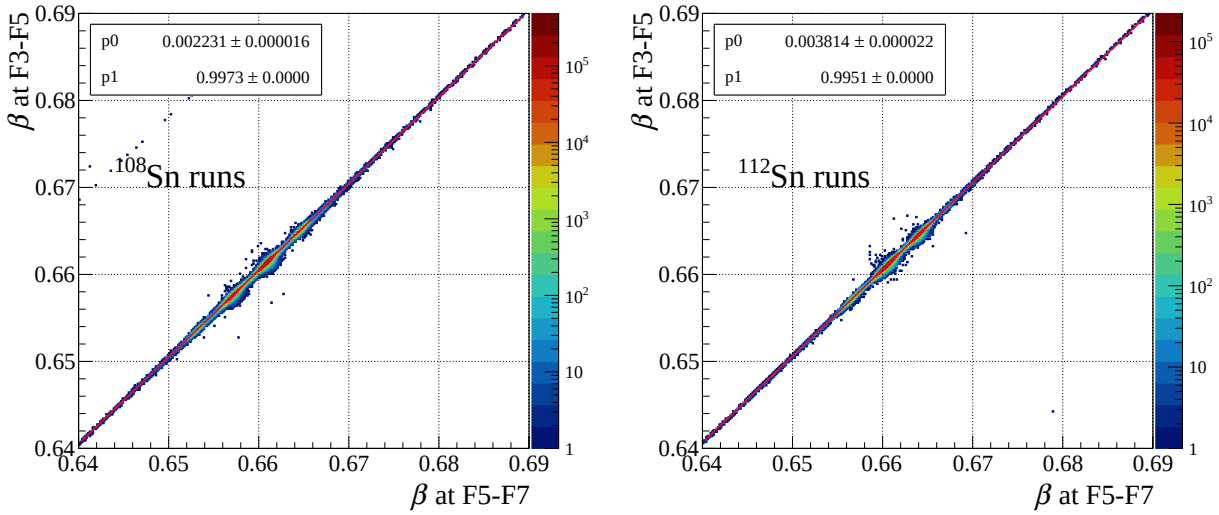

(a) ^{108}Sn beam runs. (b) ^{112}Sn beam runs.

Figure 4.9: β_{35}–β_{57} correlation, which is fitted by a linear function $\beta_{35} = p_0 + p_1\beta_{57}$. In the left-top legends in each panel, the results of the fit are shown.

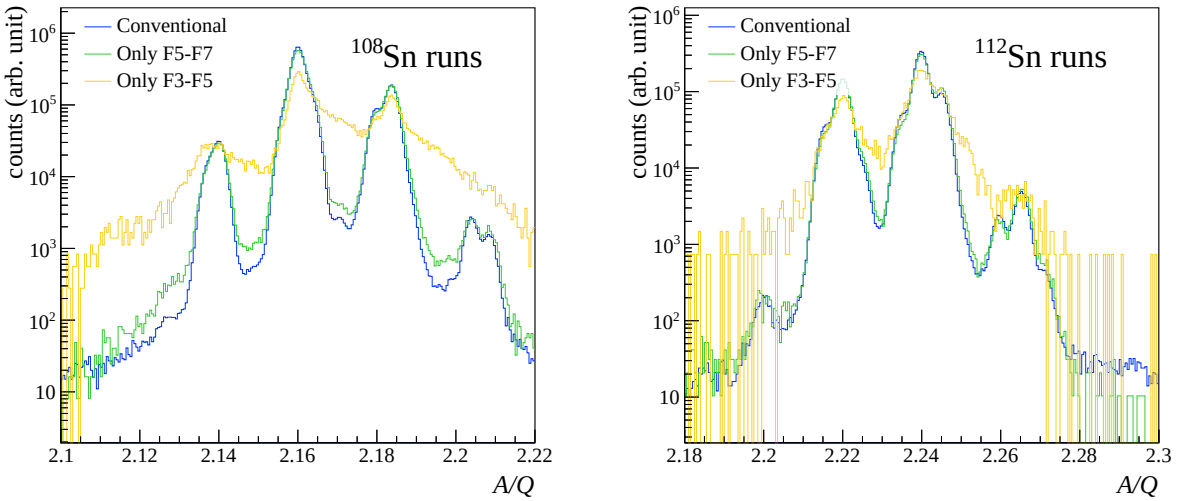

(a) ^{108}Sn beam runs. (b) ^{112}Sn beam runs.

Figure 4.10: A/Q spectra reconstructed by different procedures. Blue histogram presents the A/Q spectrum reconstructed by the conventional TOF-$B\rho$ method using events where ion-optical vectors of beam particles at three foci were all successfully reconstructed. Green and yellow histograms are constructed from events where only $B\rho_{57}$ was available but $B\rho_{35}$ was unavailable (due to a fail of tracking at F3) and those where the abvailability was opposite (a fail of tracking at F7), respectively. Blue and green histograms are almost identical while the resolution of the yellow one is worse compared to the ohter two. Note that histograms are normalized by their integrals.

Table 4.5: Overall A/Q reconstruction efficiency. The reconstruction effciency was calculated as the ratio of the number of events satisfying $1 < A/Q < 3$ to the total number of events. The "Conventional" reconstruction procedure requires ion-optical vectors at all of foci: F3, F5, and F7. In the method "Only $B\rho_{57}$", the A/Q was reconstructed without using $B\rho_{35}$ when the PPACs failed the trajectory reconstruction at F3.

Beam setting	A/Q reconstruction efficiency (%)	
	Conventional	Conventional + Only $B\rho_{57}$
^{108}Sn	83.6	93.9
^{112}Sn	89.5	98.1

4.1.5 Beam isotope identification in Z vs. A/Q

Figure 4.11 presents the two-dimensional PID spectra in the space of atomic number Z vs. mass-to-charge ratio A/Q reconstructed in each set of data. The data of the neutron-rich Sn beams were analyzed similarly, but the slewing correction of PMT signals was not applied since the positions of PMTs had been periodically shifted vertically during the measurement in the ^{132}Sn and ^{124}Sn isotope settings not to irradiate plastics too much. Thanks to the shift of the plastic, the TOF_{37} resolution for the neutron-rich Sn beams was found to be comparable with the one for the neutron-deficient Sn beams presented in this thesis. The gate conditions to select the RI of interests, ^{108,112,124,132}Sn, were defined by a two-dimensional normal distribution fitted to the spectra, which is expressed as:

$$
\begin{aligned}
u &= (A/Q - \mu_{A/Q})/\sigma_{A/Q}, \\
v &= (Z - \mu_Z)/\sigma_Z, \\
z &= u^2 + v^2 - 2\rho uv, \\
p(A/Q, Z) &= \frac{1}{2\pi\sigma_{A/Q}\sigma_Z\sqrt{1-\rho^2}} \exp\left\{\left(-z/2(1-\rho^2)\right)\right\},
\end{aligned}
\tag{4.9}
$$

where μ and σ represent the mean and the standard deviation of the normal distribution, respectively, and ρ indicates the degree of correlation between the two variables: Z and A/Q. Table 4.6 lists the fit results. The events within the ellipsoidal region of $\pm 3\sigma$ from the central coordinate of distributions $(\mu_{A/Q}, \mu_Z)$, drawn by red lines in the figure, will be used in the later analysis. Table 4.7 summarizes the event reduction based on the Sn beam selections.

Table 4.6: Parameters of two-dimensional normal function fitted to the Sn isotope peaks in the Z vs. A/Q spectra.

Beam isotope	μ_Z	σ_Z	$\mu_{A/Q}$	$\sigma_{A/Q}$	ρ
^{108}Sn	49.9928	0.209834	2.16003	0.00150375	-0.0636639
^{112}Sn	49.9842	0.208148	2.23995	0.00162915	-0.0661349
^{124}Sn	49.9344	0.206928	2.4801	0.00170198	-0.0674846
^{132}Sn	49.9517	0.212966	2.64	0.00139823	-0.051702

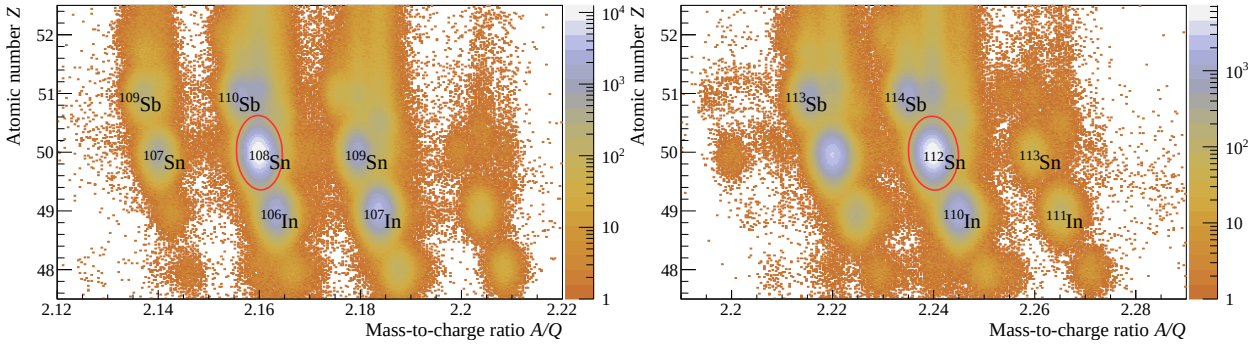

(a) Beam PID for ^{108}Sn runs.

(b) Beam PID for ^{112}Sn runs.

(c) Beam PID for ^{124}Sn runs.

(d) Beam PID for ^{132}Sn runs.

Figure 4.11: Two-dimensional Z vs. A/Q spectra obtained by analyzing the data of the beamline detectors installed in the BigRIPS, for four kinds of RI beam settings: (a) ^{108}Sn, (b) ^{112}Sn, (c) ^{124}Sn, and (d) ^{132}Sn isotopes. Red ellipsoids indicate the gate for respective Sn isotopes, which are defined by 3σ from the mean value.

Table 4.7: Summary of the event statistics with respect to the RI beam identification. First column: isotope settings for the analyzed data. Second: the total number of analyzed events. Third: the number of events satisfying $1 < A/Q < 3$. Forth: the number of events within the ellipsoidal Sn isotope gates. Fifth: the ratio of the forth column to the second column.

Beam isotope	Total events	$1 < A/Q < 3$	3σ gate	3σ/total
^{108}Sn	6.7×10^6	6.3×10^6	2741221	41.0 %
^{112}Sn	4.6×10^6	4.6×10^6	1810222	39.0 %
^{124}Sn	4.7×10^6	2.9×10^6	255095	5.4 %
^{132}Sn	8.9×10^6	8.8×10^6	3888400	43.8 %

4.2 Beam Position and Energy on the Sn Target

In the present experiment, two BDCs were installed upstream of the Sn target to analyze and extrapolate the beam trajectory onto the target plane (see Sect. 3.2.6). In this section, the BDC analysis and the extrapolation of beam particles under the SAMURAI magnetic field are described.

4.2.1 BDC Analysis

The BDC employs a drift chamber with an $xx'yy'xx'yy'$ configuration with 16 wires in 5 mm pitch per plane, whose signals induced on wires were digitized by the VME-AMT multi-hit TDC. From the arrival time of beam-induced drift electrons and the position of the wire, the position of the beam trajectory perpendicular to the wire can be calculated. The top panels of Fig. 4.12 present the TDC distributions in the two BDCs. Because the electric-field density increases and the electron's drift velocity becomes higher in the proximity to the wires, the TDC distributions are not uniform. On the other hand, a typical profile of RI beams at RIBF has a diameter of the order of a few cm, and it is practically assumable that injected beams uniformly distribute around a certain wire. Therefore, a nonlinear conversion of the arrival time into the drift distance, the so-called the space-time conversion (STC) function, is required. Such STC function F_{STC} for a certain TDC value "TDC" is presented in the bottom panels of Fig. 4.12, which can be defined as:

$$F_{\mathrm{STC}}(TDC) = 2.5 \times \frac{\int_{TDC}^{T_{\mathrm{max}}} f_{\bar{T}}\, d\bar{T}}{\int_{T_{\mathrm{min}}}^{T_{\mathrm{max}}} f_{\bar{T}}\, d\bar{T}}, \tag{4.10}$$

where f_T represent the TDC distribution of drift electrons ranging from T_{min} to T_{max}. The factor 2.5 is attributed to the half of wire pitch. The drift distance is then provided by the STC function for an arbitrary TDC value within the TDC distribution. The sign of the reconstructed position, i.e., left or right of wires, is considered in the trajectory reconstruction stage.

Trajectory reconstruction The trajectories of incident beams were obtained by interpolating and extrapolating the two (x, y) positions reconstructed in the respective BDCs. In each BDC, the beam trajectory was reconstructed using the least square method, similarly to the PPAC analysis. The algorithm requires at least three hits reconstructed out of four layers in X or Y directions. When multiple hits were found in certain layers, all of the possible linear trajectories were reconstructed and the track with the minimum chi-square value was assigned as the best track, as shown in Fig. 4.13. The sign of the associated hits was also considered. In fact, since sensitive wires in adjacent layers are staggered alternately so that their positions are shifted in half of the wire pitch, a possible pattern of signs is limited, *e.g.*, positive in an X layer and negative in the next X' layer. The trajectory reconstructed in each BDC was interpolated to the center of each BDC located at $z = z_1$ and $z = z_2$ to obtain two positions Sn beams passed through: (x_1, y_1, z_1) and (x_2, y_2, z_2). Then, the linear trajectory of incident beams upstream of the target can be calculated as:

$$x_{prj} = \frac{x_2 - x_1}{z_2 - z_1} \cdot (z_{prj} - z_1) + x_1. \tag{4.11}$$

Here x_{prj} is the x position of the incident-beam trajectory extrapolated onto the plane $z = z_{prj}$.

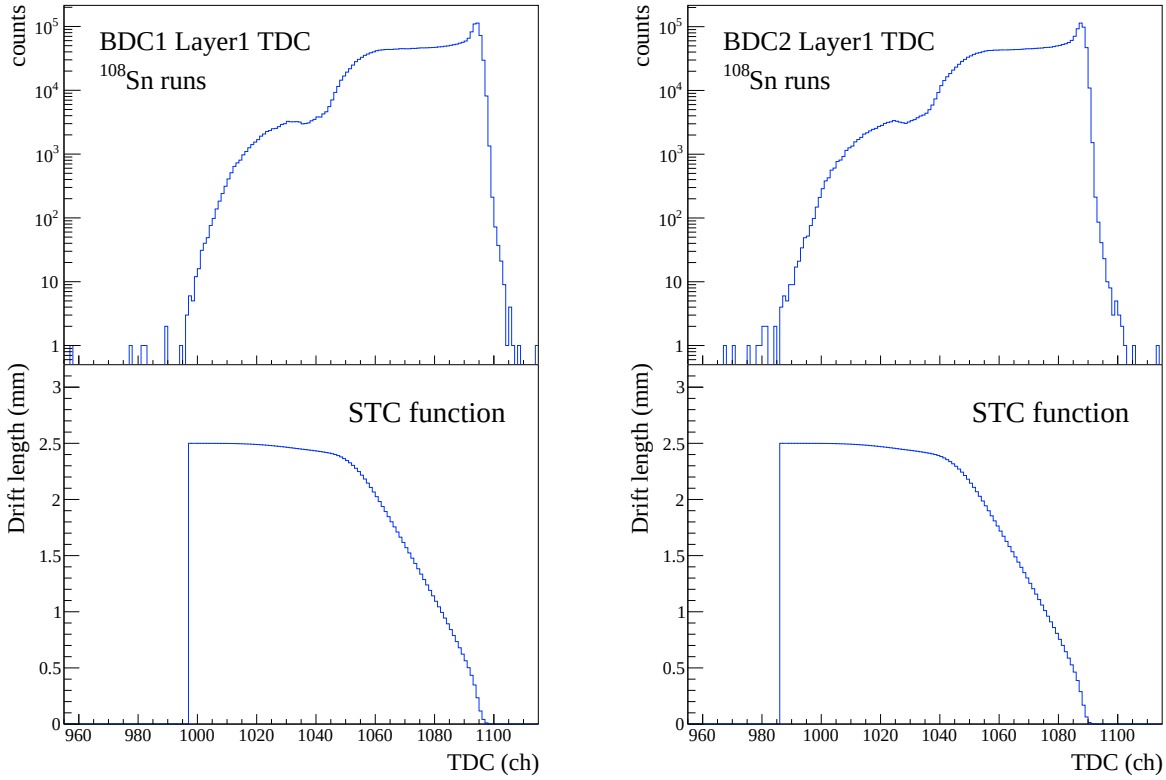

Figure 4.12: TDC distributions and STC functions of the two BDCs.

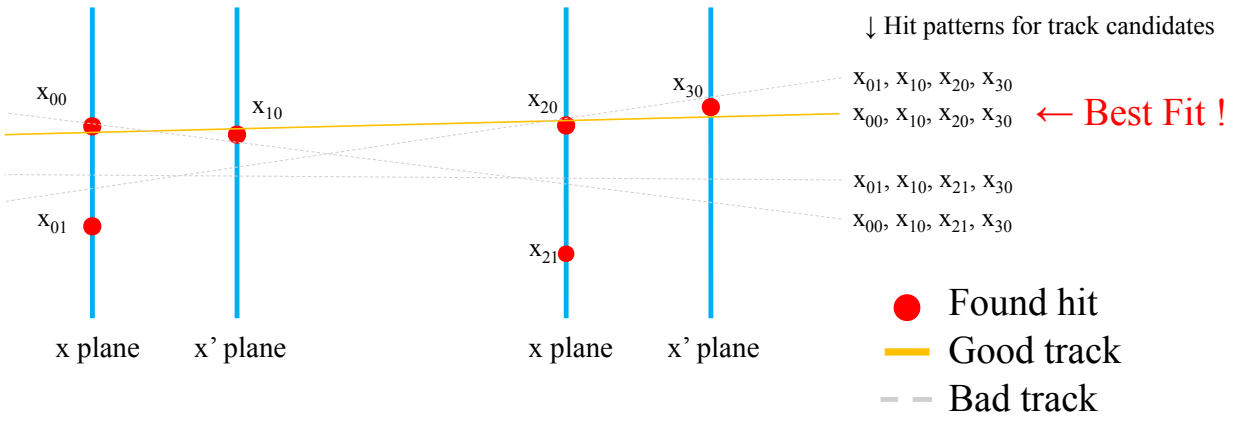

Figure 4.13: Conceptual illustration of the trajectory reconstruction in the x–z plane within a single BDC. Out of all possible candidates, the track with the minimum χ^2 value is chosen as the best track in the analysis.

4.2.2 Beam projection under magnetic field

Since Sn targets were located under the SAMURAI magnetic field, incident beams are bent before hitting the target (see Fig. A.1 in Appendix A.2). The bending of beams modifies the effective thickness of the material, which should be considered in the determination of the beam energies. To determine the energy, position, and angle of incident beams on target, the beam particle was propagated in a minute step by step, considering the magnetic field and energy losses in the material installed in the beam path.

Propagation of beams under magnetic field Figure 4.14 presents the conceptual drawing of the step-by-step propagation. The propagation begins at the exit of the second BDC, $z = z_{\mathrm{BDC2}}$, approximately 2 m upstream from the center of SAMURAI magnet where the magnetic field is in an order of 10^{-3} T. The beam energy at $z = z_{\mathrm{BDC2}}$ was deduced from the $B\rho_{57}$ value with considering energy deposits in material. Passages of the two double-PPACs, the MUSIC, the plastic counter, the two SBTs, and the two BDCs were considered, and the total kinetic-energy loss was calculated as $\sim$ 7% based on LISE++. The (x, y) position and yaw-pitch angle (a, b) at $z = z_{\mathrm{BDC2}}$ were obtained by the trajectory reconstructed by the BDCs (Eq. 4.11). The curvature radius ρ can be calculated based on the equation of motion, as:

$$\rho = \frac{1}{B_y(x, y, z)} \cdot \frac{p}{q}, \tag{4.12}$$

where $B_y(x, y, z)$ indicates the y-component of the magnetic field at the coordinate (x, y, z), p and q are the momentum and charge of beam particles, respectively. For the B_y, the SAMURAI magnetic field map under 0.5 T calculated by the TOSCA code was used. With those initial conditions, the particle is propagated by a step along the curvature with the energy loss in the total

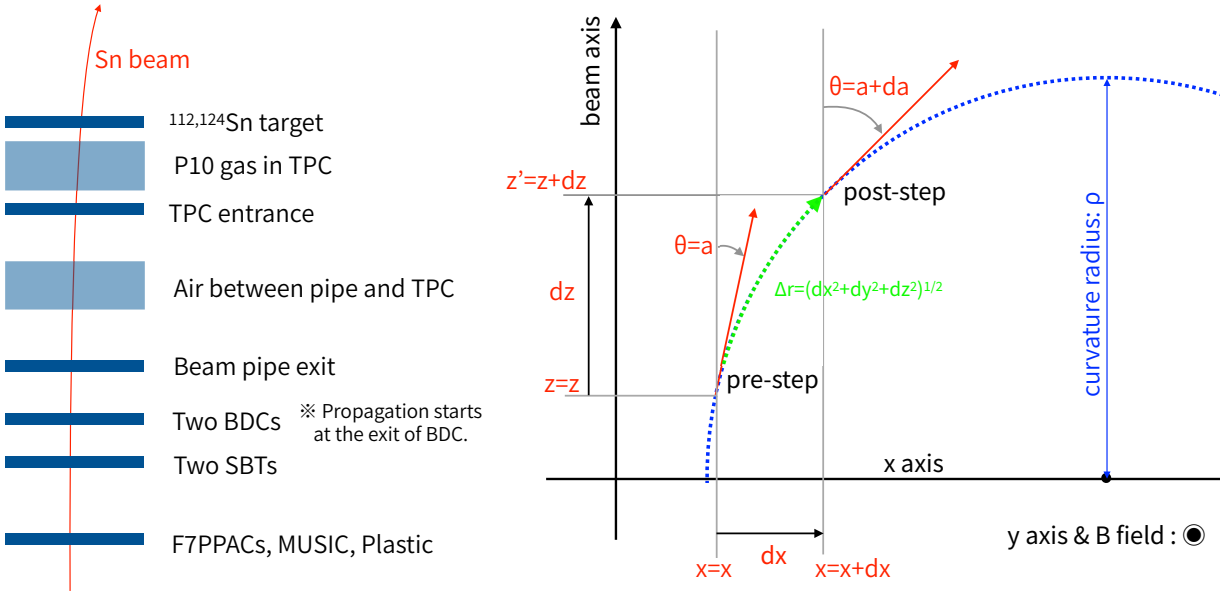

Figure 4.14: Conceptual drawings of the beam propagation under the SAMURAI magnetic field. Left: material considered in the determination of the beam energy. Right: a top view of the propagating beam particle in a certain step and that in a next step.

Table 4.8: List of material considered in the beam propagation. The ΔE rates were calculated by the LISE++, where the mean values were employed. The ΔE rates for the half thickness of the employed Sn target were calculated so that the energy at the midpoint of the target can be obtained. For relative positions of each stuff along the beam axis, see Fig. 3.22.

Name	Material	Thickness (mm)	Density (g/cm^3)	ΔE rate (%)
Beam pipe exit	Kapton	0.05	1.42	0.2
Pipe to TPC	Air	141.75	0.0012	0.4
TPC entrance	Mylar	0.004	1.397	0.1
TPC gas	P10	274.184	0.001534	1.0
Sn target	^{112}Sn	0.3852 (half)	7.282	5.2 for ^{108}Sn beam
	^{124}Sn	0.4175 (half)		5.1 for ^{132}Sn beam

step length of $\Delta r = \sqrt{dx^2 + dy^2 + dz^2}$. The one step was defined so that a small displacement along z axis becomes $dz = 1$ mm. The process continued until the beam reaches the z coordinate of the target midpoint. Table 4.8 summarizes the material considered in this propagation procedure together with the relevant typical energy loss rate for respective Sn isotopes.

Phase space of incident Sn beams Figure 4.15 presents the phase space of incident ^{132}Sn and ^{108}Sn beams projected onto the Sn targets. Table 4.9 lists the mean and root-mean-square values of the phase-space distributions. Note that the means of the horizontal angles are negative since incident beams are bent in the magnet and then impinge on the target. The x-position distributions are centered to nearly zero, which was adjusted by optimizing the D5 and D6 magnets so that beam particles hit the center of the Sn target.

Table 4.9: Properties of beam profiles on target. The mean and root-mean-square (rms) values of position and angle distributions for respective Sn beams. Positions are shown in mm and angles in mrad.

Isotope	Beam position (x, y) on target (mm)				Beam angle (a, b) on target (mrad)			
	mean$_x$	mean$_y$	rms$_x$	rms$_y$	mean$_a$	mean$_b$	rms$_a$	rms$_b$
^{108}Sn	-0.17	-0.77	4.21	3.99	-55.18	-0.44	1.20	2.10
^{112}Sn	2.25	-0.71	4.13	4.09	-53.85	-0.41	1.15	1.78
^{124}Sn	5.35	0.82	11.00	9.43	-47.92	0.32	3.79	5.93
^{132}Sn	3.06	0.75	7.45	5.30	-44.19	0.60	2.58	3.32

Beam energy on target Figure 4.16 presents the kinetic energy distributions of four Sn beams projected on the midpoint of the target with considering energy losses in the material. Their mean values and root mean squares are listed in Table 4.10. The beam energy will be used to define the center of mass of the reaction system in the later analysis.

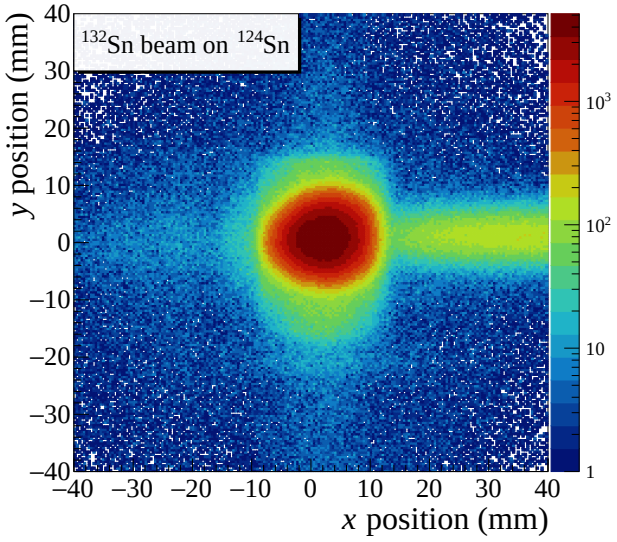

(a) x vs. y positions of ^{132}Sn beams.

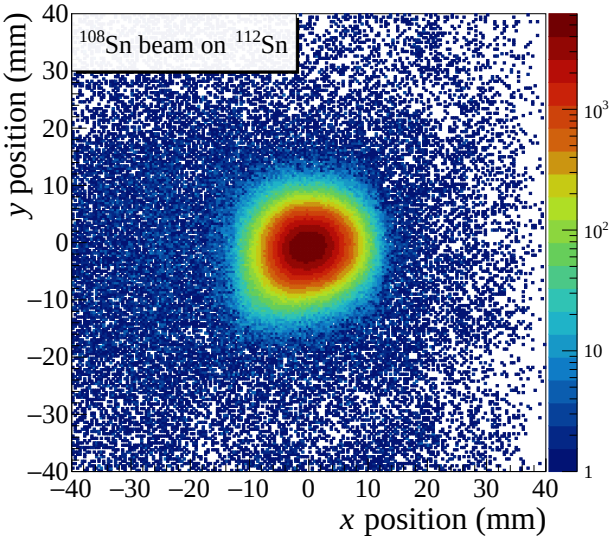

(b) x vs. y positions of ^{108}Sn beams.

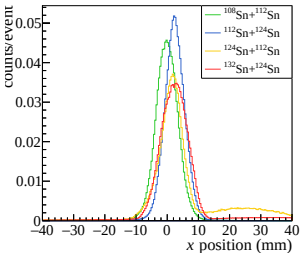

(c) Beam x position.

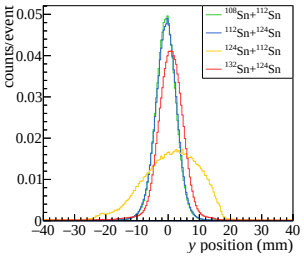

(d) Beam y position.

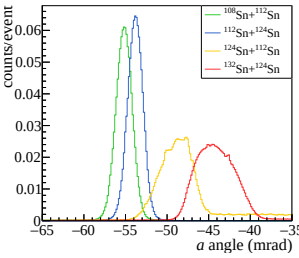

(e) Beam a angle.

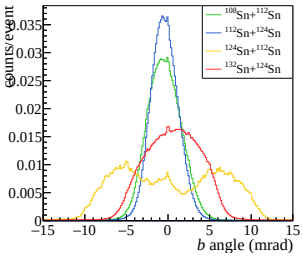

(f) Beam b angle.

Figure 4.15: Phase space of incident Sn beams projected onto the plane of Sn targets. In the top panels, the beam profile of x vs. y positions for ^{132}Sn beams (a) and that for ^{108}Sn beams (b) are shown. In the bottom panels, distributions of positions and angles of incident Sn beams on target are presented (c–f).

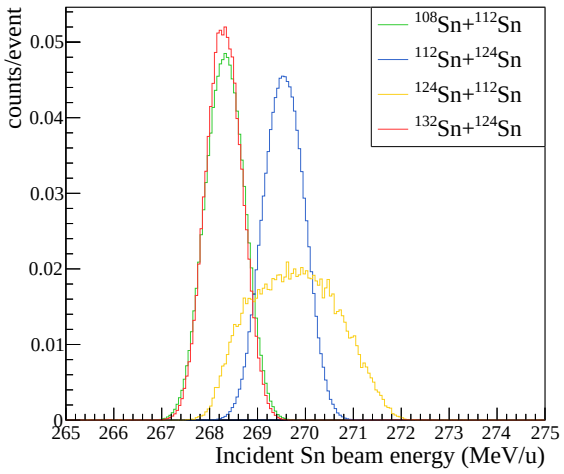

Figure 4.16: Sn beam energy per nucleon at the midpoint of the target.

Table 4.10: Mean ($\langle E_{\mathrm{beam}} \rangle$) and root-mean-square (rms) values of the per-nucleon kinetic-energy distributions of incident Sn beams projected on the midpoint of the target.

System	$\langle E_{\mathrm{beam}} \rangle$	$\mathrm{rms}_{E_{\mathrm{beam}}}$
^{108}Sn+^{112}Sn	268.32	0.40
^{112}Sn+^{124}Sn	269.55	0.42
^{124}Sn+^{112}Sn	269.78	0.87
^{132}Sn+^{124}Sn	268.30	0.38

4.3 Event Reconstruction by the SπRIT TPC

To decode a vast amount of data of the SπRIT TPC and to reconstruct charged-particle tracks emitted from a reaction vertex in an event-by-event basis, a task-based analysis framework, called as SπRITROOT, has been developed [203–207]. It is based on the C++ analysis framework ROOT [208] which is commonly used in particle physics, nuclear physics, and astrophysics communities. The GEANT4 environment is also implemented for a simulation. In this section, the procedure for reconstructing collision events is briefly described.

Overview of the SπRITROOT

GETDecoder As described in Sect. 3.2.2, the GET system stores the digitized waveforms of the 12,096 pads into twelve independent files. The GETDecoder [204, 205] has been developed as an unpacker of the raw data from the GET system. The decoder reads files in parallel to extract the data of a single event, assigns the channel-to-pad mapping, subtracts pedestals and the fixed pattern noise, calibrates the gain of each channel based on the pulser data, and then produces arrays of waveforms in a ROOT-friendly format to facilitate the later processes.

Pulse shape analysis Charged-particle-induced pulses in the waveform were analyzed based on a template fit method. The pulse-shape template was constructed as an average of normalized good pulses in the collision data. Here good pulses were extracted from pads containing a single pulse with an amplitude of 1000–3000 in the ADC unit. Figure 4.17 presents an example of the template fit on multiple pulses in one pad, with fit parameters of their amplitudes and edges of starting time. A successfully fitted pulse is treated as a "hit", which will be used in the following stages. The single hit finding efficiency was deduced as 95 ± 1%, and the two-hit separation efficiency in one pad was found to be saturated at 98% for a two-hit distance of $d_{\mathrm{sep}} > 20$ mm [203].

Track finding The track finding process consists of a cycle of the association of hits with a helical track based on the Riemann fit [209], see Ref. [203] for a detail. This process begins with grouping

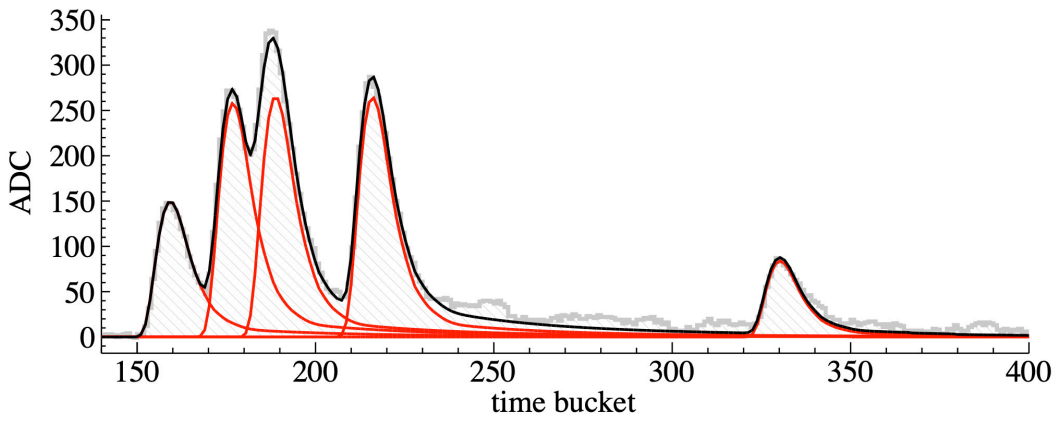

Figure 4.17: Example of the template fit on multiple pulses in a signle pad. Adapted from Ref. [205].

hits in the region far from the target, where tracks are well separated from each other and it is easy to connect hits into a particular track. Hits in the neighboring pads are connected with the initial hit, and a fragment of a track (called as tracklet) is built in a few times connections. By fitting a linear track to a tracklet, it is diagnosed whether this tracklet is reasonable as a seed of a helical track. If the block is too wide, not like a single trajectory, the process stops and goes to a next cycle. After building the tracklet as a good seed, the hit associations are based on the following cycle: (1) the grouped hits are fitted by a helical track using the Riemann fit, (2) the fitted helical track is shortly extrapolated toward the target side, (3) hits in the proximity of the extrapolated track are connected, and (4) a cycle of (1)–(3) is repeated until a new candidate of hits cannot be found in the neighboring pads. Finally, both ends of the track are extrapolated toward walls of the field cage to associate isolated hits with the track so that broken tracks can be also reconstructed. The hits belonging to the fitted helical track are removed from the array of available hits, and then, a new cycle begins with finding a starting point from the array of the remaining hits.

Hit clusterization To obtain a precise position where charged particles traverse, hits aligned perpendicular to the track were clusterized, as presented in Fig. 4.18. The position of clusters is deduced as a charge-weighted position, $x_c = \sum_i q_i x_i / \sum_i q_i$, with q_i and x_i being charge (amplitude) and position of the i-th hit, respectively. As charged particles are bent in the TPC, the direction of the clusterization was determined depending on the crossing angle θ of tracks to the x-axis. The clusterization was applied in the x (wire) direction for $45° < |\theta| < 135°$, and in the z (beam) direction for another region of θ, as shown in Fig. 4.18.

***E* × *B* correction** It was necessary to correct positions of hits and clusters with taking the $\boldsymbol{E} \times \boldsymbol{B}$ effect into account [207]. Two sources induce the $\boldsymbol{E} \times \boldsymbol{B}$ force to drifting electrons: (1) the nonuniformity of E field in the field cage and that of B field in the SAMURAI magnet, and (2) the space charge made of slow-moving positive ions due to the passages of heavy beams through the TPC. The effect from the source (1) was deduced by Garfield simulations where the SAMURAI magnetic field map is implemented. As for (2), a sheet of positive charge below the beam trajectory was assumed to calculate the E field. The charge density was optimized run by run depending on the average beam intensity. Then, the force acting on the drift electrons was calculated with these effects.

De-saturation correction When the electronics were saturated due to a huge signal induced by passages of heavy or low-momentum particles, the deduction of charge and position of hits would fail. Since we optimized the TPC gain high enough for detecting charged pions, there were many saturated pads. The real charge information in such saturated hits was compensated by presuming that the charge induced on the pad plane follows a certain well-defined distribution, the so-called pad response function (PRF). The PRF along the clusterization direction was deduced from the unsaturated hits, depending on each crossing angle of tracks, as shown in Fig. 4.18. Then, the charge of the saturated signal was deduced from the PRF together with the unsaturated hits around the saturated one. This de-saturation method extended the dynamic range by a factor of five [206].

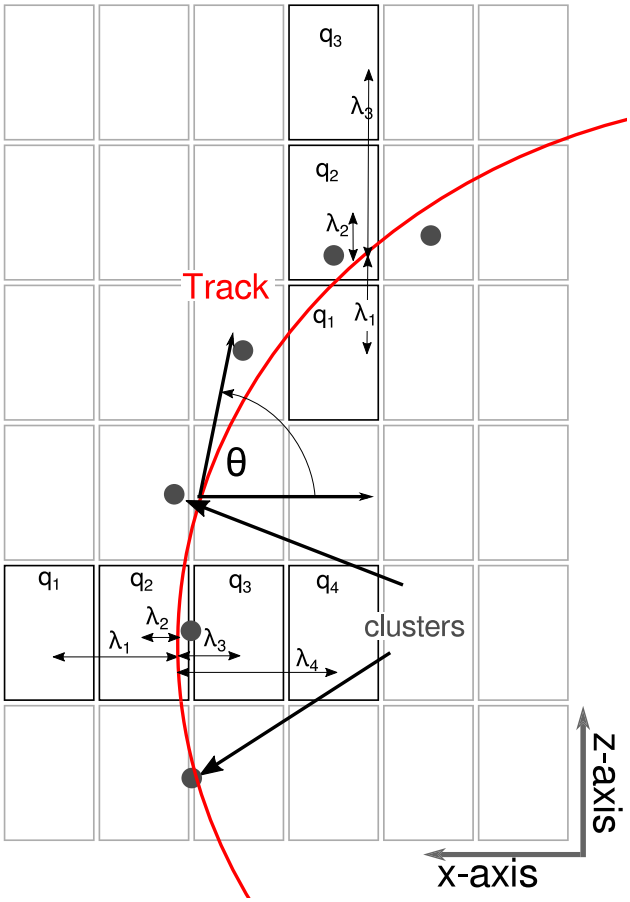

Figure 4.18: Top view of a track reconstruction from hit clusters made in x and z directions. The bold pads aligned in x or z directions indicate clusterization in x and z directions from hits with charges q_i, respectively. The de-saturation process of clusters are considered by the pad response function – the charge distribution as a function of distance between the track and the center of pads, denoted by λ_i. Adapted from Ref. [206].

Fiducial volume Clusters reconstructed in edges of the active volume were excluded because they were expected to be formed from hits less than what those should be and to lose the information. The fiducial volume was defined as $|x| \leq 420\,\text{mm}$ and $-522\,\text{mm} \leq y \leq -64\,\text{mm}$, where origins of $x = 0$ and $y = 0$ are identical with the center of and the height of the pad plane. In Addition, we excluded clusters close to the target within a semiellipsoidal boundary centered at the target with radii of $r_x = 120\,\text{mm}$, $r_y = 100\,\text{mm}$, and $r_z = 220\,\text{mm}$, to avoid using ones heavily contaminated by multiple tracks. Only clusters inside the fiducial volume will be used for a precise determination of curvature radii of respective tracks in the next step.

GENFIT package for magnetic rigidity reconstruction Magnetic rigidity (p/Z) of respective tracks were reconstructed based on the Kalman filtering algorithm implemented in the GENFIT toolkit [210]. The Kalman filter is a method to infer a time evolution of a certain object from a time-dependent observable with an error. Charged particles travel in the P10 gas with ionizing atoms along their paths, i.e., clusters along tracks represent a result of the time evolution of charged particles. The Kalman filter makes extrapolations from each cluster toward its anteroposterior ones

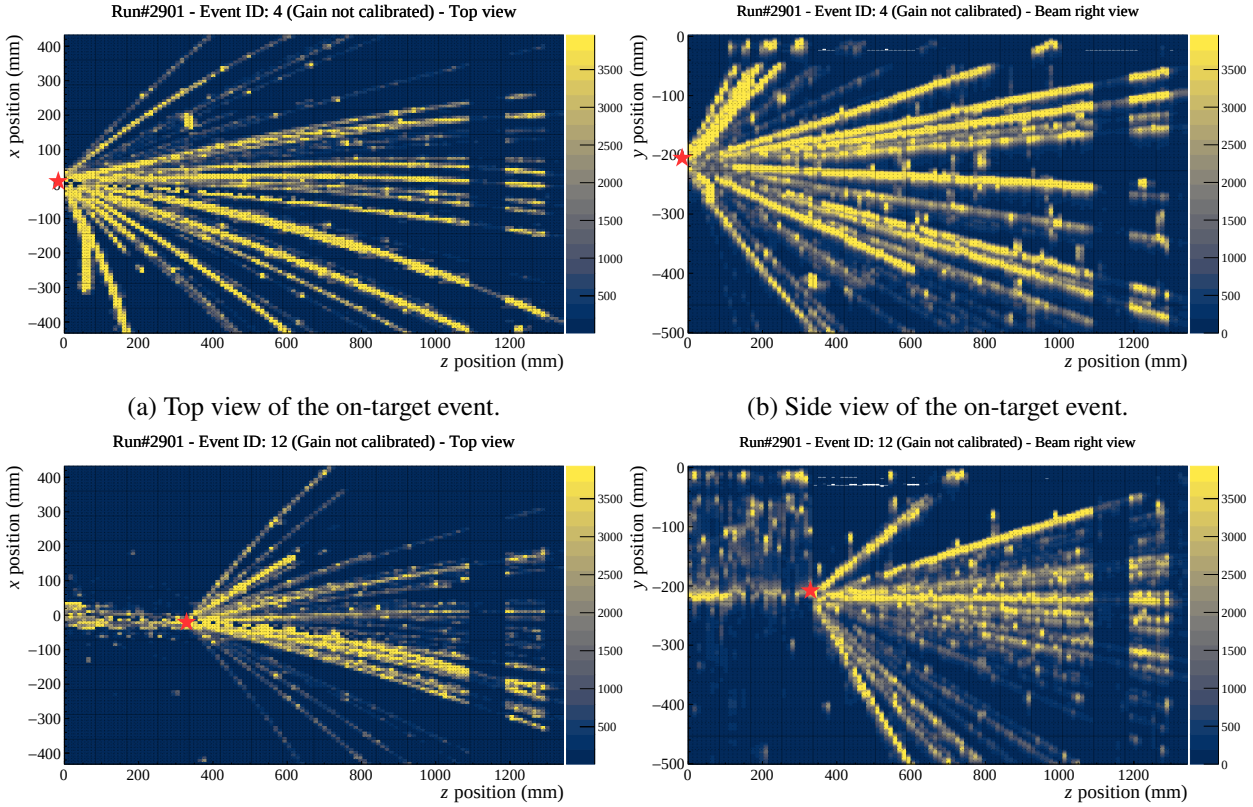

(a) Top view of the on-target event.

(b) Side view of the on-target event.

(c) Top view of the active-target event.

(d) Side view of the active-target event.

Figure 4.19: Event viewers from top and side of the TPC, representing the highest ADC values in each pixel. The on-target and active-target events in the ^{132}Sn + ^{124}Sn data are shown in the top and bottom panels, respectively. The red star shown in each panel indicate the position of the reconstructed vertex for each event. The pixel size in the top viewers indicate the area of the pad, while that in the side viewers indicate the area of the pad-z × drift length in 10 Tbs = 400 ns of time, respectively. For the dim regions at around 1092 mm $< z <$ 1188 mm and $z >$ 1296 mm, the voltage of anode wires was lowered to 1240 V, which corresponds to reducing the gas gain by a factor of 10, to deal with a leak-in of electrons.

along the track. The motion of charged particles traversing the P10 gas under a magnetic field is taken into account for the representation of the extrapolation. The position deviations between each extrapolation and the actual cluster were minimized so that smooth curve trajectories of charged particles having a time-evolving feature are reconstructed. The initial magnetic rigidity vector at the moment of the emission is obtained by extrapolating tracks to the vertex position. From calibration runs using $Z = 1$–3 beams at a momentum of about 1700 MeV/c, the momentum resolutions were deduced as approximately 1.5% for deuterons and 2% for tritons [203].

RAVE package for vertex reconstruction The reaction vertex was reconstructed by the Adaptive Vertex Fitter (AVF) [211] implemented in the RAVE toolkit [212]. The AVF method is an iterative re-weighted Kalman filter that assigns weights to each track so that the primary vertex can be found with less influenced by mis-associated and/or mis-reconstructed tracks. The track parameters obtained from the GENFIT were used as inputs of the AVF. As shown in Fig. 4.19, the AVF successfully reconstructs the vertex for both on-target and active-target reaction events. Figure 4.20 presents the z-position distribution of the reconstructed vertex with the z-origin ($z = 0$) taken as

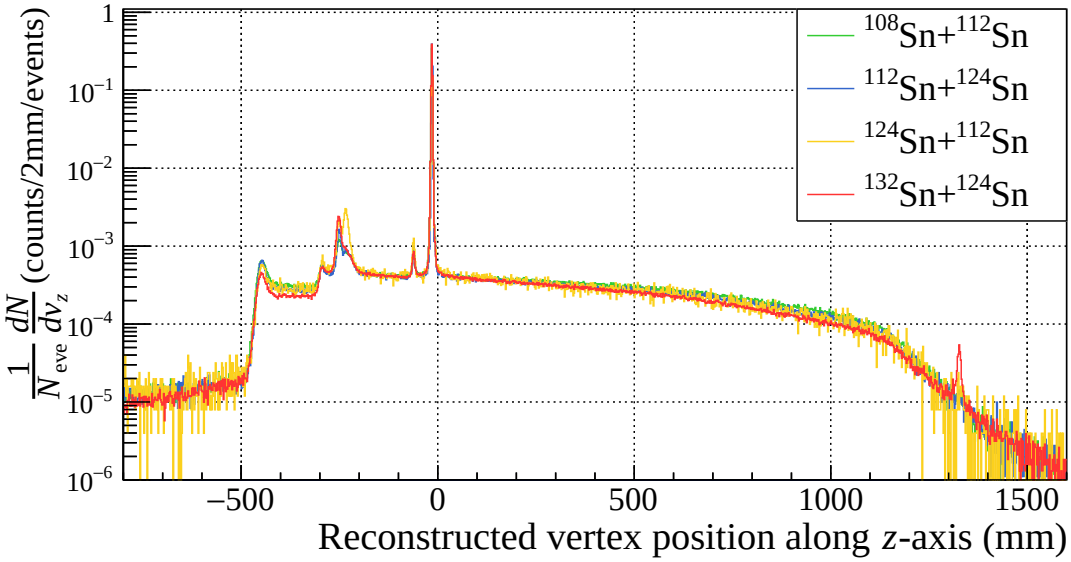

Figure 4.20: Vertex position distribution along the beam axis. The peaks indicating the on-target event ($z \sim -15$ mm), the vacuum pipe with the exit window ($z < -450$ mm), the entrance window of the TPC ($z \sim -300$ mm), the active veto array ($z \sim -250$ mm), and the target ladder ($z \sim -60$ mm) are evident. Events of active-target reactions ($z > 0$ mm) have a decreasing trend due to the requirement of the MTD multiplicity.

the upstream edge of the pad plane. The highest peak at around $z = -15$ mm corresponds to the on-target Sn + Sn reaction, which will be selected in the later analysis. And besides, x–y positions of vertices reconstructed at around the on-target peak were found to be well correlated with the incident beam positions, as shown in Fig. 4.21.

Re-fit of tracks with the beam-projected cluster After the vertex reconstruction, tracks were refitted with including a reaction point as an additional cluster to improve the momentum resolution. Such the additional cluster was introduced by the projection of incident beams onto the z position of the reconstructed vertex. With this refit, the particle identification capability was improved so that $Z = 1$–3 isotopes can be separated in the TPC. Since a mis-projection of incident beams, due to misreconstruction of the trajectory by BDCs, can cause a strong bias in determining the magnetic rigidity of tracks, only events observing a good vertex–beam correlation (such as Fig. 4.21) were selected, which will be described in the following section.

Truncated mean energy loss: $\langle dE/dx \rangle$ The mean energy loss per unit length of the track – $\langle dE/dx \rangle$ – was calculated from the charge of clusters. When charged particles traverse material with a moderate thickness, *e.g.*, gas or a thin silicon detector, it is known that the energy loss follows the Landau probability distribution with a high-energy tail component, see Sect. 34.2.9 of Ref. [213]. In the GENFIT track representation, dE/dx samples of each cluster can be calculated as its charge over length, which approximately follows the Landau distribution as well. To eliminate the effect of the high-dE/dx tail component, the $\langle dE/dx \rangle$ of each track was calculated with truncating the 30% of the samples with the highest dE/dx values as the estimator, which is a conventional procedure also for other TPC analysis, see Sect. 35.6.5 of Ref. [213]. The truncated energy loss $\langle dE/dx \rangle$ vs. magnetic rigidity provides the particle identification, as described in the following section.

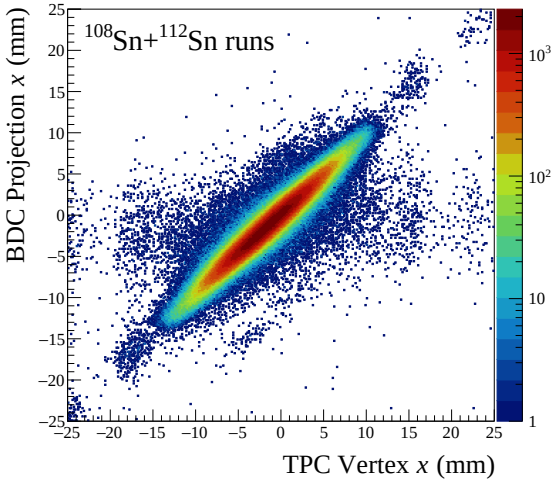

(a) x-position correlation for ^{108}Sn + ^{112}Sn reactions.

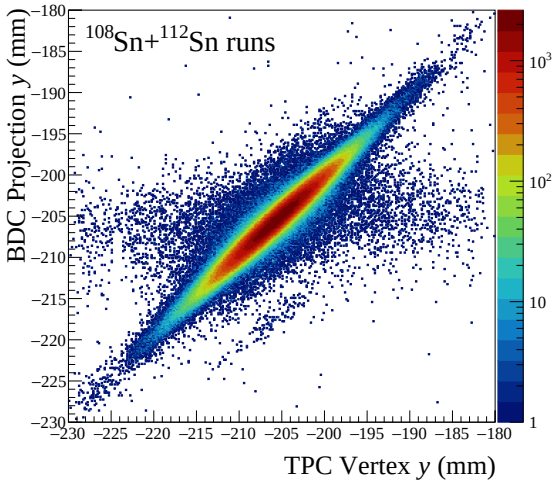

(b) y-position correlation for ^{108}Sn + ^{112}Sn reactions.

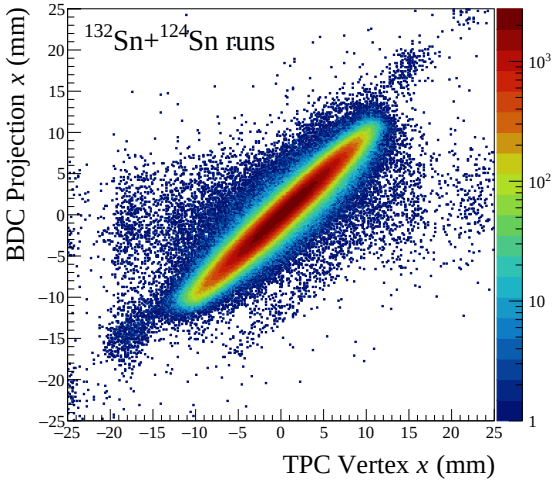

(c) x-position correlation for ^{132}Sn + ^{124}Sn reactions.

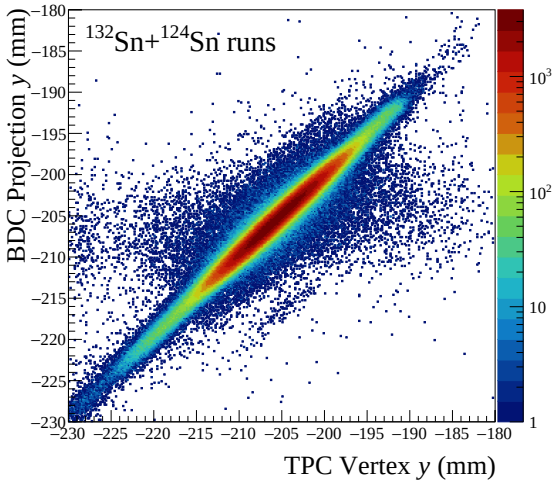

(d) y-position correlation for ^{132}Sn + ^{124}Sn reactions.

Figure 4.21: Position correlations between reconstructed vertices vs. incident beams at the vertex-z plane. On-target reactions were selected based on the Gaussian fit to the on-target peak in the vertex z position distribution, i.e., events within three standard deviations from the mean value of the fitted Gaussian were used. The beam was propagated toward the z position of the reconstructed vertex, using method described in Sect. 4.2.2.

Gating grid fast closed event

As described in Sect. 3.3.2, the fast clear signal closes the gating grid forcibly in the halfway of the digitization of signals in the GET system to protect the electronics from being fed into huge charge. The fast clear is mainly activated by the pileup of beam particles. When the system is fast-cleared, a large part of the TPC becomes insensitive, and thus such events should be excluded. The fast cleared events can be identified by an existence of a particular spike noise on the pads due to the abrupt voltage change of wires of the closing gating grid. Although the rate of the fast cleared events was about 7–8% out of the total accumulated events, the number is reduced to less than 0.2% under the Sn beam gate defined in Sect. 4.1.5. This is because the energy deposit in the MUSIC becomes much higher in the beam-pileup events, and consequently the reconstructed atomic number Z becomes too high to be accepted by the Sn isotope gate.

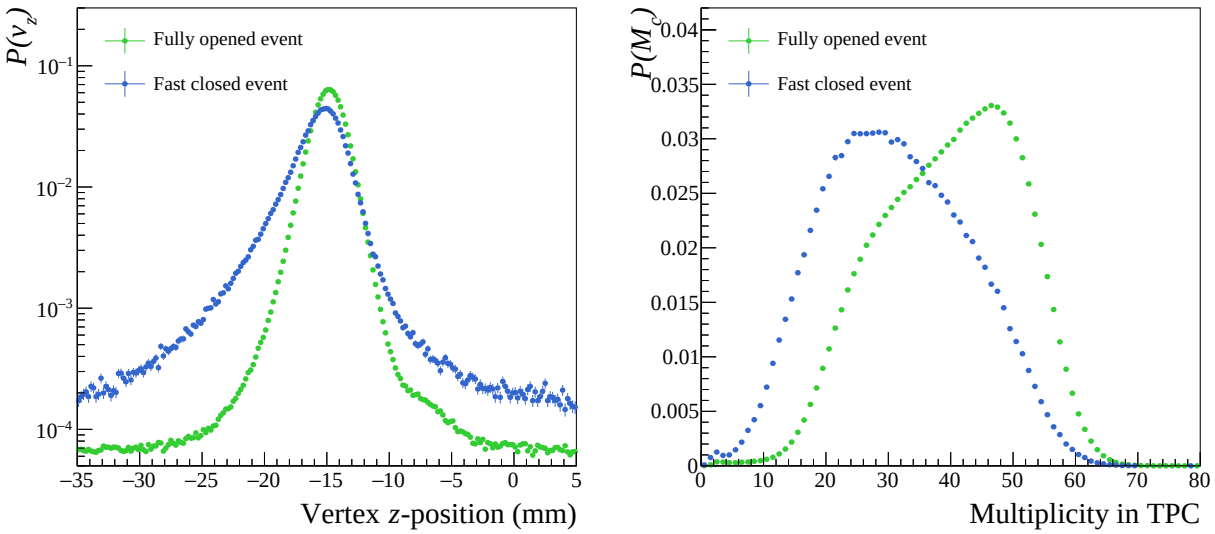

(a) Vertex position distribution along z-axis.

(b) Track multiplicity distribution.

Figure 4.22: Probability distributions for the gating grid fully-opened events and for the fast-closed events in the ^{132}Sn + ^{124}Sn runs. Left: vertex position distribution along z-axis. Right: track multiplicity distribution with loosely selecting the on-target events as $-25\,\text{mm} \leq v_z \leq -5\,\text{mm}$.

Figure 4.22 presents the vertex z-position distributions and the track multiplicity distributions for two cases of event samples: an existence or an absence of the fast clear. In the fast-cleared events, the on-target peak width is widened and the mean multiplicity is lowered as simply expected. Here, the track multiplicity is obtained as the number of vertex-associated tracks which satisfy $d_{\text{POCA}} \leq 20\,\text{mm}$. The d_{POCA} represents the minimum distance of respective tracks from the vertex position, which can be obtained by the point of closest approach (POCA) in the GENFIT tool. Note that the d_{POCA} was calculated for the tracks before refits with including the additional cluster given by the beam projection. This is because the refitting with the additional cluster forces all of the tracks to be strongly associated with the vertex even if some of the tracks don't originate from the vertex, *e.g.*, a ghost track or a scattered track.

Quality assurance of reconstructd tracks

Several requirements of the track quality were defined in the later analysis as follows.

- The $d_{\text{POCA}} \leq 20\,\text{mm}$ was required for calculating the TPC multiplicity. The multiplicity will be used to select central collision events, described in Sect. 4.6.
- The $(d_{\text{POCA}} \leq 20\,\text{mm}) \cap (n_{\text{Cluster}} \geq 15)$, with n_{Cluster} denoting the number of clusters belonging to the track, was required in the PID analysis in Sect. 4.7.
- The $(d_{\text{POCA}} \leq 20\,\text{mm}) \cap (n_{\text{Cluster}} \geq 15) \cap (\boldsymbol{R}_{\text{H}}) \cap \left(-30^\circ \leq \phi \leq 20^\circ\right)$ was additionally required in the last part of the analysis on the transverse momentum vs. rapidity phase-space distribution, where $\boldsymbol{R}_{\text{H}}$ denotes the gate on the charged-particle PID spectrum of dE/dx vs. p/Z for identifying hydrogen isotopes and ϕ denotes the azimuthal angle of tracks.

4.4 Selection of the On-target Events

4.4.1 Selection of vertices reconstructed on target

Figure 4.23 presents the vertex z-position distributions around $z = -15$ mm of the on-target peak as a function of run number for the ^{108}Sn + ^{112}Sn and ^{132}Sn + ^{124}Sn systems, along with those using overall runs of each system in the right panels. The z position of vertices is fairly stable throughout each measurement. The on-target events were selected by the condition: $|v_z - \mu_z| \leq 3\sigma_z$, with v_z, μ_z and σ_z being the z-position of vertices, mean and standard deviation obtained by the Gaussian + constant fit to the overall vertex z position distribution in the right panel of Fig. 4.23, respectively. The fit results are listed in Table 4.11.

The vertex x- and y-positions (v_x and v_y) were also gated to select vertices reconstructed inside the target frame of 30 mm (x) × 40 mm (y) centered at approximately $x = 0$ mm and $y = -205$ mm. Namely, the condition $|v_x| \leq 15\,\text{mm} \cap \left|v_y + 205\,\text{mm}\right| \leq 20\,\text{mm}$ was further imposed to select the on-target events. It was validated by the comparison of the geometrical position of the target frame with the v_x vs. v_y distribution for the on-target Sn + Sn events selected by a high track multiplicity requirement. Figure 4.24 presents the track multiplicity (M_c) distribution as a function

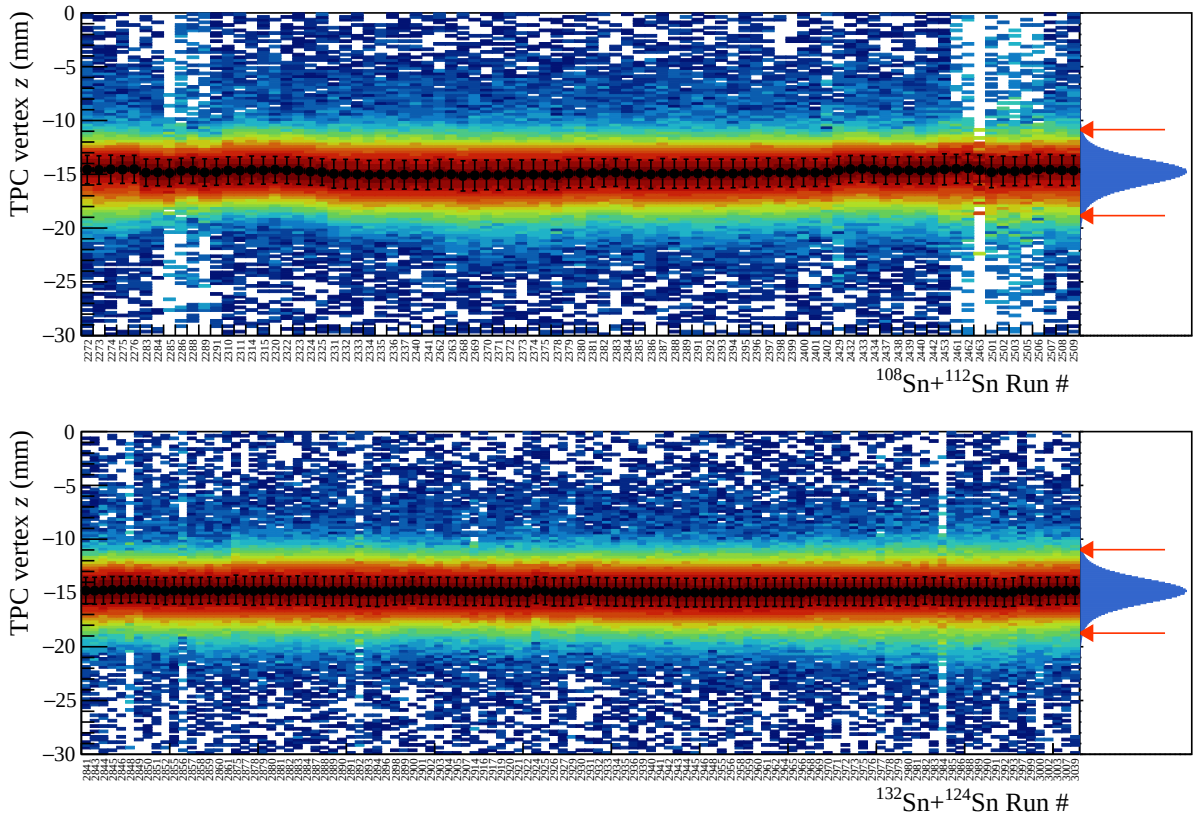

Figure 4.23: Vertex z-position distribution as a function of run number for the ^{108}Sn + ^{112}Sn system (top) and that for the ^{132}Sn + ^{124}Sn system (bottom). The black markers and error bars indicate means and standard deviations obtained by Gaussian + constant fits to the on-target peaks for each run, respectively. In the right panels, the accumulated vertex z-position distributions are presented, where the two red arrows indicate the gate defined as $\pm 3\sigma_z$ from the mean of the on-target peak.

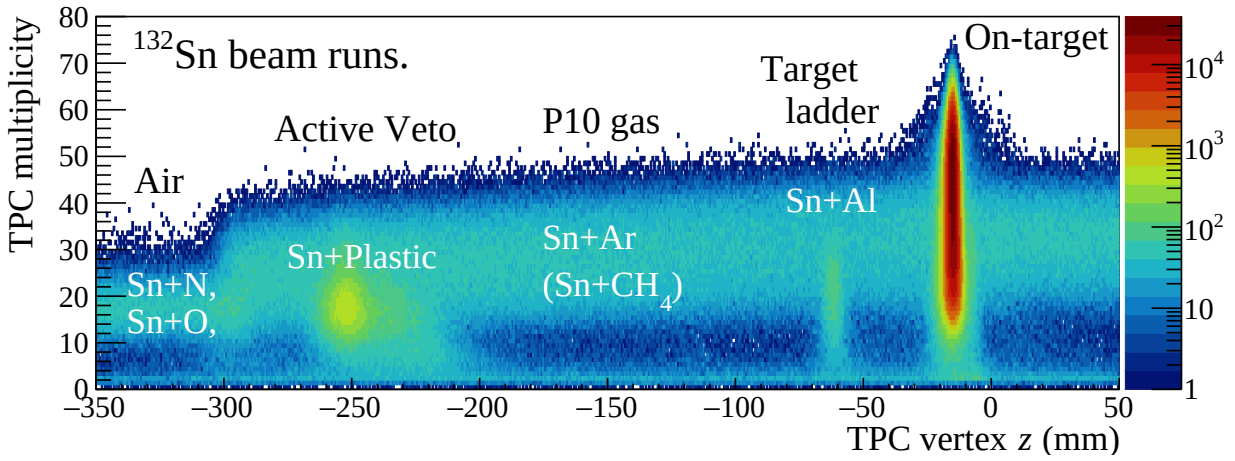

Figure 4.24: Track multiplicity distribution as a function of vertex z position in the ^{132}Sn beam runs. From downstream vertices, the reactions would be induced by the air, the P10 gas, the plastic of the active veto, the aluminum of the target ladder, and the Sn target. Only on-target Sn+Sn ($Z_{sys} = 50 + 50$) reactions can reach the high charged-particle multiplicity of $M_c \geq 50$ since the maximum M_c in a certain reaction is limited by the number of protons in the reaction system.

Table 4.11: Gaussian fit results on the on-target peak in the vertex z-position distribution and the number of events selected as on-target Sn+Sn reactions (N_{ontarget}). The on-target events were selected by: $|v_z - \mu_z| \leq 3\sigma_z \cap |v_x| \leq 15\,\text{mm} \cap \left|v_y + 205\,\text{mm}\right| \leq 20\,\text{mm}$, see text.

System	mean μ_z (mm)	stdev. σ_z (mm)	N_{ontarget}
^{108}Sn + ^{112}Sn	-14.85	1.33	1535037
^{112}Sn + ^{124}Sn	-14.42	0.98	1141396
^{124}Sn + ^{112}Sn	-14.76	1.20	151342
^{132}Sn + ^{124}Sn	-14.86	1.29	2570904

of z position of vertices in the ^{132}Sn beam runs. As is simply expected, the charged particle multiplicity detected in the SπRIT TPC strongly depends on the target material, *i.e.*, the number of protons in the reaction system. Therefore, as seen in the figure, the higher multiplicity events of $M_c \geq 50$ stem from only on-target Sn + Sn reactions. Figure 4.25 compares the v_x vs. v_y profiles with and without the high multiplicity requirement of $M_c \geq 50$. The vertex profile with $M_c \geq 50$, for selecting on-target events, is consistent with the geometrical target size.

The number of selected on-target reaction events is listed in Table 4.11.

4.4.2 Correlation requirement between TPC and BDC

As explained in Sect. 4.3, the momenta of the charged particles resulting from nuclear collisions are reconstructed based on the clusters found in the TPC and the additional cluster provided by the beam-trajectory extrapolation by the BDC. Therefore the position correlation between the reaction vertex reconstructed by the SπRIT TPC and the projected beam by the BDCs was required in the analysis. Figure 4.26 presents the x- and y-position residual distributions between vertices and

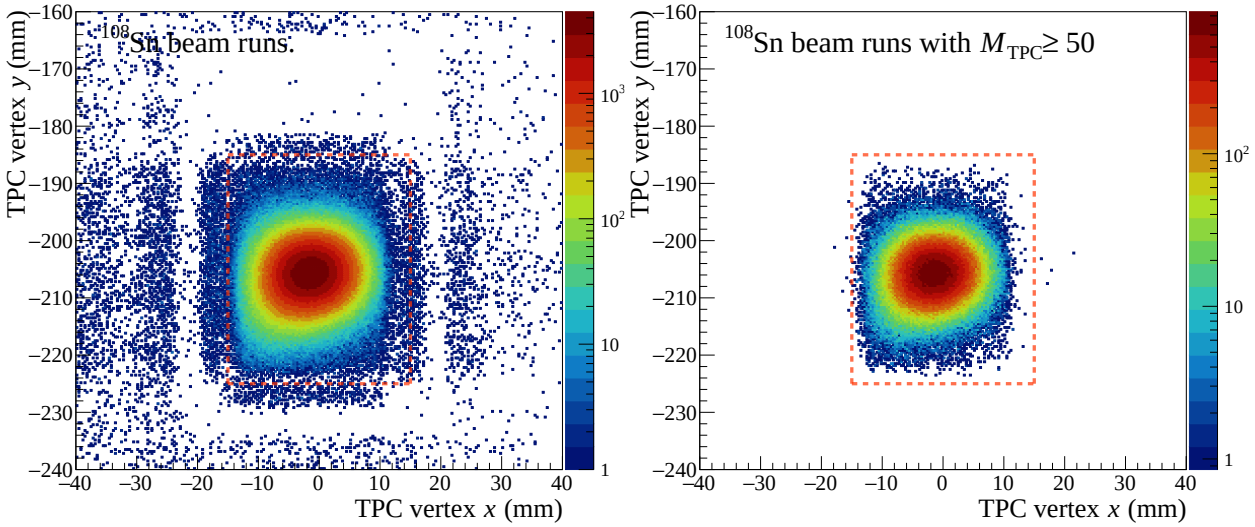

(a) Profile in xy of the vertices in ^{108}Sn beam runs.

(b) Same as the left with a higher M_c selection.

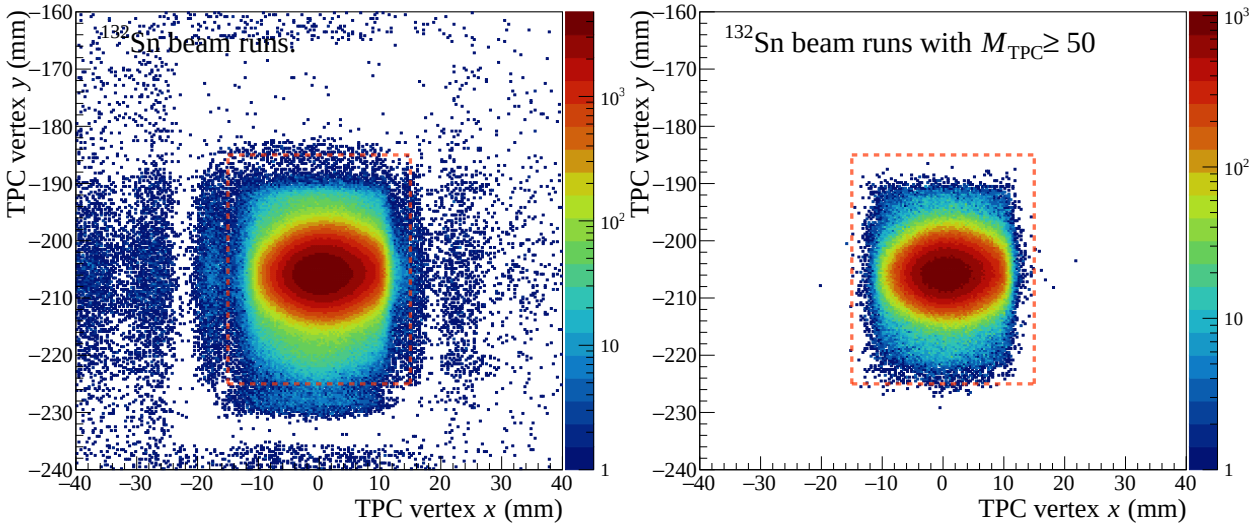

(c) Profile in xy of the vertices in ^{132}Sn beam runs.

(d) Same as the left with a higher M_c selection.

Figure 4.25: The xy profiles of the vertices at the z-position peak at the target with and without higher multiplicity requirement of $M_c \geq 50$, with top and bottom rows for the ^{108}Sn and the ^{132}Sn beam runs, respectively. The orange dotted lines ($x = \pm 15$ mm and $y = -185$ mm, -225 mm) indicate the geometical target size, which is consistent with the image from vertices in the higher multiplicity events as shown in the right column.

incident beams, fitted by Gaussian functions for defining gate conditions, where the fit results are listed in Table 4.12. The gate conditions were placed on the residuals as $\pm 3\sigma$ from the mean values. Because this correlation requirement is only relevant to the analysis using momenta of reconstructed tracks, which starts at Sect. 4.7, the condition on the vertex–beam position residual will not be imposed in the following data reduction stage.

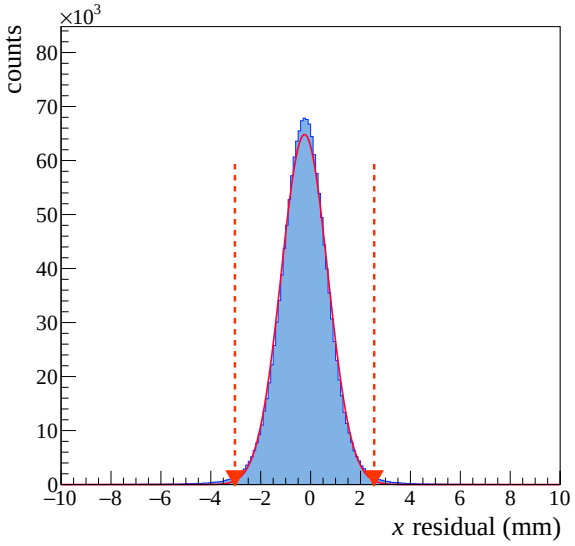

(a) x-position residual in the ^{108}Sn + ^{112}Sn system.

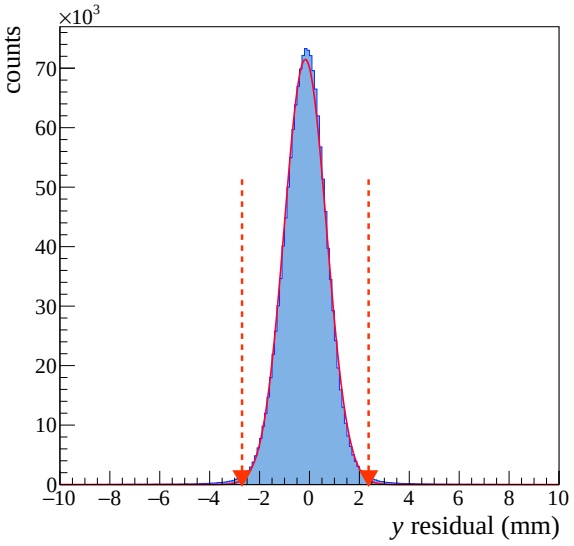

(b) y-position residual in the ^{108}Sn + ^{112}Sn system.

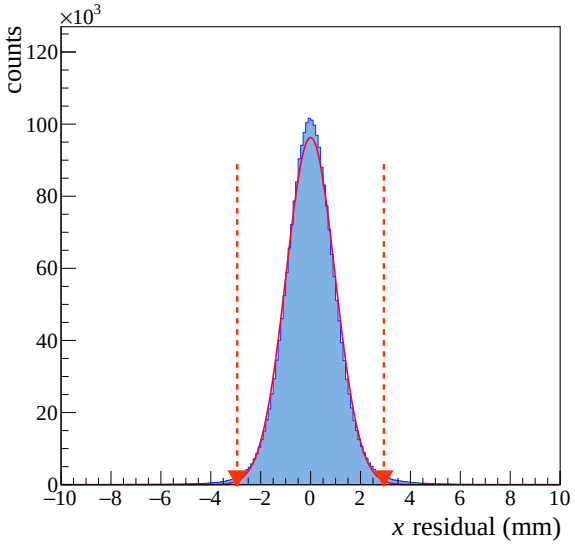

(c) x-position residual in the ^{132}Sn + ^{124}Sn system.

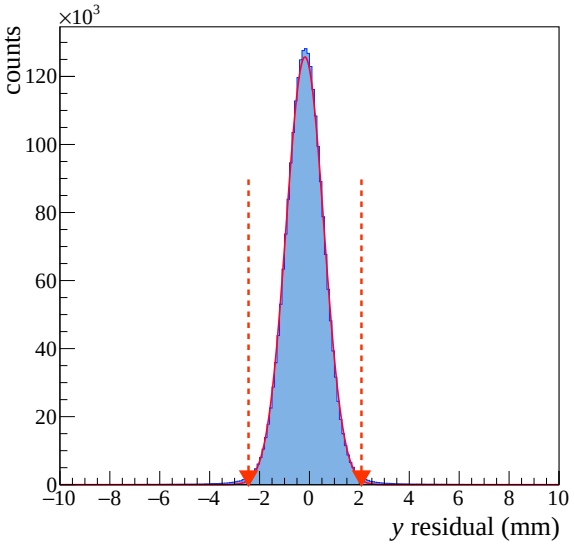

(d) y-position residual in the ^{132}Sn + ^{124}Sn system.

Figure 4.26: Residual distributions between the vertex reconstructed by the TPC and the beam position extrapolated by the BDC for on-target events in the ^{108}Sn + ^{112}Sn system (top) and those in the ^{132}Sn + ^{124}Sn system (bottom). The red arrows indicate the upper and lower limit of the gate condition defined as $\pm 3\sigma$ from the mean values.

Table 4.12: Gaussian fit results on the vertex–beam position residuals.

System	mean$_x$ (mm)	σ_x (mm)	mean$_y$ (mm)	σ_y (mm)
^{108}Sn+^{112}Sn	-0.243	0.930	-0.166	0.845
^{112}Sn+^{124}Sn	-0.367	0.868	-0.160	0.977
^{124}Sn+^{112}Sn	-0.458	0.931	-0.274	0.865
^{132}Sn+^{124}Sn	-0.003	0.980	-0.180	0.754

4.5 Measurement of Reaction Cross Section

Since we optimized the hardware trigger so that central collision events with small impact parameters were effectively accumulated, as described in Table 3.8 (Sect. 3.4), it is important to determine the cross section of reactions that activated the trigger, for normalizing the centrality of each system. In this section, we describe the cross section of the triggered Sn + Sn reactions.

Definition of the cross section

The cross section of the reactions acceptable by the experimental trigger condition can be calculated from the triggerable on-target event rate $\dot{N}_{\text{Triggerable}}$ and the incident beam rate $\dot{N}_{\text{Incident}}$, and the area density of the target n_{area} as:

$$\sigma_{\text{Triggerable}} = \frac{\dot{N}_{\text{Triggerable}}}{\dot{N}_{\text{Incident}} \cdot n_{\text{area}}} \simeq \frac{N_{\text{Triggerable}}}{N_{\text{Incident}} \cdot n_{\text{area}}}, \tag{4.13}$$

$$n_{\text{area}} = \frac{\rho d}{M} N_A. \tag{4.14}$$

Here, the beam intensity and the trigger efficiency are assumed to be stable enough so that the ratio $\dot{N}_{\text{Triggerable}}/\dot{N}_{\text{Incident}}$ is equivalent to the ratio of their integration $N_{\text{Triggerable}}/N_{\text{Incident}}$, which can be calculated from the scaler counts for each run. The ρ, d, and M represent the thickness (cm), the density (g/cm^3), and the molar mass of the target nucleus (g/mol), respectively. The $N_A \simeq 6.02 \times 10^{23}$ mol^{-1} is the Avogadro constant.

The mass thickness (ρd) of Sn targets employed in the present experiment were 561(2) mg/cm^2 for the ^{112}Sn target and 608(3) mg/cm^2 for the ^{124}Sn target. The $N_{\text{Triggerable}}$ and the N_{Incident} were deduced as follows.

Number of incident beams The number of incident Sn beams (N_{Incident}) is deduced from the coincidence count of four PMTs of the SBT (N_{SBT}) and the OR count of four MPPCs of the active veto (N_{AV}) with considering the beam loss before reaching the target, which can be described as:

$$N_{\text{Incident}} = \left(N_{\text{SBT}} P_{\text{SBT-to-AV}} - N_{\text{AV}}\right) P_{\text{AV-to-Target}}, \tag{4.15}$$

with the beam survival probability between material X and Y $P_{\text{X-to-Y}}$ as:

$$P_{\text{X-to-Y}} = \prod_j \left(1 - p_j\right), \quad (j \in \text{Materials from X to Y}), \tag{4.16}$$

$$p_j = \sigma_R \times n_{\text{area},j}, \qquad \sigma_R = \pi (R_{\text{Sn}} + R_j)^2. \tag{4.17}$$

Here p_j is the total reaction probability in j-th material, σ_R is the total reaction cross section for the Sn beams interacting with the j-th material. For materials between the SBT and the Sn target, see Fig. 3.22 and Table 4.8. The total reaction cross section was calculated based on the sharp nuclear boundary approximation with the nuclear radius $R_i = 1.15 \times A_i^{1/3}$ for the nucleus i. Typical values of $P_{\text{SBT-to-AV}}$ and $P_{\text{AV-to-Target}}$ were about 98.6% and 99.9%, respectively, as tabulated in Table 4.13. The count rate of N_{AV} to N_{SBT} was approximately 1.8% in each run.

Number of the triggerable on-target reactions The number of the triggerable on-target reaction events was deduced from the count of the triggered event (N_{DAQ}), the live rate of the DAQ system (ϵ_{Live}), and the on-target event rate out of all of the reconstructed vertices ($R_{\text{On-target}}$) as:

$$N_{\mathrm{Triggerable}} = \frac{N_{\mathrm{DAQ}} \cdot R_{\text{On-Target}}}{\epsilon_{\mathrm{Live}}}, \tag{4.18}$$

$$\epsilon_{\mathrm{Live}} = 1 - \epsilon_{\mathrm{Dead}} = 1 - \frac{N_{\mathrm{SBT}\cap\mathrm{Busy}}}{N_{\mathrm{SBT}}}. \tag{4.19}$$

Here a dead time of the DAQ system, denoted by ϵ_{Dead}, was calculated by the ratio of the coincidence count between SBT and busy signals ($N_{\mathrm{SBT}\cap\mathrm{Busy}}$) to the N_{SBT}. The averaged values of the $R_{\mathrm{On-Target}}$ and the ϵ_{Live} are listed in Table 4.13.

Triggerable reaction cross sections

Figure 4.27 presents the triggerable reaction cross sections calculated for the two reactions: the ^{108}Sn + ^{112}Sn system and the ^{132}Sn + ^{124}Sn system. The probability distribution of the $\sigma_{\mathrm{Triggerable}}$ of each run was assumed to form a Gaussian function whose width was given by the statistical uncertainty of $\sigma_{\mathrm{Triggerable}}$. The summation of the $\sigma_{\mathrm{Triggerable}}$ probability distributions weighted by the number of events for each run is shown in the right panels of Fig. 4.27. The mean and root-mean-square values for the weighted $\sigma_{\mathrm{Triggerable}}$ distribution are shown in Table 4.13. The systematic uncertainty in the determination of the mean $\sigma_{\mathrm{Triggerable}}$ was deduced to be less than 1% by (1) widening and loosening the on-target gate condition to calculate the $R_{\text{On-target}}$ in Eq. 4.18 and (2) by changing the live rate calculation based on the SBT scaler counts (N_{SBT} and $N_{\mathrm{SBT}\cap\mathrm{Busy}}$) to that based on the 100 kHz clock ones (N_{Clock} and $N_{\mathrm{Clock}\cap\mathrm{Busy}}$) in Eq. 4.19.

Table 4.13: Triggerable reaction cross section $\sigma_{\mathrm{Triggerable}}$ for four systems with several factors used for the calculations. The $\langle\sigma_{\mathrm{Triggerable}}\rangle$ is calculated from the Gaussian-weighted $\sigma_{\mathrm{Triggerable}}$ distribution, see Fig. 4.27 and text in detail. The RMS values of $\sigma_{\mathrm{Triggerable}}$ distributions are given as errors in the rightest column. The survival probabilities $P_{\text{SBT-to-AV}}$ and $P_{\text{AV-to-Tgt}}$ are fixed values while the $R_{\text{On-Target}}$ and the ϵ_{Live} are given as averaged values of overall runs for each system.

System	$P_{\text{SBT-to-AV}}$ (%)	$P_{\text{AV-to-Tgt}}$ (%)	$R_{\text{On-Target}}$ (%)	ϵ_{Live} (%)	$\langle\sigma_{\mathrm{Triggerable}}\rangle$ (barn)
^{108}Sn + ^{112}Sn	98.63	99.87	61.3	83.73	1.42 ± 0.018
^{112}Sn + ^{124}Sn	98.61	99.87	63.11	85.49	1.52 ± 0.017
^{124}Sn + ^{112}Sn	98.54	99.87	60.05	79.88	1.38 ± 0.042
^{132}Sn + ^{124}Sn	98.5	99.86	67.18	78.59	1.53 ± 0.025

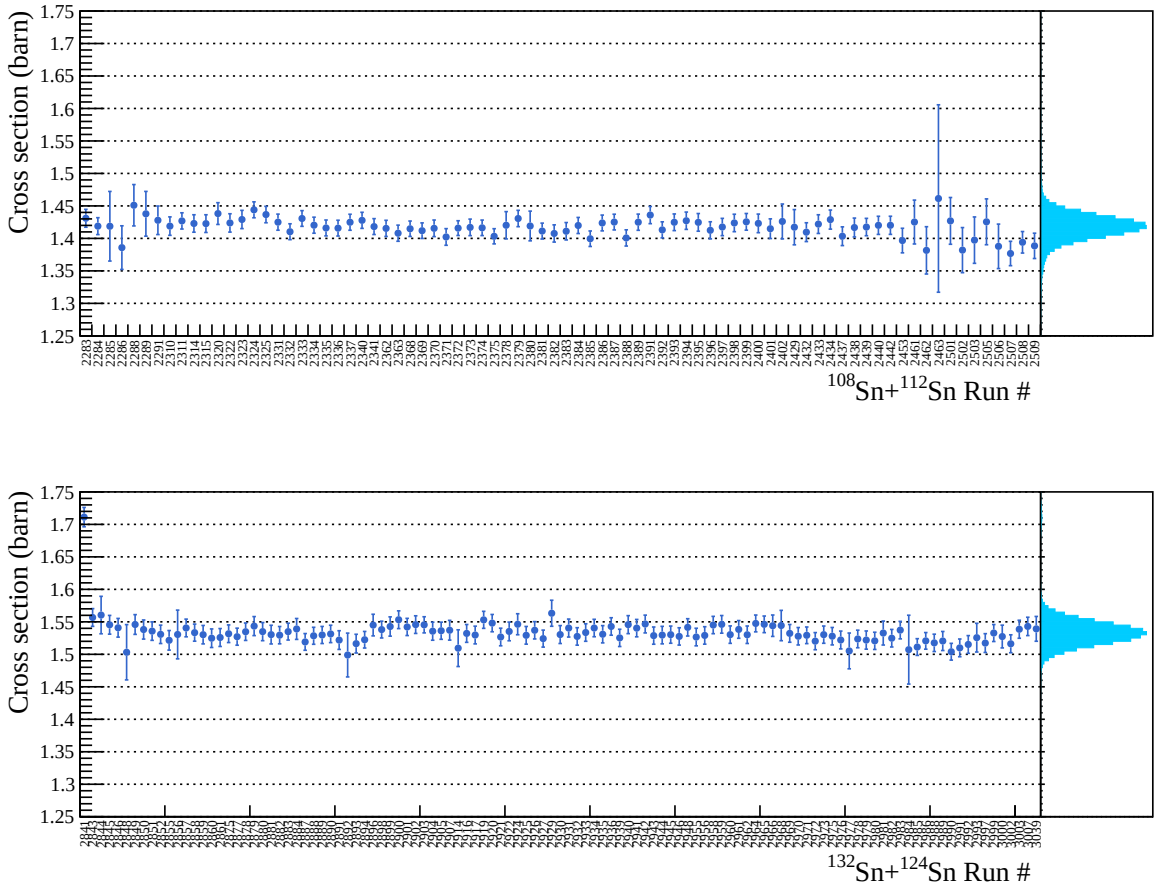

Figure 4.27: The triggerable reaction cross section ($\sigma_{\text{Triggerable}}$) as a function of run number for the $^{108}\text{Sn} + ^{112}\text{Sn}$ system (top) and that for the $^{132}\text{Sn} + ^{124}\text{Sn}$ system (bottom). Given errors are statistical errors. In the right panels, the sum of $\sigma_{\text{Triggerable}}$ probability distributions are presented, see text.

4.6 Selection of Central Collisions

In heavy-ion collisions, the impact parameter b is not a direct observable but has to be deduced from observables characterizing the global collision geometry. If we postulate that a global observable g or g' has a monotonic correlation or anti-correlation with the impact parameter, respectively, the differential cross section $\mathrm{d}\sigma(g)/\mathrm{d}g$ or $\mathrm{d}\sigma(g')/\mathrm{d}g'$ follows [214]:

$$\int_0^g \frac{\mathrm{d}\sigma(\bar{g})}{\mathrm{d}\bar{g}}\,\mathrm{d}\bar{g} = \pi b^2(g) \quad \text{or} \quad \int_{g'}^{\infty} \frac{\mathrm{d}\sigma(\bar{g}')}{\mathrm{d}\bar{g}'}\,\mathrm{d}\bar{g}' = \pi b^2(g'). \tag{4.20}$$

Various observables such as the charged-particle multiplicity (M_c), the ratio of transverse-to-longitudinal kinetic energy ($Erat = \sum E_t / \sum E_l$), the longitudinal component of the quadrupole moment tensor ($Q_{zz} = \sum 2p_z^2 - p_x^2 - p_y^2$), and a recent neural-network technique have been adopted to estimate the event-by-event impact parameter, *e.g.*, see Ref. [47] and references therein. In the present study, we chose the charged-particle multiplicity M_c detected in the SπRIT TPC as an estimator of the impact parameter. The charged-particle multiplicity is rather simple among various observables, and thus, the event samples selected according to M_c could be less biased. Note that the b–M_c relationship is approximately monotonic anti-correlation with some level of a fluctuation, not a one-to-one correspondence. Therefore, even if one selects only the event samples registering a particular number of charged-particle multiplicity, the impact parameter of the selected samples forms a distribution with a certain width.

To normalize different Sn + Sn systems, a scaled impact parameter $b_0 = b/b_{\mathrm{max}}$ was defined, which has been also used for the same purpose in the previous studies [10, 48, 62]. Here, b_{max} indicates the maximum impact parameter of two colliding nuclei calculated by the sharp nuclear boundary approximation [215] as $b_{\mathrm{max}} = r_0(A_P^{1/3} + A_T^{1/3})$ with $r_0 = 1.15$ and $A_{P(T)}$ being the mass number of a projectile (target) nucleus. Given a certain minimum multiplicity threshold m_c, the scaled impact parameter b_0 can be calculated by the square root of the cumulative M_c distribution according to the Eq. 4.20, as:

$$b_0(m_c) = \frac{\sqrt{\langle \sigma_{\mathrm{Triggerable}} \rangle / \pi}}{b_{\mathrm{max}}} \cdot \left(\sum_{M_c = m_c}^{\infty} \frac{\mathrm{d}P(M_c)}{\mathrm{d}M_c} \right)^{1/2}. \tag{4.21}$$

Figure 4.28 presents the probability distribution of M_c per event ($\mathrm{d}P(M_c)/\mathrm{d}M_c$) for four Sn + Sn collision systems. A slight difference observed in different systems may originate from the different projectile-target mass asymmetries of each system. For example, the projectile Sn isotope is heavier than the target one in the neutron-rich $^{132(124)}$Sn + $^{124(112)}$Sn system. Because we conducted the measurement of the four Sn + Sn systems with approximately the same incident energy per nucleon, the center-of-mass velocity in the laboratory frame is faster in the neutron-rich $^{132(124)}$Sn + $^{124(112)}$Sn system than in the neutron-deficient $^{108(112)}$Sn + $^{112(124)}$Sn system. Consequently, the production as well as the detection of particles in laboratory forward angles can be enhanced in the neutron-rich systems more than the neutron-deficient systems. This natural conjecture is reasonable as the trend of the M_c distributions depends on the degree of projectile-target asymmetries, *i.e.*, the trend in the figure is found to vary in the order of ^{124}Sn + ^{112}Sn (the most asymmetric with a heavier projectile) $\rightarrow$ ^{132}Sn + ^{124}Sn $\rightarrow$ ^{108}Sn + ^{112}Sn $\rightarrow$ ^{112}Sn + ^{124}Sn. Figure 4.29 presents the response function

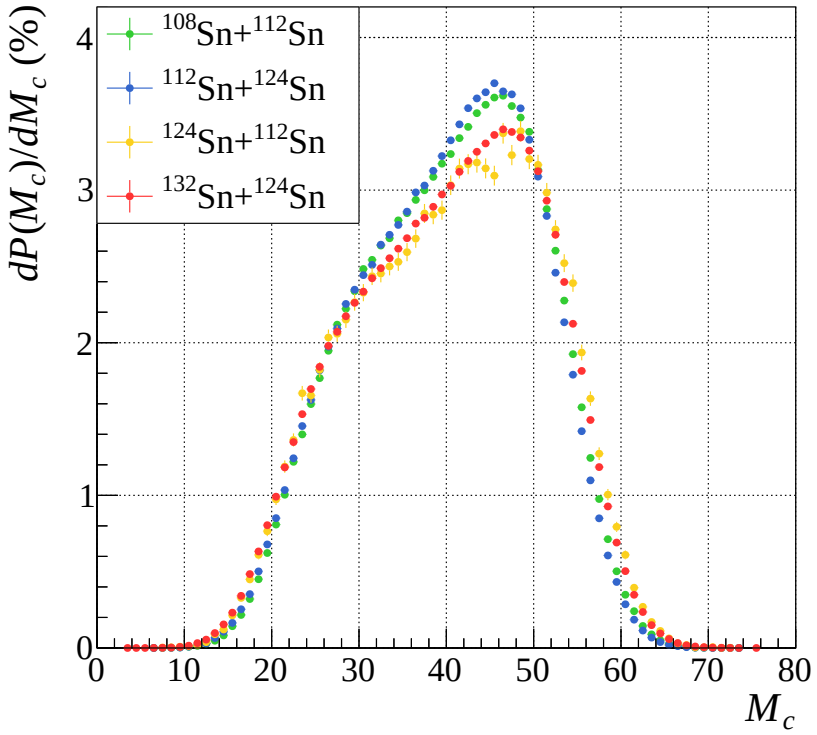

Figure 4.28: Probability distributions of the charged-particle multiplicity detected in the SπRIT TPC for four Sn + Sn systems. A slight difference in different systems may result from the projectile-target mass asymmetry of the system and the forward-angle acceptance of the TPC, see the text in detail.

Table 4.14: Charged-particle-multiplicity threshold for selecting the most central ($b_0 \leq 0.15$) event samples. The corresponding range of b_0 and the number of events selected by the high M_c requirement are also listed.

System	M_c selection	b_0 range	N_{central}
^{108}Sn + ^{112}Sn	$M_c \geq 55$	$0 \leq b_0 < 0.1480$	88040
^{112}Sn + ^{124}Sn	$M_c \geq 55$	$0 \leq b_0 < 0.1393$	47588
^{124}Sn + ^{112}Sn	$M_c \geq 56$	$0 \leq b_0 < 0.1464$	4693
^{132}Sn + ^{124}Sn	$M_c \geq 56$	$0 \leq b_0 < 0.1436$	134478

of the scaled impact parameter based on the multiplicity distributions and Eq. 4.21. In the present work, the condition of $b_0 \leq 0.15$ was applied to select the most central collision event samples. Since the M_c is a discrete value, the M_c bin closest to $b_0 = 0.15$ was adopted as the threshold. The corresponding M_c thresholds are 55 for the ^{108}Sn + ^{112}Sn system and 56 for the ^{132}Sn + ^{124}Sn system, which are tabulated in Table 4.14.

The systematic uncertainty in the selection of central collisions was evaluated by considering variations of the b_{max} calculation and the procedure to obtain the charged particle multiplicity in the TPC. In Ref. [215], the sharp nuclear boundary approximation itself is expected to have at least 1.5% uncertainty on the radius coefficient r_0. However, more variations (8–10%) of the b_{max} can be found by semiempirical calculations which consider the density distribution of the nuclear surface,

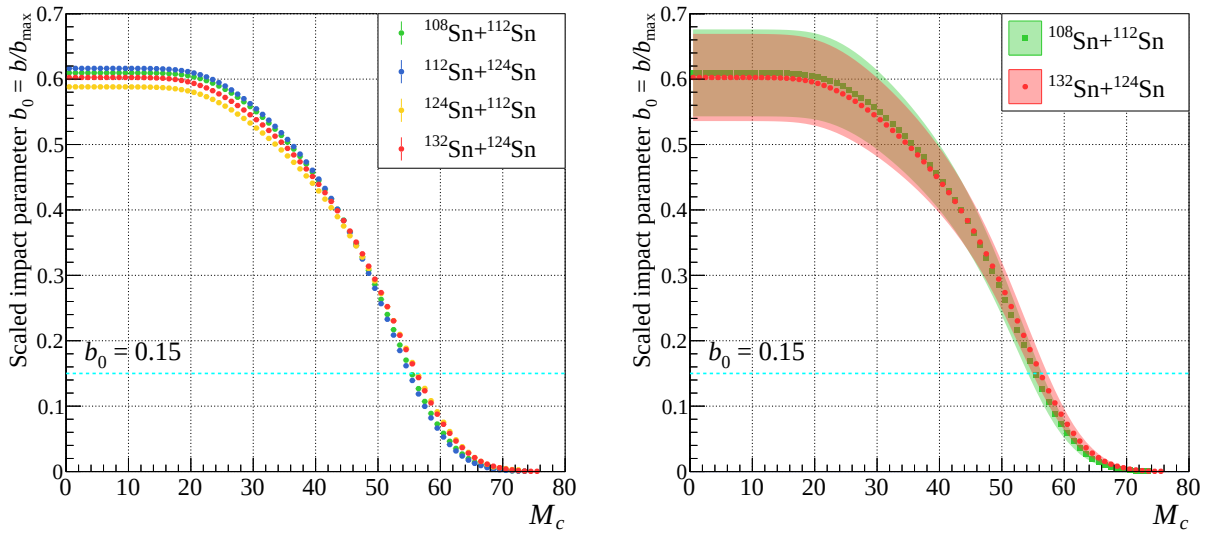

Figure 4.29: Response function of the scaled impact parameter (b_0) with a particular charged particle multiplicity (M_c). Left: the b_0 response functions for four systems calculated from $\mathrm{d}P(M_c)/\mathrm{d}M_c$ distributions. The cyan dotted lines lie on $b_0 = 0.15$. The multiplicity bin which is the closest to $b_0 = 0.15$ was employed as the threshold multiplicity for selecting the most central events. Right: the b_0 response functions with envelopes indicating systematic uncertainties in the determination of b_0. Only two systems are shown for a visibility.

as listed in Table 4.15. To estimate the uncertainty derived from the analysis procedure, the b_0 response function was constructed with loosened and tightened analysis conditions so that (1) a gate width on the vertex z position ($|v_z - \mu_z| \leq 3\sigma_z$) was varied by $2\sigma_z$–$4\sigma_z$ from the means, and (2) a threshold distance from tracks to the vertex ($d_{\mathrm{POCA}} \leq 20\,\mathrm{mm}$) for counting the charged-particle multiplicity was varied by $\pm 2\,\mathrm{mm}$. The relative deviations from the default b_0 response function increase along M_c almost monotonically, and reach approximately 2% for the variation (1) and 30% for the (2) at the $M_c = 70$ bin. The b_0 response functions with including the statistic uncertainty and the systematic ones are shown in the right panel of Fig. 4.29, where the uncertainties were given by the quadratic sum. With the consideration of uncertainties, the multiplicity threshold for selecting the most central event samples can vary by ± 1, which will be considered in the evaluation of the systematic uncertainties in the rapidity spectra.

Table 4.15: Maximum impact parameters calculated by several theoretical model parametrizations of the total reaction cross section.

$b_{\mathrm{max}} = \sqrt{\sigma_R/\pi}$ (fm)	^{108}Sn + ^{112}Sn	$^{112(124)}$Sn + $^{124(112)}$Sn	^{132}Sn + ^{124}Sn
Hard sphere [215]: $1.15(A_P^{1/3} + A_T^{1/3})$	11.02	11.28	11.59
Modified Karol's model [216]	12.22	12.52	12.87
Modified Kox's model [217][a]	10.78	11.04	11.35

[a] For the parametrization of the σ_R, the asymmetry factor F_{asym} in the Eq. (2) in Ref. [217] was ignored since the asymmetries of the system in the present work are too large compared to those considered in the reference. Therefore the provided values in this table are a kind of lower limits.

4.7 Particle Identification in the SπRIT TPC

In this section, the procedure of the particle identification (PID) for hydrogen isotopes according to their mean energy loss (dE/dx) in the P10 gas and the magnitude of magnetic rigidity ($R = p/q$) is described. These two observables were converted into a mass of particles using an empirical function which was optimized so as to fit the experimental dE/dx vs. p/q relationship. Fit parameters of the empirical function were found to depend on the track emission angles, and thus, the converted mass was a calibrated quantity concerning the angles. Based on the mass distributions, each hydrogen isotope was selected and their mutual contaminations were evaluated.

Conversion of the energy loss and magnetic rigidity into mass

First, we briefly describe a method to convert the energy loss and rigidity into mass. The mean energy loss of a charged particle traversing material depends on its charge, mass, and velocity, which is known as the empirical Bethe-Bloch formula. To obtain an empirical expression of the dE/dx vs. p/q relation for hydrogen isotopes, their loci in the PID spectra were fitted by the following Bethe-Bloch-based function[1] with constraining the charge of an incident particle as $z = 1$:

$$\langle dE/dx \rangle_{\mathrm{fit}}(m, R) = a_0 + a_1 \frac{C}{\beta^{a_2}} \left[\frac{1}{2} \ln \left(\frac{2 m_e c^2 \beta^2 \gamma^2 W_{\mathrm{max}}}{I^2} \right) - \beta^{a_2} - \frac{\delta(\beta\gamma)}{2} \right]. \tag{4.22}$$

Here, m, $R = p$, $\beta = R/\sqrt{R^2 + m^2}$, and $\gamma = 1/\sqrt{1 - \beta^2}$ represent a mass, a magnetic rigidity equivalent to a momentum, a velocity, and the Lorentz factor of hydrogen isotopes, respectively, and $a_{i\,(i=0,1,2)}$ are fit parameters. The a_0 and a_1 represent the offset and the normalization factors, respectively. The β^2-dependent terms were slightly modified by $\beta^2 \rightarrow \beta^{a_2}$. The mass of particles can be deduced by numerically solving the equation

$$\langle dE/dx \rangle_{\mathrm{measure}} - \langle dE/dx \rangle_{\mathrm{fit}}(m, R_{\mathrm{measure}}, a_i) = 0, \tag{4.23}$$

in terms of an unknown variable m, with inputs of the mean energy loss $\langle dE/dx \rangle_{\mathrm{measure}}$ and magnetic rigidity R_{measure} measured for respective tracks, and fitted parameters a_i. The calculation was based on a simplified version of the Newton method, the so-called secant method.

4.7.1 Empirical fits on PID spectra in different emission angles

In the present work, the measured dE/dx distribution was found to slightly depend on the emission angle. Possibly this may be attributed to a technical reason, but is also related to the physical fact that the most probable energy loss rate in thin absorbers such as a gas detector depends on the material thickness [213]. In the case of the TPC operation, the detector thickness corresponds to the length of hit clusters, which varies by the emission angles and by the bending of charged

[1] The denotations in Eq. 4.22 are provided here. The $C = 0.21571593$ is a constant, m_e is the electron mass, W_{max} is the maximum kinetic-energy transfer in a single collision between the incident particle and an atom in the material, I is the mean excitation potential of the material, and $\delta(\beta\gamma)$ is the density effect correction.

particles. To calibrate this effect, the PID spectra of dE/dx vs. magnetic rigidity were constructed for different yaw-pitch angle segments, and each of them was fitted by Eq. 4.22. To be meaningful, the yaw and pitch angles (θ_{yaw} and θ_{pitch}) were defined with respect to the readout pad plane of the TPC, given as:

$$\theta_{\mathrm{yaw}} = \arctan\left(p_x/p_z\right), \qquad \theta_{\mathrm{pitch}} = \arctan\left(p_y/p_z\right), \tag{4.24}$$

with $p_{x,y,z}$ represent the three-vector component of the momentum in the TPC coordinate. The distribution of θ_{yaw} vs. θ_{pitch} space is already presented in Fig. 3.9. As an angular bin for the calibration, we segmented the region by $\mathrm{d}\theta_{\mathrm{yaw}} = 30°$ and $\mathrm{d}\theta_{\mathrm{pitch}} = 10°$.

Figures 4.30 and 4.31 present examples of angle-dependent PID spectra along with the fit functions of Eq. 4.22 on the loci of hydrogen isotopes. The functions are simultaneously fitted for the three loci of hydrogen isotopes by minimizing the sum of chi squares calculated for the protons, deuterons, and tritons. The drawn markers in the figure indicate the mean dE/dx values of each isotope as a function of magnetic rigidity, which were obtained by fitting the rigidity-sliced dE/dx distributions with Gaussian functions. The width of the rigidity slice was $50\,\mathrm{MeV}/c$. The Gaussian fittings were performed only for rigidity regions with enough statistics not to fail the fitting. In the vicinity of the beam trajectory, *i.e.*, at small θ_{yaw} and θ_{pitch} angles, the reconstruction of tracks could be strongly influenced by the huge charges induced by the beam particles [189]. Because this beam-induced effect deviates the position and charge of the hit clusters largely, the parameter map has a locality at the small angle regions. Thus, the small-angle region of $(-60° \leq \theta_{\mathrm{yaw}} \leq 60°) \cap (-30° \leq \theta_{\mathrm{pitch}} \leq 25°)$ was segmented in finer binning of $\mathrm{d}\theta_{\mathrm{yaw}} = 10°$ and $\mathrm{d}\theta_{\mathrm{pitch}} = 5°$. These normal and finer parameter maps as functions of θ_{yaw} and θ_{pitch} were smoothly merged by two-dimensional interpolations.

In Fig. 4.32, mass spectra obtained with the parameters a_i calibrated angle by angle and those by a single set of parameters are compared, showing that the mass resolution was improved thanks to the calibration. The standard deviations of respective mass peaks in the rigidity range of $900\,\mathrm{MeV}/c \leq p/q \leq 1000\,\mathrm{MeV}/c$ are approximately $92\,\mathrm{MeV}/c^2$, $140\,\mathrm{MeV}/c^2$, and $200\,\mathrm{MeV}/c^2$ for protons, deuterons, and tritons, respectively.

4.7.2 Selection of hydrogen isotopes

Track quality In the following analysis on particular hydrogen isotopes, we restricted the track's azimuthal angle: $\phi = \arctan\left(p_y/p_x\right)$. The selected azimuthal angle range was $-30° \leq \phi \leq 20°$, in which a relatively large effective detector volume is guaranteed and the beam-induced effect deteriorating the track reconstruction mainly at above and below the beam trajectory can be avoidable. Further, a stable efficiency and a high separation capability are expected in the considered ϕ range because most of emitted charged particles are bent to the beam-right ($\phi \sim \pm 180°$) side and the opposite $\phi \sim 0°$ side tends to be less density of charged particles. Note that the incident beam angle was considered event by event in the calculation of momenta of tracks, *i.e.*, xyz axes directions are not always fixed. The azimuthal-angle restriction will be compensated by multiplying the yield of selected hydrogen isotopes by a factor of $360/50$, assuming the azimuthal symmetry of the particle production. In conjunction with the quality assurance mentioned in Sect. 4.3, the condition of $d_{\mathrm{POCA}} \leq 20\,\mathrm{mm} \cap n_{\mathrm{Cluster}} \geq 15 \cap -30° \leq \phi \leq 20°$ was applied.

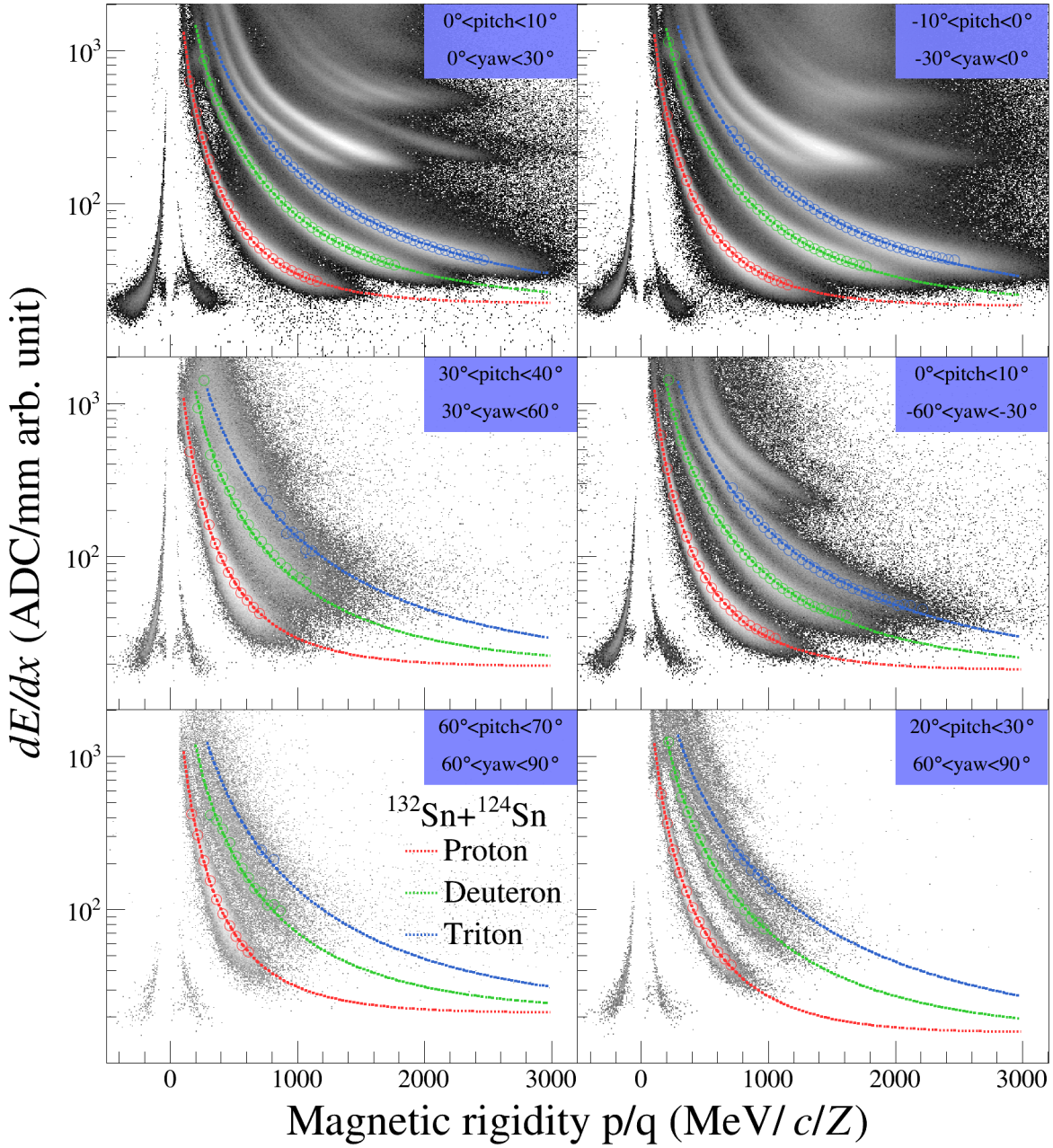

Figure 4.30: PID spectra for the central ^{132}Sn + ^{124}Sn collisions in certain emission angles. Red, green, and blue markers indicate the mean dE/dx values as a function of rigidity for protons, deuterons and tritons, respectively. In each angle bin, three PID loci are simultaneously fitted by the empirical function, drawn by the dotted lines. In the forward angle region in the top panels, the loci of each particle are clearly seen since the tracks are likely to have a enough number of clusters to reconstruct dE/dx and magnetic rigidity with high resolution. At large θ_{pitch} angle regions, only short tracks are reconstructed, and consequently, the resolution of each isotope becomes quite worse.

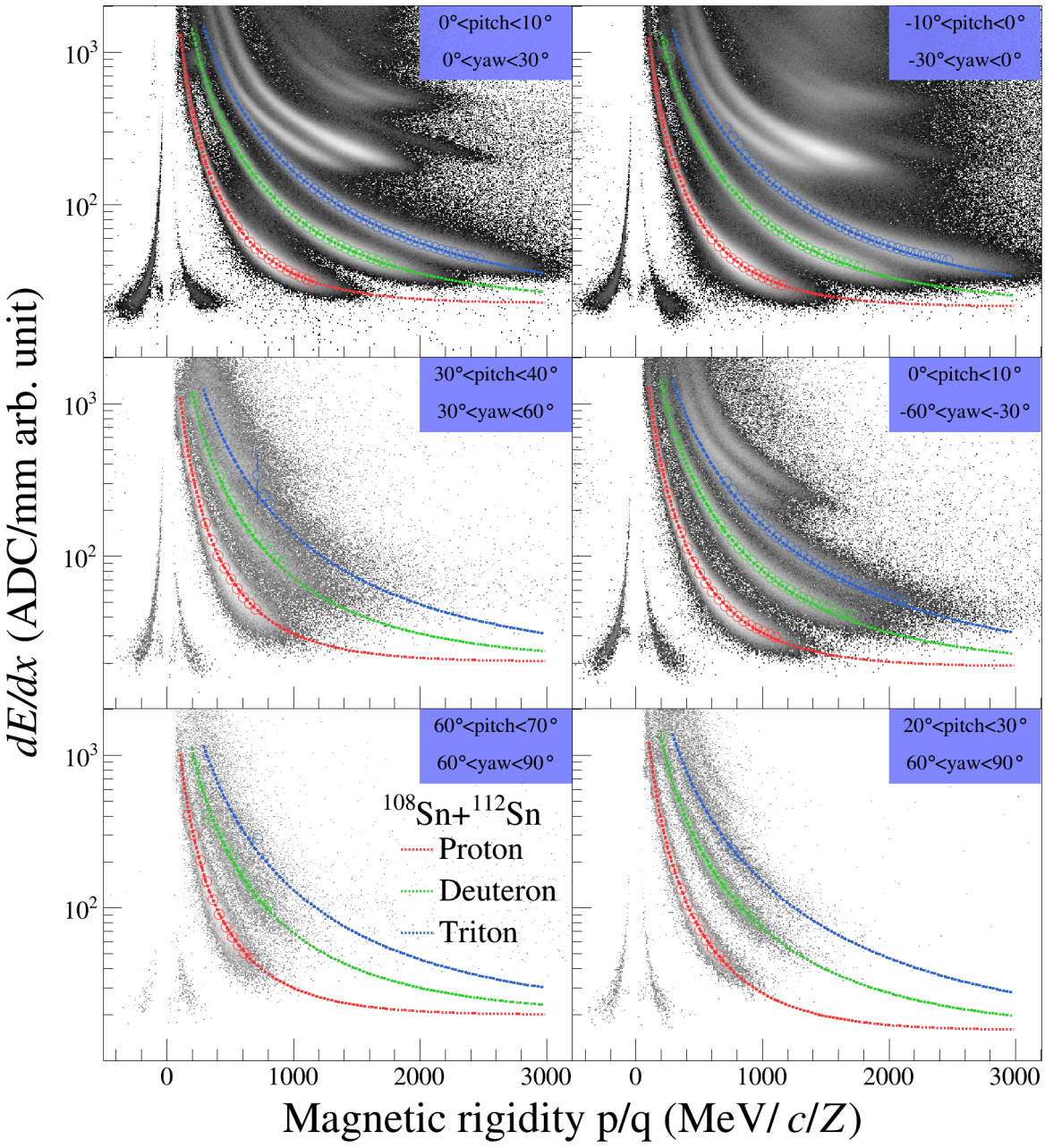

Figure 4.31: Same as Fig. 4.30, but for the central ^{108}Sn + ^{112}Sn collisions.

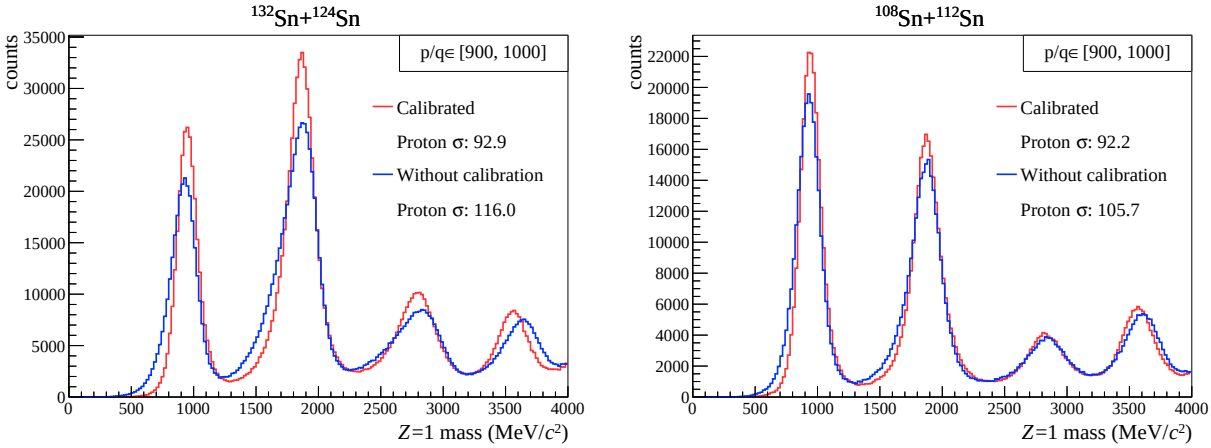

Figure 4.32: Particle mass spectra in the rigidity range of $900\,\mathrm{MeV}/c \leq p/q \leq 1000\,\mathrm{MeV}/c$ with/without the emission-angle calibration for the two systems. In the legends, standard deviations of the proton peaks obtained by Gaussian fits are presented. Note that the peak appearing around $m = 3600\,\mathrm{MeV}/c^2$ is a ^{3}He component. Because Eq. 4.23 was solved with postulating a constraint of $z = 1$, unphysical mass can be calculated for isotopes heavier than heliums ($z \geq 2$).

Mass gate To identify hydrogen isotopes, their mass peaks were gated by certain ranges based on results of Gaussian fits. Figure 4.33 presents mass spectra in three mass regions around the proton mass ($m_p \simeq 938.27\,\mathrm{MeV}/c^2$), deuteron mass ($m_d \simeq 1875.61\,\mathrm{MeV}/c^2$), and triton mass ($m_t \simeq 2808.92\,\mathrm{MeV}/c^2$), each of which was constructed for different magnetic rigidity bins. The three peaks – the peak of the particle of interest and its neighbors – were fitted by a triple Gaussian function to select the isotope as well as to estimate the contamination from the neighbors. The gate conditions of each hydrogen isotopes were defined as $|m - \mu_p| \leq 4\sigma_p$, $|m - \mu_d| \leq 3\sigma_d$, and $|m - \mu_t| \leq 2.5\sigma_t$ for protons, deuterons, and tritons, respectively, with μ and σ being fitted mean and standard deviation values. These widths were defined so that the yields of each isotope are not strongly influenced by a small deviation of the gate width. Figure 4.34 presents the two-dimensional mass vs. magnetic rigidity spectra for central collisions of $^{132}\mathrm{Sn} + {}^{124}\mathrm{Sn}$ and $^{108}\mathrm{Sn} + {}^{112}\mathrm{Sn}$ systems, with overdrawn by the mass gates obtained in each rigidity bin. To define the continuous gate conditions as a function of magnetic rigidity, the mass gates for each rigidity bin were fitted by second-order polynomial functions, as shown in Fig. 4.34. Since the polynomial gates become too wide in the higher magnetic rigidity region, constant mass ranges were also applied as the limit for identifying each particle, *i.e.*, the mass of protons, deuterons, and tritons are should be within the range of $(500, 1400)$, $(1400, 2300)$, and $(2300, 3400)\ \mathrm{MeV}/c^2$, respectively. And besides, the lower limits of momenta of each hydrogen isotope were applied to cut away particles with very high dE/dx suffered by the electronics saturation and not likely to be separated and identified. An upper mass limit for tritons was also defined as $m \leq (0.6R + 2650)\ \mathrm{MeV}/c^2$ to distinguish tritons from a large contamination by the ^{3}He locus, as shown in Fig. 4.34. Table 4.16 summarizes the mass gates on each hydrogen isotope. The identification efficiency will be treated as the systematic uncertainty originating from the variations of gate width, which will be discussed in Sect. 4.9.

Probability assignment Even if one selected the track by the mass gate, it is not necessarily the particle of interest but perhaps another particle species with the mass largely fluctuated from the nominal value of the objective particle. In order to subtract such a contaminant inside the gate, the

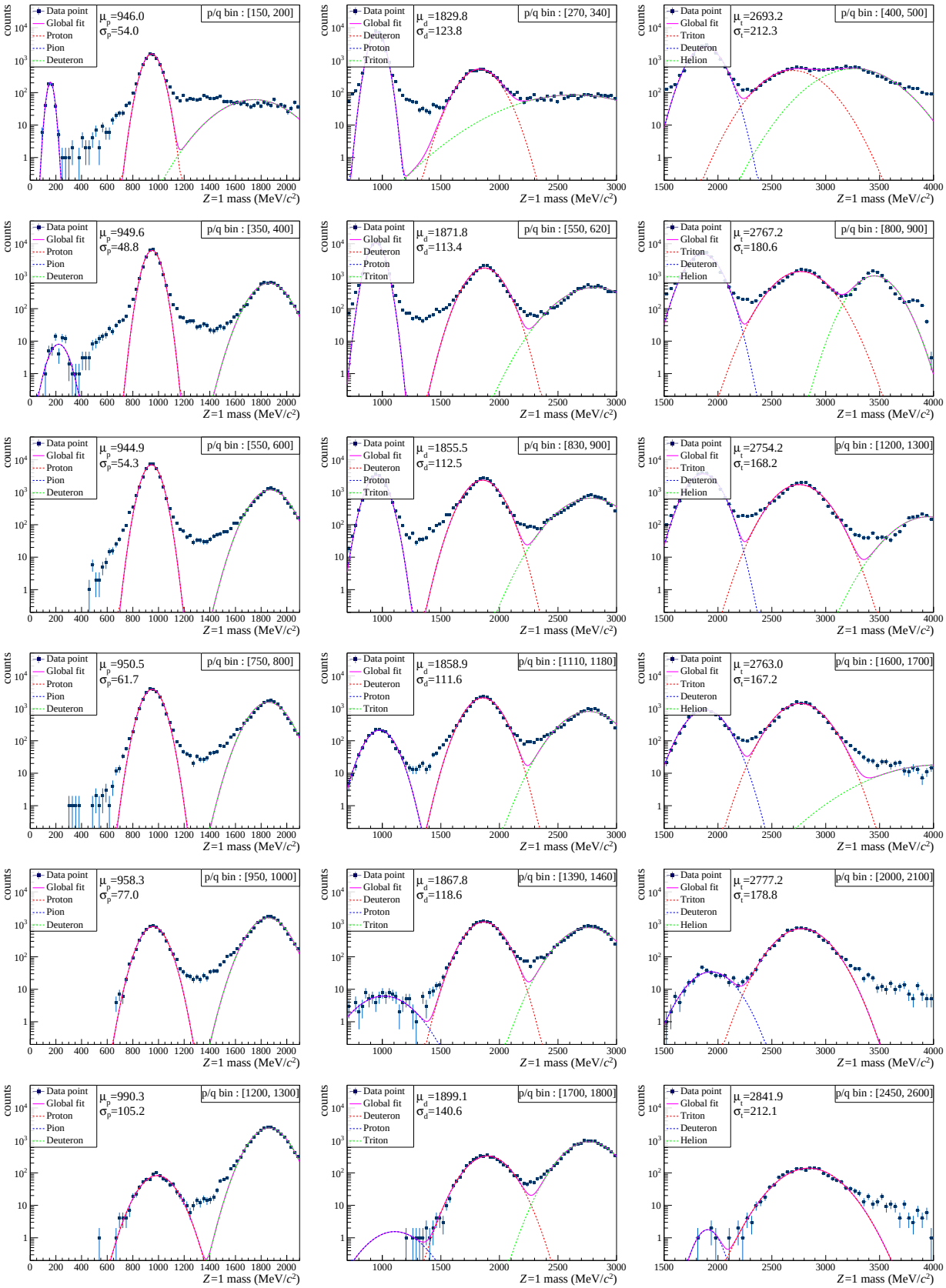

Figure 4.33: Rigidity-sliced mass spectra along with the triple Gaussian fits on three peaks. Each column contains the spectra constructed for six different magnetic rigidity bins indicated in the right-top legends, for three kinds of mass ranges around protons (left), deuterons (middle), and tritons (right).

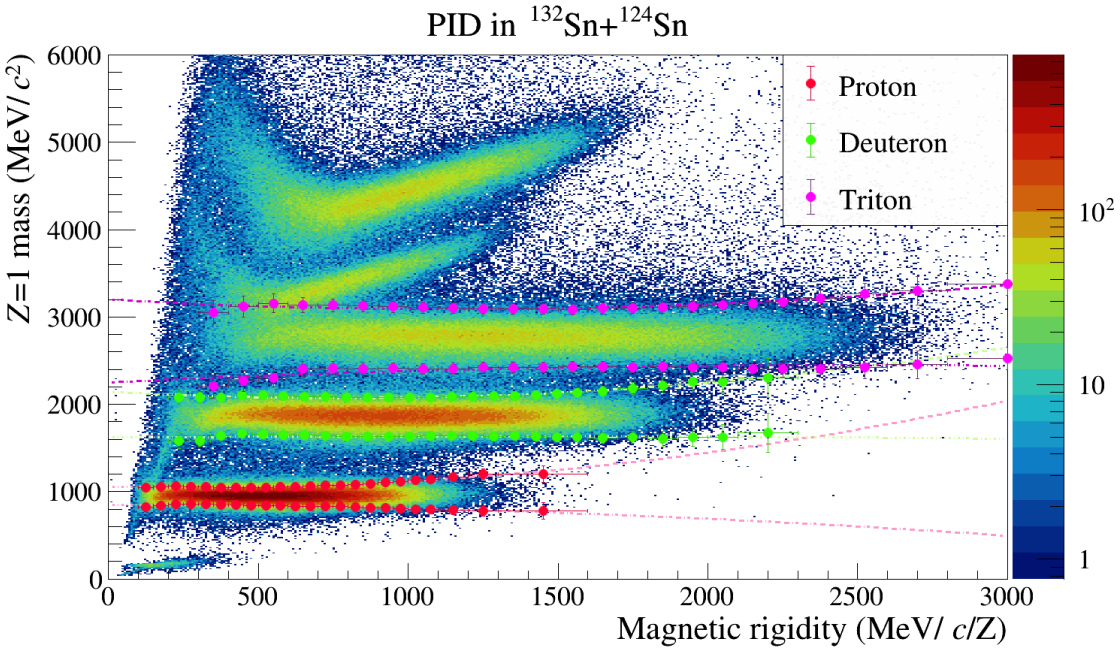

(a) Mass vs. magnetic rigidity spectrum for central ^{132}Sn + ^{124}Sn collisions.

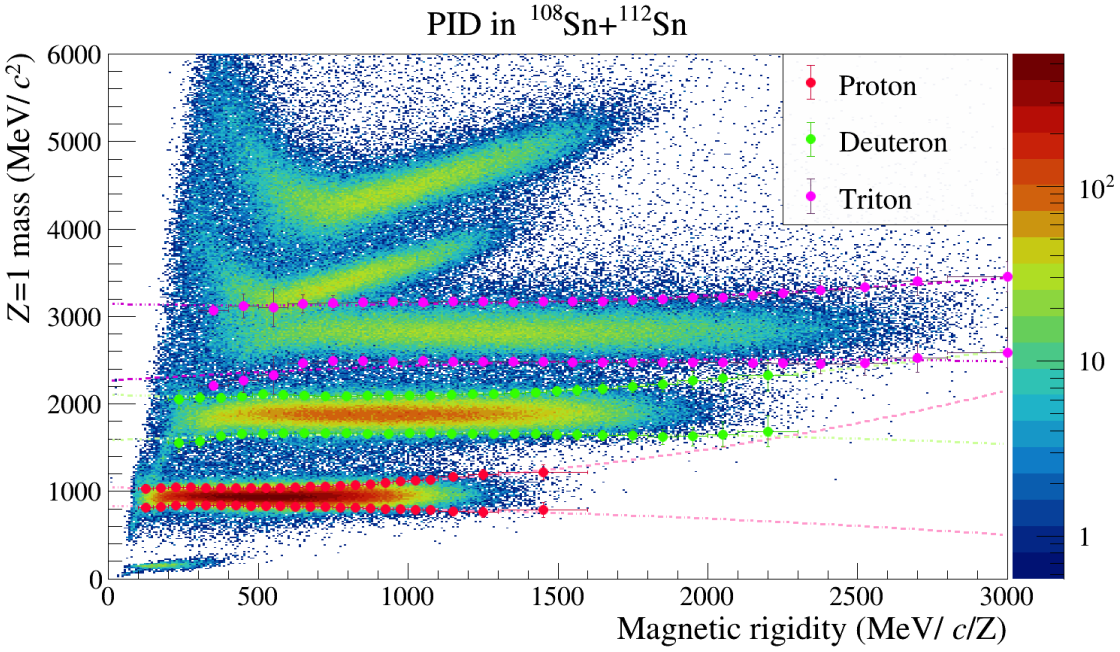

(b) Mass vs. magnetic rigidity spectrum for central ^{108}Sn + ^{112}Sn collisions.

Figure 4.34: Two-dimensional mass vs. magnetic rigidity spectra for the two systems. Red, green, and purple circles drawn along the loci of each hydrogen isotope indicate the 2σ from Gaussian-fitted mean values as a function of rigidity. The same-colored dotted lines along markers are second-order polynomial fits, indicating the upper and lower ends of the mass gate.

Table 4.16: Summary of the gate conditions for hydrogen isotopes.

Particle	Momentum threshold	Rigidity-dependent mass gate (MeV/c^2)
Proton	$p_p \leq 100\,\mathrm{MeV}/c$	$\left\|m-\mu_p\right\| \leq 4\sigma_p \cap m \in [500, 1400]$
Deuteron	$p_d \leq 200\,\mathrm{MeV}/c$	$\|m-\mu_d\| \leq 3\sigma_d \cap m \in [1400, 2300]$
Triton	$p_t \leq 300\,\mathrm{MeV}/c$	$\|m-\mu_t\| \leq 2.5\sigma_t \cap m \in [2300, 3400] \cap m \leq 0.6R+2650$

probability that a particular track with mass m and magnetic-rigidity magnitude R is registered as a particle i was calculated using the fit results as:

$$P_i(m,R) = \frac{g_i(m,R)}{g_i(m,R)+g_j(m,R)+g_k(m,R)}, \tag{4.25}$$

where $g_i(m,R)$ represents the Gaussian function fitted to the peak of the particle i in a certain magnetic rigidity bin containing the R, and j and k indicate particles with a lighter and heavier mass than the particle i, respectively. More explicitly, (i,j,k) are (p,π,d), (d,p,t), and $(t,d,{}^3\mathrm{He})$. When the selected track is filled into the spectrum for the particle i, the probability $P_i(m,R)$ was weighted to the track. The systematic uncertainty derived from the probability assignment was evaluated by changing the fit function for the mass peaks from a Gaussian form to a Voigt function (a convolution of Gaussian and Lorentz functions), see Sect. 4.9 later.

4.7.3 Differential yield of selected hydrogen isotopes

In the followings, the production yield of hydrogen isotopes in the transverse momentum (p_T) vs. scaled rapidity (y_0) phase space will be discussed, where each quantity is defined as:

$$p_T = \sqrt{p_x^2+p_y^2}, \tag{4.26}$$

$$y_0 = y/y_{NN}^{\mathrm{c.m.}} - 1, \tag{4.27}$$

$$y = \frac{1}{2}\ln\frac{E+p_z}{E-p_z}, \tag{4.28}$$

where $p_{x,y,z}$, E, and y indicate the components of the four-momentum vector and the rapidity of the detected particle in the laboratory frame, respectively. Note that the incident-beam angle was considered in calculating the momentum of detected particles. The $y_{NN}^{\mathrm{c.m.}}$ is the rapidity of the nucleon-nucleon (NN) center of mass in the laboratory frame, which is calculated from the momentum of the NN center of mass:

$$\begin{aligned}\boldsymbol{p}_{\boldsymbol{NN}}^{\mathbf{c.m.}} &= (0,0,p_{z,NN}^{\mathrm{c.m.}},E_{NN}^{\mathrm{c.m.}}) \\ &= (0,0,\sqrt{E_{\mathrm{beam}}(E_{\mathrm{beam}}+2m_u)},E_{\mathrm{beam}}+2m_u),\end{aligned} \tag{4.29}$$

where E_{beam} is the kinetic energy per nucleon of incident Sn beams and $m_u \simeq 931.478\,\mathrm{MeV}/c^2$ represent the atomic mass unit. The mean value of $y_{NN}^{\mathrm{c.m.}}$ was approximately 0.371 for both ^{132}Sn + ^{124}Sn and ^{108}Sn + ^{112}Sn reactions, but event-by-event values were adopted in the analysis.

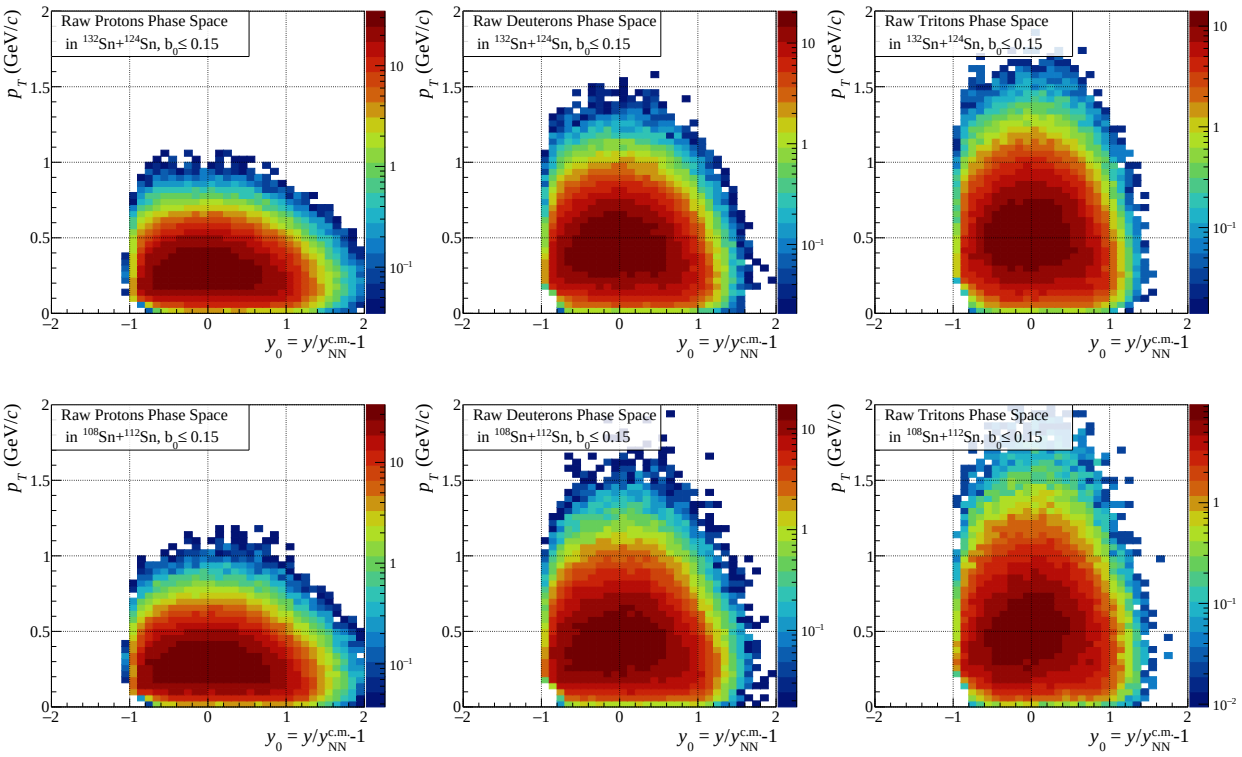

Figure 4.35: Uncorrected differential yields in the p_T vs. y_0 phase space for protons (left), deuterons (middle), and tritons (right) emitted in central collisions of the ^{132}Sn + ^{124}Sn system (top) and ^{108}Sn + ^{112}Sn system (bottom).

Raw p_T vs. y_0 phase space Figure 4.35 presents the raw (uncorrected) differential yield distribution per event in the p_T vs. y_0 phase space,

$$\frac{1}{N_{\text{event}}}\frac{\mathrm{d}^2 N_{\text{raw}}}{\mathrm{d}p_T\,\mathrm{d}y_0} = \frac{1}{N_{\text{event}}}\frac{N(y_0,p_T)}{\Delta p_T \Delta y_0}\frac{P_i(m,R)}{\epsilon_\phi}. \tag{4.30}$$

Here $N(y_0, p_T)$ is the number of detected particles with the scaled rapidity y_0 and transverse momentum p_T, which was filled into the two-dimensional histogram with a bin width of $\Delta p_T = 0.04\,\mathrm{GeV}/c$ and $\Delta y_0 = 0.1$. The $P_i(m,R)$ is the probability provided by Eq. 4.25, where i represents a particle type that runs over protons, deuterons, and tritons. The $(\epsilon_\phi)^{-1} = 360/50$ involves the efficiency due to the azimuthal angle cut. The correction of the obtained spectra will be based on a Monte Carlo simulation, discussed in Sect. 4.8, which uses the raw p_T vs. y_0 phase space as an initial condition of the iterative process. The p_T-integrated yields as a function of scaled rapidity:

$$\frac{1}{N_{\text{event}}}\frac{\mathrm{d}N_{\text{raw}}}{\mathrm{d}y_0} = \sum_{p_T\text{ bin}}\frac{1}{N_{\text{event}}}\frac{N(y_0,p_T)}{\Delta p_T \Delta y_0}\frac{P_i(m,R)}{\epsilon_\phi}\cdot\Delta p_T, \tag{4.31}$$

are presented in Fig. 4.36.

Contamination rate Figure 4.37 presents the contamination rate ($1/P_i(m,R)$) for each p_T-y_0 bin. The target rapidity regions ($y_0 \sim -1$) of deuterons and tritons are contaminated mainly by low-momentum tritons and ^{3}He particles, respectively, as is also observed in Fig. 4.33. And

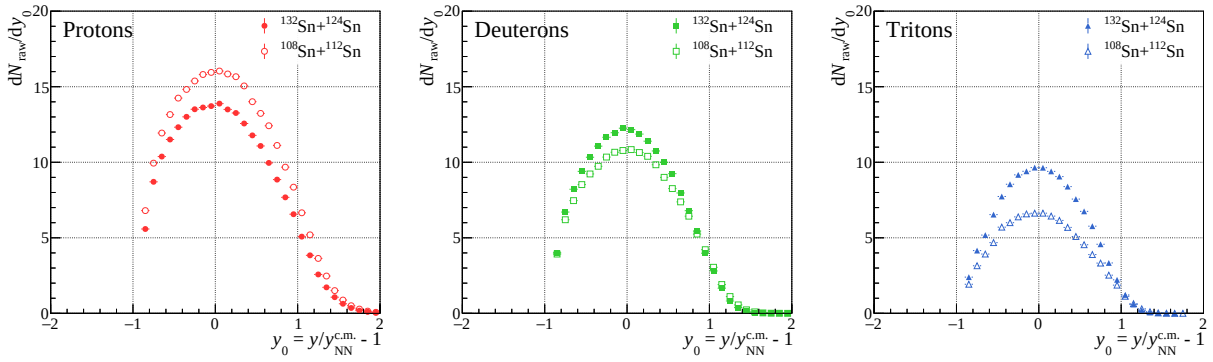

Figure 4.36: Uncorrected dN_{raw}/dy_0 spectra for protons (left), deuterons (middle), and tritons (right) emitted in central collisions of the ^{132}Sn + ^{124}Sn system (filled markers) and ^{108}Sn + ^{112}Sn system (open markers).

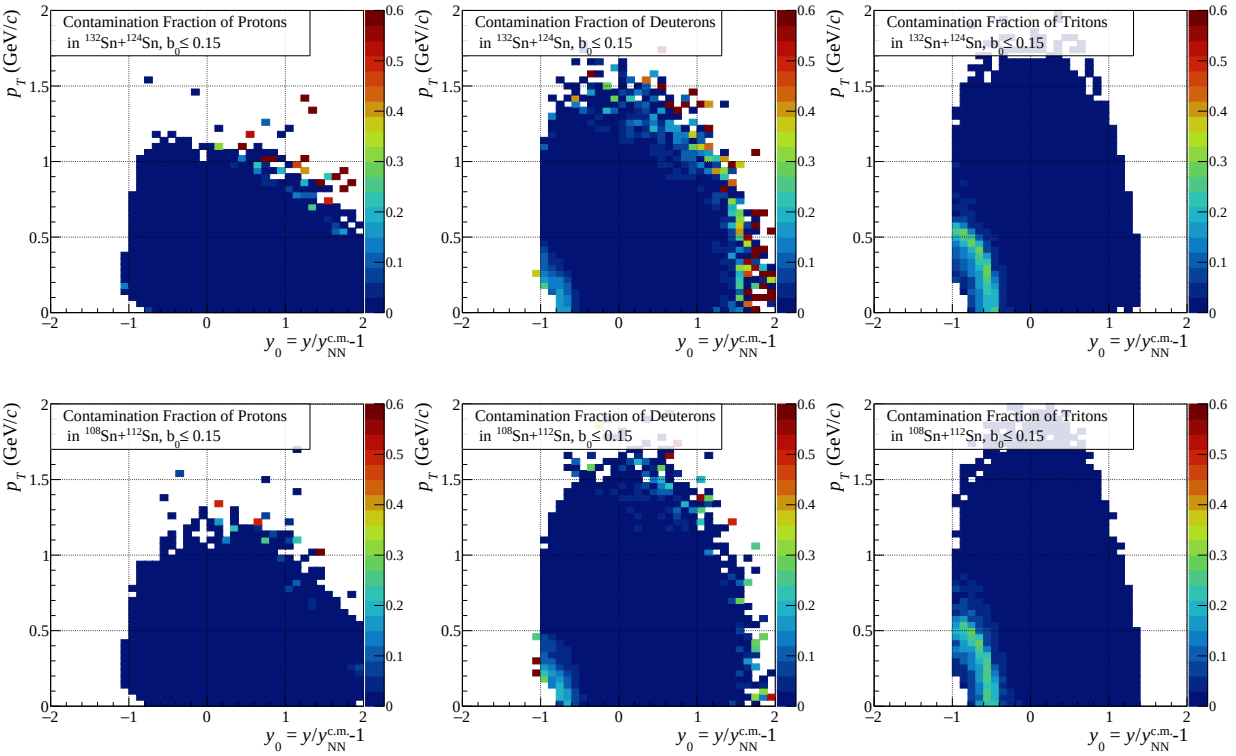

Figure 4.37: Contamination rate as functions of p_T vs. y_0 for protons (left), deuterons (middle), and tritons (right) in central collisions of ^{132}Sn + ^{124}Sn (top) and ^{108}Sn + ^{112}Sn (bottom) systems.

besides, deuterons faster than 1500 MeV/c of momentum are contaminated by tritons. The largest contamination in triton spectra by ^{3}He was deduced as approximately 20–30% in the momentum range around 500 MeV/c. Shown in Fig. 4.38 are the overall contamination rates for each hydrogen isotope as a function of scaled rapidity, calculated as:

$$\frac{dN_{total}/dy_0 - dN_{raw}/dy_0}{dN_{total}/dy_0}, \tag{4.32}$$

where N_{total} is the number of particles without being weighted by $P_i(m, R)$. The contamination in proton dN_{raw}/dy_0 spectra is almost negligible, *i.e.*, less than 1% within the range of $-1 \leq y_0 \leq 1.5$.

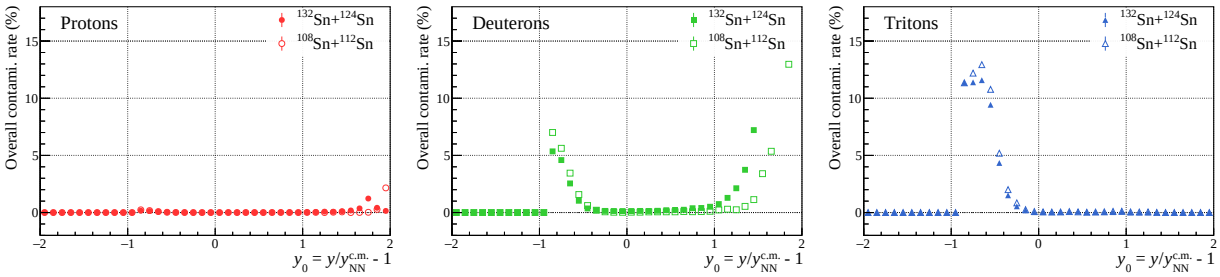

Figure 4.38: Overall contamination rate as a function of scaled rapidity for protons (left), deuterons (middle), and tritons (right) emitted in central collisions of the ^{132}Sn + ^{124}Sn system (filled markers) and ^{108}Sn + ^{112}Sn system (open markers). Error bars are ignored.

4.8 Spectrum Corrections

In this section, the procedure to correct the raw differential yields of hydrogen isotopes in the transverse momentum vs. scaled rapidity phase spaces is described. Since the detection of charged particles in the TPC and the determination of their momenta could be influenced by multiple factors, the correction factor consists of convolutions of such factors. Some of the components that potentially affect the yield measurement are as follows.

Detector efficiency The detection efficiency of the SπRIT TPC can be attributed to the hardware threshold, geometrical acceptance, and the track-reconstruction software. Since the hardware gain was optimized for detecting minimum-ionizing charged pions, the angle-dependent geometrical acceptance is a main contribution of the inefficiency. For example, forward-going charged particles, accompanied with a sufficient number of hit clusters, are efficiently reconstructed while upward-going ones are hard to be detected due to a lack of clusters.

Bin smearing effect Owing to a finite momentum resolution that causes a bin-smearing and/or bin-shifting issues, the original yield distribution can be deformed. To take into account this effect so that the measured distribution can be converted into the original one, a correction function or a correction matrix is necessary. In the present work, the two-dimensional correction function in the p_T vs. y_0 space will be estimated.

High multiplicity effect In central collision events, a copious number of charged particles can be produced, which leaves electron-ion pairs widespread within the TPC active volume. In such an environment, some charged-particle tracks are likely to get close to each other and/or be overlapped, and subsequently, different tracks can be merged and clusters that should belong to a particular track can be missed. As the multiplicity and spatial distribution of charged particles change event by event, it is not easy to simulate realistically such a complicated environment.

Other inefficiencies Except for above mentioned, the injection of heavy-ion beams, the gating grid operation, the field uniformity, and the electronics saturation induced by high-energy δ electrons can be the source of inefficiencies. Similar to the high-multiplicity effect, it is difficult to reproduce such actual effects based on a simple simulation.

In order to evaluate the complicated correction function, the embedding technique was applied.

4.8.1 Monte Carlo embedding technique

The embedding technique has been applied to estimate the efficiency of a tracking detector for high-multiplicity events of heavy-ion collisions [218]. In the embedding method, the simulated charged-particle-induced signals are embedded into the raw data of a real event and analyzed with the same framework as the real data, and then, the number of simulated tracks in the array of reconstructed tracks is counted. As the real data is used, this technique allows us to take realistic detector effects into account as well as possible, without a full simulation. The procedure to

generate dummy signals and to extract the simulated tracks from the array of reconstructed tracks are as follows.

The GEANT4 tool implemented in the SπRITROOT was used to simulate the spatial distribution of the energy deposit induced by a single charged particle traversing in the realistic geometry of the SπRIT TPC. The energy-to-ionization conversion, the electrons drift with a spatial diffuseness, the wire amplification, and the charge spread across several pads based on the pad response function are considered. The waveform (flash-ADC) in the GET electronics was produced by convoluting the pulse-shape template with the charge induced on pads as a function of arrival time. The simulated ADC values, hits, and clusters are tagged as "embedded" so that we can trace them in the reconstruction process. The simulated track is identified based on the existence of the embedded clusters in a particular reconstructed track, *i.e.*, the condition of $n_{\mathrm{EmbedCluster}}/n_{\mathrm{Cluster}} \geq 0.5$ was applied, where $n_{\mathrm{EmbedCluster}}$ and n_{Cluster} represent the number of embedded clusters and that of total clusters belonging to the track, respectively. Imposing this condition can exclude real tracks that accidentally contain embedded clusters.

In this work, we generated about 10^6 of Monte Carlo protons, deuterons, and tritons for each. They were distributed uniformly in the p_T vs. y_0 space with ranges of $-1 \leq y_0 \leq 2$ and $0 \leq p_T \leq p_T^{\mathrm{max}}$, with $p_T^{\mathrm{max}} = 1.2, 1.4, 1.6\,\mathrm{GeV}/c$ for protons, deuterons, and tritons, respectively. The azimuthal angle distribution was uniform within the restricted range of $-35° \leq \phi \leq 35°$. The simulated tracks were embedded into the central collision events in the real data of $^{132}\mathrm{Sn} + {}^{124}\mathrm{Sn}$ and $^{108}\mathrm{Sn} + {}^{112}\mathrm{Sn}$ systems, which were selected in advance according to the data reduction analysis. From the array of the reconstructed tracks, the simulated track was identified by the requirement: $(n_{\mathrm{EmbedCluster}}/n_{\mathrm{Cluster}} \geq 0.5) \cap (d_{\mathrm{POCA}} \leq 20\,\mathrm{mm}) \cap (n_{\mathrm{Cluster}} \geq 15) \cap (-30° \leq \phi \leq 20°)$ to compensate for the track quality assignment applied in the real data analysis.

4.8.2 Procedure for unfolding

The correction function $C(y_0, p_T)$ can be obtained as:

$$C(y_0, p_T) = \frac{f_{\mathrm{init}}(y_0, p_T, w)}{f_{\mathrm{reco}}(y_0, p_T, w)}, \tag{4.33}$$

Here f_{init} and f_{reco} represent the p_T vs. y_0 distribution constructed by initial simulated tracks and that by reconstructed simulated tracks, respectively. The number of initial simulated tracks was weighted by the factor w depending on the initial p_T-y_0 bin. Because of the momentum-bin smearing and shifting, the detector filter $f_{\mathrm{init}} \rightarrow f_{\mathrm{reco}}$ can depend on the initial phase-space distribution f_{init}. Thus, the correction function has to be constructed with appropriately weighting f_{init} so that the weighted f_{init} is identical with the real distribution. In the present work, we iterated the following correction process to obtain the correct weighting factor for f_{init}.

1. The array of tracks containing simulated momenta and that containing reconstructed momenta are produced. The reconstructed track and its initial track are associated with each other.

2. As a weighting factor in the first iteration, the raw p_T vs. y_0 phase-space distribution is adopted, as an approximation of the original phase space which can be measured if the detector has 100% of efficiency and an infinite momentum resolution.

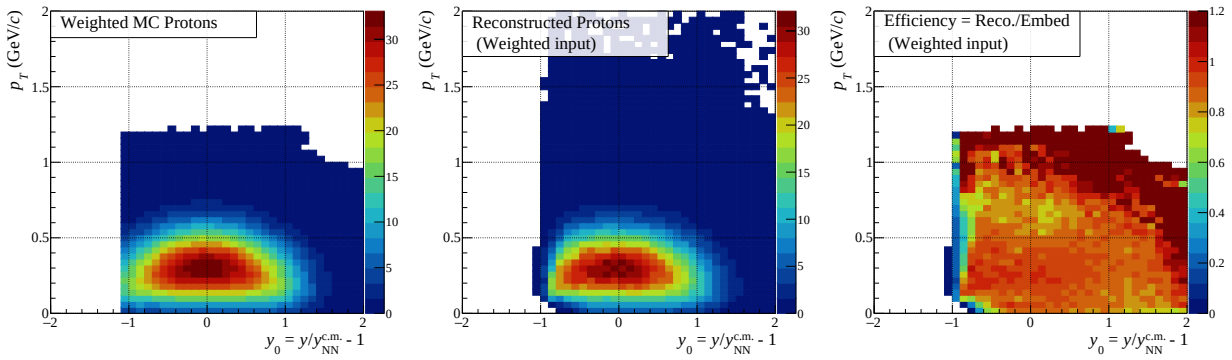

(a) $f_{\text{init}}(y_0, p_T, w)$. (b) $f_{\text{reco}}(y_0, p_T, w)$. (c) $f_{\text{reco}}/f_{\text{init}}$ with weights.

Figure 4.39: Example of the first iterative correction with weighting the initial distribution by the raw p_T vs. y_0 phase space of protons in central ^{132}Sn + ^{124}Sn collisions. (a): the initial phase space of the weighted Monte Carlo protons. (b): the reconstructed phase space. (c): the ratio of $f_{\text{reco}}/f_{\text{init}}$ as a kind of the efficiency function.

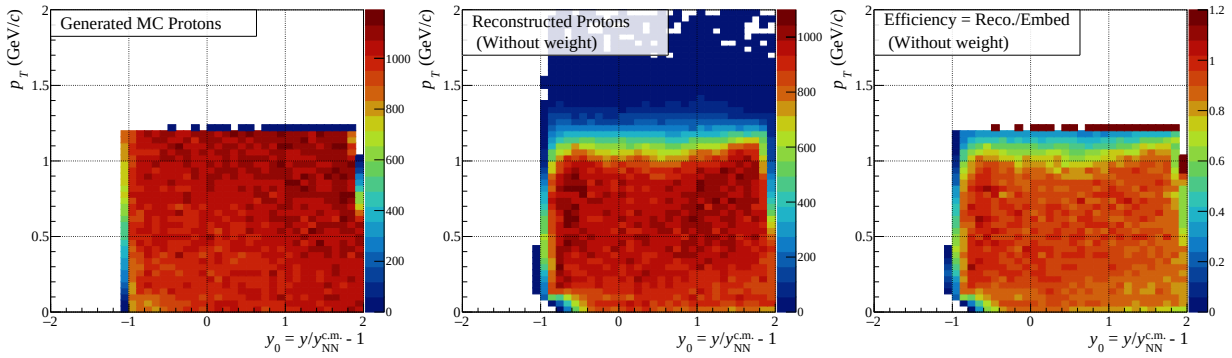

(a) $f_{\text{init}}(y_0, p_T, w = 1)$. (b) $f_{\text{reco}}(y_0, p_T, w = 1)$. (c) $f_{\text{reco}}/f_{\text{init}}$ with $w = 1$.

Figure 4.40: Same as Fig. 4.39 but the simulated tracks are not weighted (always $w = 1$).

3. With weighting the initial tracks according to their p_T-y_0 bin, the initial and reconstructed phase spaces, f_{init} and f_{reco}, and the correction function $C(y_0, p_T)$ are produced.

4. The corrected p_T vs. y_0 phase space is obtained by multiplying the $C(y_0, p_T)$ constructed in process 3 by the raw phase space. Since this corrected phase space is expected to provide a better approximation of the original phase space, it will be used as a new weighting factor in the next iteration step.

5. Processes 3 and 4 are iterated until the corrected phase space converges.

Figures 4.39 and 4.40 present two examples of the first iterative processes for protons embedded into central ^{132}Sn + ^{124}Sn collision events, with and without weighting the initial phase-space distribution, respectively. The calculated efficiency functions, obtained as $1/C(y_0, p_T)$, differ from each other, which indicates that the estimation of the correction function is influenced by the initial phase space distribution due to the bin smearing and shifting.

In fact, the correction function and the corrected phase space distributions were found to be well converged after two times iterations, as shown in Fig. 4.41. This means that the raw p_T vs. y_0 phase-space distributions are good approximation of the original spectra, partly because

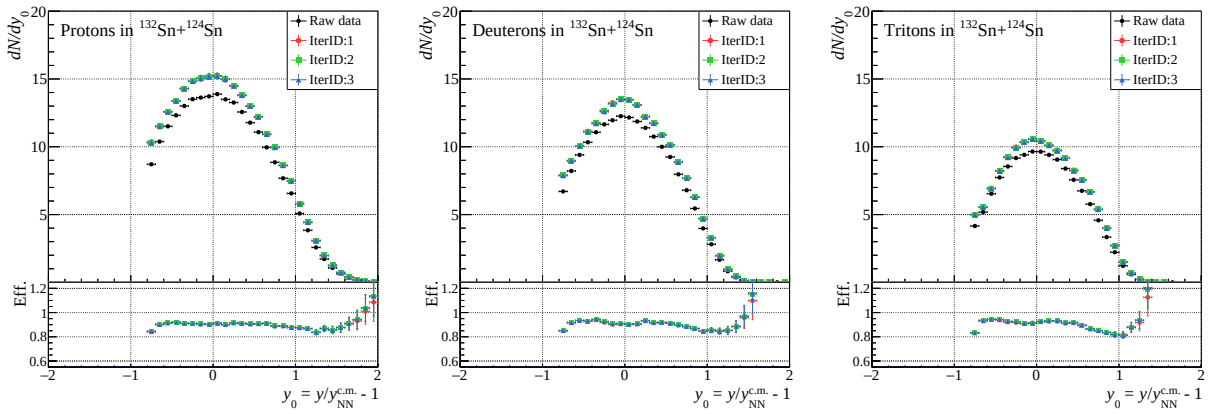

(a) Protons in ^{132}Sn + ^{124}Sn. (b) Deuterons in ^{132}Sn + ^{124}Sn. (c) Tritons in ^{132}Sn + ^{124}Sn.

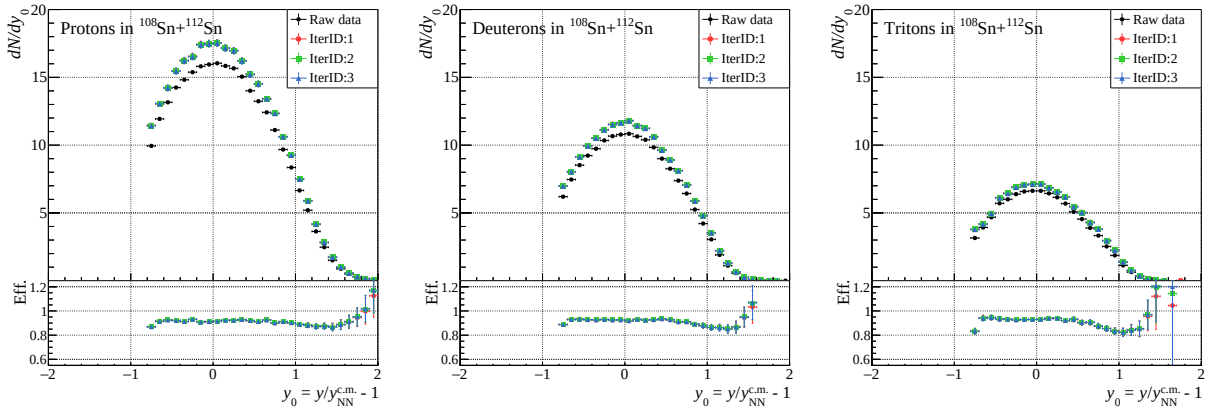

(d) Protons in ^{108}Sn + ^{112}Sn. (e) Deuterons in ^{108}Sn + ^{112}Sn. (f) Tritons in ^{108}Sn + ^{112}Sn.

Figure 4.41: Raw $\mathrm{d}N/\mathrm{d}y_0$ spectra of hydrogen isotopes in the two Sn + Sn systems (black circles) and those obtained in each iterative correction process (red, green, blue markers). In the bottom of the each panel, the efficiency functions as a function of scaled rapidity in each iteration are presented. They are almost converged in two times iterations (green boxes and blue triangles).

we restricted the azimuthal angle somewhat severely so that only tracks expected to be efficiently reconstructed were used in the real data analysis. The robustness of this iterative correction process was demonstrated well by varying the weighting factor for the initial phase space distribution in the first iteration. The identical correction functions were obtained after three times iterations when the initial distribution was uniform in the p_T vs. y_0 space (not weighted), and also when the initial distribution was broadened or narrowed in the y_0 axis and the p_T axis by 10% each.

Figure 4.42 presents the efficiency functions (as an inverse of the correction function) for hydrogen isotopes in central collisions of ^{132}Sn+^{124}Sn and ^{108}Sn+^{112}Sn systems. In the high-momentum domains, the efficiencies were found to be more than 100%, meaning that the number of tracks measured at a certain p_T-y_0 bin exceeds the actual number of particles in that bin. This overcounting can be happened due to the bin smearing effect and the exponential-like decreasing trend of the high-momentum tail component of the phase-space distribution. The overall reconstruction efficiencies were calculated as the ratio between integrated yields with and without correction, which resulted to be more than 90%, as shown in Table 4.17. For each hydrogen isotope, efficiencies in the ^{132}Sn + ^{124}Sn system are about 1% larger than the ^{108}Sn + ^{112}Sn system, which may be attributed to the difference in the geometrical acceptance between the two reactions. As is described in

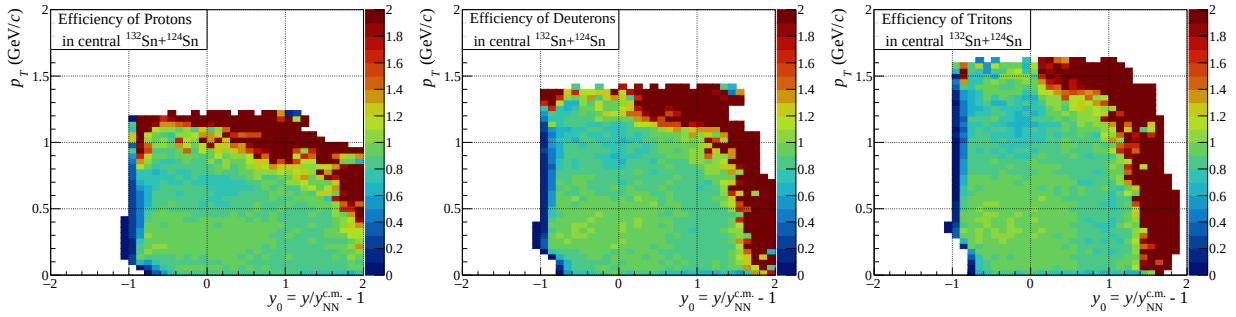

(a) Protons in ^{132}Sn + ^{124}Sn. (b) Deuterons in ^{132}Sn + ^{124}Sn. (c) Tritons in ^{132}Sn + ^{124}Sn.

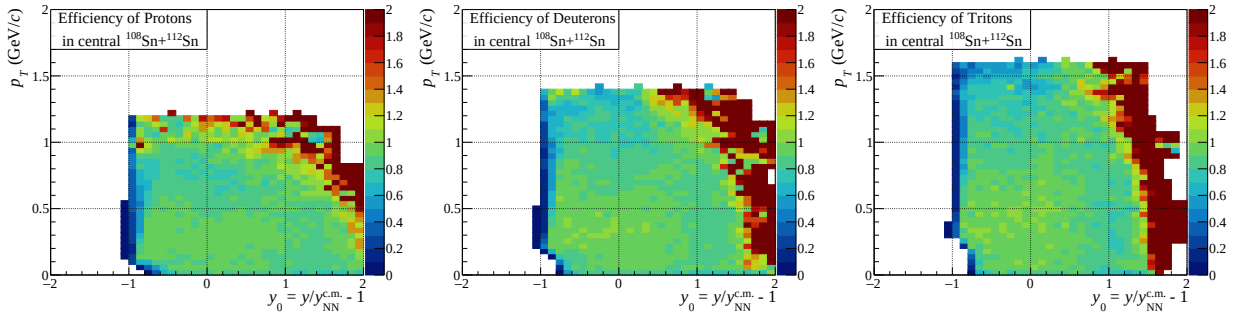

(d) Protons in ^{108}Sn + ^{112}Sn. (e) Deuterons in ^{108}Sn + ^{112}Sn. (f) Tritons in ^{108}Sn + ^{112}Sn.

Figure 4.42: Efficiency functions as a function of p_T-y_0 phase space for protons (left), deuterons (middle), and tritons (right) in central collisions of ^{132}Sn + ^{124}Sn (top) and ^{108}Sn + ^{112}Sn (bottom) systems.

Table 4.17: Overall efficiency of hydrogen isotopes in each reaction system. Given errors are statistical errors.

System	ϵ_p (%)	ϵ_d (%)	ϵ_t (%)
^{132}Sn + ^{124}Sn	90.1 ± 0.3	90.9 ± 0.3	90.9 ± 0.4
^{108}Sn + ^{112}Sn	91.3 ± 0.3	91.9 ± 0.4	91.8 ± 0.5

Sect. 4.5, the system dependence of the charged-particle multiplicity detected in the TPC reflects the projectile-target mass asymmetry. Therefore, the spatial ionized charge distribution inside the TPC active volume traversed by charged particles from reactions is also expected to depend on the reaction system, which can affect the track reconstruction efficiency.

4.8.3 Correction for energy loss in Sn target

The charged particles emitted from reactions experience the energy loss within the Sn target (ΔE_{target}). The energy loss depends on the initial momentum and on the thickness of the target material which is determined by the position of reaction vertices and the polar angle of emitted particles. In order to correct the measured momentum to the original momentum, the correction factor was deduced based on the calculation result of the LISE++ code. Figure 4.43 presents the momentum loss rate of hydrogen isotopes in the ^{124}Sn target as a function of initial momentum for different polar angles. Here, the reaction was assumed to happen always at the midpoint of

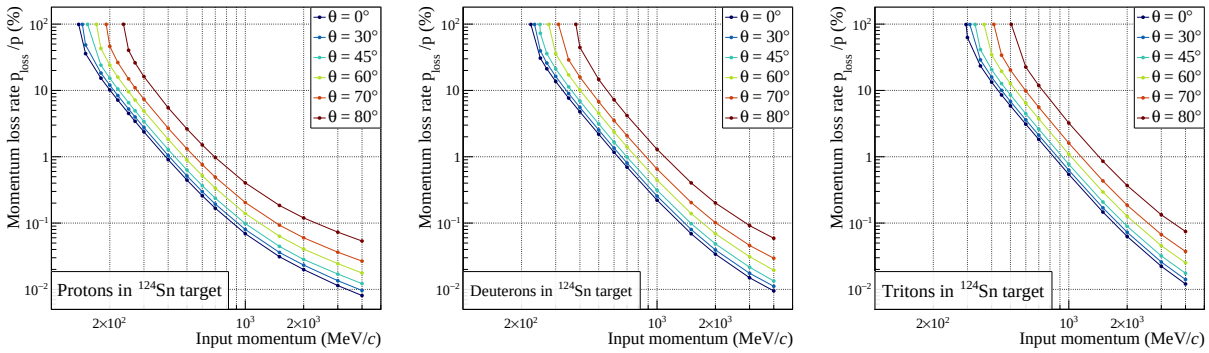

(a) Protons in ^{124}Sn target. (b) Deuterons in ^{124}Sn target. (c) Tritons in ^{124}Sn target.

Figure 4.43: The momentum-loss rate of hydrogen isotopes in the 280 mg/cm^2-thick solid ^{124}Sn as a function of initial momentum for different polar angles θ in the laboratory frame.

the Sn target, *i.e.*, the energy loss was calculated for the 304 mg/cm^2-thick (half of the employed thickness: 608 mg/cm^2) solid ^{124}Sn material. Since we optimized the thickness of the two Sn isotope targets so that the energy loss in each target becomes approximately identical, a similar result was obtained for the ^{112}Sn target, assuming the 280.5 mg/cm^2-thick solid ^{112}Sn material. The correction factor of the momentum magnitude can be calculated as $p_{\mathrm{init}}/p_{\mathrm{out}}$, where p_{init} is the initial momentum magnitude and $p_{\mathrm{out}} = p_{\mathrm{init}} - p_{\mathrm{loss}}$ is the momentum after passing through the target material. To consider the polar angle dependence, the two-dimensional map of the $\Delta E_{\mathrm{target}}$ correction function was constructed as a function of p_{out} vs. polar angle θ. For the measured track with a particular momentum p_{measure} and a polar angle $\theta_{\mathrm{measure}}$, the momentum magnitude was recalculated as $(p_{\mathrm{init}}/p_{\mathrm{out}})p_{\mathrm{measure}}$, where the correction factor $p_{\mathrm{init}}/p_{\mathrm{out}}$ is obtained by interpolating the two-dimensional correction function map toward the coordinate $(p_{\mathrm{measure}}, \theta_{\mathrm{measure}})$.

The left panel of Fig. 4.44 presents the efficiency-corrected $\mathrm{d}N/\mathrm{d}y_0$ distributions of protons in the ^{132}Sn + ^{124}Sn system with and without the $\Delta E_{\mathrm{target}}$ correction. Since this correction modifies the measured momentum toward a higher value, particularly for low-momentum and/or large polar-angle tracks close to the target rapidity domain, the yield at $y_0 < -0.5$ becomes lower and that at $y_0 > -0.5$ becomes higher oppositely. The right panel of Fig. 4.44 presents the $\Delta E_{\mathrm{target}}$ correction factors as a function of scaled rapidity for hydrogen isotopes in the two Sn + Sn systems, which were calculated as the yield ratio between before and after the correction. Although the correction largely affects the yield at negative scaled rapidity, it becomes approximately the order of 1% at the positive side. Thanks to the optimization of the Sn target thickness, the shown trends are similar for the two systems. In the present work, we calculated the $\Delta E_{\mathrm{target}}$ correction factors as an average with assuming the half-thickness of the Sn targets. The uncertainty of the $\Delta E_{\mathrm{target}}$ correction originating from the position fluctuation of reaction vertices within the Sn target will be considered as the systematic uncertainty in the $\mathrm{d}N/\mathrm{d}y_0$ spectra, see Sect. 4.9.

4.8.4 High-p_T contribution

Since the SπRIT TPC has a limitation in the p_T acceptance, high-p_T particles could not be measured. In order to extrapolate the acceptance toward the high-p_T domain and to evaluate its contribution to

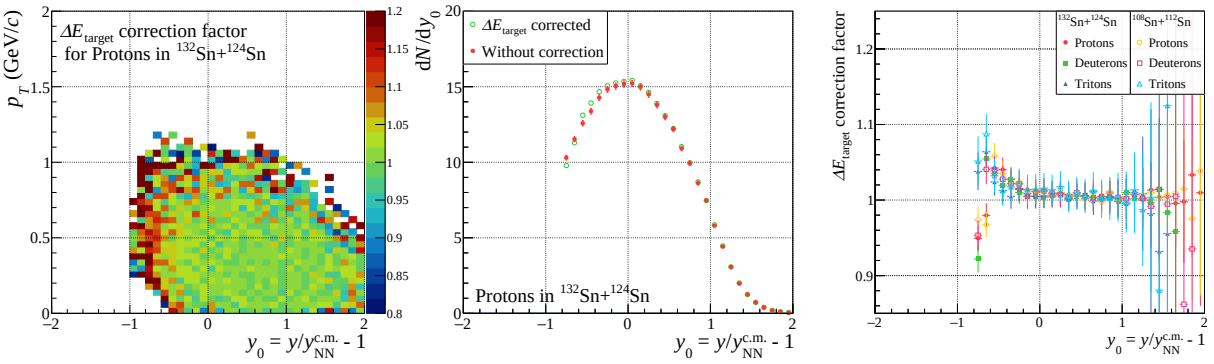

(a) p_T vs. y_0 correction factor for protons in the ^{124}Sn target.

(b) dN/dy_0 with (green) and without (red) corrections.

(c) Correction factor as a function of scaled rapidity.

Figure 4.44: The effect of the ΔE_{target} correction in the phase space. Note that the color axis of the panel (a) is limited to 0.8–1.2.

the dN/dy_0 yields, the invariant yields as a function of p_T were fitted by the following two kinds of empirical functions. One of them is a simple power-law function provided as:

$$\frac{1}{2\pi p_T}\frac{\mathrm{d}^2N}{\mathrm{d}p_T\,\mathrm{d}y_0} \propto e^{-p_T^n/c}, \tag{4.34}$$

where n and c are the fit parameters. As another function, we adopted the so-called blast wave formula [146], expressed as:

$$\frac{1}{2\pi p_T}\frac{\mathrm{d}^2N}{\mathrm{d}p_T\,\mathrm{d}y_0} \propto Ee^{-\gamma_r E/T}\left[\left(\gamma_r + \frac{T}{E}\right)\frac{\sinh\alpha}{\alpha} - \frac{T}{E}\cosh\alpha\right], \tag{4.35}$$

where E and p are the total energy and momentum of the particle in the center-of-mass frame, the Lorentz factor $\gamma_r = 1/\sqrt{1-\beta_r^2}$ with the radial flow velocity β_r, and $\alpha = (\gamma_r \cdot \beta_r \cdot p)/T$ with the thermal freeze-out temperature T. The radial flow velocity was fixed to 0.3, 0.23, and 0.16[2] for protons, deuterons, and tritons, respectively. Free fit parameters are a normalization and T. The invariant yields with a bin width of $\Delta y_0 = 0.1$ were well fitted by these functions (see Fig. 5.2 in the next chapter). The contribution from the high-p_T particles was evaluated by comparing the integral of fit functions:

$$\int \frac{1}{2\pi p_T}\frac{\mathrm{d}^2N}{\mathrm{d}p_T\,\mathrm{d}y_0} 2\pi p_T\,\mathrm{d}p_T\,, \tag{4.36}$$

for the full-p_T range and for the high-p_T range. The high-p_T ranges were taken as $p_T \geq 0.9\,\mathrm{GeV}/c$ for protons, $p_T \geq 1.2\,\mathrm{GeV}/c$ for deuterons, and $p_T \geq 1.4\,\mathrm{GeV}/c$ for tritons. As a result of both the power-law and blast-wave fits, the high-p_T contribution was found to be negligibly small for all rapidity bins, *i.e.*, the order of 0.1% of the dN/dy_0 yield in each rapidity bin at most. Since the fit functions are just empirical and the contribution to the yield from high-p_T particles is sufficiently small compared to other uncertainties, we ignored this high-p_T contribution. Namely, the dN/dy_0 distributions were constructed by integrating the corrected d^2N /dp_T dy_0 phase space along the p_T axis without any extrapolations.

[2]These β_r values were obtained by fits on p_T spectra at $|y_0| \leq 0.1$ bins, and treated as fixed parameters for other rapidity bins.

4.9 Evaluation of Systematic Uncertainties

In this section, the systematic uncertainties in the $\mathrm{d}N/\mathrm{d}y_0$ spectra of hydrogen isotopes and those in their spectral ratios are evaluated. Table 4.18 lists the source of uncertainties investigated here. For each source and each variation of the condition, $\mathrm{d}N/\mathrm{d}y_0$ spectra and their ratios were constructed and compared with the spectra constructed with the default set of conditions, see a number of figures in Appendix E. The bin-by-bin deviation from the default spectrum was calculated as a relative residual function, $\delta X_{\mathrm{syst.}}(y_0) = \left(X_{\mathrm{syst.}} - X_{\mathrm{def.}}\right)/X_{\mathrm{def.}}$, where $X_{\mathrm{syst.}}$ and $X_{\mathrm{def.}}$ indicate a spectrum with varied conditions and that with the default ones, respectively. To determine how to assign each uncertainty, the constructed $\delta X_{\mathrm{syst.}}(y_0)$ were categorized by three types of situations where (1) the residuals correlate with the scaled rapidity, and (2) the residuals deviate independently with the scaled rapidity. For each type, we evaluated the systematic uncertainties as follows:

(1) y_0-correlated uncertainty When the $\delta X_{\mathrm{syst.}}(y_0)$ shows a correlation depending on scaled rapidities, the bin-by-bin residual values as a y_0-correlated uncertainty were assigned to each bin of the spectrum. To avoid the bin-by-bin fluctuation, the smeared $\delta X_{\mathrm{syst.}}(y_0)$ was used.

(2) y_0-uncorrelated uncertainty When the $\delta X_{\mathrm{syst.}}(y_0)$ just deviates independent to scaled rapidities, a single value as a y_0-uncorrelated uncertainty was assigned to all bins of the spectrum. As the y_0-uncorrelated uncertainty, the root-mean-square of the relative residual distribution was adopted. Here, the residual distribution was constructed from $\delta X_{\mathrm{syst.}}$ values of each rapidity bin which were weighted by the squared inverse of the statistical uncertainty of the $\mathrm{d}N/\mathrm{d}y_0$ spectra, *i.e.*, $w = 1/\delta^2_{\mathrm{stat.}}$.

Table 4.18: List of items considered in evaluating the systematic uncertainties.

Items	Default condition	Variations to check systematics
Data set	Full data set	Halved data sets.
Central collision	$b_0 < 0.15$	M_c threshold variation by ± 1.
d_{POCA} cut	$d_{\mathrm{POCA}} < 20\,\mathrm{mm}$	$d_{\mathrm{POCA}} \leq 14\,\mathrm{mm}$ and $d_{\mathrm{POCA}} \leq 26\,\mathrm{mm}$.
n_{Cluster} cut	$n_{\mathrm{Cluster}} \geq 15$	$n_{\mathrm{Cluster}} \geq 9$ and $n_{\mathrm{Cluster}} \geq 21$.
ϕ angle cut	$-30° \leq \phi \leq 20°$	$-24° \leq \phi \leq 14°$ and $-36° \leq \phi \leq 26°$.
PID gate	Selection by mass	Mass gate width variation by $\pm 10\%$.
Particle probability	Gaussian probability	Probability by Voigt function
$\Delta E_{\mathrm{target}}$ correction	Half target thickness	No or full target.

4.9.1 Treatment of each systematic uncertainty

Here, assigned types of systematic uncertainties for each source are described. The $\mathrm{d}N/\mathrm{d}y_0$ spectra and their spectral ratios (single and double d/p and t/p ratios) constructed with the varied conditions, as well as the residual functions are presented in Appendix E. The obtained uncertainties are summarized in Tables 4.20 and 4.21 in the following section.

Systematic uncertainty due to data set As far as we analyzed the data, parameters and reconstructed quantities seem to be reasonably stable throughout each measurement. A possible uncertainty originating from the stability of the data was estimated by comparing the result using the full set of data and that using the halved sets of data. The relative residual functions were found not to correlate with scaled rapidities (as seen in Fig. E.1), and therefore, the y_0-uncorrelated uncertainty was assigned to the spectra.

Systematic uncertainty due to the track-multiplicity requirement In default, we selected central collision events with $b_0 < 0.15$ of the scaled impact parameter. As described in Sect. 4.6, the uncertainty in the determination of the scaled impact parameter approximately corresponds to a variation of the high multiplicity requirements by ±1. Table 4.19 lists the relationship between respective multiplicity thresholds and corresponding upper limits of the scaled impact parameter. A higher multiplicity requirement can select more central collision events and vice versa. As is presented in Figs. E.2(a)–E.2(f), the yields of hydrogens are enhanced in the midrapidity domain ($y_0 \sim 0$) and lowered in the high-rapidity domain ($y_0 > 1$) in the higher-multiplicity event selection, *i.e.*, a strong stopping. The opposite trend is observed in the lower-multiplicity selection. Thus, the y_0-correlated uncertainty was assigned to the $\mathrm{d}N/\mathrm{d}y_0$ spectra. As for single and double spectral ratios, the deviation does not correlate with the scaled rapidity, and the y_0-uncorrelated uncertainties were assigned.

Table 4.19: The scaled impact parameter b_0 variations with respect to the minimum charged-particle multiplicity requirement for selecting central collision events.

	The variation of multiplicity thresholds from default						
System	-3	-2	-1	0 (default)	+1	+2	+3
^{132}Sn + ^{124}Sn	0.2082	0.1864	0.1647	0.1436	0.1235	0.1049	0.0877
^{108}Sn + ^{112}Sn	0.2169	0.1935	0.1703	0.1480	0.1268	0.1072	0.0889

Systematic uncertainty due to the d_{POCA} cut and n_{Cluster} cut The track quality assignments on d_{POCA} and n_{Cluster} were varied by $d_{\mathrm{POCA}} \leq 14\,\mathrm{mm}$ and $d_{\mathrm{POCA}} \leq 26\,\mathrm{mm}$, and by $n_{\mathrm{Cluster}} \geq 9$ and $n_{\mathrm{Cluster}} \geq 21$. The systematic variations of $\mathrm{d}N/\mathrm{d}y_0$ spectra were found to be y_0-correlated for the ^{132}Sn + ^{124}Sn system but to be y_0-uncorrelated for the ^{108}Sn + ^{112}Sn system, as seen in

Figs. E.3(a)–E.3(f) and Figs. E.4(a)–E.4(f). In fact, this difference between the different systems was caused by an artificial reason in the correction procedure. By examining the residual functions with spectrum corrections and those without corrections, it was found that the difference originated from the position of primary vertices of embedded Monte Carlo tracks, which was slightly different for the two Sn + Sn systems. Eventually, the y_0-correlated uncertainty was assigned to the $\mathrm{d}N/\mathrm{d}y_0$ spectra of hydrogen isotopes in the ^{132}Sn+^{124}Sn system while the y_0-uncorrelated one was assigned to the same spectra in the ^{108}Sn + ^{112}Sn system. Also for the spectral ratios, the y_0-uncorrelated uncertainties were assigned.

Systematic uncertainty due to the azimuthal angle cut The azimuthal angle selection was varied as $-24° \leq \phi \leq 14°$ and $-36° \leq \phi \leq 26°$. As is presented in Fig. E.5, it was found that the residual functions show the y_0-uncorrelated deviation. The y_0-uncorrelated uncertainties were assigned to each spectrum.

Systematic uncertainty due to the PID gate The width of the mass gate for selecting each hydrogen isotope was varied by ±10% from the default ones. As shown in Figs. E.6(a)–E.6(f), a narrower gate width makes the yield smaller depending on the isotopes, and vice versa. In the d/p and t/p double spectral ratios, the variation is reasonably canceled, indicating that the widths of the mass spectra for each isotope are almost the same for the two reaction systems. Therefore, we assigned the y_0-correlated uncertainty to the $\mathrm{d}N/\mathrm{d}y_0$ spectra and the single ratios, while the y_0-uncorrelated uncertainty was assigned to the double ratios.

Systematic uncertainty due to the particle probability assignment In default, the probability that a particular track is the particle of interest was estimated by the Gaussian function fitted on the mass spectra. As an alternative estimation, a Voigt function was applied for calculating the probability. Since the Voigt function has a wider tail component compared to the Gaussian, the estimated contamination rate becomes larger. Therefore, the yields of respective hydrogen isotopes decrease by changing the fit function to the Voigt one, as seen in Fig. E.7. Because the system dependence and the mass number dependence of this systematic variation differ from each other, the y_0-correlated uncertainties were assigned to all kinds of spectra.

Systematic uncertainty due to the $\Delta E_{\mathrm{target}}$ correction The $\Delta E_{\mathrm{target}}$ correction assumes the half thicknesses of targets both for ^{112}Sn and ^{124}Sn. The systematic variations were estimated by assuming the two extreme cases: a zero thickness and a full thickness of Sn targets. From Fig. E.8, the y_0-correlated uncertainties were assigned to the $\mathrm{d}N/\mathrm{d}y_0$ spectra. For the spectral ratios, the variations are moderately canceled and the y_0-uncorrelated uncertainties were assigned.

4.9.2 Total systematic uncertainties

The total systematic uncertainty of the $\mathrm{d}N/\mathrm{d}y_0$ spectra of hydrogen isotopes and their single and double spectral ratios were calculated by the quadratic sum of each type of uncertainties bin by bin. Tables 4.20 and 4.21 summarize the systematic uncertainties assigned to the $\mathrm{d}N/\mathrm{d}y_0$ spectra

and those assigned to the spectral ratios, respectively. Note that the averaged values are shown for the y_0-correlated uncertainties, denoted by "Type A" in the table. The systematic uncertainties investigated in this work are canceled well in the double spectral ratios, compared to uncertainties in the $\mathrm{d}N/\mathrm{d}y_0$ spectra. The uncertainties in the single d/p and t/p spectral ratios are moderately the same order with the $\mathrm{d}N/\mathrm{d}y_0$.

Table 4.20: Systematic uncertainties in the $\mathrm{d}N/\mathrm{d}y_0$ spectra stemming from each variation. The column "Type" represents the type of uncertainty. The y_0-correlated and y_0-uncorrelated uncertainties are denoted by A and B, respectively. Note that the averaged values are presented in the case A, though the uncertainties are assigned to the dN/dy_0 spectra in bin by bin. The total systematic uncertainty ($\delta_{\mathrm{syst.}}$) is calculated by the quadratic sum of listed uncertainties. When the variation is categorized as the y_0-correlated uncertainty, where positive and negative uncertainties were separately assigned, larger absolute values were used to calculate the $\delta_{\mathrm{syst.}}$.

	Systematic uncertainties in the $\mathrm{d}N/\mathrm{d}y_0$ spectra (%)						
	^{132}Sn + ^{124}Sn			^{108}Sn + ^{112}Sn			
Items	p	d	t	p	d	t	Type
Data set	0.99	0.88	0.92	0.98	1.45	1.33	B
b_0 selection	$^{+0.36}_{-2.24}$	$^{+0.30}_{-1.95}$	$^{+0.63}_{-1.81}$	$^{+0.52}_{-2.05}$	$^{+0.66}_{-1.96}$	$^{+1.23}_{-1.99}$	A
d_{POCA} cut	$^{+1.25}_{-0.33}$	$^{+1.17}_{-0.30}$	$^{+1.31}_{-0.32}$	0.20	0.34	0.61	A/B
n_{Cluster} cut	$^{+1.04}_{0.22}$	$^{+0.80}_{-0.04}$	$^{+0.65}_{-0.11}$	0.41	0.25	0.23	A/B
ϕ angle cut	0.66	0.61	0.80	0.89	0.82	1.10	B
PID gate	$^{+0.26}_{-0.39}$	$^{+0.68}_{-1.07}$	$^{+0.78}_{-1.50}$	$^{+0.24}_{-0.34}$	$^{+0.67}_{-1.08}$	$^{+1.17}_{-1.72}$	A
Particle probability[a]	-0.85	-2.09	-3.18	-0.61	-1.61	-3.44	A
$\Delta E_{\mathrm{target}}$ correction	$^{+0.50}_{-0.81}$	$^{+0.39}_{-0.76}$	$^{+0.57}_{-1.04}$	$^{+0.49}_{-0.90}$	$^{+0.37}_{-1.01}$	$^{+0.84}_{-1.70}$	A
Total $\delta_{\mathrm{syst.}}$ (max)	3.25	3.61	4.51	2.73	3.40	5.01	

[a] For evaluating the systematic uncertainty stemming from the probability assignment, we adopted the Voigt function with a wider width compared to the Gaussian, which means that the contamination rate is evaluated to be larger than the default. Therefore, the variation of the $\mathrm{d}N/\mathrm{d}y_0$ spectra with the Voigt-based probability from the default spectra is always negative.

Table 4.21: List of systematic uncertainties in the single and double cluster-to-proton spectral ratios.

	Systematic uncertainties in the spectral ratios (%)						
Item	$(d/p)_{132}$	$(d/p)_{108}$	$(t/p)_{132}$	$(t/p)_{108}$	$DR_{d/p}$	$DR_{t/p}$	Type
Data set	1.02	1.90	1.36	1.45	1.87	1.60	B
b_0 selection	1.03	1.02	1.67	1.37	0.95	1.19	B
d_{POCA} cut	0.29	0.42	0.48	0.65	0.28	0.34	B
n_{Cluster} cut	0.52	0.33	0.57	0.34	0.26	0.26	B
ϕ cut	0.84	0.94	1.04	1.24	0.88	1.09	B
PID gate	$^{+0.42}_{-0.68}$	$^{+0.42}_{-0.73}$	$^{+0.23}_{-1.42}$	$^{+0.60}_{-1.66}$	0.18	0.54	A/B
Probability	-1.60	-1.23	-2.60	-2.89	-0.39	1.09	A
$\Delta E_{\mathrm{target}}$ correction	2.10	1.98	2.48	2.05	0.47	0.64	B
Total $\delta_{\mathrm{syst.}}$	3.25	3.44	4.60	4.62	2.39	2.69	

5 Results

Figure 5.1 presents the transverse momentum vs. scaled rapidity phase-space distributions of hydrogen isotopes in central ($b_0 < 0.15$) collisions of ^{132}Sn + ^{124}Sn and ^{108}Sn + ^{112}Sn systems at an incident energy of 270 MeV/nucleon. All corrections described in the previous sections are applied, *i.e.*, the azimuthal angle acceptance, the embedding-based correction, and the ΔE_{target} correction. A wide and seamless acceptance of the SπRIT TPC as well as its powerful identification capability enabled us to access a broad range of kinematical phase spaces of respective $Z = 1$ particles without any interpolations and extrapolations, except for the target rapidity region, which is a great advantage compared to the previous studies [10, 12, 62].

Figure 5.2 presents the y_0-sliced invariant yields of hydrogen isotopes in the two Sn+Sn systems as a function of p_T, fitted by empirical fit functions described in Sect. 4.8.4. Both power-law and blast-wave fits give a good parametrization of the p_T spectra in a wide range of rapidities. The freeze-out temperature T can be deduced as a fit parameter of the blast-wave formula. In the midrapidity domain of $|y_0| \leq 0.1$, $T \simeq 32.4$ MeV and 35.8 MeV for protons, $T \simeq 44.6$ MeV and 44.8 MeV for deuterons, and $T \simeq 50.8$ MeV and 54.3 MeV for tritons in the ^{132}Sn + ^{124}Sn system and the ^{108}Sn + ^{112}Sn system, respectively. Here, these values are given as averages of T parameters obtained by varying the p_T range of the fitting for each spectrum. The mass-number dependence is at least consistent with that reported in Ref. [146] which analyzed the p_T spectra of protons and deuterons from ^{96}Ru + ^{96}Ru and ^{96}Zr + ^{96}Zr collisions at 400 MeV/nucleon. Although the systematic investigation of the p_T invariant yield is also interesting, it is out of the main focus of this dissertation, and thus, we hand over its detailed physical discussion to a future investigation.

Figure 5.3 presents the p_T-integrated $\mathrm{d}N/\mathrm{d}y_0$ distributions of hydrogen isotopes in central collisions of the two Sn + Sn systems at $y_0 \geq -0.5$. The given errors are the quadratic sums of the statistical and systematic errors, assigned to the distribution point by point. The data points with uncertainties of the $\mathrm{d}N/\mathrm{d}y_0$ distributions are tabulated in Tables D.1–D.6. Each distribution is peaked at around $y_0 \sim 0$. The system dependence in the midrapidity yields are evident, *i.e.*, more

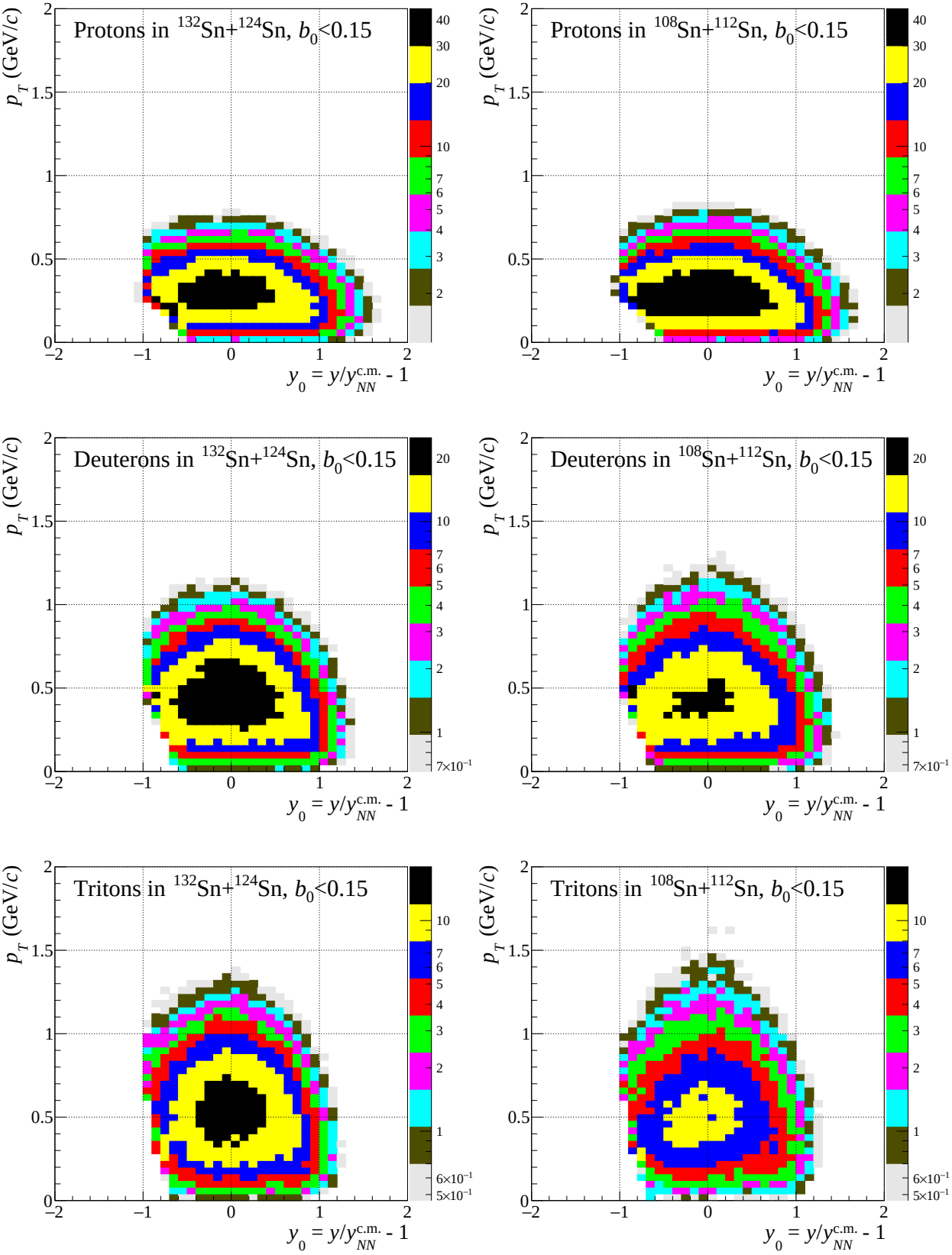

Figure 5.1: The differential yields $\mathrm{d}^2N\,/\mathrm{d}p_T\,\mathrm{d}y_0$ of hydrogen isotopes emitted in central ($b_0 < 0.15$) collisions of ^{132}Sn + ^{124}Sn and ^{108}Sn + ^{112}Sn systems at 270 MeV/nucleon. The distributions of protons, deuterons, and tritons are presented in top, middle, and bottom panels, respectively, with the ^{132}Sn + ^{124}Sn and ^{108}Sn + ^{112}Sn systems being shown in the left and right columns, respectively. The color tones correspond to the yields differing by a factor of 1.5. The maxima of the color axis are equalized for the two system, *i.e.*, 45 for protons, 25 for deuterons, and 18 for tritons.

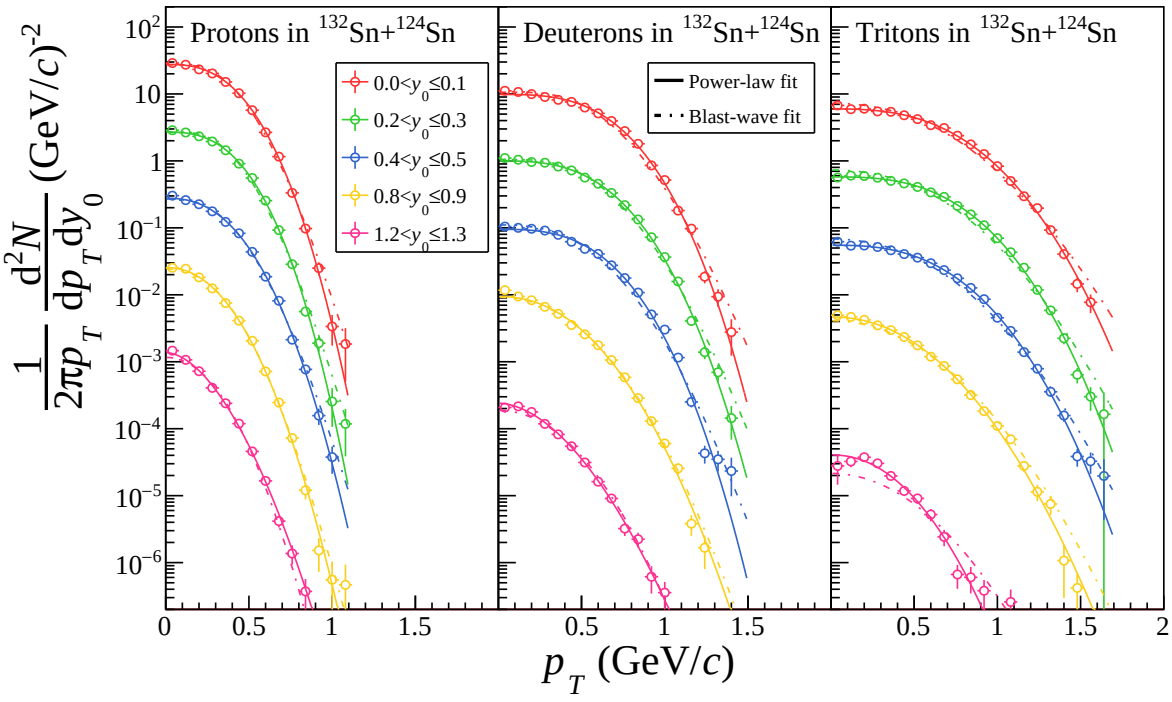

(a) Invariant yield of hydrogen isotopes in central ^{132}Sn + ^{124}Sn collisions.

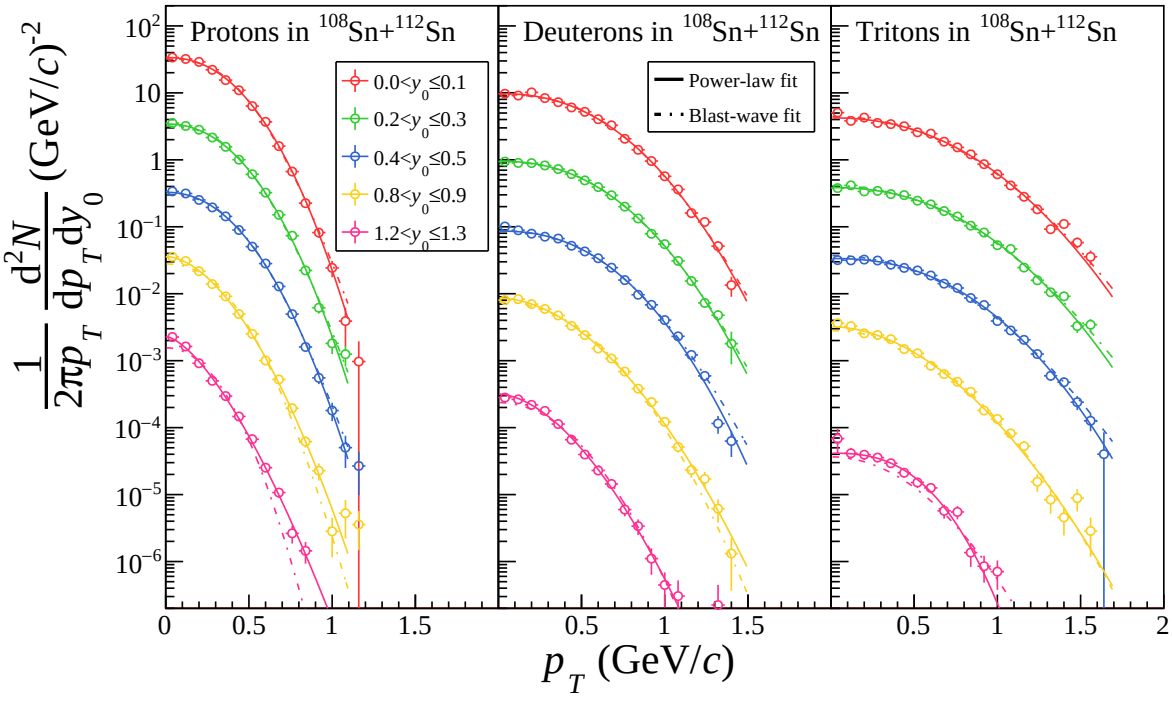

(b) Invariant yield of hydrogen isotopes in central ^{108}Sn + ^{112}Sn collisions.

Figure 5.2: Invariant yields of hydrogen isotopes in central collisions of the ^{132}Sn + ^{124}Sn system (top) and the ^{108}Sn + ^{112}Sn system (bottom). Each spectra are scaled by a factor of 10^{-1} for a visibility. Note that the assigned error bars indicate only statistical errors. The spectra are fitted with the empirical power-law function (solid lines) and the blast-wave formula (dotted lines).

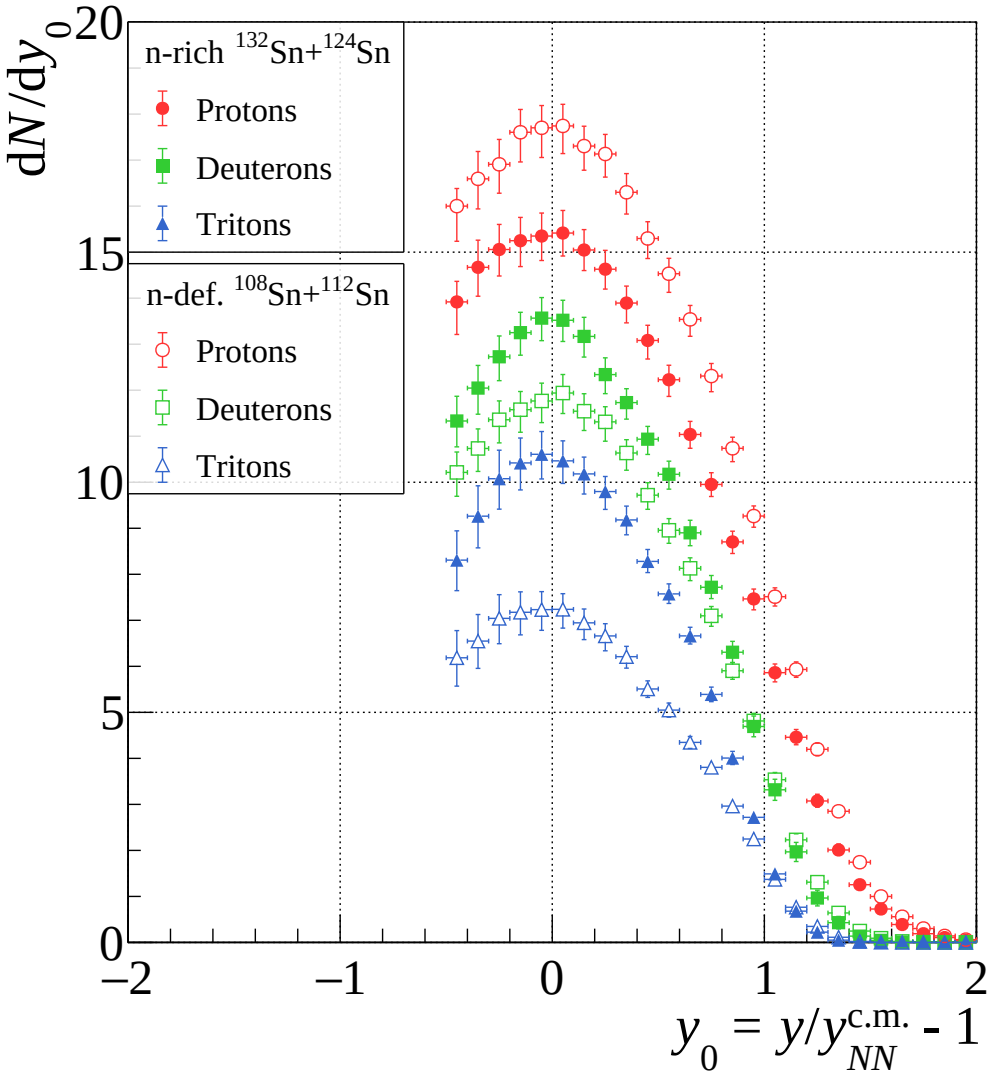

Figure 5.3: $\mathrm{d}N/\mathrm{d}y_0$ distributions of hydrogen isotopes in central ($b_0 < 0.15$) collisions of ^{132}Sn + ^{124}Sn and ^{108}Sn + ^{112}Sn systems at 270 MeV/nucleon. The rapidity range of the distributions is limited to $y_0 \geq -0.5$. The filled markers indicate protons (red circles), deuterons (green squares), and tritons (blue triangles) in the ^{132}Sn + ^{124}Sn system, while the opened markers indicate those in the ^{108}Sn + ^{112}Sn system. The vertical error bars include the statistical and systematic errors, and the horizontal ones indicate the bin width.

tritons and less protons are produced in the neutron-rich ^{132}Sn + ^{124}Sn system compared to the neutron-deficient ^{108}Sn + ^{112}Sn system. This is naturally due to the isospin-asymmetry dependence in different Sn + Sn systems.

Although the $\mathrm{d}N/\mathrm{d}y_0$ distributions seem to be nearly symmetric with respect to the NN midrapidity coordinate of $y_0 = 0$, they are found not to be perfectly symmetric. Figure 5.4 presents the ratio of the $\mathrm{d}N/\mathrm{d}y_0$ distribution to that with the y_0 sign being inverted:

$$R^{\pm y_0} = \frac{\mathrm{d}N_i/\mathrm{d}y_0}{\mathrm{d}N_i/\mathrm{d}(-y_0)}, \qquad (i = p, d, t). \tag{5.1}$$

If the $\mathrm{d}N/\mathrm{d}y_0$ are symmetrical about the $y_0 = 0$ axis, the spectra $R^{\pm y_0}$ should be unity. In the neutron-rich ^{132}Sn + ^{124}Sn system, deuterons and tritons are consistent with unity within their

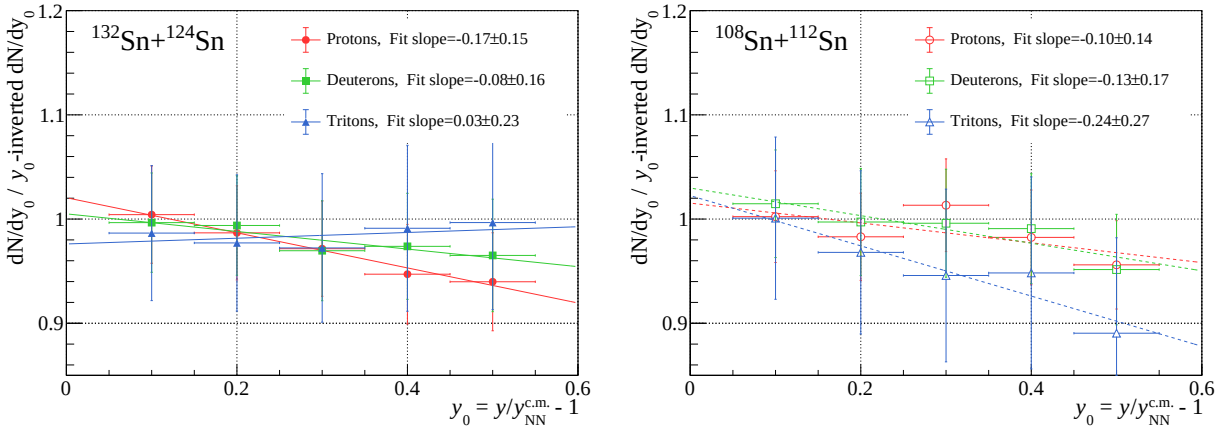

Figure 5.4: Spectral ratios of the $\mathrm{d}N/\mathrm{d}y_0$ distribution over the y_0-axis-inverted one for protons (red), deuterons (green), and tritons (blue) in the ^{132}Sn + ^{124}Sn (left) and the ^{108}Sn + ^{112}Sn (right) reactions. The spectra are fitted by linear functions, where the fitted slope values are presented in the legends.

uncertainties, but protons clearly show a negative slope differing from unity at $y_0 \geq 0.4$. On the other hand, in the neutron-deficient ^{108}Sn + ^{112}Sn system, protons and deuterons agree with unity within their uncertainties and tritons have a negative slope similarly with protons in the neutron-rich system. Such a forward-backward asymmetry implies that the system is not fully equilibrated after the collision. We also fitted linear functions to the $R^{\pm y_0}$ spectra to study the degree of asymmetry, where the fit results are shown in the figure. The obtained slopes are found to have a dependency on the mass of isotopes oppositely in each system, *i.e.*, the slope increases in the order of protons, deuterons, and tritons in the ^{132}Sn + ^{124}Sn system, and vice versa in another system. Understandably, this tendency is associated with the difference in the neutron content between projectile and target nuclei. In the ^{132}Sn + ^{124}Sn system, the projectile nucleus is more neutron rich than the target, and therefore the system tends to produce neutron-rich isotopes in the forward rapidity region. The observed asymmetry in the $\mathrm{d}N/\mathrm{d}y_0$ distributions possibly due to the asymmetry and imperfect equilibration between projectile and target nuclei will be also discussed later in the next chapter using spectral ratio observables, in relevant to the isospin mixing. As a whole trend of the asymmetry, both systems show negative slopes of $R^{\pm y_0}$ spectra, which is related to peak positions of the $\mathrm{d}N/\mathrm{d}y_0$ distributions also discussed later. Owing to the forward-backward asymmetry, one cannot simply extrapolate the $\mathrm{d}N/\mathrm{d}y_0$ distribution toward the target rapidity domain with assuming the reflection symmetry. It may be interesting to use the projectile-target flipped reactions, *e.g.*, ^{124}Sn + ^{112}Sn and ^{112}Sn + ^{124}Sn systems, to obtain some hint to deeply understand the whole shape of rapidity distributions in asymmetric heavy-ion collisions.

Table. 5.1 summarizes the integrated yields of hydrogen isotopes emitted in the positive scaled rapidity domain of $y_0 \geq 0$ and their ratios. The total forward hydrogen ($Z = 1$) yields in the two systems agree with each other within uncertainties, approximately 32, which amounts to 64–65% of the projectile charge. This means that nearly the same portion of protons are isolated as single protons from the system to constitute $Z = 1$ particles, and just the fraction of neutrons taken along by the single protons is different in the two systems. The observed agreement of forward $Z = 1$ yields in the ^{132}Sn + ^{124}Sn and ^{108}Sn + ^{112}Sn systems is not necessarily trivial since it is not clear how the yield depends on the system characteristics, *e.g.*, the neutron-number difference. However, investigating a systematic transition of the isotope abundance may be also informative for

Table 5.1: Hydrogen isotope yields integrated for the positive scaled rapidity region ($y_0 \geq 0$). Errors include the statistical and systematic uncertainties in the quadratic sum.

	Yields of hydrogen isotopes integrated at forward region of $y_0 \geq 0$.			
System	Forward p	Forward d	Forward t	Forward $Z = 1$
^{132}Sn + ^{124}Sn	13.96 ± 0.61	10.64 ± 0.53	7.67 ± 0.33	32.26 ± 0.87
^{108}Sn + ^{112}Sn	16.85 ± 0.58	9.81 ± 0.41	5.36 ± 0.22	32.02 ± 0.74
$R_{132/108}$	0.83 ± 0.03	1.08 ± 0.05	1.43 ± 0.06	1.01 ± 0.03

	Integrated cluster yields relative to protons at $y_0 \geq 0$.	
System	d/p	t/p
^{132}Sn + ^{124}Sn	0.76 ± 0.04	0.55 ± 0.02
^{108}Sn + ^{112}Sn	0.58 ± 0.02	0.32 ± 0.01
$DR_{132/108}$	1.31 ± 0.08	1.73 ± 0.10

understanding the clusterization property in heavy-ion collisions, such as the excitation function of the clustered proton fraction discussed in Ref. [62]. It is worth mentioning that the doubled forward yields of respective hydrogen isotopes in central ^{132}Sn + ^{124}Sn collisions ($A = 256$ and $N/Z = 1.56$) are consistent with those in a similar system of central ^{129}Xe+CsI collisions ($A \simeq 259$ and $N/Z \simeq 1.40$) at 250 MeV/nucleon measured by the FOPI Collaboration [62].

Figure 5.5 presents the deuteron-to-proton (d/p) and triton-to-proton (t/p) relative yields as a function of scaled rapidity in the ^{132}Sn+^{124}Sn and ^{108}Sn+^{112}Sn systems. Here, the cluster-to-proton relative yields are defined as:

$$d/p = \frac{\mathrm{d}N_d/\mathrm{d}y_0}{\mathrm{d}N_p/\mathrm{d}y_0}, \qquad t/p = \frac{\mathrm{d}N_t/\mathrm{d}y_0}{\mathrm{d}N_p/\mathrm{d}y_0}. \tag{5.2}$$

Their data points are tabulated in Tables D.7–D.10.

Figure 5.6 presents the d/p and t/p double spectral ratios as a function of scaled rapidity. Here, the cluster-to-proton double spectral ratios are defined and abbreviated as:

$$DR_{d/p} = \frac{d/p\left(^{132}\mathrm{Sn} + ^{124}\mathrm{Sn}\right)}{d/p\left(^{108}\mathrm{Sn} + ^{112}\mathrm{Sn}\right)}, \qquad DR_{t/p} = \frac{t/p\left(^{132}\mathrm{Sn} + ^{124}\mathrm{Sn}\right)}{t/p\left(^{108}\mathrm{Sn} + ^{112}\mathrm{Sn}\right)}. \tag{5.3}$$

Their data points are tabulated in Tables D.11 and D.12. It is noted that the double spectral ratios were constructed from the $\mathrm{d}N/\mathrm{d}y_0$ spectra without corrections because the correction effect was found to be canceled well by doubly taking the ratio, as described in Sect. 4.8. The spectral ratios will be discussed in comparison with the transport calculation, in the following chapter.

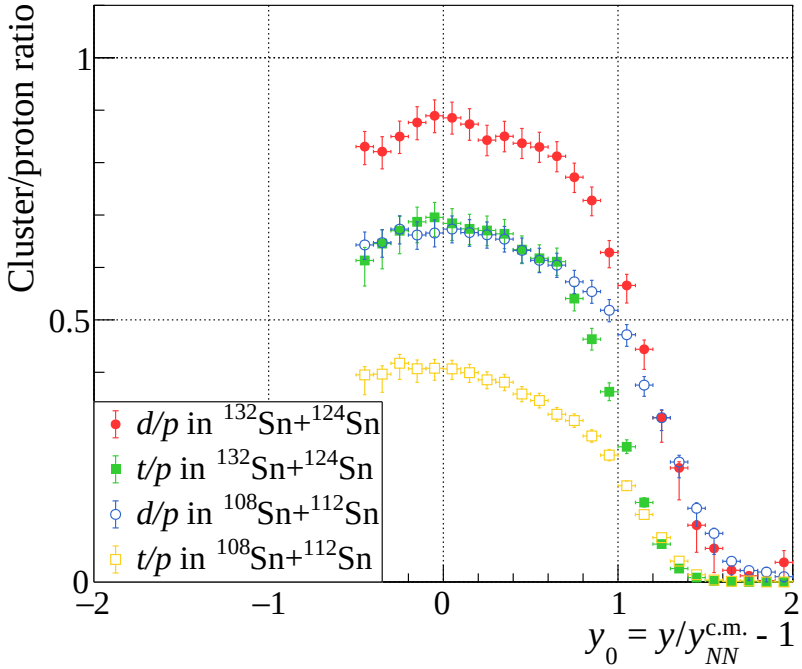

Figure 5.5: Single cluster-to-proton relative yields as a function of scaled rapidity in the two Sn + Sn systems.

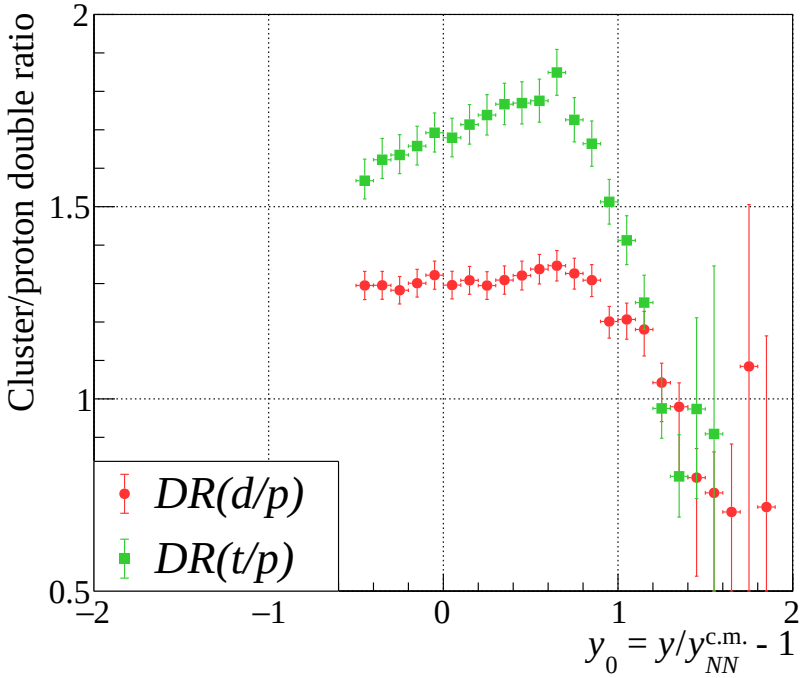

Figure 5.6: Double ratios of the cluster-to-proton relative yield in the ^{132}Sn + ^{124}Sn system over that in the ^{108}Sn + ^{112}Sn system.

6 Discussion

In this chapter, the isospin dynamics and the symmetry-energy effect in the measured central Sn+Sn collisions are discussed using the dN/dy_0 distributions of hydrogen isotopes and their spectral ratios, based on the AMD transport model calculation [17–20].

6.1 Discussion on the dN/dy_0 Distributions of Hydrogen Isotopes

At first, we attempt to obtain a clear view on the dN/dy_0 distributions by using the AMD model. A minimal description of the model is as follows, or, see supplementals in Appendix B.

Overview of the used AMD The AMD model used in this work is one of the latest versions from Ref. [20], in which refined cluster correlations were introduced, as partly described in Sect. 2.5. As an effective interaction, the Skyrme SLy4 force [219] is employed with the spin-orbit term omitted. The SLy4 parametrization provides the saturation properties of $J = 32.0\,\mathrm{MeV}$, $L = 46\,\mathrm{MeV}$, $\rho_0 = 0.160\,\mathrm{fm}^{-3}$, and $K_0 = 230\,\mathrm{MeV}$. As this slope parameter corresponds to a soft or moderate symmetry energy, we call the employed SLy4 force as "asy-soft" symmetry energy in the text. Another case of the density dependence of the symmetry energy ("asy-stiff") is obtained by modifying the density-dependent term in the SLy4 parametrization, as described in Ref. [18]. The asy-stiff parametrization gives $L = 108\,\mathrm{MeV}$ without changing the other saturation properties. In the present work, we produced about 7000 events of ^{132}Sn + ^{124}Sn and ^{108}Sn + ^{112}Sn collisions at 270 MeV/nucleon with impact parameters distributed linearly in $0 \le b \le 1.5\,\mathrm{fm}$, for each option of calculations. It is noted that the impact parameter selected as event samples of $b_0 < 0.15$ in

the experimental data is expected not to be a sharp-cut b distribution but to have a tail component toward a higher impact parameter of $b \approx 3$ fm. To investigate effects from such semi-central events, we also tested calculations with three additional assumptions of the impact parameter distribution: (1) to be linear in $0 \leq b \leq 3$ fm, (2) to be flat in $0 \leq b \leq 3$ fm, and (3) to be a Gaussian distribution centered at $b = 1.5$ fm with $\sigma_b = 0.6$ fm. The results of each calculation on the spectral ratios were found to be consistent with each other within uncertainties in the calculations, and thus, we explicitly show only the calculation with $0 \leq b \leq 1.5$ fm in the following. Because the AMD solves the equation of motion in a nonrelativistic scheme, the momentum of each calculated particle was transferred to the NN center-of-mass frame by the Galilean transformation, and then, the rapidity in this frame was calculated to construct the scaled rapidity.

Calculated dN/dy_0 distributions Figure 6.1 presents comparisons of the $\mathrm{d}N/\mathrm{d}y_0$ distributions between the experimental data and the asy-soft calculations. Drawn by the blue dash-dotted lines indicate the result of calculations with the default set of parameters of Ref. [20]. It is clearly found that the calculated spectra are wider than the data for each isotope. Especially for deuterons and tritons, they are almost flat in the midrapidity domain. This observation insists on the need of a stronger particle (cluster) production mechanism at midrapidity, meaning that the nuclear stopping for $Z = 1$ particles in AMD seems to be slightly weak compared to the actual. Therefore, we should carefully investigate whether this shortage in the stopping affects the extraction of other physical information such as the density dependence of the symmetry energy.

We tested several variations of the NN cross section, to investigate its sensitivity to the width of the $\mathrm{d}N/\mathrm{d}y_0$ distribution, where the obtained $\mathrm{d}N/\mathrm{d}y_0$ distributions are shown in Fig. 6.2. In the default set of Ref. [20], the NN cross section in medium (σ^*_{NN}) is used, which was reduced from that in free space ($\sigma^{\mathrm{free}}_{NN}$), see Eq. B.15 and texts. As other scenarios of cross sections representing a stronger stopping, we carried out calculations with, *e.g.*, (1) $\sigma^{\mathrm{free}}_{NN}$, (2) two times $\sigma^{\mathrm{free}}_{NN}$, and (3) two times σ^*_{NN}. What we found in this investigation is as follows:

- Compared to the default calculation using σ^*_{NN}, the use of $\sigma^{\mathrm{free}}_{NN}$ didn't affect much on the shape of the $\mathrm{d}N/\mathrm{d}y_0$ distributions. On the other hand, the integrated yields for $A < 4$ particles decreased by about 12% but that of α particles increased by about 11%, as tabulated in Table 6.1. This is simply because the density-independent $\sigma^{\mathrm{free}}_{NN}$ may enhance cluster correlations especially at high density, where nucleons (or clusters) are frequently fed into correlated systems. In such an environment, nucleons and light clusters are likely to be quickly consumed to form heavier particles. Due to a quick growth of clusterized systems, the yield of alpha particles increased while those of light charged particles of $A < 4$ decreased.

- The use of $2\sigma^{\mathrm{free}}_{NN}$ reduced the RMS values of the $\mathrm{d}N/\mathrm{d}y_0$ distributions of each $A \leq 4$ particle. The yield of light charged particles follows the same trend as in the case of $\sigma^{\mathrm{free}}_{NN}$.

- The use of $2\sigma^*_{NN}$ reduced the RMS values of the $\mathrm{d}N/\mathrm{d}y_0$ distributions in the same order of the case of $2\sigma^{\mathrm{free}}_{NN}$. The yield of light charged particles is not largely influenced.

- For calculations with the asy-stiff symmetry energy, a similar trend was observed.

Based on this study, we employed the $2\sigma^*_{NN}$, in which the density dependence of the cross section is also respected. As drawn by the green dotted lines in Fig. 6.1, the use of $2\sigma^*_{NN}$ increases the

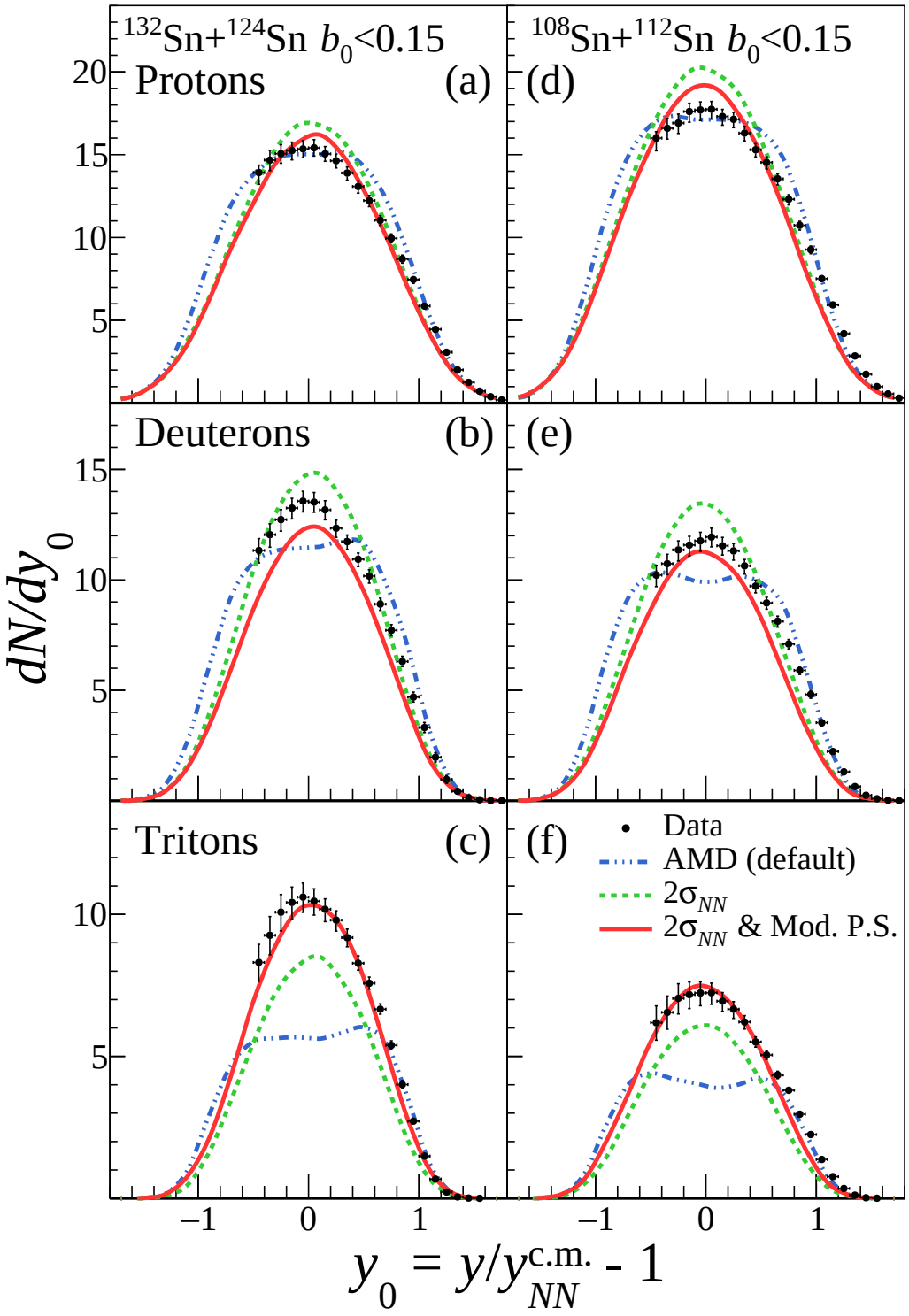

Figure 6.1: Rapidity distributions of (a) protons, (b) deuterons, and (c) tritons in central collisions of ^{132}Sn+^{124}Sn system, and those for ^{108}Sn + ^{112}Sn system (d-f), compared with the AMD calculations. Black filled circles indicate the experimental data, which are same as Fig. 5.3. Three types of colored lines indicate the AMD predictions with different set of parameters: the default set of parameters of Ref. [20] (blue dash-dotted lines), the same but for the two times σ^*_{NN} (green dotted lines, labeled as $2\sigma_{NN}$), and both increased σ^*_{NN} and the modified bound phase space for clusters (red solid lines, labeled as $2\sigma_{NN}$ & Mod. P.S.); see the text for details. The uncertainties in AMD calculations, which are not presented explicitly, are an order of 1% derived from the calculated event statistics. Adapted from Ref. [23].

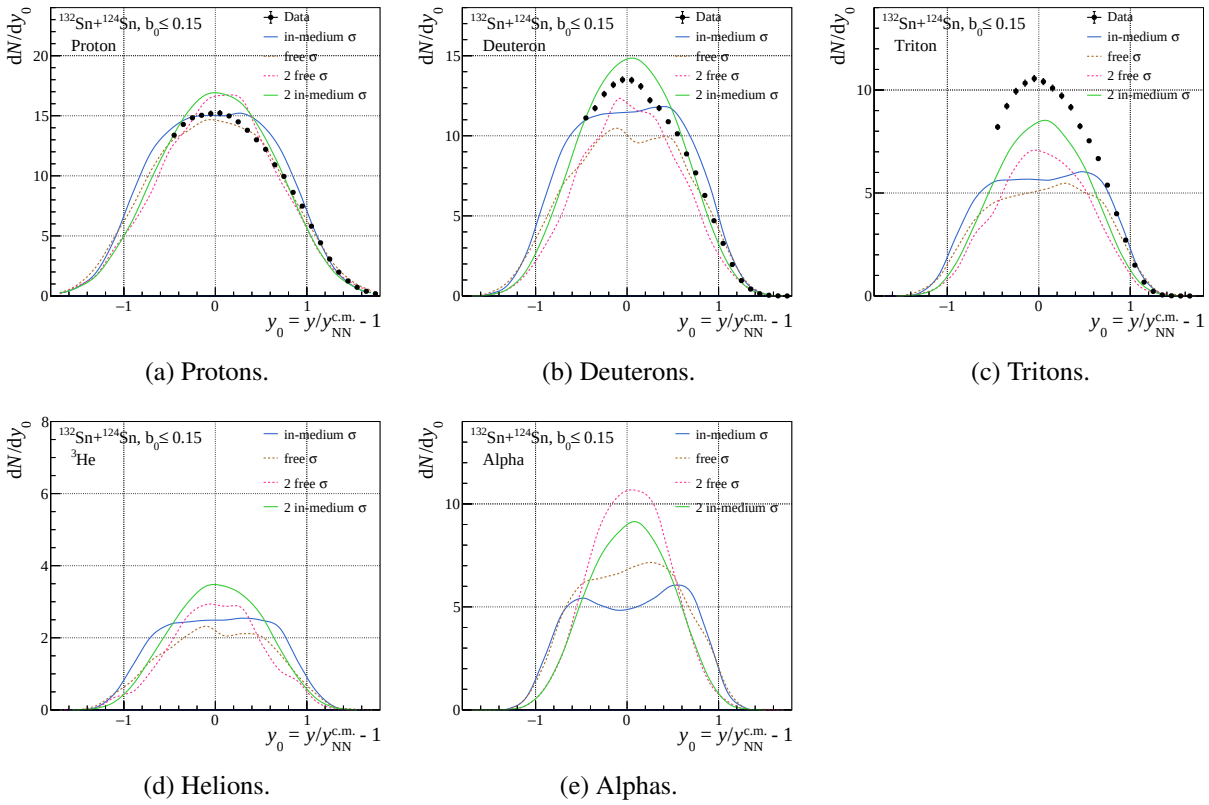

(a) Protons. (b) Deuterons. (c) Tritons.

(d) Helions. (e) Alphas.

Figure 6.2: $\mathrm{d}N/\mathrm{d}y_0$ spectra of $Z = 1, 2$ isotopes in the $^{132}\mathrm{Sn} + ^{124}\mathrm{Sn}$ system calculated with the four assumptions of NN cross sections and the asy-soft parametrization. Blue solid lines labeled by "in-medium σ" is the default assumption of Ref. [20], while other three are tested ones within this study. The use of the $\sigma_{NN}^{\mathrm{free}}$ and $2\sigma_{NN}^{\mathrm{free}}$ leads a smaller yield for $A < 4$ particles and a larger yield for α particle, see text.

yields at midrapidity, and the shape of distributions is now comparable to the experimental data.

After the increase of the in-medium NN cross section, the total yield of tritons was found to be still about 30% lower than the data. To find out how the final yield of tritons is determined, the time evolution of the triton multiplicity in the AMD was investigated. Then, tritons were found to be recognized sufficiently at approximately 40–50 fm/c from the start of the reaction. However, in the subsequent expansion phase, the multiplicity of tritons gradually decreases as the reaction time passed, while those of protons and deuterons exhibited a gradual increase simultaneously. This implies that some clusters are disintegrated somewhat easily under the mean-field propagation and/or under the low-energy NN collisions in the expanding system. Such fragility of light clusters can be attributed to the fact that the AMD treats the motion of nucleons and clusters in a classical way. The phase-space volume of classically bound clusters is not necessarily identical to a volume corresponding to a single quantum state [19]. To mitigate the loss of tritons, we introduced a modification factor into the correction term in the Hamiltonian, samely as the prescription given by Ref. [220], also see Appendix B.3. The parameters of the modification factor were optimized so that the bound phase space for the relative coordinate between a two-nucleon pair and another nucleon is enlarged to be approximately $(2\pi\hbar)^3$, where the parameters for the asy-soft calculations are listed in "term A" in Table 6.2. The volume of the original bound phase space can depend on the effective interaction implemented in the calculation, *i.e.*, the asy-soft or asy-stiff in this work. Therefore, in the case of the asy-stiff symmetry energy, we used the sum of the modification factor

Table 6.1: Integrated yields and root-mean-square (RMS) values of the $\mathrm{d}N/\mathrm{d}y_0$ distributions of $Z = 1, 2$ isotopes for different scenarios of the NN cross section. The results of the asy-soft calculation for the ^{132}Sn + ^{124}Sn system are presented.

	Integrated yields of $Z = 1, 2$ isotopes in ^{132}Sn + ^{124}Sn				
Cross section	p	d	t	^{3}He	α
Default (σ^*_{NN})	29.3	21.6	10.7	4.6	10.0
$\sigma^{\mathrm{free}}_{NN}$	27.4	18.0	9.2	3.6	11.3
$2\sigma^{\mathrm{free}}_{NN}$	26.9	17.1	9.2	3.8	12.4
$2\sigma^*_{NN}$	27.9	21.3	11.2	4.7	10.9
	RMS values of $\mathrm{d}N/\mathrm{d}y_0$ distributions of $Z = 1, 2$ isotopes				
Default	0.65	0.59	0.57	0.57	0.56
$\sigma^{\mathrm{free}}_{NN}$	0.67	0.60	0.57	0.56	0.53
$2\sigma^{\mathrm{free}}_{NN}$	0.62	0.53	0.48	0.48	0.42
$2\sigma^*_{NN}$	0.61	0.52	0.48	0.49	0.44

Table 6.2: Parameters used in the modifications for the bound phase space of $A = 2, 3$ light clusters. For details on each parameter, see Ref. [220] or Eqs. B.23–B.28 in Appendix B.3. "term A" is used for the asy-soft calculations. The sum of "term A" and "term B" is used in the asy-stiff calculations.

	ξ	a	$\hat{\xi}$	$\hat{a}$	$\bar{\xi}$	$\bar{a}$	g_0	σ	M	T_0
term A	2.0	0.6	2.0	0.2	1.0	1.2	1.0	0.25	3.0	8.2 MeV
term B							0.52	0.25	2.0	

with "term A" parameters and that with "term B" parameters so that the bound phase spaces of $A = 2, 3$ clusters also become approximately $(2\pi\hbar)^3$. Thanks to this modification, the binding energy of deuterons is reasonably reproduced in both the asy-soft and asy-stiff case. The red solid lines in Fig. 6.1 are the result of calculations with $2\sigma^*_{NN}$ and with the modified bound phase space for light clusters. Due to a slight enhancement of the triton productions, the yields of protons and deuterons are reduced a bit compared to calculations without the modification. As a whole, the $\mathrm{d}N/\mathrm{d}y_0$ distributions of hydrogen isotopes are reasonably reproduced.

Peak position of $\mathrm{d}N/\mathrm{d}y_0$ distributions When the peaks of $\mathrm{d}N/\mathrm{d}y_0$ distributions are compared between the experimental data and the theoretical calculation, they are found to be close to each other in the ^{108}Sn + ^{112}Sn system but to differ from each other in the ^{132}Sn + ^{124}Sn system. To extract the peak position, the $\mathrm{d}N/\mathrm{d}y_0$ distributions were fitted by a generalized Gaussian probability density function. Here, a common mean position of the generalized Gaussian, denoted by μ, was assumed for all hydrogen isotopes in each reaction. In the ^{108}Sn + ^{112}Sn system, the fit result gives $\mu \approx -0.021$ in the experimental data and $\mu \approx -0.020$ in the calculation. As naturally

expected, they are close to $y_{AA}^{\mathrm{c.m.}} \approx -0.014$ of the center-of-mass rapidity of the reaction system, if $\Delta\mu \approx 0.015$ of uncertainty in the fitting is taken into account. In the ^{132}Sn + ^{124}Sn system, the peak of calculated spectra is located at $\mu \approx 0.032$, consistent with $y_{AA}^{\mathrm{c.m.}} = 0.034$. However, the peak in the experimental data is found to be located at $\mu \approx -0.019$, which deviates significantly from $y_{AA}^{\mathrm{c.m.}}$ to the target rapidity side. The peak positions of each hydrogen isotope are found to be around the obtained common μ values in each reaction, differing from each other by about ± 0.01. Therefore, the deviation of peak positions from the center-of-mass rapidity in the ^{132}Sn + ^{124}Sn system is not likely related to isospin effects. This anomalous finding calls for a new systematic investigation both in theoretical interpretations and experimental confirmation in the future. The result on the flipped system, ^{112}Sn + ^{124}Sn and ^{124}Sn + ^{112}Sn systems, is to be waited for some information on the origin of the present finding.

6.2 Discussion on the Single Cluster/Proton Ratios

In the following, we mainly use the calculation with the optimized set of parameters: the doubled in-medium cross section and the modified bound phase space of clusters, for discussing the cluster-to-proton spectral ratio observables. Particularly, we concentrate on the midrapidity domain which is expected to mainly reflect the property in the high-density participant matter. The left panels of Fig. 6.3 present the d/p and t/p spectral ratios in the midrapidity domain of $|y_0| \leq 0.7$, compared to the AMD calculations. Here we give just simple arguments on the single ratios as follows:

- They have maxima at midrapidity and a decreasing trend toward positive and negative scaled rapidities, meaning that the $\mathrm{d}N/\mathrm{d}y_0$ spectral width is narrower for clusters compared to protons. This is expected to be partly due to the mass dependence in the velocity of particles with an assumption that they were emitted from the thermal source of the participant.
- The square of the d/p ratio was found to be approximately consistent with the t/p ratio. This may support an isoscaling property, *i.e.*, the isotopic yield can be expressed by an exponential form of the number of protons and neutrons in the isotope: $Y_i(Z,N) \propto \exp(\alpha Z + \beta N)$.
- If we postulate that the d/p and t/p ratios are proportional to the neutron distribution and its square, it is naturally understood that they reflect the neutron-number dependence, namely, the single ratios are larger in the neutron-rich system than the neutron-deficient one. A comparison of these "pseudo" neutrons to protons may be also interesting.

The system dependence relevant to the symmetry-energy effect will be discussed in the next section on the double ratio observables. As for the theoretical calculations, it is somewhat difficult to assign physical meanings to the calculated single cluster-to-proton ratios because they are highly sensitive to the fine adjustment of the bound phase space for light clusters. In the double ratio observables, however, it is expected that the robust part of the information can be efficiently extracted, *e.g.*, the isospin asymmetry dependence.

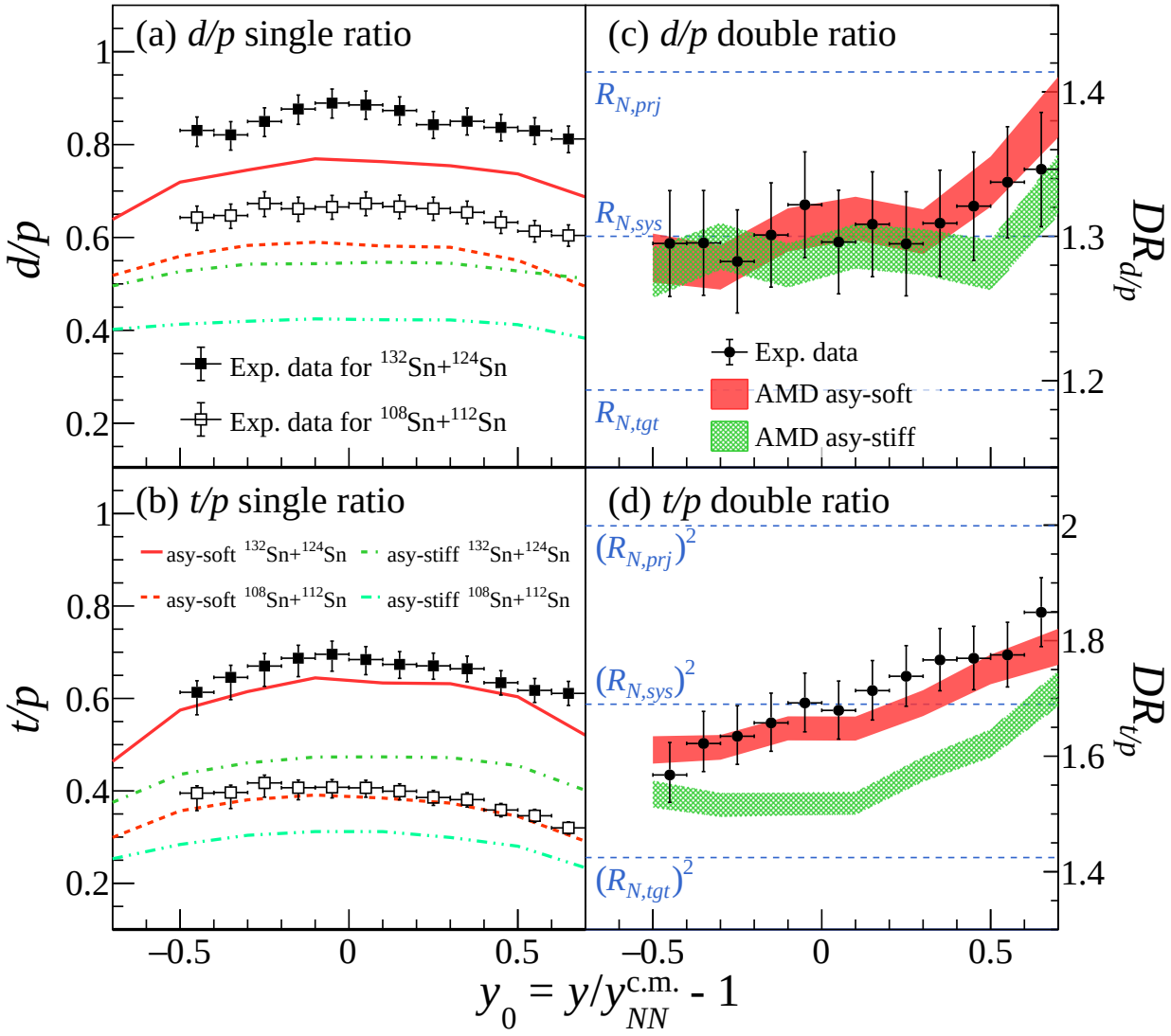

Figure 6.3: Single and double spectral ratios for d/p and t/p compared to the AMD calculations with the asy-soft and asy-stiff symmetry energies. The three blue dashed lines in the panel (c) indicate the neutron-number ratios of the neutron-rich system to the neutron-deficient system with respect to the projectile nuclei (upper line denoted with $R_{N,prj}$), target nuclei (lower line with $R_{N,tgt}$), and the total system (middle line with $R_{N,sys}$). In the panel (d), the blue dashed lines representing their squares: $\left(R_{N,prj}\right)^2$, $\left(R_{N,tgt}\right)^2$, and $\left(R_{N,sys}\right)^2$ are drawn. Note that the vertical-axis ranges of the panels (c) and (d) are scaled by the neutron-number ratios and their squares, respectively, for making it easy to understand that the t/p double ratio is more sensitive to the stiffness of the symmetry energy compared to the d/p double ratio, read the text for the details. Adapted from Ref. [23].

6.3 Discussion on the Double Cluster/Proton Ratios

In this section, we discuss the d/p and t/p double ratios ($DR_{d/p}$ and $DR_{t/p}$) in relevant to the isospin dynamics and the symmetry-energy effect in the high-density matter. The right panels of Fig. 6.3 present each DR compared to the AMD calculations. First, we discuss findings on the experimental data, and then, we discuss the result of comparisons with theoretical spectra.

6.3.1 Observation in the experimental double ratio

Neutron-number scaling at midrapidity As seen in panel (c) in Fig. 6.3, the value of $DR_{d/p}$ at $y_0 = 0$ agrees with the neutron-number ratio between the two reaction systems, $R_{N,sys} = N_{^{132}\mathrm{Sn}+^{124}\mathrm{Sn}}/N_{^{108}\mathrm{Sn}+^{112}\mathrm{Sn}} = 1.3$. Similarly, the value of $DR_{t/p}$ at $y_0 = 0$ agrees with the square of the neutron-number ratio, $\left(R_{N,sys}\right)^2$. These agreements lead to the relation: $\left(DR_{d/p}\right)^2 \simeq DR_{t/p}$, which can be interpreted as the scaling property in the light-cluster emission [154]. Such a scaling relation can be satisfied based on a simple expectation that the formation probability of deuterons or tritons is approximately proportional to ρ_n or ρ_n^2, respectively, with ρ_n being the neutron density at the coordinate where the cluster is produced. This neutron density is related to the original number of neutrons in the reaction system but can be modified by the effect from the symmetry energy. If the proton density in the two reaction systems is almost similar, the observation of $DR_{d/p} \simeq R_{N,sys}$ and $DR_{t/p} \simeq \left(R_{N,sys}\right)^2$ at $y_0 = 0$ indicates that the neutron-density ratio between the two reaction systems agrees with the neutron-number ratio, *i.e.*, $R_{\rho_n} = (\rho_n)_{^{132}\mathrm{Sn}+^{124}\mathrm{Sn}}/(\rho_n)_{^{108}\mathrm{Sn}+^{112}\mathrm{Sn}} \approx R_{N,sys}$. This relation means that the neutron density is affected by the symmetry energy, but the degree of the effect does not strongly depend on the two reaction systems, even though they have different isospin asymmetries. Therefore, this observation exhibits a weak symmetry-energy effect in the midrapidity source, and consequently, a soft symmetry energy can be expected.

Partial isospin mixing As is also presented in the figure, the experimental double ratios are settled within the specific range given by the number of neutrons in the projectile and target nuclei, written as $R_{N,tgt} < DR_{d/p} < R_{N,prj}$ and $\left(R_{N,tgt}\right)^2 < DR_{t/p} < \left(R_{N,prj}\right)^2$ within the shown rapidity range of $|y_0| \leq 0.7$, where $R_{N,tgt} = N_{^{124}\mathrm{Sn}}/N_{^{112}\mathrm{Sn}}$ and $R_{N,prj} = N_{^{132}\mathrm{Sn}}/N_{^{108}\mathrm{Sn}}$ represent the neutron-number ratios for target nuclei and projectile nuclei, respectively. The rapidity dependence of both double ratios shows a positive slope, which is clearly seen in $DR_{t/p}$, though it is hard to see in $DR_{d/p}$ due to large uncertainties. A non-zero slope indicates that the system is not equilibrated, and the difference of the projectile-target asymmetry between the two reactions is reflected in the rapidity dependence. As the $^{132}\mathrm{Sn} + ^{124}\mathrm{Sn}$ system has the neutron-rich projectile, the production of tritons relative to protons is enhanced in the forward rapidity region, and vice versa in the $^{108}\mathrm{Sn} + ^{112}\mathrm{Sn}$ system with the neutron-deficient projectile. It was found that the rapidity dependence of these double ratios at $y_0 \geq 0$ can be similarly parameterized as:

$$DR_{d/p} \simeq R_{N,sys} + \alpha_{d/p}\left(R_{N,prj} - R_{N,sys}\right)y_0, \tag{6.1}$$

$$DR_{t/p} \simeq \left(R_{N,sys}\right)^2 + \alpha_{t/p}\left(\left(R_{N,prj}\right)^2 - \left(R_{N,sys}\right)^2\right)y_0, \tag{6.2}$$

where α is a kind of the mixing coefficient. By the least square fits to the experimental $DR_{t/p}$ and $DR_{d/p}$ at $y_0 \geq 0$, $\alpha_{t/p} = 0.69 \pm 0.08$ and $\alpha_{d/p} = 0.71 \pm 0.34$ are deduced. If a perfect transparency or a full mixing is achieved in a collision, α should be 1 or 0, respectively. Therefore, the observed rapidity dependence of the double ratios can be interpreted as a partial isospin mixing in the colliding nuclei. The consistency between $\alpha_{d/p}$ and $\alpha_{t/p}$ may support that the degree of mixing also has a kind of neutron-number scaling property as is observed in the double ratios at midrapidity. Theoretically, the degree of the isospin mixing can be a probe of the neutron-proton effective-mass difference as well as the density dependence of the symmetry energy, as predicted in Ref. [153].

6.3.2 Symmetry energy investigation based on AMD

The theoretical double ratios with the two symmetry-energy stiffnesses are shown in the right panels of Fig. 6.3 by the red shaded (asy-soft) and green cross-stitching (asy-stiff) envelopes, where the vertical width represents the statistical error of calculations. The calculated results for both symmetry energy parametrizations also show the mixing property observed in the data. In particular, the asy-soft calculation reasonably reproduces the experimental data in the midrapidity domain. $DR_{t/p}$ is found to be more sensitive to the stiffness of the symmetry energy compared to $DR_{d/p}$, even if we simply postulate that the d/p and t/p are proportional to the ρ_n and ρ_n^2, respectively. Specifically speaking, in the right panels of Fig. 6.3, the symmetry-energy dependence in the t/p double ratio with the vertical-axis range scaled by R_N^2 is larger than that in the d/p double ratio scaled by R_N. This observation implies that tritons and deuterons are produced in a slightly different part of the system, which is understandable by the following reason. The symmetry energy influences the dynamics of the compressed system so that neutrons and protons are repelled from and attracted into the central high-density region of the system, respectively. This symmetry-energy effect decreases the n/p ratio in the central region and increases it in the outer surface region, depending on the stiffness of the symmetry energy and the isospin asymmetry of the system. According to the prediction in Ref. [125], the radial expansion velocity of the system shows approximately a linear dependence on the distance from the center, *i.e.*, the expansion dynamics along the radial direction is very simple and the effect on the n/p ratio in the compression phase is conserved also in the expansion phase when clusters start to be formed. Thus, the strong symmetry energy dependence in the theoretical $DR_{t/p}$ can be attributed to the fact that the tritons are dominantly produced in the central domain of the expanding system rather than the outer region. On the other hand, a weaker dependence in the theoretical $DR_{d/p}$ indicates that deuterons are produced in the outer region of the expanding system as much as in the central region so that the symmetry-energy effect suppressing the central n/p ratio (and therefore $DR_{d/p}$) is canceled by the effect enhancing the outer n/p ratio. In fact, by investigating the spatial position distributions of tritons and deuterons in the expanding system, it was found that tritons are likely to exist in the inner part of the system compared to deuterons, although the difference is very small.

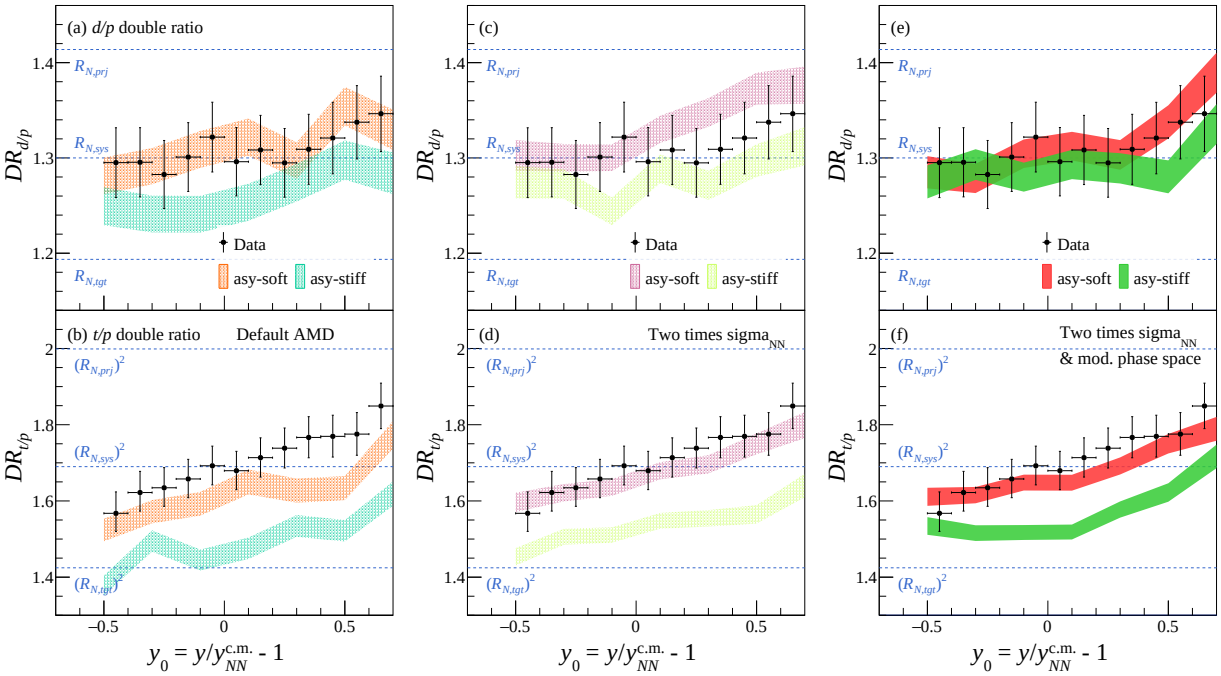

(a) Default AMD as of Ref. [20]. (b) $2\sigma^*_{NN}$. (c) $2\sigma^*_{NN}$ and modified phase space.

Figure 6.4: The systematic investigation on the parameter dependence in the cluster-to-proton double spectral ratios. The rightest panels (e) and (f) are identical to the right panels of Fig. 6.3. The leftest ones (a) and (b) are $DR_{d/p}$ and $DR_{t/p}$ with the default set of parameters of Ref. [20], respectively. Samely, the middle ones (c) and (d) are from calculations with the increased NN cross section, *i.e.*, $2\sigma^*_{NN}$.

6.3.3 Parameter dependence in the double ratios

Finally, we investigated the parameter dependence in the theoretical calculation to guarantee its robustness against the specific modifications employed in the present work. As presented in Fig. 6.4, theoretical $DR_{d/p}$ and $DR_{t/p}$ were also constructed from calculations with the two remaining cases of the parameter sets: the default one from Ref. [20] and that with $2\sigma^*_{NN}$. The differences of double ratios among the calculations using different parameter sets for a specific stiffness of the symmetry energy are consistent within the uncertainties of the experimental data in the midrapidity domain. And thus, the obtained conclusion on the stiffness of the symmetry energy does not depend critically on these parameter adjustments.

7

Concluding Remarks

In this dissertation, the rapidity distributions and spectral ratios of hydrogen isotopes emitted in central collisions of the neutron-rich ^{132}Sn + ^{124}Sn system and the neutron-deficient ^{108}Sn + ^{112}Sn system at 270 MeV/nucleon were investigated based on the AMD transport model, in relevant to the isospin dynamics and the symmetry-energy effect. This is the first systematic measurement of $Z = 1$ isotopes focusing on the isospin degrees of freedom in heavy-ion collisions with radioactive isotope beams at intermediate energies. The d/p and t/p double ratios at midrapidity were found to coincide with the neutron-number ratio between the two reaction systems and its squared value, respectively, which indicates a weak symmetry energy effect in the high-density participant. In addition, the rapidity dependence of the cluster-to-proton double ratios exhibited a partial isospin mixing between the two colliding nuclei. A strong sensitivity to the density dependence of the symmetry energy was found in the theoretical t/p double ratio in the midrapidity domain, while the d/p double ratio was weakly sensitive. This difference in the sensitivity may imply that deuterons and tritons were produced in a slightly different zone in the expanding system. In comparison to the AMD calculation, the experimental t/p double ratio favors the asy-soft parametrization of the symmetry energy corresponding to the slope parameter of $L = 46$ MeV rather than the asy-stiff one with $L = 108$ MeV.

Within the AMD model used in the present work, we confirmed that the applied adjustments on the two-nucleon cross section and on the bound phase space for $A = 2, 3$ clusters do not strongly influence the cluster-to-proton double ratios and their sensitivity to the symmetry-energy stiffness. However, the AMD is an almost unique approach that considers cluster correlations explicitly in the dynamical phase of reactions. Therefore, it is still important to estimate the theoretical uncertainties by comparing the results from different transport models, as has been done for the charged pion observables in Ref. [64]. The other transport models must follow the same procedure, namely, first to reproduce the $\mathrm{d}N/\mathrm{d}y_0$ distributions of $Z = 1$ isotopes and second to examine the spectral ratios, as the AMD did successfully with the modifications above.

In the neutron-rich mass-asymmetric ^{132}Sn + ^{124}Sn system, the peak positions of the $\mathrm{d}N/\mathrm{d}y_0$ distributions of hydrogen isotopes were found to deviate from the rapidity of the center of mass of the system ($y_{AA}^{\mathrm{c.m.}}$) to the target rapidity side, while the peak in the ^{108}Sn + ^{112}Sn system agreed with $y_{AA}^{\mathrm{c.m.}}$. In the calculated distributions, the peak is located close to the $y_{AA}^{\mathrm{c.m.}}$ in both systems. A slight artificial shift of the $\mathrm{d}N/\mathrm{d}y_0$ distributions is found not to affect much on the double ratios in the midrapidity domain and the statement on the high-density symmetry energy. The origin of this anomalous observation is not well understood, and therefore, it calls for further investigations.

In this thesis, we investigated the $\mathrm{d}N/\mathrm{d}y_0$ distributions and spectral ratios of $Z = 1$ isotopes emitted in central collisions of ^{132}Sn + ^{124}Sn and ^{108}Sn + ^{112}Sn systems, and the stiffness of the symmetry energy was discussed using the AMD code calculations. A future prospect relevant to the present work is as follows. It is first important to obtain a more complete set of data that can encompass the global character of heavy-ion collisions. Helium isotopes were also measured under nearly the same kinematical acceptance as that of $Z = 1$ isotopes. Therefore, as the data analysis progresses, the $\mathrm{d}N/\mathrm{d}y_0$ distributions, p_T invariant yields, and the collective flows of $Z = 1$ and $Z = 2$ isotopes can be extracted for the four kinds of measured Sn + Sn reactions. It is expected that a systematic analysis on these observables provides a more comprehensive insight into the compression, expansion, and fragmentation dynamics in heavy-ion collisions. Such studies may improve the knowledge on theoretical input parameters which could influence the determination of the high-density symmetry energy, *e.g.*, the isoscalar terms in the nuclear EOS, the density dependence of the two-nucleon collision cross section, and cluster correlations. To place a more stringent constraint on the symmetry energy, the $t/^3$He ratio, which has been predicted to be a good probe sensitive to the density dependence of the symmetry energy [78, 80, 87–89], will be examined. And besides, the n/p ratio observables should be a promising candidate to provide direct information on the neutron-proton dynamics in heavy-ion collisions, after analyzing the NeuLAND data. The upcoming results from the transport model evaluation project will be also of critical importance to reduce theoretical uncertainties and to extract more reliable information on the EOS of the isospin asymmetric matter through heavy-ion-collision experiments.

Acknowledgements

It has been my great pleasure to work on this interesting subject as one of the members of the SπRIT Collaboration during a doctoral course. Substantial assistance from many people was indispensable for the completion of this work, to whom I wish to present my appreciation.

First of all, I would like to thank Prof. Tetsuya Murakami with great sincerity, who is my supervisor at Kyoto University since I joined the collaboration in 2013. He gave me a precious opportunity to tackle this challenging field of physics exploring a high-density nuclear matter. His advice based on a long experience and profound knowledge of physics often made me notice something important. It was not possible to finish this thesis without his continuous guidance.

I am very grateful to Dr. Tadaaki Isobe and Dr. Mizuki Kurata-Nishimura for their direct mentoring in RIKEN. We discussed many times to determine the direction of the data analysis and to closely examine the obtained results. Whenever I asked questions related to the hardware development or analysis technique, they kindly gave me instructions and encouraged me, which boosted my motivation. It has been fortunate for me to work with them in RIKEN.

The SπRIT Collaboration itself was started around 2004 and has been progressed thanks to a great deal of effort by many researchers from worldwide. I have to appreciate all of the members involved in the collaboration, although I would like to emphasize my special thanks to colleagues I mainly worked with: Dr. Jon Barney, Dr. Giordano Cerizza, Dr. Justin Estee, Dr. Genie Jhang, Dr. Paweł Lasko, Mr. Jung Woo Lee, Dr. Jerzy Łukasik, Prof. William G. Lynch, Dr. Piotr Pawłowski, Dr. Clementine Santamaria, Mr. Chun Yuen Tsang, Prof. Manyee Betty Tsang, Dr. Rensheng Wang, Dr. Yan Zhang, and the local collaborators: Dr. Hidetada Baba, Dr. Noritsugu Nakatsuka, Dr. Shunji Nishimura, and Dr. Daisuke Suzuki. Significant contribution from the NeuLAND Collaboration, the BigRIPS team, and the accelerator operation staff was also absolutely essential for carrying out the experiment.

I would like to offer my appreciation to Prof. Akira Ono, who is the main developer of the AMD transport model. A lot of fruitful discussions with him deepened my understanding of physics on heavy-ion reactions. He repeatedly read over my manuscript and kindly gave me suggestions for brushing it up, throughout the publication process by the journal. Also, I would like to thank Prof. Natsumi Ikeno for giving us the calculated AMD events.

I would like to express my sincere gratitude to the research fellows in RIKEN. I am indebted to Prof. Hiroyoshi Sakurai, who is my supervisor at RIKEN and a director of the Nishina Center, for hosting me and supports that allowed my six-years research activity at RIKEN. Also, I would like to thank secretaries at the RI Physics Laboratory: Ms. Yu Naya, Ms. Asako Takahashi, and Ms. Asako Sakihama for their careful management of various administrative procedures.

I would like to acknowledge the financial support from RIKEN as the Junior Research Associate

program (2016–2018) and as the Research Part-time Worker (2019–2021). The computing resource for the data analysis and the theoretical calculations were provided by the HOKUSAI GreatWave system at RIKEN.

I am deeply obliged to reviewers of Physics Letters B for giving us shrewd comments so that the article was improved and the statement became clearer.

I would like to thank all of the members of the Experimental Nuclear and Hadronic (NH) Physics Laboratory at Kyoto University. NH laboratory has diversity in both terms of physics as well as member's personalities, from which I've learned a lot. Even though I didn't collaborate with them directly, I spent an enjoyable time to share each research with them when I came back to Kyoto a few times in a year.

Finally, I would like to express my sincere gratitude to my family for their heartfelt support and encouragement, no matter which I select as my own path.

January, 2022
Masanori Kaneko

Funding resources This work was supported by the Japanese MEXT KAKENHI (Grant-in-Aid for Scientific Research on Innovative Areas) grant No. 24105004; JSPS KAKENHI Nos. JP17K05432 and JP19K14709; the U.S. Department of Energy under Grant Nos. DE-SC0014530, DE-NA0002923, and DE-FG02-93ER40773; the US National Science Foundation Grant No. PHY-1565546; the Polish National Science Center under contract Nos. UMO-2013/09/B/ST2/04064 and UMO-2013/10/M/ST2/00624; and the National Research Foundation of Korea under Grant Nos. 2018R1A5A1025563, 2016K1A3A7A09005578, and 2013M7A1A1075764.

A Kinematics

In this appendix, commonly used kinematic terms in heavy-ion collisions are defined. The natural units are used, in which $\hbar = c = 1$.

A.1 Kinematic Variables

Kinematics of a particle in relativistic energies can be described by a four-momentum vector:

$$p^\mu = (p^0, p^1, p^2, p^3) = (E, \boldsymbol{p}). \tag{A.1}$$

In particular, the rest mass of a particle m is invariant independent of any inertial frames, given as:

$$m = \sqrt{E^2 - \boldsymbol{p}^2}. \tag{A.2}$$

The kinetic energy of a particle K is defined as:

$$K = E - m. \tag{A.3}$$

Let us consider a transformation from a frame S to the different frame S' which is moving with the velocity $\boldsymbol{\beta} = (0, 0, \beta)$ relative to S. The Lorentz transformation of the particle with p^μ measured at the frame S to the frame S' is given by the following matrix equation,

$$\begin{pmatrix} E' \\ p'^1 \\ p'^2 \\ p'^3 \end{pmatrix} = \begin{pmatrix} 1/\sqrt{1-\beta^2} & 0 & 0 & -\beta/\sqrt{1-\beta^2} \\ 0 & 1 & 0 & 0 \\ 0 & 0 & 1 & 0 \\ -\beta/\sqrt{1-\beta^2} & 0 & 0 & 1/\sqrt{1-\beta^2} \end{pmatrix} \begin{pmatrix} E \\ p^1 \\ p^2 \\ p^3 \end{pmatrix}. \tag{A.4}$$

In fixed-target experiments, the Cartesian coordinate (x, y, z) is conventionally defined so that the z axis is identical to the beam-moving direction. The decomposition of a momentum $\boldsymbol{p} = (p_x, p_y, p_z)$ into a transverse component and a longitudinal one with respect to the z axis provides a clear description of the kinematics in heavy-ion collisions. These two components, a transverse momentum p_T and a longitudinal momentum p_L, are given as:

$$p_T = \sqrt{p_x^2 + p_y^2}, \tag{A.5}$$

$$p_L = p_z. \tag{A.6}$$

Note that the p_T is invariant under the Lorentz transformation between systems along the z axis, *e.g.*, the transformation between the laboratory frame and the center-of-mass (c.m.) frame of the collision system. A polar angle θ and an azimuthal angle ϕ in the spherical coordinate system can be expressed as:

$$\tan\theta = p_L/|\boldsymbol{p}|, \tag{A.7}$$

$$\tan\phi = p_y/p_x. \tag{A.8}$$

Furthermore, we define a rapidity y of a particle as:

$$y = \frac{1}{2}\ln\left(\frac{E + p_L}{E - p_L}\right). \tag{A.9}$$

If one uses a transverse mass $m_T = \sqrt{p_T^2 + m^2}$, the following identities are led,

$$E = m_T \cosh y, \tag{A.10}$$

$$p_L = m_T \sinh y. \tag{A.11}$$

Or, one can associate a rapidity with a longitudinal velocity of a particle $\beta_L = p_L/E$ as:

$$\beta_L = \tanh y. \tag{A.12}$$

The use of the rapidity is convenient for grasping the global picture of kinematics since the Lorentz transformation of the rapidity y from the laboratory frame to the c.m. frame correspond to a constant translation of the rapidity by the c.m. rapidity $y_{\text{c.m.}} = \tanh^{-1}\beta_{\text{c.m.}}$,

$$y' = y - y_{\text{c.m.}}, \tag{A.13}$$

which means that the differential yield of particles as a function of rapidity is Lorentz invariant.

Finally, we can construct the Lorentz-invariant cross section as:

$$E\frac{\mathrm{d}^3\sigma}{\mathrm{d}p^3} \simeq \frac{1}{2\pi p_T}\frac{\mathrm{d}^2N}{\mathrm{d}y\,\mathrm{d}p_T}, \tag{A.14}$$

by assuming the yield averaged by a number of events is azimuthally symmetric, which is attributed by a constant $1/2\pi$. And the rapidity distribution is provided by an integration of the invariant yield,

$$\frac{\mathrm{d}N}{\mathrm{d}y} = \int_0^\infty 2\pi p_T\,\mathrm{d}p_T\left(\frac{1}{2\pi p_T}\frac{\mathrm{d}^2N}{\mathrm{d}y\,\mathrm{d}p_T}\right). \tag{A.15}$$

A.2 Coordinate Systems

In this section, the coordinate systems used in the SπRIT TPC experiment are explained. Figure A.1 is a cartoon that illustrates the coordinate frames discussed here. A coordinate fixed to the laboratory frame – the TPC coordinate – is defined as presented by the blue arrows in the top figure. The origin of the TPC coordinate is the middle point of the upstream edge of the pad plane. The reconstruction of tracks by the SπRITROOT algorithm is performed under this TPC-fixed coordinate system.

Another coordinate system is the projectile-target frame, which can be defined based on the angles of a beam particle impinging on the target, drawn by the red solid arrows in the bottom figure. Since the target was located in the SAMURAI dipole magnet, the beam particle is bent before reaching the target. The incident angle of beam particles on the target plane can be obtained by analyzing beam-tracking detectors. The physical variables of particles emitted from Sn + Sn collisions, such as the transverse momentum and the rapidity, are defined under this projectile-target frame coordinate.

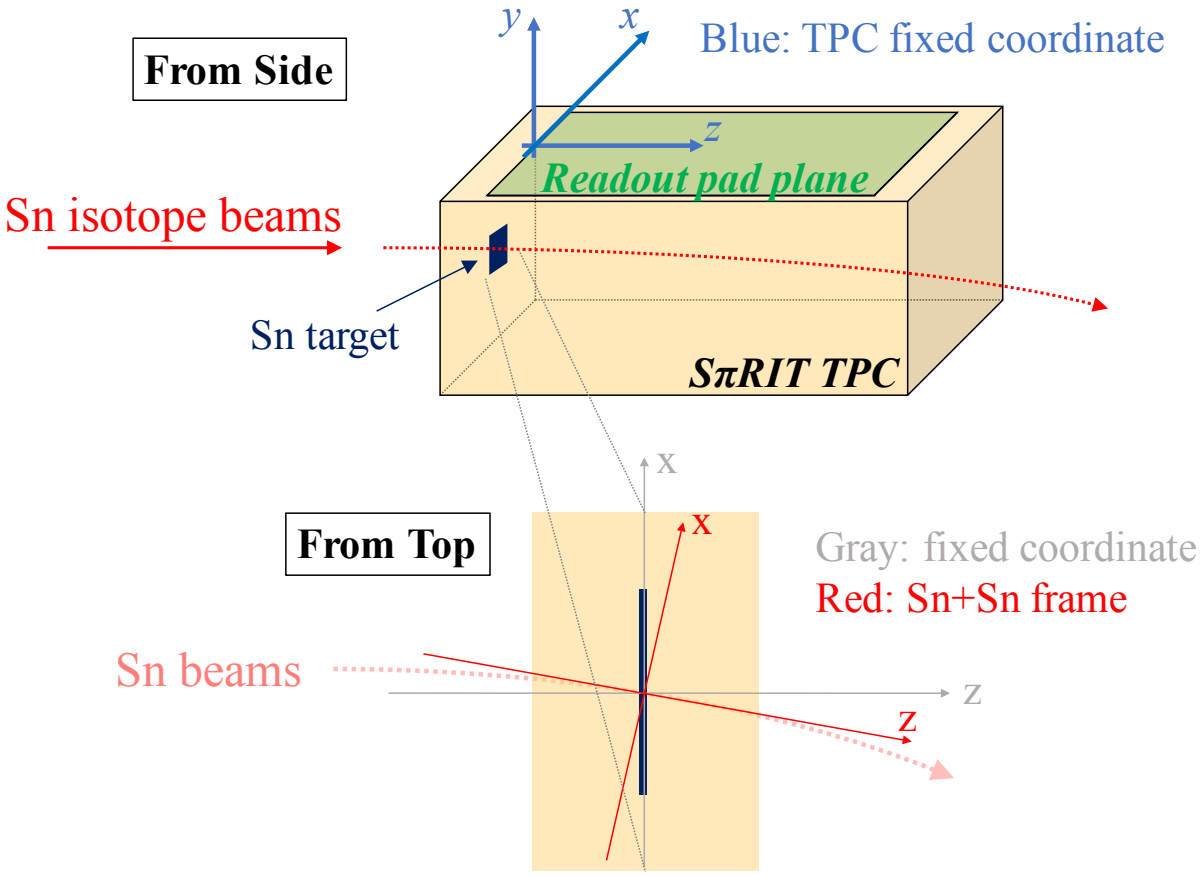

Figure A.1: Illustrations of the experimental setup with the description of the coordinate systems. Top: an illustration of the setup around the SπRIT TPC, where the TPC-fixed coordinate system is indicated by blue arrows. See text in detail. Bottom: a top view around the Sn target on which the Sn beam impinges. Drawn by the red-solid arrows is the coordinate system defined by the incident angle of the beam particle on the target.

B

Supplementals for the AMD Calculation

In this appendix, supplemental descriptions of the AMD are provided.

B.1 Formulation of the AMD

Wave function In the AMD model [17], the wave function of the A-nucleon system is described by a Slater determinant of constituent single particle states

$$|\Phi\rangle = \frac{1}{\sqrt{A!}} \det \varphi_i, \tag{B.1}$$

where φ_i is the wave function of the i-th nucleon represented by a product of the spatial wave function $\phi_{\boldsymbol{Z}_i}$ and the spin-isospin wave function χ_{α_i}

$$\varphi_i = \phi_{\boldsymbol{Z}_i} \chi_{\alpha_i}. \tag{B.2}$$

The spin-isospin state takes $p\uparrow$, $p\downarrow$, $n\uparrow$, or $n\downarrow$. The spatial wave function $\phi_{\boldsymbol{Z}_i}$ is represented by the Gaussian wave packet

$$\langle \boldsymbol{r} | \phi_{\boldsymbol{Z}_i} \rangle = \left(\frac{2\nu}{\pi}\right)^{3/4} \exp\left[-\nu\left(\boldsymbol{r} - \frac{\boldsymbol{Z}_i}{\sqrt{\nu}}\right)^2 + \frac{1}{2}\boldsymbol{Z}_i^2\right], \tag{B.3}$$

where the complex variables $Z \equiv \{\boldsymbol{Z}_i;\ i = 1, \ldots, A\}$ are the centroids of the Gaussian wave packets. The width parameter $\nu = 0.16\,\mathrm{fm}^{-2}$ is optimized so as to reasonably reproduce the experimental

nuclear binding energy. The centroid of Gaussian wave packets $\boldsymbol{Z}_i$ is given as:

$$\boldsymbol{Z}_i = \sqrt{\nu}\boldsymbol{D}_i + \frac{i}{2\hbar\sqrt{\nu}}\boldsymbol{K}_i, \tag{B.4}$$

with the phase-space coordinates

$$\frac{\langle\phi_{\boldsymbol{Z}}|\boldsymbol{r}|\phi_{\boldsymbol{Z}}\rangle}{\langle\phi_{\boldsymbol{Z}}|\phi_{\boldsymbol{Z}}\rangle} = \boldsymbol{D}, \qquad \frac{\langle\phi_{\boldsymbol{Z}}|\boldsymbol{p}|\phi_{\boldsymbol{Z}}\rangle}{\langle\phi_{\boldsymbol{Z}}|\phi_{\boldsymbol{Z}}\rangle} = \boldsymbol{K}. \tag{B.5}$$

Note that $\boldsymbol{D}_i$ and $\boldsymbol{K}_i$ do not necessarily represent the physical position and momentum of each nucleon in the nuclear system because of the antisymmetrization unless the system can be treated as a dilute nuclear gas system.

Equation of motion The time evolution of $\boldsymbol{Z}_i$ is determined classically by the equation of motion and by the two-nucleon collisions described in the following paragraph. The equation of motion is obtained by the time-dependent variational principle,

$$\delta\int_{t_1}^{t_2}\frac{\langle\Phi(Z)|(i\hbar\frac{\mathrm{d}}{\mathrm{d}t}-H)|\Phi(Z)\rangle}{\langle\Phi(Z)|\Phi(Z)\rangle}\,\mathrm{d}t = 0 \quad \text{with} \quad \delta Z(t_1) = \delta Z(t_2) = 0, \tag{B.6}$$

which leads to

$$i\hbar\sum_{j\tau}C_{i\sigma,j\tau}\frac{\mathrm{d}Z_{j\tau}}{\mathrm{d}t} = \frac{\partial\mathcal{H}}{\partial Z^*_{i\sigma}} \quad \text{or} \quad \dot{\boldsymbol{Z}}_i = \{\boldsymbol{Z}_i, \mathcal{H}\}_{\mathrm{PB}}, \tag{B.7}$$

where $\sigma,\tau = x,y,z$ are labels for the components of $\boldsymbol{Z}_i$, $\{\}_{\mathrm{PB}}$ is the expression of a Poisson bracket, the Hamiltonian $\mathcal{H}$ is the expectation value of the Hamiltonian operator H,

$$\mathcal{H}(Z,Z^*) = \frac{\langle\Phi(Z)|H|\Phi(Z)\rangle}{\langle\Phi(Z)|\Phi(Z)\rangle}, \tag{B.8}$$

and a positive definite hermitian matrix

$$C_{i\sigma,j\tau} = \frac{\partial^2}{\partial Z^*_{i\sigma}\partial Z_{j\tau}}\log\langle\Phi(Z)|\Phi(Z)\rangle\,. \tag{B.9}$$

For the mean-field calculations, the effective interaction based on the Skyrme force is implemented in the Hamiltonian H, as a part of which the density dependence of the symmetry energy is defined. It has been known in the AMD that the spurious zero-point oscillation energies of the center-of-mass motions of fragments need to be additionally corrected in the Hamiltonian [220], which will be described in Sect. B.3.

Two-nucleon collision In the AMD, the two-nucleon collision is implemented as a stochastic process induced by the residual interaction, which is treated in the physical coordinate space. The physical coordinate $W \equiv \{\boldsymbol{W}_i\}$ for a given nucleon i is defined as:

$$\boldsymbol{W}_i = \sqrt{\nu}\boldsymbol{R}_i + \frac{i}{2\hbar\sqrt{\nu}}\boldsymbol{P}_i \equiv \sum_{j=1}^{A}\left(\sqrt{Q}\right)_{ij}\boldsymbol{Z}_j, \tag{B.10}$$

where the real part $\boldsymbol{R}_i$ and the imaginary part $\boldsymbol{P}_i$ correspond to the physical position and momentum of each nucleon, respectively. The transformation matrix Q_{ij} and its square root are given by:

$$Q_{ij} = \frac{\partial}{\partial(\boldsymbol{Z}_i^* \cdot \boldsymbol{Z}_j)} \log \langle \Phi(Z) | \Phi(Z) \rangle, \tag{B.11}$$

$$Q = UDU^\dagger, \qquad \sqrt{Q} = U\sqrt{D}U^\dagger, \tag{B.12}$$

where U is the unitary matrix that diagonalizes Q and the diagonal matrix D is the eigenvalue of Q. The physical coordinate $\boldsymbol{W}$ is an extension of the canonical coordinate and has the Pauli-forbidden space, *i.e.*, $\left|\boldsymbol{W}_i - \boldsymbol{W}_j\right|$ cannot be too small. The distribution of the i-th nucleon is represented by Wigner's form, as:

$$f_i(\boldsymbol{r}, \boldsymbol{p}, t) = 8 \exp\left\{-2\nu(\boldsymbol{r} - \boldsymbol{R}_i(t))^2 - (\boldsymbol{p} - \boldsymbol{P}_i(t))^2/2\hbar^2\nu\right\}, \tag{B.13}$$

and the total distribution function is the sum of f_i.

A two-nucleon collision is treated as a quantum mechanical transition from an AMD state $|\Phi_i\rangle$ to another AMD state $\left|\Phi_j\right\rangle$ specified by the relative momentum between the scattered two nucleons $(p_{\mathrm{rel}}, \Omega)$. The transition rate can be given as:

$$v d\sigma = \frac{2\pi}{\hbar} \left| \left\langle \Phi_f \middle| V \middle| \Phi_i \right\rangle \right|^2 \delta(E_f - E_i) \frac{p_{\mathrm{rel}}^2 \, \mathrm{d}p_{\mathrm{rel}} \, \mathrm{d}\Omega}{(2\pi\hbar)^3}. \tag{B.14}$$

Here, E_i and E_f are the expectation values of the Hamiltonian operator for each state. The two-nucleon scattering cross section σ is an input for calculating the scattering matrix element. In AMD, the medium modification is introduced as:

$$\sigma_{NN}^*(\rho', \epsilon) = \sigma_0 \tanh[\sigma_{NN}^{\mathrm{free}}(\epsilon)/\sigma_0] \quad \text{with} \quad \sigma_0 = 0.5 \times (\rho')^{-2/3}. \tag{B.15}$$

Here, $\sigma_{NN}^{\mathrm{free}}(\epsilon)$ is the nucleon-nucleon scattering cross section in free space at a collision energy of ϵ. And ρ' means a kind of the phase-space density with the relative momentum threshold,

$$\rho' = (\rho_1'^{(\mathrm{ini})} \rho_1'^{(\mathrm{fin})} \rho_2'^{(\mathrm{ini})} \rho_2'^{(\mathrm{fin})})^{1/4} \quad \text{with} \tag{B.16}$$

$$\rho_i'^{(\mathrm{ini/fin})} = \left(\frac{2\nu}{\pi}\right)^{3/2} \sum_{k \neq i} \theta\left(p_{\mathrm{cut}} > \left|\boldsymbol{P}_i^{(\mathrm{ini/fin})} - \boldsymbol{P}_k\right|\right) e^{-2\nu(\boldsymbol{R}_i - \boldsymbol{R}_k)^2}, \tag{B.17}$$

where the threshold is taken as $p_{\mathrm{cut}} = (375\,\mathrm{MeV}/c) e^{-\epsilon/(225\,\mathrm{MeV})}$. The index $i = 1, 2$ here indicates a certain pair of two nucleons which may scatter. When the nucleons are judged to scatter, the scattering angle is taken randomly and new momenta are given for the two nucleons.

In addition to the change of nucleon's momenta, cluster correlations are further introduced in the final state of two-nucleon collisions so that a cluster can be formed and disintegrated as a result of two-nucleon collisions and be propagated according to the equation of motion. In the latest version of the AMD employed in this work, the suppression of the cluster formation depending on the phase-space density ρ' is also introduced, see Ref. [20] for the detail.

B.2 Skyrme Mean-Field Parametrization

The two specific density dependences of the symmetry energy employed in the present work are adopted from Ref. [18]. As an effective interaction implemented in the AMD Hamiltonian, the Skyrme SLy4 interaction [219] is employed with the spin-orbit term omitted. The density-dependent term in the SLy4 force is given by:

$$v_\rho^{(L=46)} = \frac{1}{6}t_3(1 + x_3P_\sigma)\rho(\boldsymbol{r}_1)^\alpha\delta(\boldsymbol{r}_1 - \boldsymbol{r}_2), \tag{B.18}$$

where $x_3 = 1.354$ and $t_3 = 13777.0$ are given parameters in the Skyrme force. This SLy4 parametrization gives the symmetry energy of $J = 32.0\,\mathrm{MeV}$ with the slope parameter of $L = 46\,\mathrm{MeV}$ at the saturation density of $\rho_0 = 0.160\,\mathrm{fm}^{-3}$, and the nuclear-matter incompressibility is $K_0 = 230\,\mathrm{MeV}$. This saturation property corresponds to the so-called a soft or linear density dependence of the symmetry energy. In order to parametrize a stiff symmetry energy, the density-dependent term of the SLy4 force is modified as:

$$v_\rho^{(L=108)} = \frac{1}{6}t_3(1 + x_3'P_\sigma)\rho(\boldsymbol{r}_1)^\alpha\delta(\boldsymbol{r}_1 - \boldsymbol{r}_2) + \frac{1}{6}t_3(x_3 - x_3')\rho_0^\alpha P_\sigma\delta(\boldsymbol{r}_1 - \boldsymbol{r}_2), \tag{B.19}$$

with $x_3' = 0.5$. This parametrization corresponds to the slope parameter of $L = 108\,\mathrm{MeV}$, without changing other properties at saturation density.

B.3 Correction for Zero-Point Ocillation Energy

The expectation value of the center-of-mass kinetic energy for the A-nucleon system is given by

$$\langle T_{\mathrm{CM}}\rangle = T_0 + \frac{1}{2AM}\boldsymbol{K}_{\mathrm{CM}}^2, \tag{B.20}$$

where M is the total mass of the A-nucleon system and

$$T_0 = \frac{3\hbar^2\nu}{2M}, \quad \sum_{i=1}^{A}\boldsymbol{Z}_i = \sqrt{\nu}A\boldsymbol{D}_{\mathrm{CM}} + \frac{i}{2\hbar\sqrt{\nu}}\boldsymbol{K}_{\mathrm{CM}}. \tag{B.21}$$

The T_0 represents the kinetic energy due to the zero-point oscillation of the center-of-mass motion. This extra term can appear because each nucleon is represented by a Gaussian wave packet, and the center-of-mass wave packet is also given by a Gaussian wave packet with a certain fixed width.

When a fragmentation process is treated in the AMD, this spurious zero-point kinetic energy may cause a serious problem. For example, in a process of a ^{12}C breaking down into three α particles, the energy equivalent to their binding-energy difference, *i.e.*, $E_{^{12}\mathrm{C}} - 3E_\alpha$ is necessary. However, in the AMD, the energies of their ground states are given as $\langle H\rangle_{^{12}\mathrm{C}} = -E_{^{12}\mathrm{C}} + T_0$ and $3\langle H\rangle_\alpha = 3(-E_\alpha + T_0)$. Accordingly, their difference is $E_{^{12}\mathrm{C}} - 3E_\alpha + 2T_0$. As seen in this example, the extra energy is necessary for the fragmentation process, and the surplus energy needs to be subtracted in the combination process. In general, an energy T_0 is necessary or unnecessary

when the number of fragments changes by one. With $\nu = 0.15\,\mathrm{fm}^{-2}$, $T_0 \sim 10\,\mathrm{MeV}$, which is not negligible.

This spurious zero-point energy is phenomenologically subtracted as follows. The sum of zero-point energies appearing in the Hamiltonian in Eq. B.7 is replaced so as to cancel the unphysical terms as:

$$\mathcal{H}(Z) = \frac{\langle\Phi(Z)|H|\Phi(Z)\rangle}{\langle\Phi(Z)|\Phi(Z)\rangle} - \frac{3\hbar^2\nu}{2M}A + T_0(A - N_\mathrm{F}). \tag{B.22}$$

Here the N_F is a continuous function depending on $D = \mathrm{Re}\{Z\}$, *i.e.*, the real part of the centroidal coordinates of Gaussian wave packets. The function N_F is defined to be consistent with the number of fragments in a particular configuration of D. By this prescription, the term $-T_0 N_F$ in Eq. B.22 works as a repulsive potential when the number of fragments increases and is expected to assist the fragmentation process, and vice versa for the combination process. Practically, the N_F is defined as a function of the relative distance of nucleons $d_{ij} = \left|\boldsymbol{D}_i - \boldsymbol{D}_j\right|$,

$$N_\mathrm{F} = \sum_{i=1}^{A} \frac{g(k_i)}{n_i m_i}. \tag{B.23}$$

Here the quantities n_i, m_i, and k_i are provided as:

$$n_i = \sum_{j=1}^{A} \hat{f}_{ij}, \quad m_i = \sum_{j=1}^{A} \frac{1}{n_j} f_{ij}, \quad k_i = \sum_{j=1}^{A} \bar{f}_{ij}, \tag{B.24}$$

respectively, with

$$\hat{f}_{ij} = F(d_{ij}, \hat{\xi}, \hat{a}), \quad f_{ij} = F(d_{ij}, \xi, a), \quad \bar{f}_{ij} = F(d_{ij}, \bar{\xi}, \bar{a}), \tag{B.25}$$

$$F(d, \xi, a) = \begin{cases} 1 & (d \le a), \\ e^{-\xi(d-a)^2} & (d > a). \end{cases} \tag{B.26}$$

The function $g(k)$ is provided as:

$$g(k) = 1 + g_0 e^{-(k-M)^2/2\sigma^2}, \tag{B.27}$$

which should be equal to 1 in principle. Namely, if we use $g(k) = 1$, the N_F is always approximately equal to the number of fragments in the system. The second term $g_0 e^{-(k-M)^2/2\sigma^2}$ is effective only when a nucleus with a particular mass M is considered. In the default version of AMD, the parameters in $g(k)$ are usually optimized for $A = 12$ fragments, which has resulted in a reasonable reproduction of the binding energy of a ^{12}C nucleus [220].

In this work, the parameters used in the function N_F are optimized so that the phase space for relative coordinates between nucleons forming an $A = 2$ or $A = 3$ fragment becomes approximately $(2\pi\hbar)^3$. The amount of the correction depends on the mean-field representation, *i.e.*, the asy-soft or asy-stiff symmetry energy. Although the correction is defined to be effective for $A = 3$ clusters in the asy-soft case, the correction for $A = 2$ clusters is further added in the asy-stiff case. Explicitly,

$$g(k) = \begin{cases} 1 + e^{-8(k-3)^2} & (\text{asy-soft}), \\ 1 + e^{-8(k-3)^2} + 0.52e^{-8(k-2)^2} & (\text{asy-stiff}). \end{cases} \tag{B.28}$$

are used for the correction term in each calculation, where the parameters are given in Table 6.2. Table B.1 lists the calculated binding energies of light clusters for the asy-soft and asy-stiff symmetry energies with and without the center-of-mass energy correction.

Table B.1: Total binding energies (MeV) of light cluster nuclei in different options of the AMD. The terms "asy-soft" and "asy-stiff" have the same meaning as those in the text. "asy-soft-gfg" and "asy-stiff-gfg′" indicate that the bound phase space for $A = 2$ clusters and that for $A = 2, 3$ clusters are modified in the asy-soft and asy-stiff calculations, respectively.

	asy-soft	asy-soft-gfg	asy-stiff	asy-stiff-gfg′
^2n $(n\uparrow n\downarrow)$	2.71	2.71	-5.81	-10.07
^{2}H $(p\uparrow p\downarrow)$	3.46	3.46	-5.05	-9.32
d $(p\uparrow n\uparrow)$	-7.07	-7.08	1.44	-2.82
$p\uparrow n\downarrow$	-2.91	-2.91	-2.91	-7.18
t	-12.41	-20.61	-12.41	-20.61
^{3}He	-11.71	-19.91	-11.71	-19.91
α	-27.69	-27.69	-27.69	-27.69

B.4 Connection of the Nonrelativistic Calculation to the Relativistic World

In the AMD, the equation of motion is solved under the nonrelativistic framework while the relativistic kinematics should be considered in the real world. The connection of the nonrelativistic calculation to the relativistic world can be done consistently in the NN center-of-mass frame as follows. Here we consider a case where a beam particle with mass m_1 and incident kinetic energy E_b in the laboratory frame is bombarded on a particle with mass m_2 in a fixed target. In the nonrelativistic scheme, the velocity of the incident beam particle v_1 is given as:

$$v_1 = \sqrt{\frac{2E_b}{m_1}}. \tag{B.29}$$

Under the Galileian transformation, the velocities of the two particles in the NN center-of-mass frame can be given as:

$$\frac{p_1}{m_1} = \frac{1}{2}\sqrt{\frac{2E_b}{m_1}}, \qquad \frac{p_2}{m_2} = -\frac{1}{2}\sqrt{\frac{2E_b}{m_1}}, \tag{B.30}$$

where p_1 and p_2 are momenta of the particles in the NN center-of-mass frame. Then, the following relation can be led,

$$E_b = \frac{(2p_1)^2}{2m_1}, \qquad \frac{p_1}{m_1} = -\frac{p_2}{m_2}. \tag{B.31}$$

On the other hand, under the relativistic world, the Lorentz invariant s of the considering system

can be calculated as:

$$\begin{aligned} s &= \left(E_1^{\text{lab}} + m_2\right)^2 - \left(p_1^{\text{lab}}\right)^2 \\ &= \left(E_1^{\text{lab}}\right)^2 - \left(p_1^{\text{lab}}\right)^2 + 2E_1^{\text{lab}} m_2 + m_2^2 \\ &= m_1^2 + 2(E_b + m_1)m_2 + m_2^2 \\ &= m_1^2 + 2m_1 m_2 + m_2^2 + 2E_b m_2 \\ &= (m_1 + m_2)^2 + 2E_b m_2. \end{aligned} \tag{B.32}$$

In the NN center-of-mass frame, the s is calculated from the velocity β in the center-of-mass frame with $\gamma = 1/\sqrt{1-\beta^2}$:

$$\begin{aligned} s &= (m_1\gamma + m_2\gamma)^2 - (m_1\gamma\beta - m_2\gamma\beta)^2 \\ &= (m_1\gamma)^2 - (m_1\gamma\beta)^2 + (m_2\gamma)^2 - (m_2\gamma\beta)^2 + 2m_1 m_2\gamma^2 + 2m_1 m_2\gamma^2\beta^2 \\ &= m_1^2 + m_2^2 + 2m_1 m_2 - 2m_1 m_2 + 2m_1 m_2\gamma^2 + 2m_1 m_2\gamma^2\beta^2 \\ &= (m_1 + m_2)^2 + 4m_1 m_2\gamma^2\beta^2. \end{aligned} \tag{B.33}$$

Since the s is invariant under the Lorentz transformation between arbitrary frames, the following relation, which is equivalent to the nonrelativistic case of Eq. B.31, is obtained:

$$E_b = 2m_1\gamma^2\beta^2 = \frac{(2p_1)^2}{2m_1}, \qquad \frac{p_1}{m_1} = -\frac{p_2}{m_2}. \tag{B.34}$$

Therefore, momenta of particles calculated in the nonrelativistic scheme can be treated in the same way as the real world within the transformation to the NN center-of-mass frame.

C
Data Set

Table C.1 summarizes the run numbers used in this work.

Table C.1: List of regular runs used in this work.

System	#runs	Run numbers
^{108}Sn + ^{112}Sn	85	2272, 2273, 2274, 2275, 2276, 2283, 2284, 2285, 2286, 2288, 2289, 2291, 2310, 2311, 2314, 2315, 2320, 2322, 2323, 2324, 2325, 2331, 2332, 2333, 2334, 2335, 2336, 2337, 2340, 2341, 2362, 2363, 2368, 2369, 2370, 2371, 2372, 2373, 2374, 2375, 2378, 2379, 2380, 2381, 2382, 2383, 2384, 2385, 2386, 2387, 2388, 2389, 2391, 2392, 2393, 2394, 2395, 2396, 2397, 2398, 2399, 2400, 2401, 2402, 2429, 2432, 2433, 2434, 2437, 2438, 2439, 2440, 2442, 2453, 2461, 2462, 2463, 2501, 2502, 2503, 2505, 2506, 2507, 2508, 2509
^{112}Sn + ^{124}Sn	60	2542, 2543, 2544, 2546, 2547, 2548, 2552, 2553, 2554, 2555, 2556, 2557, 2558, 2559, 2560, 2562, 2563, 2564, 2565, 2566, 2567, 2568, 2569, 2570, 2571, 2572, 2573, 2574, 2575, 2578, 2579, 2580, 2581, 2582, 2583, 2584, 2585, 2586, 2587, 2588, 2589, 2590, 2591, 2592, 2593, 2594, 2595, 2596, 2597, 2598, 2599, 2600, 2601, 2617, 2618, 2619, 2620, 2621, 2622, 2623
^{124}Sn + ^{112}Sn	68	3059, 3061, 3062, 3065, 3066, 3068, 3069, 3071, 3074, 3075, 3076, 3077, 3078, 3080, 3081, 3082, 3083, 3084, 3085, 3087, 3088, 3089, 3090, 3091, 3092, 3093, 3094, 3095, 3097, 3098, 3102, 3103, 3138, 3139, 3140, 3141, 3142, 3143, 3144, 3145, 3146, 3148, 3149, 3150, 3151, 3152, 3153, 3154, 3155, 3156, 3157, 3158, 3159, 3165, 3166, 3167, 3168, 3169, 3170, 3171, 3172, 3177, 3179, 3180, 3181, 3182, 3183, 3184
^{132}Sn + ^{124}Sn	113	2841, 2843, 2844, 2845, 2846, 2848, 2849, 2850, 2851, 2852, 2855, 2856, 2857, 2858, 2859, 2860, 2861, 2875, 2877, 2878, 2879, 2880, 2881, 2882, 2883, 2884, 2887, 2888, 2889, 2890, 2891, 2892, 2893, 2894, 2896, 2898, 2899, 2900, 2901, 2902, 2903, 2904, 2905, 2907, 2914, 2916, 2917, 2919, 2920, 2921, 2922, 2924, 2925, 2926, 2927, 2929, 2930, 2931, 2932, 2933, 2934, 2935, 2936, 2939, 2940, 2941, 2942, 2943, 2944, 2945, 2946, 2948, 2955, 2956, 2958, 2959, 2960, 2961, 2962, 2964, 2965, 2966, 2968, 2969, 2970, 2971, 2972, 2973, 2975, 2976, 2977, 2978, 2979, 2980, 2981, 2982, 2983, 2984, 2985, 2986, 2988, 2989, 2990, 2991, 2992, 2993, 2997, 2999, 3000, 3002, 3003, 3007, 3039

D

Table of Hydrogen Yields and Relative Yields

The point-by-point values and uncertainties of the obtained single $\mathrm{d}N/\mathrm{d}y_0$ spectra of protons, deuterons, and tritons in central collisions of $^{132}\mathrm{Sn}+{}^{124}\mathrm{Sn}$ and $^{108}\mathrm{Sn}+{}^{112}\mathrm{Sn}$ systems are presented in Tables D.1–D.6. The data table of the d/p and t/p relative yields in each system, and their double ratios are shown in Tables D.7–D.12. Note that the $\mathrm{d}N/\mathrm{d}y_0$ spectra and the single relative yields were constructed with efficiency corrections, which includes the statistical errors derived from the correction function, while the double ratios were constructed without efficiency corrections, assuming that the fluctuations in correction functions for the two systems are fairly canceled by taking the ratio between the two systems.

Table D.1: Data table of the proton $\mathrm{d}N/\mathrm{d}y_0$ distribution in central ($b_0 < 0.15$) collisions of the ^{132}Sn + ^{124}Sn system at 270 MeV/nucleon.

y_0 bin	$\mathrm{d}N/\mathrm{d}y_0$	Statistical error	Systematic error
-0.45 ± 0.05	13.919	0.194 (1.392%)	+0.402(2.892%) −0.681(4.890%)
-0.35 ± 0.05	14.670	0.202 (1.380%)	+0.554(3.776%) −0.594(4.051%)
-0.25 ± 0.05	15.058	0.206 (1.367%)	+0.504(3.348%) −0.538(3.571%)
-0.15 ± 0.05	15.249	0.208 (1.367%)	+0.461(3.024%) −0.522(3.425%)
-0.05 ± 0.05	15.350	0.210 (1.366%)	+0.453(2.954%) −0.488(3.182%)
0.05 ± 0.05	15.415	0.210 (1.359%)	+0.444(2.880%) −0.453(2.938%)
0.15 ± 0.05	15.047	0.205 (1.363%)	+0.393(2.609%) −0.397(2.639%)
0.25 ± 0.05	14.629	0.200 (1.364%)	+0.358(2.446%) −0.383(2.619%)
0.35 ± 0.05	13.894	0.192 (1.381%)	+0.315(2.264%) −0.385(2.774%)
0.45 ± 0.05	13.081	0.182 (1.392%)	+0.275(2.102%) −0.360(2.751%)
0.55 ± 0.05	12.227	0.173 (1.412%)	+0.264(2.158%) −0.318(2.604%)
0.65 ± 0.05	11.038	0.159 (1.444%)	+0.235(2.129%) −0.254(2.304%)
0.75 ± 0.05	9.952	0.149 (1.496%)	+0.207(2.080%) −0.215(2.164%)
0.85 ± 0.05	8.704	0.133 (1.525%)	+0.191(2.195%) −0.214(2.461%)
0.95 ± 0.05	7.465	0.119 (1.588%)	+0.178(2.390%) −0.206(2.754%)
1.05 ± 0.05	5.862	0.098 (1.667%)	+0.161(2.754%) −0.174(2.971%)
1.15 ± 0.05	4.459	0.079 (1.781%)	+0.149(3.344%) −0.142(3.192%)
1.25 ± 0.05	3.074	0.061 (1.985%)	+0.133(4.318%) −0.121(3.939%)
1.35 ± 0.05	2.009	0.045 (2.247%)	+0.122(6.079%) −0.115(5.703%)
1.45 ± 0.05	1.254	0.034 (2.685%)	+0.117(9.294%) −0.112(8.909%)
1.55 ± 0.05	0.726	0.024 (3.310%)	+0.105(14.507%) −0.103(14.186%)
1.65 ± 0.05	0.390	0.017 (4.294%)	+0.084(21.574%) −0.083(21.345%)
1.75 ± 0.05	0.190	0.011 (5.957%)	+0.061(32.219%) −0.060(31.556%)
1.85 ± 0.05	0.106	0.008 (7.837%)	+0.051(47.774%) −0.050(46.753%)
1.95 ± 0.05	0.048	0.005 (10.796%)	+0.029(61.332%) −0.028(59.600%)

Table D.2: Data table of the deuteron $\mathrm{d}N/\mathrm{d}y_0$ distribution in central ($b_0 < 0.15$) collisions of the $^{132}\mathrm{Sn} + ^{124}\mathrm{Sn}$ system at 270 MeV/nucleon.

y_0 bin	$\mathrm{d}N/\mathrm{d}y_0$	Statistical error	Systematic error
-0.45 ± 0.05	11.331	0.157 (1.388%)	+0.514(4.532%) −0.540(4.762%)
-0.35 ± 0.05	12.046	0.164 (1.364%)	+0.464(3.852%) −0.543(4.511%)
-0.25 ± 0.05	12.726	0.171 (1.345%)	+0.419(3.290%) −0.490(3.847%)
-0.15 ± 0.05	13.251	0.178 (1.341%)	+0.405(3.053%) −0.456(3.445%)
-0.05 ± 0.05	13.566	0.179 (1.321%)	+0.409(3.018%) −0.455(3.357%)
0.05 ± 0.05	13.520	0.179 (1.324%)	+0.396(2.929%) −0.425(3.140%)
0.15 ± 0.05	13.169	0.176 (1.337%)	+0.375(2.848%) −0.413(3.137%)
0.25 ± 0.05	12.340	0.165 (1.335%)	+0.325(2.630%) −0.380(3.079%)
0.35 ± 0.05	11.731	0.158 (1.349%)	+0.257(2.190%) −0.323(2.751%)
0.45 ± 0.05	10.936	0.150 (1.369%)	+0.234(2.142%) −0.296(2.703%)
0.55 ± 0.05	10.173	0.142 (1.394%)	+0.247(2.426%) −0.291(2.856%)
0.65 ± 0.05	8.901	0.128 (1.443%)	+0.240(2.701%) −0.249(2.796%)
0.75 ± 0.05	7.718	0.116 (1.509%)	+0.228(2.951%) −0.216(2.805%)
0.85 ± 0.05	6.306	0.100 (1.587%)	+0.214(3.393%) −0.204(3.233%)
0.95 ± 0.05	4.693	0.081 (1.736%)	+0.212(4.521%) −0.209(4.443%)
1.05 ± 0.05	3.317	0.063 (1.911%)	+0.220(6.642%) −0.221(6.648%)
1.15 ± 0.05	1.968	0.045 (2.272%)	+0.201(10.204%) −0.204(10.388%)
1.25 ± 0.05	0.965	0.028 (2.952%)	+0.167(17.341%) −0.169(17.538%)
1.35 ± 0.05	0.430	0.018 (4.085%)	+0.135(31.324%) −0.135(31.433%)
1.45 ± 0.05	0.137	0.009 (6.779%)	+0.071(51.506%) −0.070(51.318%)
1.55 ± 0.05	0.046	0.005 (10.708%)	+0.034(74.983%) −0.034(74.541%)
1.65 ± 0.05	0.008	0.002 (21.625%)	+0.008(96.636%) −0.008(93.616%)
1.75 ± 0.05	0.002	0.001 (34.972%)	+0.004(232.811%) −0.002(100.758%)
1.85 ± 0.05	0.000	—	—
1.95 ± 0.05	0.001	0.001 (59.266%)	+0.005(403.276%) −0.001(109.366%)

Table D.3: Data table of the triton $\mathrm{d}N/\mathrm{d}y_0$ distribution in central ($b_0 < 0.15$) collisions of the ^{132}Sn + ^{124}Sn system at 270 MeV/nucleon.

y_0 bin	$\mathrm{d}N/\mathrm{d}y_0$	Statistical error	Systematic error
-0.45 ± 0.05	8.308	0.123 (1.482%)	+0.624(7.511%) −0.652(7.847%)
-0.35 ± 0.05	9.263	0.135 (1.457%)	+0.646(6.973%) −0.675(7.291%)
-0.25 ± 0.05	10.077	0.145 (1.436%)	+0.602(5.974%) −0.646(6.407%)
-0.15 ± 0.05	10.420	0.148 (1.419%)	+0.521(4.995%) −0.568(5.450%)
-0.05 ± 0.05	10.608	0.150 (1.417%)	+0.471(4.442%) −0.515(4.851%)
0.05 ± 0.05	10.465	0.146 (1.395%)	+0.410(3.915%) −0.468(4.471%)
0.15 ± 0.05	10.181	0.144 (1.415%)	+0.336(3.296%) −0.413(4.053%)
0.25 ± 0.05	9.798	0.140 (1.427%)	+0.296(3.022%) −0.362(3.693%)
0.35 ± 0.05	9.181	0.134 (1.458%)	+0.269(2.929%) −0.294(3.202%)
0.45 ± 0.05	8.280	0.123 (1.482%)	+0.228(2.752%) −0.209(2.528%)
0.55 ± 0.05	7.574	0.116 (1.527%)	+0.185(2.436%) −0.172(2.272%)
0.65 ± 0.05	6.661	0.106 (1.588%)	+0.154(2.318%) −0.141(2.118%)
0.75 ± 0.05	5.390	0.091 (1.686%)	+0.130(2.411%) −0.129(2.387%)
0.85 ± 0.05	4.007	0.074 (1.838%)	+0.125(3.122%) −0.120(2.994%)
0.95 ± 0.05	2.719	0.057 (2.105%)	+0.100(3.672%) −0.104(3.829%)
1.05 ± 0.05	1.490	0.039 (2.592%)	+0.056(3.782%) −0.086(5.778%)
1.15 ± 0.05	0.680	0.024 (3.466%)	+0.024(3.512%) −0.066(9.758%)
1.25 ± 0.05	0.224	0.012 (5.530%)	+0.010(4.515%) −0.031(13.926%)
1.35 ± 0.05	0.050	0.005 (10.157%)	+0.004(8.114%) −0.005(9.333%)
1.45 ± 0.05	0.010	0.002 (19.162%)	+0.004(36.062%) −0.001(9.542%)
1.55 ± 0.05	0.001	0.001 (37.305%)	+0.005(332.369%) −0.000(29.530%)
1.65 ± 0.05	0.000	—	—
1.75 ± 0.05	0.000	—	—
1.85 ± 0.05	0.000	—	—
1.95 ± 0.05	0.000	—	—

Table D.4: Data table of the proton $\mathrm{d}N/\mathrm{d}y_0$ distribution in central ($b_0 < 0.15$) collisions of the ^{108}Sn + ^{112}Sn system at 270 MeV/nucleon.

y_0 bin	$\mathrm{d}N/\mathrm{d}y_0$	Statistical error	Systematic error
−0.45 ± 0.05	16.000	0.227 (1.420%)	+0.308(1.924%) −0.729(4.558%)
−0.35 ± 0.05	16.593	0.232 (1.396%)	+0.547(3.299%) −0.611(3.682%)
−0.25 ± 0.05	16.909	0.232 (1.370%)	+0.488(2.888%) −0.584(3.453%)
−0.15 ± 0.05	17.605	0.241 (1.370%)	+0.433(2.459%) −0.598(3.398%)
−0.05 ± 0.05	17.702	0.242 (1.367%)	+0.419(2.369%) −0.598(3.377%)
0.05 ± 0.05	17.743	0.241 (1.361%)	+0.403(2.272%) −0.550(3.100%)
0.15 ± 0.05	17.305	0.236 (1.363%)	+0.361(2.085%) −0.469(2.708%)
0.25 ± 0.05	17.133	0.233 (1.362%)	+0.356(2.077%) −0.445(2.596%)
0.35 ± 0.05	16.301	0.224 (1.374%)	+0.339(2.078%) −0.416(2.555%)
0.45 ± 0.05	15.297	0.213 (1.393%)	+0.295(1.928%) −0.380(2.484%)
0.55 ± 0.05	14.531	0.207 (1.423%)	+0.263(1.810%) −0.348(2.394%)
0.65 ± 0.05	13.539	0.194 (1.435%)	+0.232(1.714%) −0.312(2.306%)
0.75 ± 0.05	12.308	0.184 (1.493%)	+0.202(1.638%) −0.286(2.326%)
0.85 ± 0.05	10.737	0.164 (1.531%)	+0.177(1.648%) −0.239(2.222%)
0.95 ± 0.05	9.266	0.147 (1.591%)	+0.163(1.757%) −0.193(2.084%)
1.05 ± 0.05	7.513	0.127 (1.687%)	+0.145(1.926%) −0.159(2.113%)
1.15 ± 0.05	5.932	0.108 (1.814%)	+0.124(2.098%) −0.133(2.238%)
1.25 ± 0.05	4.197	0.084 (1.999%)	+0.104(2.471%) −0.104(2.469%)
1.35 ± 0.05	2.850	0.064 (2.254%)	+0.097(3.418%) −0.094(3.293%)
1.45 ± 0.05	1.744	0.047 (2.704%)	+0.087(4.997%) −0.087(4.966%)
1.55 ± 0.05	0.999	0.034 (3.388%)	+0.074(7.417%) −0.077(7.659%)
1.65 ± 0.05	0.559	0.024 (4.345%)	+0.064(11.387%) −0.068(12.142%)
1.75 ± 0.05	0.303	0.017 (5.758%)	+0.057(18.829%) −0.060(19.812%)
1.85 ± 0.05	0.142	0.011 (7.922%)	+0.044(31.101%) −0.045(31.542%)
1.95 ± 0.05	0.061	0.007 (11.587%)	+0.027(43.479%) −0.026(42.778%)

Table D.5: Data table of the deuteron $\mathrm{d}N/\mathrm{d}y_0$ distribution in central ($b_0 < 0.15$) collisions of the $^{108}\mathrm{Sn} + ^{112}\mathrm{Sn}$ system at 270 MeV/nucleon.

y_0 bin	$\mathrm{d}N/\mathrm{d}y_0$	Statistical error	Systematic error
-0.45 ± 0.05	10.214	0.150 (1.466%)	+0.417(4.081%) −0.497(4.865%)
-0.35 ± 0.05	10.734	0.157 (1.459%)	+0.395(3.679%) −0.474(4.412%)
-0.25 ± 0.05	11.358	0.161 (1.419%)	+0.377(3.316%) −0.476(4.190%)
-0.15 ± 0.05	11.577	0.162 (1.400%)	+0.360(3.113%) −0.463(3.996%)
-0.05 ± 0.05	11.766	0.164 (1.390%)	+0.351(2.984%) −0.441(3.746%)
0.05 ± 0.05	11.939	0.167 (1.395%)	+0.366(3.067%) −0.413(3.460%)
0.15 ± 0.05	11.544	0.161 (1.393%)	+0.344(2.980%) −0.387(3.352%)
0.25 ± 0.05	11.312	0.160 (1.413%)	+0.287(2.539%) −0.389(3.438%)
0.35 ± 0.05	10.636	0.151 (1.419%)	+0.246(2.317%) −0.343(3.222%)
0.45 ± 0.05	9.719	0.141 (1.450%)	+0.232(2.386%) −0.273(2.808%)
0.55 ± 0.05	8.956	0.133 (1.489%)	+0.216(2.407%) −0.250(2.786%)
0.65 ± 0.05	8.130	0.125 (1.541%)	+0.190(2.338%) −0.237(2.911%)
0.75 ± 0.05	7.097	0.114 (1.607%)	+0.168(2.362%) −0.196(2.766%)
0.85 ± 0.05	5.903	0.101 (1.712%)	+0.150(2.542%) −0.155(2.627%)
0.95 ± 0.05	4.813	0.089 (1.843%)	+0.140(2.910%) −0.153(3.173%)
1.05 ± 0.05	3.536	0.073 (2.051%)	+0.139(3.943%) −0.161(4.555%)
1.15 ± 0.05	2.229	0.054 (2.435%)	+0.120(5.365%) −0.138(6.207%)
1.25 ± 0.05	1.310	0.040 (3.051%)	+0.107(8.139%) −0.113(8.636%)
1.35 ± 0.05	0.641	0.026 (4.114%)	+0.093(14.464%) −0.093(14.505%)
1.45 ± 0.05	0.248	0.015 (6.239%)	+0.066(26.786%) −0.066(26.804%)
1.55 ± 0.05	0.091	0.009 (9.521%)	+0.042(45.918%) −0.042(46.062%)
1.65 ± 0.05	0.022	0.004 (17.386%)	+0.015(67.238%) −0.015(67.111%)
1.75 ± 0.05	0.006	0.002 (30.411%)	+0.005(84.449%) −0.005(83.875%)
1.85 ± 0.05	0.003	0.001 (46.116%)	+0.002(95.070%) −0.002(93.631%)
1.95 ± 0.05	0.000	—	—

Table D.6: Data table of the triton $\mathrm{d}N/\mathrm{d}y_0$ ditribution in central ($b_0 < 0.15$) collisions of the ^{108}Sn + ^{112}Sn system at 270 MeV/nucleon.

y_0 bin	$\mathrm{d}N/\mathrm{d}y_0$	Statistical error	Systematic error
-0.45 ± 0.05	6.186	0.103 (1.672%)	+0.582(9.404%) −0.607(9.814%)
-0.35 ± 0.05	6.549	0.108 (1.655%)	+0.567(8.658%) −0.583(8.905%)
-0.25 ± 0.05	7.042	0.114 (1.619%)	+0.502(7.133%) −0.538(7.645%)
-0.15 ± 0.05	7.174	0.115 (1.604%)	+0.429(5.977%) −0.477(6.653%)
-0.05 ± 0.05	7.232	0.115 (1.587%)	+0.374(5.167%) −0.435(6.015%)
0.05 ± 0.05	7.238	0.115 (1.584%)	+0.320(4.426%) −0.392(5.411%)
0.15 ± 0.05	6.945	0.112 (1.619%)	+0.279(4.018%) −0.347(4.992%)
0.25 ± 0.05	6.661	0.107 (1.604%)	+0.243(3.653%) −0.305(4.579%)
0.35 ± 0.05	6.210	0.103 (1.660%)	+0.199(3.207%) −0.227(3.655%)
0.45 ± 0.05	5.508	0.094 (1.709%)	+0.149(2.707%) −0.157(2.854%)
0.55 ± 0.05	5.049	0.090 (1.778%)	+0.124(2.455%) −0.126(2.486%)
0.65 ± 0.05	4.347	0.081 (1.867%)	+0.100(2.297%) −0.103(2.374%)
0.75 ± 0.05	3.805	0.075 (1.969%)	+0.081(2.129%) −0.088(2.319%)
0.85 ± 0.05	2.963	0.065 (2.186%)	+0.064(2.146%) −0.069(2.345%)
0.95 ± 0.05	2.248	0.055 (2.457%)	+0.053(2.366%) −0.051(2.283%)
1.05 ± 0.05	1.370	0.041 (3.026%)	+0.043(3.125%) −0.031(2.290%)
1.15 ± 0.05	0.765	0.030 (3.877%)	+0.024(3.113%) −0.017(2.169%)
1.25 ± 0.05	0.348	0.019 (5.497%)	+0.010(2.820%) −0.013(3.814%)
1.35 ± 0.05	0.113	0.010 (8.977%)	+0.005(3.993%) −0.008(6.927%)
1.45 ± 0.05	0.021	0.004 (17.593%)	+0.001(4.363%) −0.003(13.356%)
1.55 ± 0.05	0.004	0.001 (34.719%)	+0.002(46.955%) −0.001(22.599%)
1.65 ± 0.05	0.000	—	—
1.75 ± 0.05	0.000	—	—
1.85 ± 0.05	0.000	—	—
1.95 ± 0.05	0.000	—	—

Table D.7: Data table of the deuteron-to-proton (d/p) relative yield in central collisions of the ^{132}Sn + ^{124}Sn system at 270 MeV/nucleon.

y_0 bin	d/p	Statistical error	Systematic error
-0.45 ± 0.05	0.830	0.016 (1.965%)	+0.024(2.878%) −0.030(3.648%)
-0.35 ± 0.05	0.821	0.016 (1.941%)	+0.024(2.877%) −0.029(3.501%)
-0.25 ± 0.05	0.850	0.016 (1.918%)	+0.024(2.873%) −0.028(3.292%)
-0.15 ± 0.05	0.877	0.017 (1.915%)	+0.025(2.854%) −0.028(3.230%)
-0.05 ± 0.05	0.889	0.017 (1.900%)	+0.025(2.828%) −0.027(3.091%)
0.05 ± 0.05	0.885	0.017 (1.897%)	+0.025(2.809%) −0.026(2.937%)
0.15 ± 0.05	0.873	0.017 (1.909%)	+0.024(2.786%) −0.026(2.956%)
0.25 ± 0.05	0.843	0.016 (1.908%)	+0.023(2.765%) −0.025(2.968%)
0.35 ± 0.05	0.850	0.016 (1.930%)	+0.023(2.758%) −0.025(2.888%)
0.45 ± 0.05	0.837	0.016 (1.953%)	+0.023(2.753%) −0.024(2.875%)
0.55 ± 0.05	0.830	0.016 (1.984%)	+0.023(2.750%) −0.024(2.919%)
0.65 ± 0.05	0.812	0.017 (2.042%)	+0.022(2.750%) −0.024(3.013%)
0.75 ± 0.05	0.772	0.016 (2.125%)	+0.021(2.750%) −0.024(3.128%)
0.85 ± 0.05	0.728	0.016 (2.201%)	+0.020(2.749%) −0.024(3.355%)
0.95 ± 0.05	0.629	0.015 (2.353%)	+0.017(2.749%) −0.025(3.995%)
1.05 ± 0.05	0.566	0.014 (2.536%)	+0.016(2.749%) −0.030(5.359%)
1.15 ± 0.05	0.444	0.013 (2.887%)	+0.012(2.749%) −0.036(8.146%)
1.25 ± 0.05	0.313	0.011 (3.558%)	+0.009(2.749%) −0.045(14.456%)
1.35 ± 0.05	0.218	0.010 (4.663%)	+0.006(2.749%) −0.060(27.595%)
1.45 ± 0.05	0.108	0.008 (7.291%)	+0.003(2.749%) −0.051(47.148%)
1.55 ± 0.05	0.064	0.007 (11.208%)	+0.002(2.749%) −0.046(71.189%)
1.65 ± 0.05	0.022	0.005 (22.047%)	+0.001(2.749%) −0.021(92.411%)
1.75 ± 0.05	0.012	0.004 (35.476%)	+0.000(2.749%) −0.012(100.683%)
1.85 ± 0.05	0.002	0.001 (50.169%)	+0.000(2.749%) −0.002(101.199%)
1.95 ± 0.05	0.037	0.023 (60.242%)	+0.001(2.749%) −0.038(101.143%)

Table D.8: Data table of the triton-to-proton (t/p) relative yield in central collisions of the ^{132}Sn + ^{124}Sn system at 270 MeV/nucleon.

y_0 bin	t/p	Statistical error	Systematic error
−0.45 ± 0.05	0.613	0.012 (2.033%)	+0.022(3.527%) −0.047(7.686%)
−0.35 ± 0.05	0.646	0.013 (2.007%)	+0.023(3.535%) −0.046(7.189%)
−0.25 ± 0.05	0.670	0.013 (1.983%)	+0.024(3.549%) −0.042(6.251%)
−0.15 ± 0.05	0.687	0.014 (1.970%)	+0.025(3.569%) −0.038(5.465%)
−0.05 ± 0.05	0.696	0.014 (1.968%)	+0.025(3.589%) −0.034(4.881%)
0.05 ± 0.05	0.684	0.013 (1.947%)	+0.025(3.607%) −0.030(4.365%)
0.15 ± 0.05	0.674	0.013 (1.965%)	+0.024(3.616%) −0.027(4.019%)
0.25 ± 0.05	0.671	0.013 (1.974%)	+0.024(3.610%) −0.026(3.841%)
0.35 ± 0.05	0.664	0.013 (2.008%)	+0.024(3.597%) −0.025(3.740%)
0.45 ± 0.05	0.634	0.013 (2.033%)	+0.023(3.590%) −0.023(3.694%)
0.55 ± 0.05	0.617	0.013 (2.079%)	+0.022(3.616%) −0.023(3.682%)
0.65 ± 0.05	0.611	0.013 (2.147%)	+0.022(3.667%) −0.023(3.692%)
0.75 ± 0.05	0.541	0.012 (2.253%)	+0.020(3.703%) −0.020(3.728%)
0.85 ± 0.05	0.463	0.011 (2.388%)	+0.017(3.766%) −0.017(3.766%)
0.95 ± 0.05	0.363	0.010 (2.637%)	+0.014(3.894%) −0.014(3.847%)
1.05 ± 0.05	0.258	0.008 (3.082%)	+0.011(4.145%) −0.010(3.969%)
1.15 ± 0.05	0.152	0.006 (3.897%)	+0.007(4.532%) −0.006(4.146%)
1.25 ± 0.05	0.072	0.004 (5.875%)	+0.004(5.254%) −0.003(4.447%)
1.35 ± 0.05	0.026	0.003 (10.403%)	+0.002(6.877%) −0.001(4.206%)
1.45 ± 0.05	0.008	0.002 (19.349%)	+0.001(10.147%) −0.000(3.654%)
1.55 ± 0.05	0.002	0.001 (37.451%)	+0.000(16.497%) −0.000(3.895%)
1.65 ± 0.05	0.000	—	—
1.75 ± 0.05	0.000	—	—
1.85 ± 0.05	0.000	—	—
1.95 ± 0.05	0.000	—	—

Table D.9: Data table of the deuteron-to-proton (d/p) relative yield in central collisions of the ^{108}Sn + ^{112}Sn system at 270 MeV/nucleon.

y_0 bin	d/p	Statistical error	Systematic error
-0.45 ± 0.05	0.643	0.013 (2.041%)	+0.021(3.236%) −0.024(3.806%)
-0.35 ± 0.05	0.647	0.013 (2.019%)	+0.021(3.238%) −0.025(3.786%)
-0.25 ± 0.05	0.673	0.013 (1.973%)	+0.022(3.231%) −0.025(3.692%)
-0.15 ± 0.05	0.662	0.013 (1.959%)	+0.021(3.225%) −0.024(3.630%)
-0.05 ± 0.05	0.666	0.013 (1.950%)	+0.021(3.200%) −0.023(3.472%)
0.05 ± 0.05	0.673	0.013 (1.949%)	+0.021(3.171%) −0.023(3.384%)
0.15 ± 0.05	0.667	0.013 (1.949%)	+0.021(3.150%) −0.023(3.382%)
0.25 ± 0.05	0.662	0.013 (1.962%)	+0.021(3.141%) −0.022(3.313%)
0.35 ± 0.05	0.654	0.013 (1.975%)	+0.021(3.138%) −0.021(3.218%)
0.45 ± 0.05	0.633	0.013 (2.011%)	+0.020(3.132%) −0.020(3.199%)
0.55 ± 0.05	0.614	0.013 (2.060%)	+0.019(3.127%) −0.020(3.219%)
0.65 ± 0.05	0.604	0.013 (2.106%)	+0.019(3.124%) −0.020(3.230%)
0.75 ± 0.05	0.573	0.013 (2.194%)	+0.018(3.124%) −0.019(3.258%)
0.85 ± 0.05	0.554	0.013 (2.297%)	+0.017(3.124%) −0.018(3.318%)
0.95 ± 0.05	0.518	0.013 (2.434%)	+0.016(3.123%) −0.018(3.452%)
1.05 ± 0.05	0.472	0.013 (2.656%)	+0.015(3.123%) −0.018(3.875%)
1.15 ± 0.05	0.376	0.011 (3.036%)	+0.012(3.123%) −0.018(4.815%)
1.25 ± 0.05	0.313	0.011 (3.647%)	+0.010(3.123%) −0.022(6.942%)
1.35 ± 0.05	0.229	0.011 (4.691%)	+0.007(3.123%) −0.028(12.236%)
1.45 ± 0.05	0.141	0.010 (6.800%)	+0.004(3.123%) −0.033(23.455%)
1.55 ± 0.05	0.093	0.009 (10.106%)	+0.003(3.151%) −0.039(42.093%)
1.65 ± 0.05	0.039	0.007 (17.921%)	+0.001(3.247%) −0.025(63.574%)
1.75 ± 0.05	0.022	0.007 (30.952%)	+0.001(3.364%) −0.018(81.039%)
1.85 ± 0.05	0.019	0.009 (46.791%)	+0.001(3.527%) −0.017(91.366%)
1.95 ± 0.05	0.010	0.008 (80.335%)	+0.000(3.857%) −0.010(94.757%)

Table D.10: Data table of the triton-to-proton (t/p) relative yield in central collisions of the ^{108}Sn + ^{112}Sn system at 270 MeV/nucleon.

y_0 bin	t/p	Statistical error	Systematic error
−0.45 ± 0.05	0.395	0.009 (2.193%)	+0.013(3.340%) −0.037(9.322%)
−0.35 ± 0.05	0.396	0.009 (2.165%)	+0.013(3.377%) −0.034(8.481%)
−0.25 ± 0.05	0.417	0.009 (2.121%)	+0.014(3.443%) −0.030(7.076%)
−0.15 ± 0.05	0.407	0.009 (2.110%)	+0.014(3.528%) −0.024(6.021%)
−0.05 ± 0.05	0.408	0.009 (2.095%)	+0.015(3.557%) −0.021(5.229%)
0.05 ± 0.05	0.407	0.008 (2.088%)	+0.014(3.457%) −0.018(4.543%)
0.15 ± 0.05	0.399	0.008 (2.116%)	+0.013(3.363%) −0.017(4.153%)
0.25 ± 0.05	0.386	0.008 (2.104%)	+0.013(3.343%) −0.015(3.898%)
0.35 ± 0.05	0.381	0.008 (2.155%)	+0.013(3.315%) −0.014(3.637%)
0.45 ± 0.05	0.359	0.008 (2.205%)	+0.012(3.287%) −0.012(3.444%)
0.55 ± 0.05	0.346	0.008 (2.277%)	+0.011(3.278%) −0.012(3.375%)
0.65 ± 0.05	0.320	0.008 (2.355%)	+0.011(3.287%) −0.011(3.422%)
0.75 ± 0.05	0.308	0.008 (2.471%)	+0.010(3.324%) −0.011(3.449%)
0.85 ± 0.05	0.279	0.007 (2.669%)	+0.009(3.348%) −0.010(3.417%)
0.95 ± 0.05	0.242	0.007 (2.927%)	+0.008(3.364%) −0.008(3.402%)
1.05 ± 0.05	0.184	0.006 (3.464%)	+0.006(3.442%) −0.006(3.419%)
1.15 ± 0.05	0.129	0.006 (4.280%)	+0.005(3.565%) −0.004(3.344%)
1.25 ± 0.05	0.085	0.005 (5.849%)	+0.003(3.785%) −0.003(3.221%)
1.35 ± 0.05	0.040	0.004 (9.255%)	+0.002(4.551%) −0.001(3.219%)
1.45 ± 0.05	0.014	0.002 (17.799%)	+0.001(6.002%) −0.000(3.254%)
1.55 ± 0.05	0.004	0.001 (34.884%)	+0.000(8.861%) −0.000(3.305%)
1.65 ± 0.05	0.001	0.001 (106.160%)	+0.000(14.953%) −0.000(3.486%)
1.75 ± 0.05	0.002	0.002 (89.705%)	+0.000(15.523%) −0.000(3.512%)
1.85 ± 0.05	0.000	—	—
1.95 ± 0.05	0.000	—	—

Table D.11: Data table of the deuteron-to-proton double spectral ratio $DR_{d/p}$.

y_0 bin	$DR_{d/p}$	Statistical error	Systematic error
-0.45 ± 0.05	1.295	0.020 (1.551%)	+0.031(2.360%) −0.031(2.372%)
-0.35 ± 0.05	1.295	0.020 (1.512%)	+0.031(2.360%) −0.031(2.360%)
-0.25 ± 0.05	1.283	0.019 (1.475%)	+0.030(2.363%) −0.030(2.360%)
-0.15 ± 0.05	1.301	0.019 (1.457%)	+0.031(2.363%) −0.031(2.360%)
-0.05 ± 0.05	1.322	0.019 (1.448%)	+0.031(2.362%) −0.031(2.360%)
0.05 ± 0.05	1.296	0.019 (1.446%)	+0.031(2.361%) −0.031(2.360%)
0.15 ± 0.05	1.308	0.019 (1.460%)	+0.031(2.360%) −0.031(2.360%)
0.25 ± 0.05	1.295	0.019 (1.477%)	+0.031(2.360%) −0.031(2.360%)
0.35 ± 0.05	1.309	0.020 (1.516%)	+0.031(2.360%) −0.031(2.364%)
0.45 ± 0.05	1.321	0.021 (1.575%)	+0.031(2.360%) −0.031(2.368%)
0.55 ± 0.05	1.337	0.022 (1.634%)	+0.032(2.360%) −0.032(2.374%)
0.65 ± 0.05	1.346	0.023 (1.725%)	+0.032(2.360%) −0.032(2.394%)
0.75 ± 0.05	1.326	0.024 (1.843%)	+0.031(2.360%) −0.032(2.442%)
0.85 ± 0.05	1.309	0.026 (2.020%)	+0.031(2.360%) −0.033(2.546%)
0.95 ± 0.05	1.201	0.027 (2.253%)	+0.028(2.360%) −0.034(2.804%)
1.05 ± 0.05	1.207	0.032 (2.619%)	+0.028(2.360%) −0.040(3.346%)
1.15 ± 0.05	1.181	0.038 (3.232%)	+0.028(2.360%) −0.057(4.852%)
1.25 ± 0.05	1.042	0.044 (4.257%)	+0.025(2.360%) −0.091(8.726%)
1.35 ± 0.05	0.980	0.058 (5.894%)	+0.023(2.360%) −0.171(17.499%)
1.45 ± 0.05	0.795	0.073 (9.219%)	+0.019(2.360%) −0.246(30.904%)
1.55 ± 0.05	0.756	0.105 (13.902%)	+0.018(2.360%) −0.417(55.139%)
1.65 ± 0.05	0.706	0.176 (24.941%)	+0.017(2.360%) −0.607(86.046%)
1.75 ± 0.05	1.084	0.420 (38.755%)	+0.026(2.360%) −1.085(100.028%)
1.85 ± 0.05	0.719	0.445 (61.905%)	+0.017(2.360%) −0.719(100.028%)
1.95 ± 0.05	3.135	2.703 (86.211%)	+0.074(2.360%) −3.136(100.028%)

Table D.12: Data table of the triton-to-proton double spectral ratio $DR_{t/p}$.

y_0 bin	$DR_{t/p}$	Statistical error	Systematic error
-0.45 ± 0.05	1.568	0.027 (1.750%)	$^{+0.049(3.125\%)}_{-0.039(2.466\%)}$
-0.35 ± 0.05	1.622	0.028 (1.710%)	$^{+0.048(2.967\%)}_{-0.040(2.466\%)}$
-0.25 ± 0.05	1.635	0.027 (1.668%)	$^{+0.045(2.766\%)}_{-0.040(2.466\%)}$
-0.15 ± 0.05	1.658	0.027 (1.649%)	$^{+0.044(2.629\%)}_{-0.041(2.466\%)}$
-0.05 ± 0.05	1.692	0.028 (1.640%)	$^{+0.043(2.565\%)}_{-0.042(2.466\%)}$
0.05 ± 0.05	1.679	0.028 (1.638%)	$^{+0.043(2.542\%)}_{-0.041(2.466\%)}$
0.15 ± 0.05	1.714	0.028 (1.659%)	$^{+0.044(2.539\%)}_{-0.042(2.466\%)}$
0.25 ± 0.05	1.738	0.029 (1.687%)	$^{+0.044(2.539\%)}_{-0.043(2.466\%)}$
0.35 ± 0.05	1.767	0.031 (1.745%)	$^{+0.045(2.540\%)}_{-0.044(2.466\%)}$
0.45 ± 0.05	1.769	0.032 (1.831%)	$^{+0.045(2.543\%)}_{-0.044(2.466\%)}$
0.55 ± 0.05	1.775	0.034 (1.922%)	$^{+0.045(2.534\%)}_{-0.044(2.466\%)}$
0.65 ± 0.05	1.849	0.038 (2.055%)	$^{+0.046(2.512\%)}_{-0.046(2.466\%)}$
0.75 ± 0.05	1.726	0.038 (2.229%)	$^{+0.043(2.495\%)}_{-0.043(2.466\%)}$
0.85 ± 0.05	1.664	0.042 (2.526%)	$^{+0.042(2.495\%)}_{-0.041(2.466\%)}$
0.95 ± 0.05	1.513	0.044 (2.929%)	$^{+0.038(2.515\%)}_{-0.037(2.466\%)}$
1.05 ± 0.05	1.412	0.053 (3.728%)	$^{+0.037(2.587\%)}_{-0.035(2.466\%)}$
1.15 ± 0.05	1.251	0.062 (4.985%)	$^{+0.034(2.755\%)}_{-0.031(2.466\%)}$
1.25 ± 0.05	0.975	0.074 (7.568%)	$^{+0.030(3.076\%)}_{-0.024(2.466\%)}$
1.35 ± 0.05	0.798	0.104 (13.042%)	$^{+0.030(3.728\%)}_{-0.020(2.466\%)}$
1.45 ± 0.05	0.974	0.232 (23.800%)	$^{+0.051(5.231\%)}_{-0.024(2.466\%)}$
1.55 ± 0.05	0.909	0.430 (47.328%)	$^{+0.077(8.470\%)}_{-0.022(2.466\%)}$
1.65 ± 0.05	2.785	3.220 (115.605%)	$^{+0.244(8.774\%)}_{-0.069(2.466\%)}$
1.75 ± 0.05	0.000	—	—
1.85 ± 0.05	0.000	—	—
1.95 ± 0.05	0.000	—	—

E

Supplemental Figures in the Systematic Uncertainty Evaluation

In this appendix, supplemental figures used for evaluating the systematic uncertainties in the $\mathrm{d}N/\mathrm{d}y_0$ spectra and their single and double spectral ratios are presented. Each figure presents 12 spectra constructed with varying the condition, along with the ratio of the spectrum with varied condition to the default spectrum in the bottom panels.

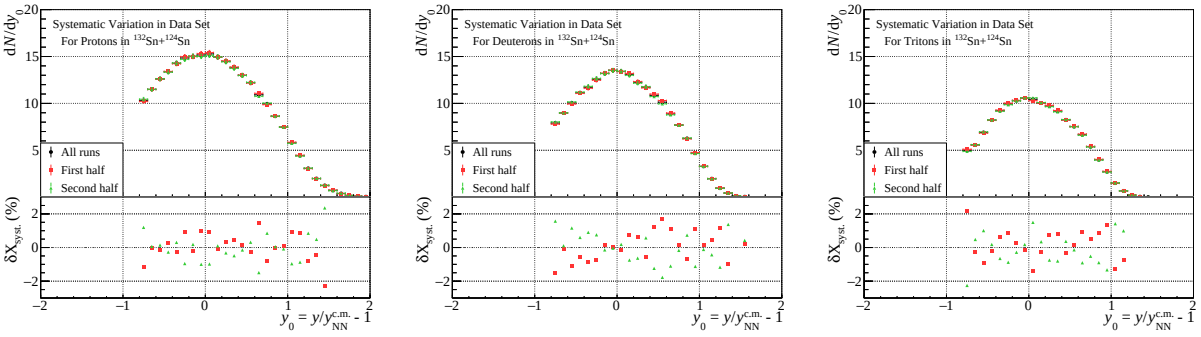

(a) Protons in ^{132}Sn + ^{124}Sn.

(b) Deuterons in ^{132}Sn + ^{124}Sn.

(c) Tritons in ^{132}Sn + ^{124}Sn.

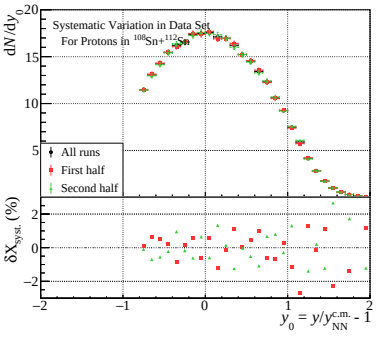

(d) Protons in ^{108}Sn + ^{112}Sn.

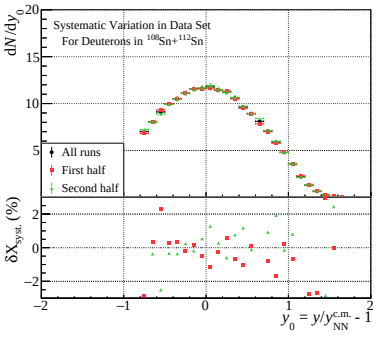

(e) Deuterons in ^{108}Sn + ^{112}Sn.

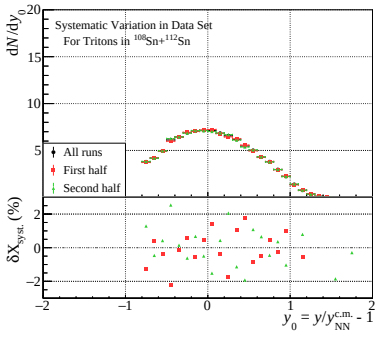

(f) Tritons in ^{108}Sn + ^{112}Sn.

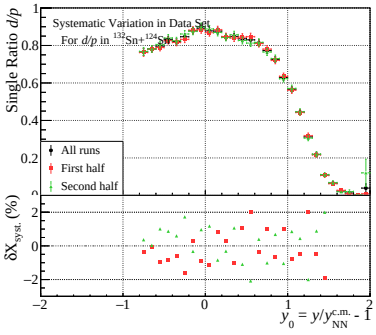

(g) d/p in ^{132}Sn + ^{124}Sn.

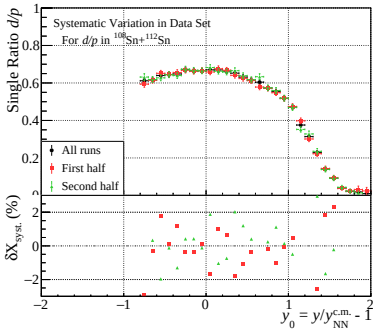

(h) d/p in ^{108}Sn + ^{112}Sn.

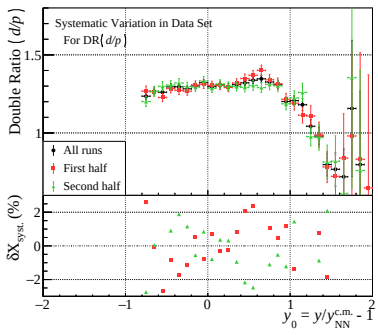

(i) $DR_{d/p}$.

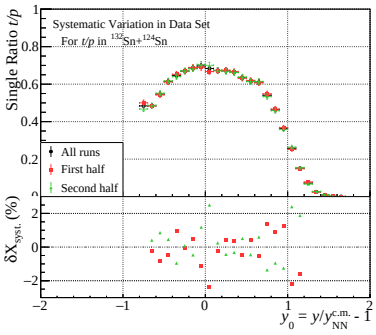

(j) t/p in ^{132}Sn + ^{124}Sn.

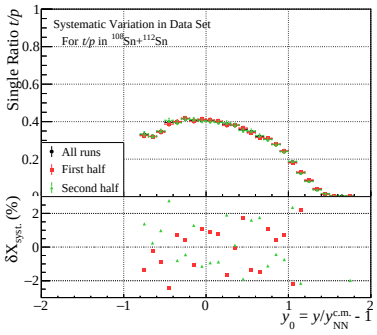

(k) t/p in ^{108}Sn + ^{112}Sn.

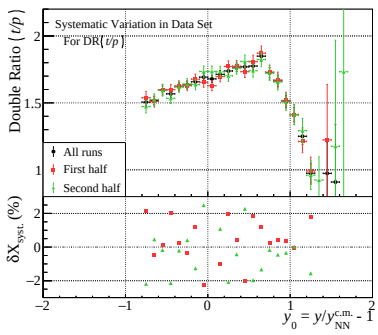

(l) $DR_{t/p}$.

Figure E.1: Systematic variations derived from the data set. The dN/dy_0 distributions ((a)–(f)), the single and double d/p spectral ratios ((g)–(i)), and the single and double t/p spectral ratios ((j), (k)) are presented. In each figure, the top panel presents the respective spectra with the default set of data and those with the halved sets of data, while the bottom one present the residual function $\delta X_{\text{syst.}}(y_0)$.

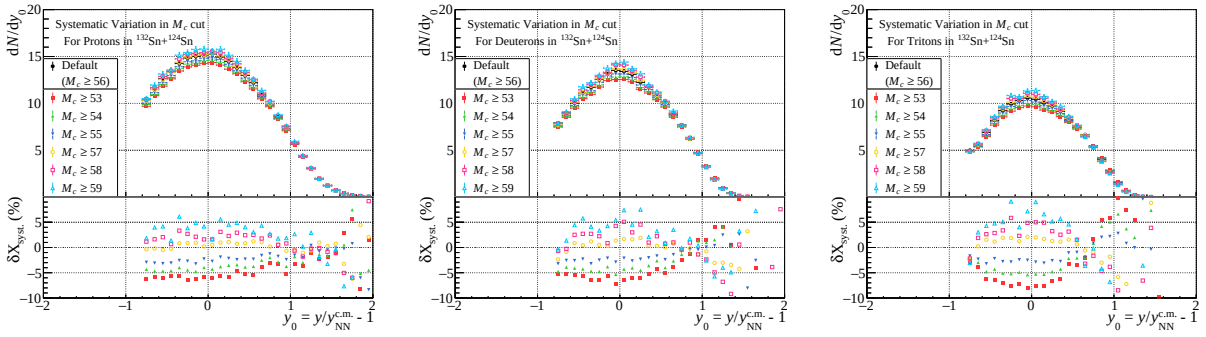

(a) Protons in ^{132}Sn + ^{124}Sn.

(b) Deuterons in ^{132}Sn + ^{124}Sn.

(c) Tritons in ^{132}Sn + ^{124}Sn.

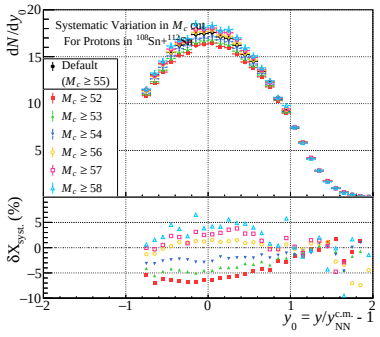

(d) Protons in ^{108}Sn + ^{112}Sn.

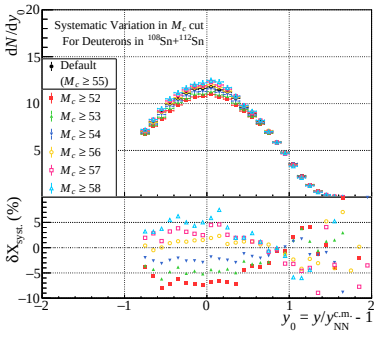

(e) Deuterons in ^{108}Sn + ^{112}Sn.

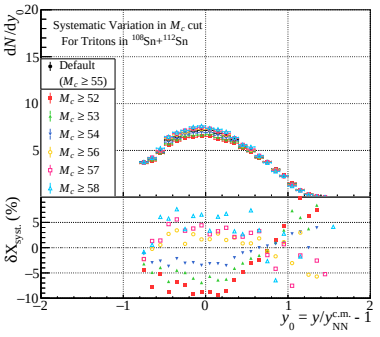

(f) Tritons in ^{108}Sn + ^{112}Sn.

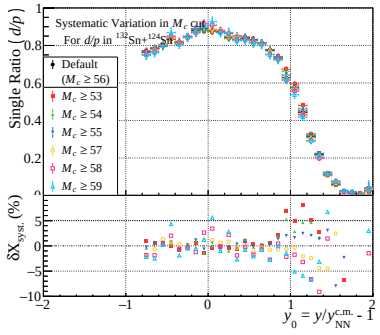

(g) d/p in ^{132}Sn + ^{124}Sn.

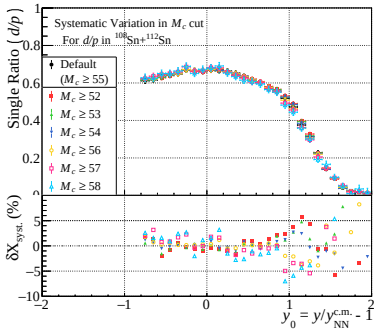

(h) d/p in ^{108}Sn + ^{112}Sn.

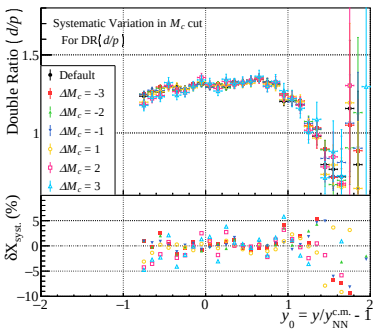

(i) $DR_{d/p}$.

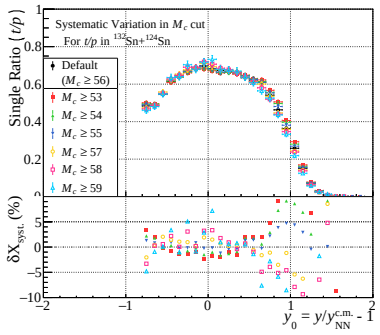

(j) t/p in ^{132}Sn + ^{124}Sn.

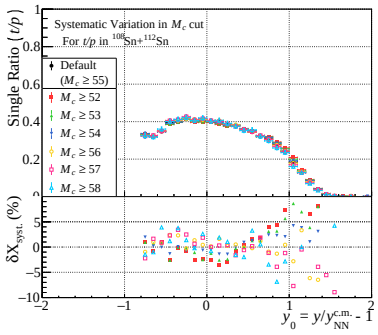

(k) t/p in ^{108}Sn + ^{112}Sn.

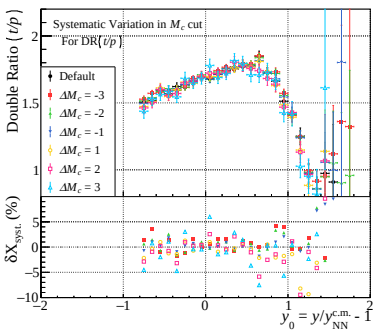

(l) $DR_{t/p}$.

Figure E.2: Systematic variations derived from the minimum multiplicity threshold. Each figure contains the same kind of spectra as those in Fig. E.1. Note that a wider y-axis range of ±10% is taken in bottom panels in each figure, since the multiplicity selection affects the $\mathrm{d}N/\mathrm{d}y_0$ spectra strongly compared to other types of variations.

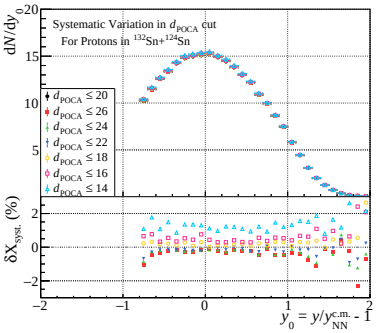

(a) Protons in ^{132}Sn + ^{124}Sn.

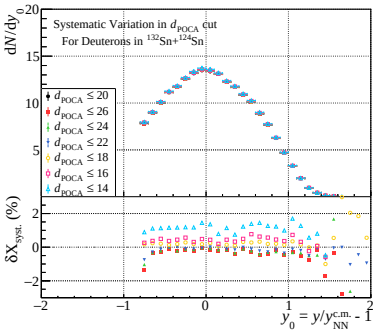

(b) Deuterons in ^{132}Sn + ^{124}Sn.

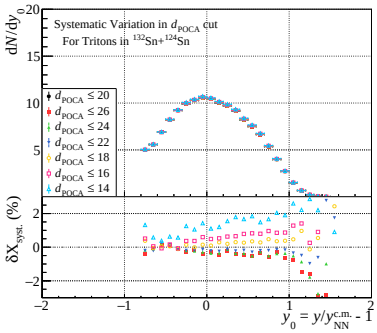

(c) Tritons in ^{132}Sn + ^{124}Sn.

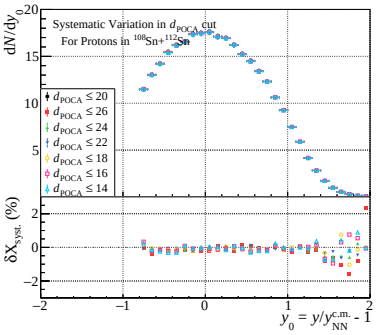

(d) Protons in ^{108}Sn + ^{112}Sn.

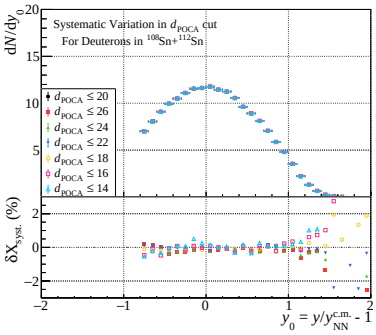

(e) Deuterons in ^{108}Sn + ^{112}Sn.

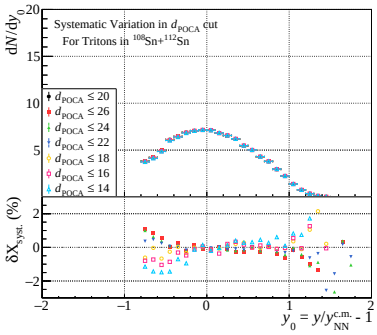

(f) Tritons in ^{108}Sn + ^{112}Sn.

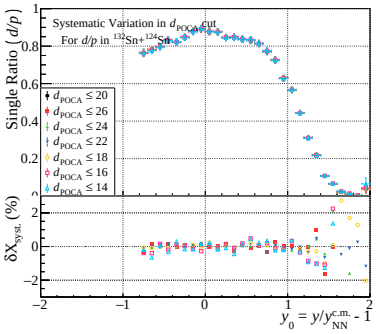

(g) d/p in ^{132}Sn + ^{124}Sn.

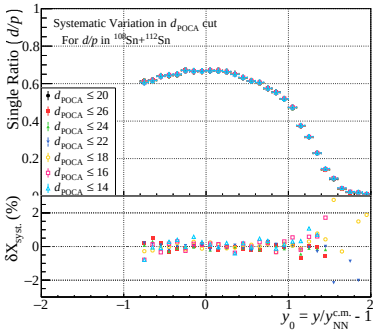

(h) d/p in ^{108}Sn + ^{112}Sn.

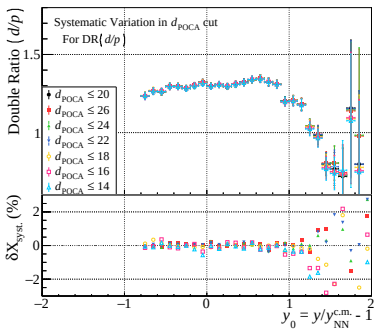

(i) $DR_{d/p}$.

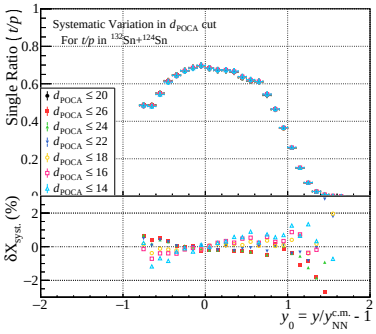

(j) t/p in ^{132}Sn + ^{124}Sn.

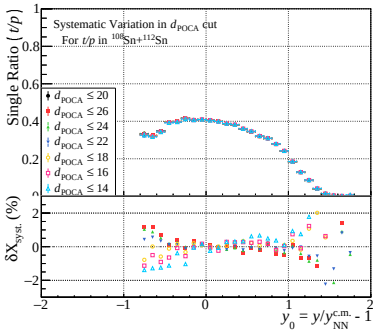

(k) t/p in ^{108}Sn + ^{112}Sn.

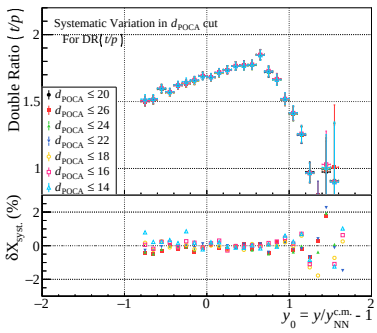

(l) $DR_{t/p}$.

Figure E.3: Systematic variations derived from the d_{POCA} threshold. Each figure contains the same kind of spectra as those in Fig. E.1.

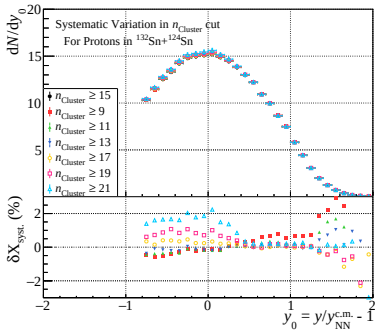

(a) Protons in ^{132}Sn + ^{124}Sn.

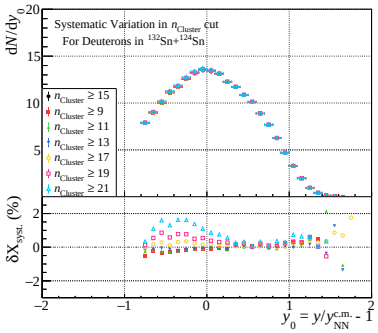

(b) Deuterons in ^{132}Sn + ^{124}Sn.

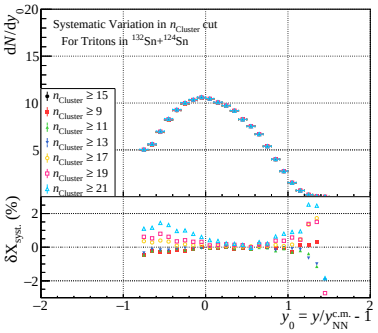

(c) Tritons in ^{132}Sn + ^{124}Sn.

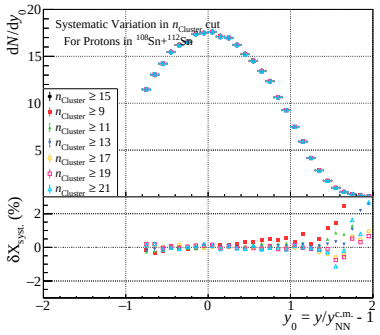

(d) Protons in ^{108}Sn + ^{112}Sn.

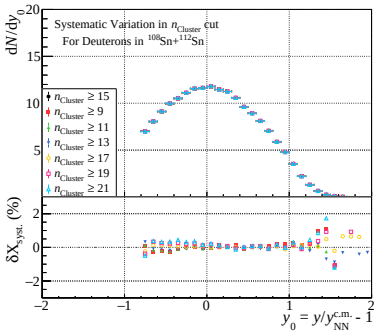

(e) Deuterons in ^{108}Sn + ^{112}Sn.

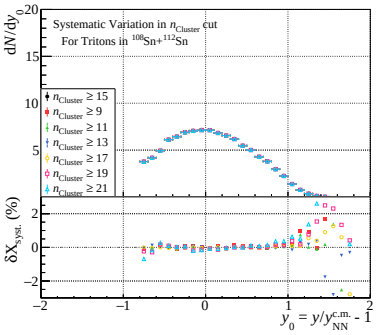

(f) Tritons in ^{108}Sn + ^{112}Sn.

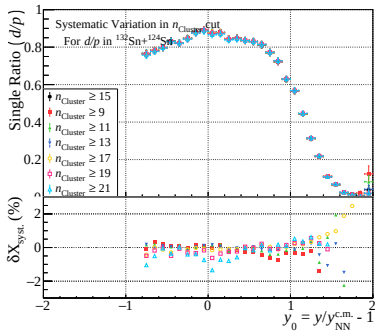

(g) d/p in ^{132}Sn + ^{124}Sn.

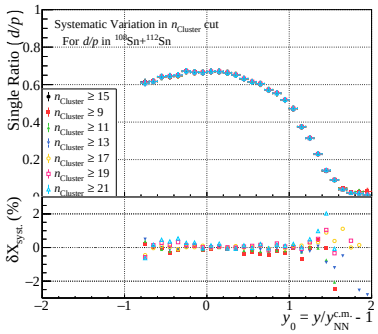

(h) d/p in ^{108}Sn + ^{112}Sn.

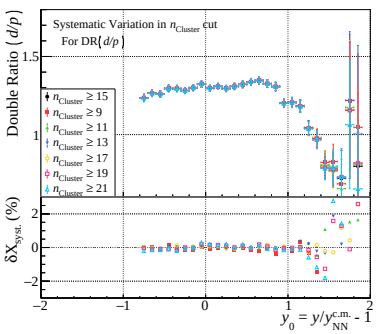

(i) $DR_{d/p}$.

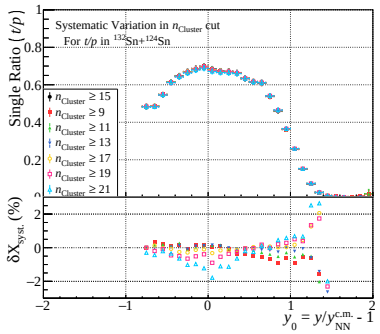

(j) t/p in ^{132}Sn + ^{124}Sn.

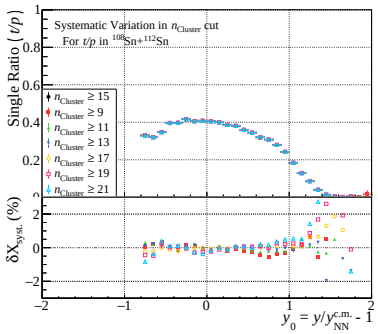

(k) t/p in ^{108}Sn + ^{112}Sn.

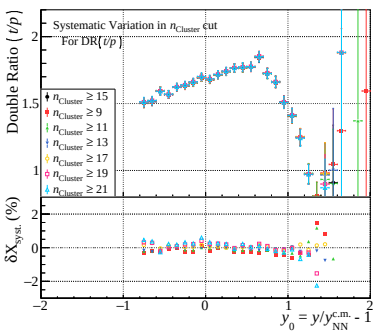

(l) $DR_{t/p}$.

Figure E.4: Systematic variations derived from the n_{Cluster} threshold. Each figure contains the same kind of spectra as those in Fig. E.1.

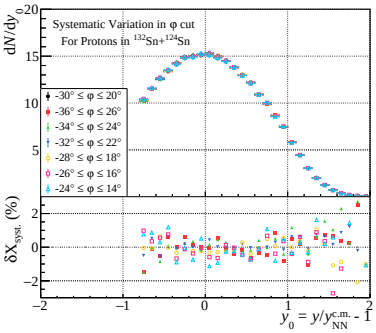

(a) Protons in ^{132}Sn + ^{124}Sn.

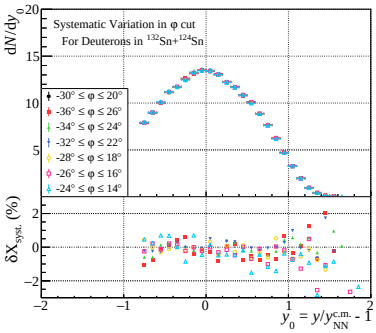

(b) Deuterons in ^{132}Sn + ^{124}Sn.

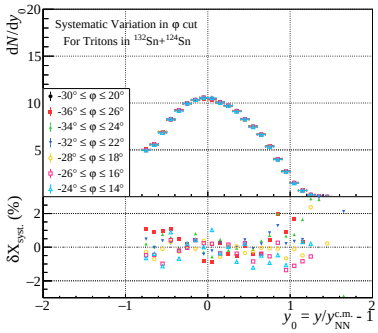

(c) Tritons in ^{132}Sn + ^{124}Sn.

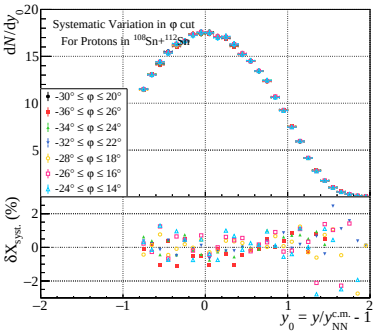

(d) Protons in ^{108}Sn + ^{112}Sn.

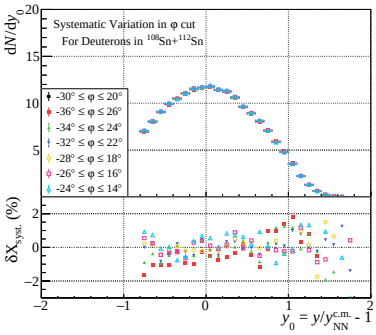

(e) Deuterons in ^{108}Sn + ^{112}Sn.

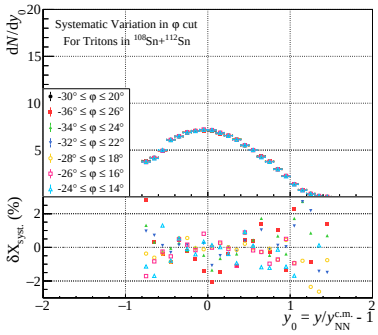

(f) Tritons in ^{108}Sn + ^{112}Sn.

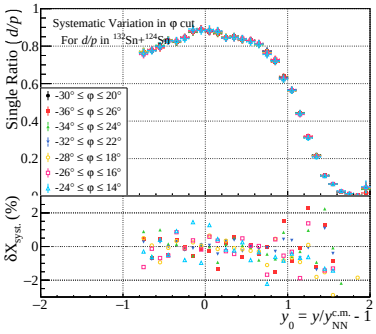

(g) d/p in ^{132}Sn + ^{124}Sn.

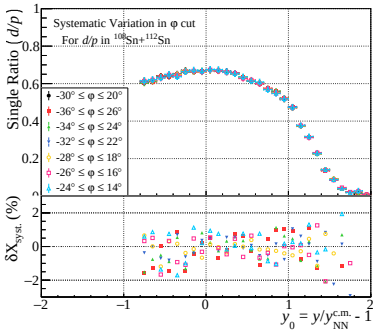

(h) d/p in ^{108}Sn + ^{112}Sn.

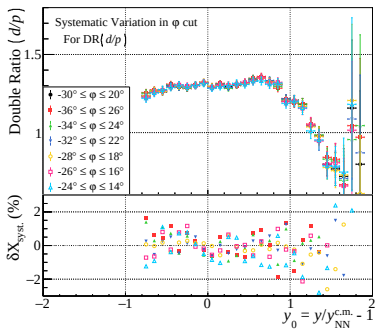

(i) $DR_{d/p}$.

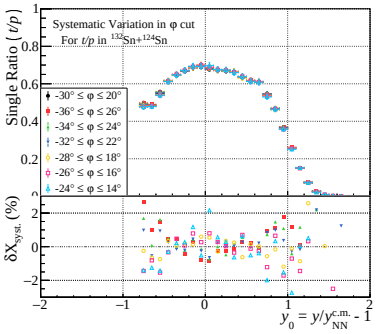

(j) t/p in ^{132}Sn + ^{124}Sn.

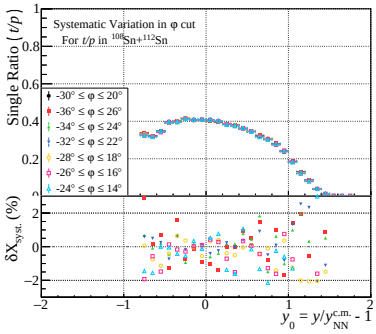

(k) t/p in ^{108}Sn + ^{112}Sn.

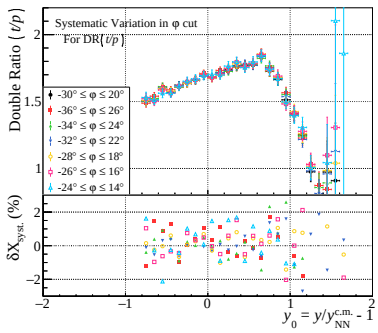

(l) $DR_{t/p}$.

Figure E.5: Systematic variations derived from the ϕ angle cut. Each figure contains the same kind of spectra as those in Fig. E.1.

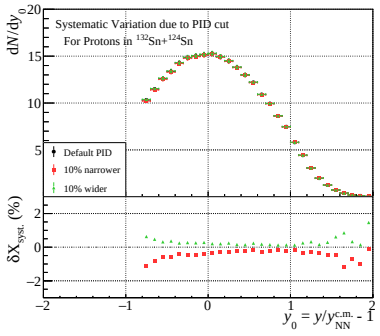

(a) Protons in ^{132}Sn + ^{124}Sn.

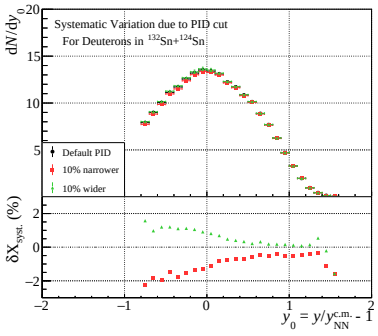

(b) Deuterons in ^{132}Sn + ^{124}Sn.

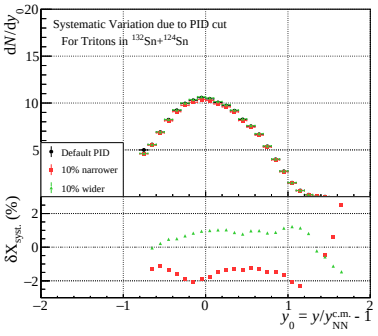

(c) Tritons in ^{132}Sn + ^{124}Sn.

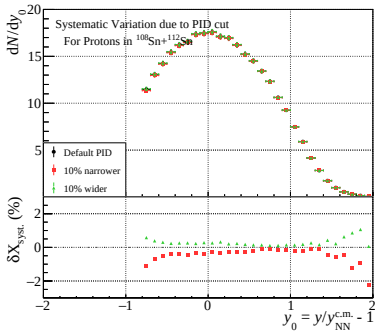

(d) Protons in ^{108}Sn + ^{112}Sn.

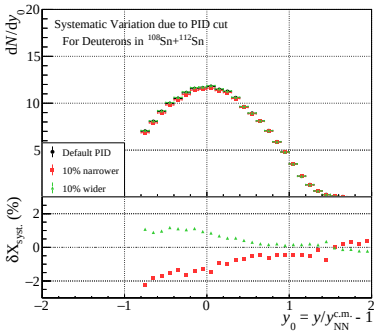

(e) Deuterons in ^{108}Sn + ^{112}Sn.

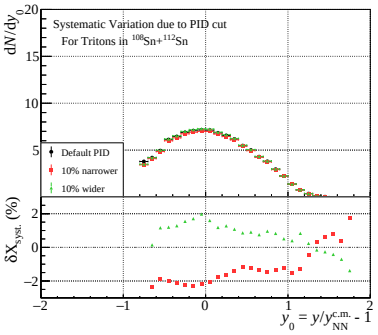

(f) Tritons in ^{108}Sn + ^{112}Sn.

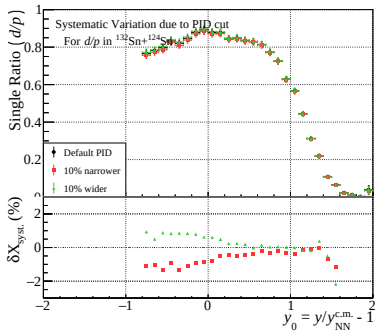

(g) d/p in ^{132}Sn + ^{124}Sn.

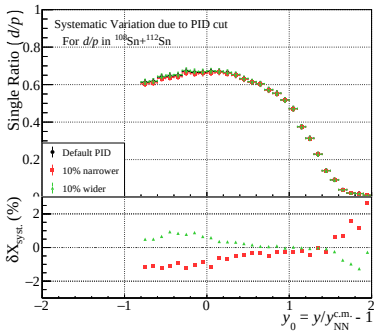

(h) d/p in ^{108}Sn + ^{112}Sn.

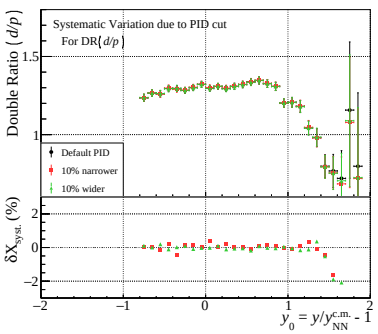

(i) $DR_{d/p}$.

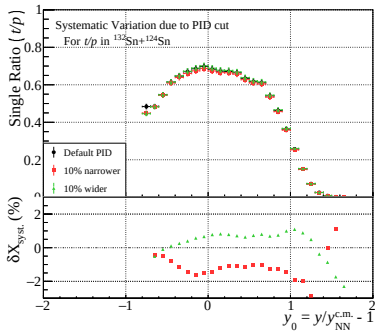

(j) t/p in ^{132}Sn + ^{124}Sn.

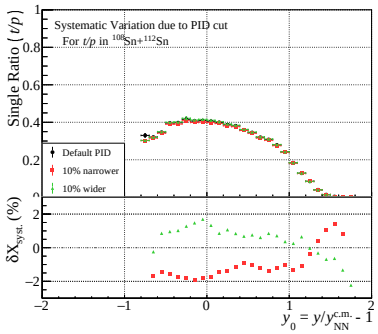

(k) t/p in ^{108}Sn + ^{112}Sn.

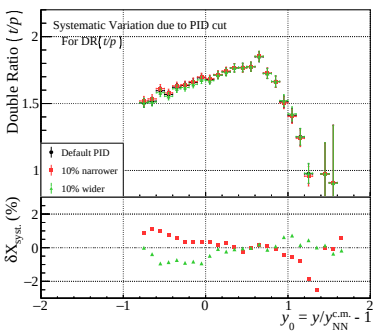

(l) $DR_{t/p}$.

Figure E.6: Systematic variations derived from the PID gate. Each figure contains the same kind of spectra as those in Fig. E.1.

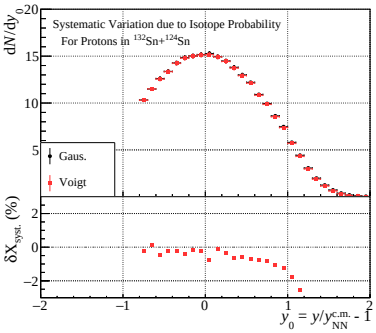

(a) Protons in ^{132}Sn + ^{124}Sn.

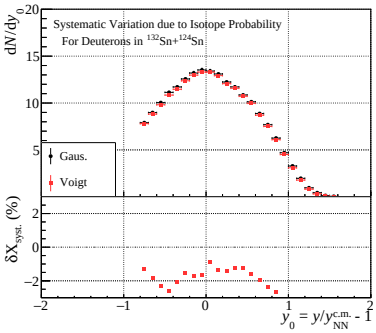

(b) Deuterons in ^{132}Sn + ^{124}Sn.

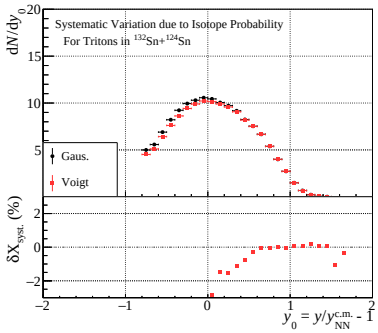

(c) Tritons in ^{132}Sn + ^{124}Sn.

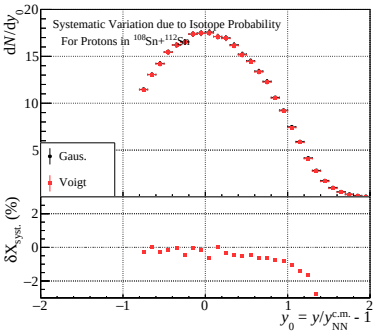

(d) Protons in ^{108}Sn + ^{112}Sn.

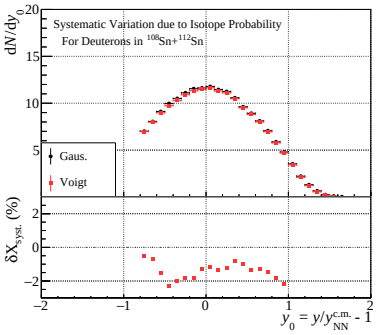

(e) Deuterons in ^{108}Sn + ^{112}Sn.

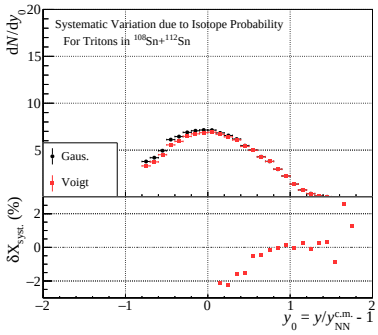

(f) Tritons in ^{108}Sn + ^{112}Sn.

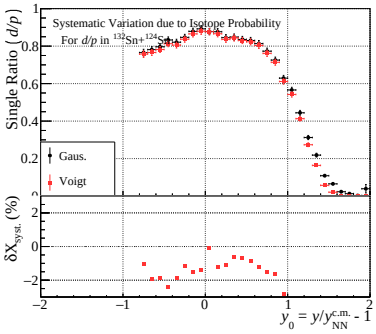

(g) d/p in ^{132}Sn + ^{124}Sn.

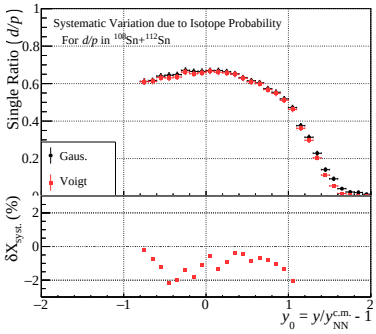

(h) d/p in ^{108}Sn + ^{112}Sn.

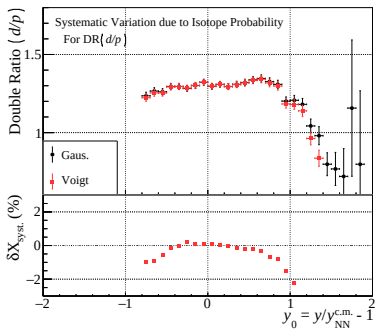

(i) $DR_{d/p}$.

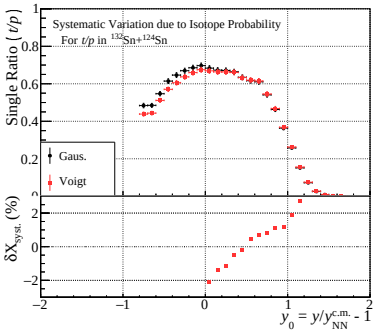

(j) t/p in ^{132}Sn + ^{124}Sn.

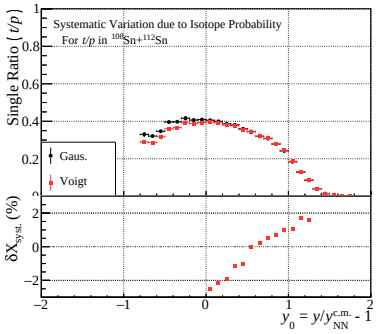

(k) t/p in ^{108}Sn + ^{112}Sn.

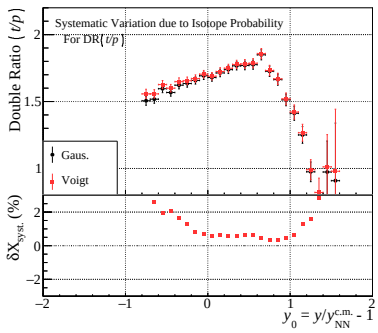

(l) $DR_{t/p}$.

Figure E.7: Systematic variations derived from the probability assignment. Each figure contains the same kind of spectra as those in Fig. E.1.

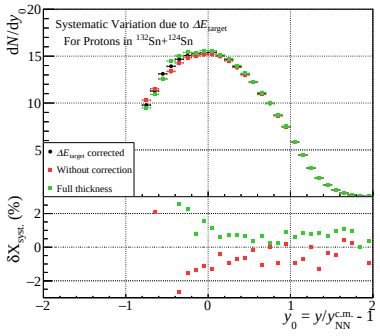

(a) Protons in ^{132}Sn + ^{124}Sn.

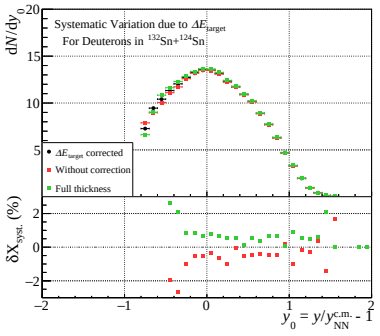

(b) Deuterons in ^{132}Sn + ^{124}Sn.

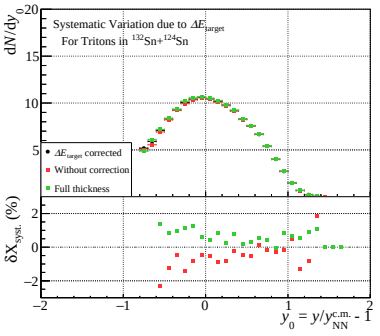

(c) Tritons in ^{132}Sn + ^{124}Sn.

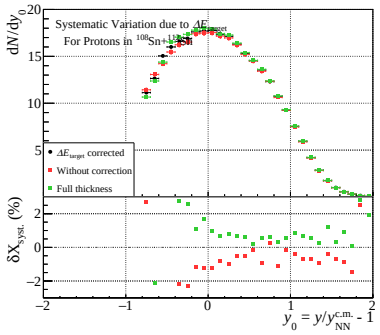

(d) Protons in ^{108}Sn + ^{112}Sn.

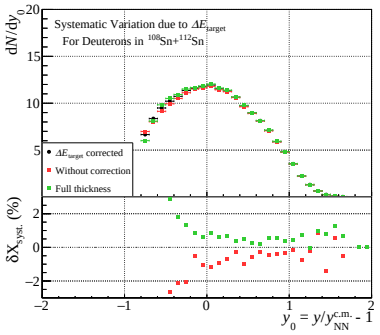

(e) Deuterons in ^{108}Sn + ^{112}Sn.

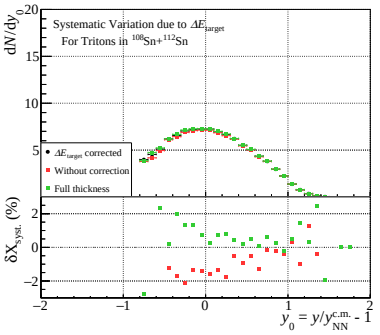

(f) Tritons in ^{108}Sn + ^{112}Sn.

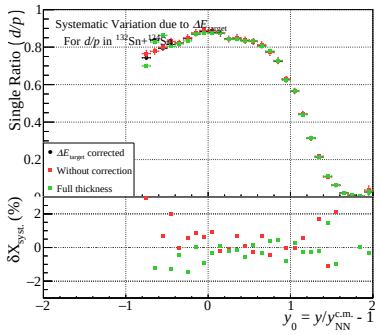

(g) d/p in ^{132}Sn + ^{124}Sn.

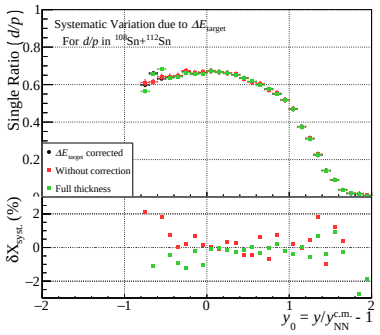

(h) d/p in ^{108}Sn + ^{112}Sn.

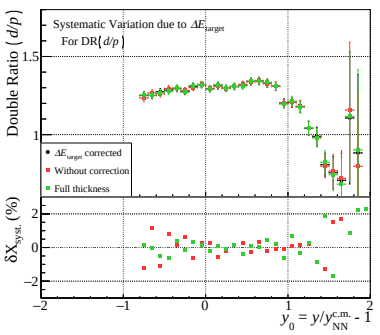

(i) $DR_{d/p}$.

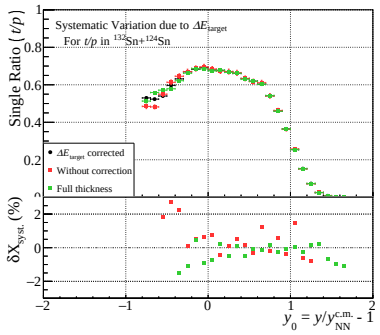

(j) t/p in ^{132}Sn + ^{124}Sn.

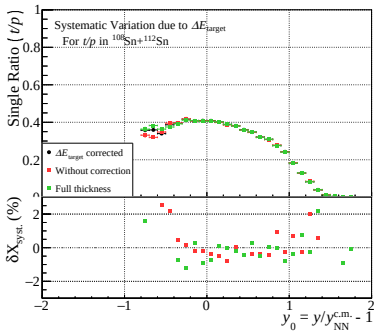

(k) t/p in ^{108}Sn + ^{112}Sn.

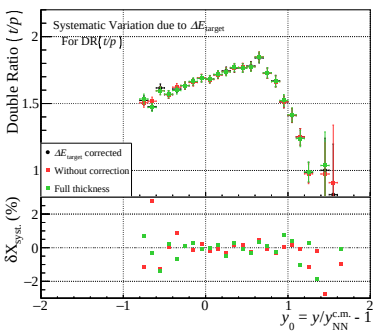

(l) $DR_{t/p}$.

Figure E.8: Systematic variations derived from the ΔE_{target} correction. Each figure contains the same kind of spectra as those in Fig. E.1.

Bibliography

[1] B. P. Abbott, *et al.*, GW170817: Observation of Gravitational Waves from a Binary Neutron Star Inspiral, Physical Review Letters **119**, 161101 (2017).

[2] B. P. Abbott, *et al.*, Multi-messenger Observations of a Binary Neutron Star Merger, The Astrophysical Journal **848**, L12 (2017).

[3] B. P. Abbott, *et al.*, Gravitational waves and gamma-rays from a binary neutron star merger: GW170817 and GRB 170817A, The Astrophysical Journal **848**, L13 (2017).

[4] A. Goldstein, *et al.*, An ordinary short gamma-ray burst with extraordinary implications: Fermi -GBM detection of GRB 170817A, The Astrophysical Journal **848**, L14 (2017).

[5] V. Savchenko, *et al.*, INTEGRAL detection of the first prompt gamma-ray signal coincident with the gravitational-wave event GW170817, The Astrophysical Journal **848**, L15 (2017).

[6] S. J. Smartt, *et al.*, A kilonova as the electromagnetic counterpart to a gravitational-wave source, Nature **551**, 75 (2017).

[7] D. Kasen, *et al.*, Origin of the heavy elements in binary neutron-star mergers from a gravitational-wave event, Nature **551**, 80 (2017).

[8] R. Chornock, *et al.*, The electromagnetic counterpart of the binary neutron star merger LIGO/virgo GW170817. IV. Detection of near-infrared signatures of r-process nucleosynthesis with gemini-south, The Astrophysical Journal **848**, L19 (2017).

[9] N. R. Tanvir, *et al.*, The emergence of a lanthanide-rich kilonova following the merger of two neutron stars, The Astrophysical Journal **848**, L27 (2017).

[10] W. Reisdorf, *et al.*, Systematics of pion emission in heavy ion collisions in the 1A GeV regime, Nuclear Physics A **781**, 459 (2007).

[11] P. Russotto, *et al.*, Symmetry energy from elliptic flow in ^{197}Au+^{197}Au, Physics Letters B **697**, 471 (2011).

[12] P. Russotto, *et al.*, Results of the ASY-EOS experiment at GSI: The symmetry energy at suprasaturation density, Physical Review C **94**, 034608 (2016).

[13] Z. Xiao, *et al.*, Circumstantial evidence for a soft nuclear symmetry energy at suprasaturation densities, Physical Review Letters **102**, 062502 (2009).

[14] Z.-Q. Feng *et al.*, Probing high-density behavior of symmetry energy from pion emission in heavy-ion collisions, Physics Letters B **683**, 140 (2010).

[15] M. D. Cozma, *et al.*, Toward a model-independent constraint of the high-density dependence of the symmetry energy, Physical Review C **88**, 044912 (2013).

[16] M. D. Cozma, Feasibility of constraining the curvature parameter of the symmetry energy using elliptic flow data, The European Physical Journal A **54**, 40 (2018).

[17] A. Ono, *et al.*, Antisymmetrized Version of Molecular Dynamics with Two-Nucleon Collisions and its Application to Heavy Ion Reactions, Progress of Theoretical Physics **87**, 1185 (1992).

[18] N. Ikeno, *et al.*, Probing neutron-proton dynamics by pions, Physical Review C **93**, 044612 (2016).

[19] A. Ono, Cluster correlations in multifragmentation, Journal of Physics: Conference Series **420**, 012103 (2013).

[20] A. Ono, in *Proceedings of 13th International Conference on Nucleus-Nucleus Collisions* (Journal of the Physical Society of Japan, Saitama, Japan, 2020).

[21] M. Kaneko, *et al.*, Kyoto Multiplicity Array for the SπRIT experiment, RIKEN Accelerator Progress Report **50**, 172 (2017).

[22] A technical paper on the multiplicity trigger detector is under preparation, which is going to be submitted to NIM journal.

[23] M. Kaneko, *et al.*, Rapidity distributions of Z = 1 isotopes and the nuclear symmetry energy from Sn+Sn collisions with radioactive beams at 270 MeV/nucleon, Physics Letters B **822**, 136681 (2021).

[24] X. Roca-Maza *et al.*, Nuclear equation of state from ground and collective excited state properties of nuclei, Progress in Particle and Nuclear Physics **101**, 96 (2018).

[25] P. Danielewicz, *et al.*, Determination of the Equation of State of Dense Matter, Science **298**, 1592 (2002).

[26] J. M. Lattimer *et al.*, Neutron star observations: Prognosis for equation of state constraints, Physics Reports **442**, 109 (2007).

[27] I. Bombaci *et al.*, Asymmetric nuclear matter equation of state, Physical Review C **44**, 1892 (1991).

[28] A. Steiner, *et al.*, Isospin asymmetry in nuclei and neutron stars, Physics Reports **411**, 325 (2005).

[29] C.-H. Lee, *et al.*, Nuclear symmetry energy, Physical Review C **57**, 3488 (1998).

[30] I. Lagaris *et al.*, Variational calculations of asymmetric nuclear matter, Nuclear Physics A **369**, 470 (1981).

[31] J. Xu, *et al.*, Locating the inner edge of the neutron star crust using terrestrial nuclear laboratory data, Physical Review C **79**, 035802 (2009).

[32] C. Gonzalez-Boquera, *et al.*, Higher-order symmetry energy and neutron star core-crust transition with Gogny forces, Physical Review C **96**, 065806 (2017).

[33] H. Jiang, *et al.*, Model dependence of the I^4 term in the symmetry energy for finite nuclei, Physical Review C **91**, 054302 (2015).

[34] J. Blaizot, Nuclear compressibilities, Physics Reports **64**, 171 (1980).

[35] D. H. Youngblood, *et al.*, Incompressibility of nuclear matter from the giant monopole resonance, Physical Review Letters **82**, 691 (1999).

[36] S. Shlomo, *et al.*, Deducing the nuclear-matter incompressibility coefficient from data on isoscalar compression modes, The European Physical Journal A - Hadrons and Nuclei **30**, 23 (2006).

[37] G. Colò, *et al.*, Microscopic determination of the nuclear incompressibility within the non-relativistic framework, Physical Review C **70**, 024307 (2004).

[38] L.-W. Chen *et al.*, Correlations between the nuclear breathing mode energy and properties of asymmetric nuclear matter, Journal of Physics G: Nuclear and Particle Physics **39**, 035104 (2012).

[39] J. R. Stone, *et al.*, Incompressibility in finite nuclei and nuclear matter, Physical Review C **89**, 044316 (2014).

[40] J. Aichelin *et al.*, Subthreshold kaon production as a probe of the nuclear equation of state, Physical Review Letters **55**, 2661 (1985).

[41] C. Fuchs, *et al.*, Origin of subthreshold K^+ production in heavy ion collisions, Physical Review C **56**, R606 (1997).

[42] C. Fuchs, *et al.*, Probing the nuclear equation of state by K^+ production in heavy-ion collisions, Physical Review Letters **86**, 1974 (2001).

[43] C. Sturm, *et al.*, Evidence for a soft nuclear equation-of-state from kaon production in heavy-ion collisions, Physical Review Letters **86**, 39 (2001).

[44] A. Schmah, *et al.*, Kaon and pion emission in asymmetric C+Au and Au+C collisions at 1.0A GeV and 1.8A GeV, Physical Review C **71**, 064907 (2005).

[45] C. Fuchs *et al.*, Modelization of the EOS, The European Physical Journal A - Hadrons and Nuclei **30**, 5 (2006).

[46] C. Hartnack, *et al.*, Hadronic matter is soft, Physical Review Letters **96**, 012302 (2006).

[47] A. Andronic, *et al.*, Systematics of stopping and flow in Au+ Au collisions, The European Physical Journal A - Hadrons and Nuclei **30**, 31 (2006).

[48] W. Reisdorf, *et al.*, Systematics of azimuthal asymmetries in heavy ion collisions in the 1A GeV regime, Nuclear Physics A **876**, 1 (2012).

[49] A. Le Fèvre, *et al.*, Constraining the nuclear matter equation of state around twice saturation density, Nuclear Physics A **945**, 112 (2016).

[50] Y. Wang, *et al.*, Determination of the nuclear incompressibility from the rapidity-dependent elliptic flow in heavy-ion collisions at beam energies 0.4A–1.0A GeV, Physics Letters B **778**, 207 (2018).

[51] G. Taranto, *et al.*, Selecting microscopic equations of state, Physical Review C **87**, 045803 (2013).

[52] C. J. Horowitz, *et al.*, A way forward in the study of the symmetry energy: Experiment, theory, and observation, Journal of Physics G: Nuclear and Particle Physics **41**, 093001 (2014).

[53] M. Baldo *et al.*, The Nuclear Symmetry Energy, Progress in Particle and Nuclear Physics **91**, 203 (2016).

[54] V. Baran, *et al.*, Isospin effects in nuclear fragmentation, Nuclear Physics A **703**, 603 (2002).

[55] P. Möller, *et al.*, New finite-range droplet mass model and equation-of-state parameters, Physical Review Letters **108**, 052501 (2012).

[56] P. Danielewicz, *et al.*, Symmetry energy III: Isovector skins, Nuclear Physics A **958**, 147 (2017).

[57] P. Danielewicz *et al.*, Symmetry energy II: Isobaric analog states, Nuclear Physics A **922**, 1 (2014).

[58] M. A. Famiano, *et al.*, Neutron and Proton Transverse Emission Ratio Measurements and the Density Dependence of the Asymmetry Term of the Nuclear Equation of State, Physical Review Letters **97**, 052701 (2006).

[59] M. B. Tsang, *et al.*, Isospin diffusion and the nuclear symmetry energy in heavy ion reactions, Physical Review Letters **92**, 062701 (2004).

[60] M. B. Tsang, *et al.*, Constraints on the density dependence of the symmetry energy, Physical Review Letters **102**, 122701 (2009).

[61] T. X. Liu, *et al.*, Isospin observables from fragment energy spectra, Physical Review C **86**, 024605 (2012).

[62] W. Reisdorf, *et al.*, Systematics of central heavy ion collisions in the 1A GeV regime, Nuclear Physics A **848**, 366 (2010).

[63] Y. Wang, *et al.*, ^{3}H/^{3}He ratio as a probe of the nuclear symmetry energy at sub-saturation densities, The European Physical Journal A **51**, 37 (2015).

[64] G. Jhang, *et al.*, Symmetry energy investigation with pion production from Sn+Sn systems, Physics Letters B **813**, 136016 (2021).

[65] J. Estee, *et al.*, Probing the symmetry energy with the spectral pion ratio, Physical Review Letters **126**, 162701 (2021).

[66] Z. Kohley, *et al.*, Investigation of transverse collective flow of intermediate mass fragments, Physical Review C **82**, 064601 (2010).

[67] Z. Kohley, *et al.*, Transverse collective flow and midrapidity emission of isotopically identified light charged particles, Physical Review C **83**, 044601 (2011).

[68] Z. Kohley, *et al.*, Sensitivity of intermediate mass fragment flows to the symmetry energy, Physical Review C **85**, 064605 (2012).

[69] M. B. Tsang, *et al.*, Constraints on the symmetry energy and neutron skins from experiments and theory, Physical Review C **86**, 015803 (2012).

[70] B.-A. Li *et al.*, Constraining the neutron–proton effective mass splitting using empirical constraints on the density dependence of nuclear symmetry energy around normal density, Physics Letters B **727**, 276 (2013).

[71] J. M. Lattimer *et al.*, CONSTRAINING THE SYMMETRY PARAMETERS OF THE NUCLEAR INTERACTION, The Astrophysical Journal **771**, 51 (2013).

[72] M. Oertel, *et al.*, Equations of state for supernovae and compact stars, Reviews of Modern Physics **89**, 015007 (2017).

[73] Y. Zhang, *et al.*, Constraints on the symmetry energy and its associated parameters from nuclei to neutron stars, Physical Review C **101**, 034303 (2020).

[74] B. Alex Brown, Neutron radii in nuclei and the neutron equation of state, Physical Review Letters **85**, 5296 (2000).

[75] J. Xu, Transport approaches for the description of intermediate-energy heavy-ion collisions, Progress in Particle and Nuclear Physics **106**, 312 (2019).

[76] R. Chen, *et al.*, Single-nucleon potential decomposition of the nuclear symmetry energy, Physical Review C **85**, 024305 (2012).

[77] B.-A. Li, *et al.*, Equation of state of asymmetric nuclear matter and collisions of neutron-rich nuclei, Physical Review Letters **78**, 1644 (1997).

[78] Q. Li, *et al.*, Probing the density dependence of the symmetry potential at low and high densities, Physical Review C **72**, 034613 (2005).

[79] B.-A. Li, *et al.*, Double neutron/proton ratio of nucleon emissions in isotopic reaction systems as a robust probe of nuclear symmetry energy, Physics Letters B **634**, 378 (2006).

[80] Q. Li, *et al.*, Probing the symmetry energy and the degree of isospin equilibrium, Physical Review C **73**, 051601 (2006).

[81] S. Kumar, *et al.*, Sensitivity of neutron to proton ratio toward the high density behavior of the symmetry energy in heavy-ion collisions, Physical Review C **85**, 024620 (2012).

[82] B.-A. Li, Neutron-proton differential flow as a probe of isospin-dependence of the nuclear equation of state, Physical Review Letters **85**, 4221 (2000).

[83] B.-A. Li, Probing the High Density Behavior of the Nuclear Symmetry Energy with High Energy Heavy-Ion Collisions, Physical Review Letters **88**, 192701 (2002).

[84] B.-A. Li, High density behaviour of nuclear symmetry energy and high energy heavy-ion collisions, Nuclear Physics A **708**, 365 (2002).

[85] V. Greco, *et al.*, Relativistic effects in the search for high density symmetry energy, Physics Letters B **562**, 215 (2003).

[86] M. Cozma, Neutron–proton elliptic flow difference as a probe for the high density dependence of the symmetry energy, Physics Letters B **700**, 139 (2011).

[87] L.-W. Chen, *et al.*, Light cluster production in intermediate energy heavy-ion collisions induced by neutron-rich nuclei, Nuclear Physics A **729**, 809 (2003).

[88] Y. Zhang *et al.*, Probing the density dependence of the symmetry potential with peripheral heavy-ion collisions, Physical Review C **71**, 024604 (2005).

[89] G.-C. Yong, *et al.*, Triton-^{3}He relative and differential flows as probes of the nuclear symmetry energy at supra-saturation densities, Physical Review C **80**, 044608 (2009).

[90] B.-A. Li, *et al.*, Near-threshold pion production with radioactive beams, Physical Review C **71**, 014608 (2005).

[91] G. Ferini, *et al.*, Isospin effects on subthreshold kaon production at intermediate energies, Physical Review Letters **97**, 202301 (2006).

[92] G.-C. Yong, *et al.*, Single and double π^-/π^+ ratios in heavy-ion reactions as probes of the high-density behavior of the nuclear symmetry energy, Physical Review C **73**, 034603 (2006).

[93] Z.-G. Xiao, *et al.*, Probing nuclear symmetry energy at high densities using pion, kaon, eta and photon productions in heavy-ion collisions, The European Physical Journal A **50**, 37 (2014).

[94] N. Ikeno, *et al.*, Erratum: Probing neutron-proton dynamics by pions [Phys. Rev. C 93, 044612 (2016)], Physical Review C **97**, 069902 (2018).

[95] G.-C. Yong, Modeling pion production in heavy-ion collisions at intermediate energies, Physical Review C **96**, 044605 (2017).

[96] M. B. Tsang, *et al.*, Pion production in rare-isotope collisions, Physical Review C **95**, 044614 (2017).

[97] Q. Li, *et al.*, Σ^-/Σ^+ ratio as a candidate for probing the density dependence of the symmetry potential at high nuclear densities, Physical Review C **71**, 054907 (2005).

[98] W.-J. Xie, *et al.*, Symmetry energy and pion production in the Boltzmann–Langevin approach, Physics Letters B **718**, 1510 (2013).

[99] J. Hong *et al.*, Subthreshold pion production within a transport description of central Au + Au collisions, Physical Review C **90**, 024605 (2014).

[100] J. Xu, *et al.*, Energy dependence of pion in-medium effects on the π^-/π^+ ratio in heavy-ion collisions, Physical Review C **87**, 067601 (2013).

[101] W.-M. Guo, *et al.*, Effects of nuclear symmetry energy and in-medium NN cross section in heavy-ion collisions at beam energies below the pion production threshold, Physical Review C **90**, 044605 (2014).

[102] G.-C. Yong, Cross-checking the symmetry energy at high densities, Physical Review C **93**, 044610 (2016).

[103] W.-M. Guo, *et al.*, Effects of pion potential and nuclear symmetry energy on the π^-/π^+ ratio in heavy-ion collisions at beam energies around the pion production threshold, Physical Review C **91**, 054616 (2015).

[104] Z.-Q. Feng, *et al.*, In-medium and isospin effects on particle production near threshold energies in heavy-ion collisions, Physical Review C **92**, 044604 (2015).

[105] Z. Zhang *et al.*, Medium effects on pion production in heavy ion collisions, Physical Review C **95**, 064604 (2017).

[106] M. D. Cozma, Constraining the density dependence of the symmetry energy using the multiplicity and average p_T ratios of charged pions, Physical Review C **95**, 014601 (2017).

[107] B.-A. Li, Symmetry potential of the $\Delta(1232)$ resonance and its effects on the π^-/π^+ ratio in heavy-ion collisions near the pion-production threshold, Physical Review C **92**, 034603 (2015).

[108] W.-M. Guo, *et al.*, Effect of Δ potential on the π^-/π^+ ratio in heavy-ion collisions at intermediate energies, Physical Review C **92**, 054619 (2015).

[109] N. Ikeno, *et al.*, Effects of Pauli blocking on pion production in central collisions of neutron-rich nuclei, Physical Review C **101**, 034607 (2020).

[110] T. Song *et al.*, Modifications of the pion-production threshold in the nuclear medium in heavy ion collisions and the nuclear symmetry energy, Physical Review C **91**, 014901 (2015).

[111] B.-A. Li, *et al.*, Effects of the kinetic symmetry energy reduced by short-range correlations in heavy-ion collisions at intermediate energies, Physical Review C **91**, 044601 (2015).

[112] M. Cozma, The impact of energy conservation in transport models on the π^-/π^+ multiplicity ratio in heavy-ion collisions and the symmetry energy, Physics Letters B **753**, 166 (2016).

[113] J. Xu, *et al.*, Understanding transport simulations of heavy-ion collisions at 100A and 400A MeV: Comparison of heavy-ion transport codes under controlled conditions, Physical Review C **93**, 044609 (2016).

[114] Y.-X. Zhang, *et al.*, Comparison of heavy-ion transport simulations: Collision integral in a box, Physical Review C **97**, 034625 (2018).

[115] A. Ono, *et al.*, Comparison of heavy-ion transport simulations: Collision integral with pions and Δ resonances in a box, Physical Review C **100**, 044617 (2019).

[116] Y. Leifels, *et al.*, Exclusive studies of neutron and charged particle emission in collisions of ^{197}Au +^{197}Au at 400 MeV/nucleon, Physical Review Letters **71**, 963 (1993).

[117] D. Lambrecht, *et al.*, Energy dependence of collective flow of neutrons and protons in ^{197}Au +^{197}Au collisions, Zeitschrift für Physik A Hadrons and Nuclei **350**, 115 (1994).

[118] Y. Wang, *et al.*, Constraining the high-density nuclear symmetry energy with the transverse-momentum-dependent elliptic flow, Physical Review C **89**, 044603 (2014).

[119] Y. Wang, *et al.*, Study of the nuclear symmetry energy from the rapidity-dependent elliptic flow in heavy-ion collisions around 1 GeV/nucleon regime, Physics Letters B **802**, 135249 (2020).

[120] Z.-Q. Feng, Nuclear in-medium effects and collective flows in heavy-ion collisions at intermediate energies, Physical Review C **85**, 014604 (2012).

[121] Y. Wang, *et al.*, Collective flow of light particles in Au + Au collisions at intermediate energies, Physical Review C **89**, 034606 (2014).

[122] W. Reisdorf, *et al.*, Nuclear stopping from 0.09A to 1.93A GeV and its correlation to flow, Physical Review Letters **92**, 232301 (2004).

[123] L.-W. Chen, *et al.*, Effects of momentum-dependent nuclear potential on two-nucleon correlation functions and light cluster production in intermediate energy heavy-ion collisions, Physical Review C **69**, 054606 (2004).

[124] A. Ono, Dynamics of clusters and fragments in heavy-ion collisions, Progress in Particle and Nuclear Physics **105**, 139 (2019).

[125] A. Ono, Cluster production within antisymmetrized molecular dynamics, EPJ Web of Conferences **122**, 11001 (2016).

[126] D. D. S. Coupland, *et al.*, Influence of transport variables on isospin transport ratios, Physical Review C **84**, 054603 (2011).

[127] W. Reisdorf, *et al.*, Central collisions of Au on Au at 150, 250 and 400 A·MeV, Nuclear Physics A **612**, 493 (1997).

[128] S. Hudan, *et al.*, Characteristics of the fragments produced in central collisions of ^{129}Xe+^{nat}Sn from 32A to 50 A MeV, Physical Review C **67**, 064613 (2003).

[129] B. Borderie *et al.*, Nuclear multifragmentation and phase transition for hot nuclei, Progress in Particle and Nuclear Physics **61**, 551 (2008).

[130] Y. Zhang, *et al.*, Effect of isospin-dependent cluster recognition on the observables in heavy ion collisions, Physical Review C **85**, 051602 (2012).

[131] K. Zbiri, *et al.*, Transition from participant to spectator fragmentation in Au+Au reactions between 60A and 150A MeV, Phys. Rev. C **75**, 034612 (2007).

[132] K. Ikeda, *et al.*, The systematic structure-change into the molecule-like structures in the self-conjugate 4n nuclei, Progress of Theoretical Physics Supplement **E68**, 464 (1968).

[133] S. Adachi, *et al.*, Systematic analysis of inelastic α scattering off self-conjugate A=4n nuclei, Physical Review C **97**, 014601 (2018).

[134] J. Tanaka, *et al.*, Formation of α clusters in dilute neutron-rich matter, Science **371**, 260 (2021).

[135] A. Arcones, *et al.*, Influence of light nuclei on neutrino-driven supernova outflows, Physical Review C **78**, 015806 (2008).

[136] S. Typel, *et al.*, Composition and thermodynamics of nuclear matter with light clusters, Physical Review C **81**, 015803 (2010).

[137] S. Typel, *et al.*, Effects of the liquid-gas phase transition and cluster formation on the symmetry energy, The European Physical Journal A **50**, 17 (2014).

[138] G. Röpke, Parametrization of light nuclei quasiparticle energy shifts and composition of warm and dense nuclear matter, Nuclear Physics A **867**, 66 (2011).

[139] G. Röpke, Nuclear matter equation of state including two-, three-, and four-nucleon correlations, Physical Review C **92**, 054001 (2015).

[140] S. S. Avancini, *et al.*, Light clusters and pasta phases in warm and dense nuclear matter, Physical Review C **95**, 045804 (2017).

[141] P. Danielewicz *et al.*, Production of deuterons and pions in a transport model of energetic heavy-ion reactions, Nuclear Physics A **533**, 712 (1991).

[142] P. Danielewicz *et al.*, Blast of light fragments from central heavy-ion collisions, Physical Review C **46**, 2002 (1992).

[143] G. Tian, *et al.*, Cluster correlation and fragment emission in ^{12}C+^{12}C at 95 MeV/nucleon, Physical Review C **97**, 034610 (2018).

[144] J. I. Kapusta, Mechanisms for deuteron production in relativistic nuclear collisions, Physical Review C: Nuclear Physics **21**, 1301 (1980).

[145] E. Santini, *et al.*, Fragment formation in central heavy ion collisions at relativistic energies, Nuclear Physics A **756**, 468 (2005).

[146] B. Hong, *et al.*, Proton and deuteron rapidity distributions and nuclear stopping in ^{96}Ru(^{96}Zr)+^{96}Ru(^{96}Zr) collisions at 400AMeV, Physical Review C **66**, 034901 (2002).

[147] T. Gaitanos, *et al.*, Stopping and isospin equilibration in heavy ion collisions, Physics Letters B **595**, 209 (2004).

[148] Y. Zhang, *et al.*, In-medium NN cross sections determined from the nuclear stopping and collective flow in heavy-ion collisions at intermediate energies, Physical Review C **75**, 034615 (2007).

[149] S. Kumar, *et al.*, Effect of the symmetry energy on nuclear stopping and its relation to the production of light charged fragments, Physical Review C **81**, 014601 (2010).

[150] F. Rami, *et al.*, Isospin tracing: A probe of nonequilibrium in central heavy-ion collisions, Physical Review Letters **84**, 1120 (2000).

[151] P. Li, *et al.*, Effects of the in-medium nucleon-nucleon cross section on collective flow and nuclear stopping in heavy-ion collisions in the Fermi-energy domain, Physical Review C **97**, 044620 (2018).

[152] A. Hombach, *et al.*, Isospin equilibration in relativistic heavy-ion collisions, The European Physical Journal A - Hadrons and Nuclei **5**, 77 (1999).

[153] J. Su, *et al.*, Effects of symmetry energy and effective k-mass splitting on central ^{96}Ru(^{96}Zr)+^{96}Zr(^{96}Ru) collisions at 50 to 400 MeV/nucleon, Physical Review C **96**, 024601 (2017).

[154] Z. Chajecki, *et al.*, Scaling properties of light-cluster production, arXiv:1402.5216 [nucl-ex] (2014), arXiv:1402.5216 [nucl-ex] .

[155] Y. Yano, The RIKEN RI beam factory project: A status report, Nuclear Instruments and Methods in Physics Research Section B: Beam Interactions with Materials and Atoms **261**, 1009 (2007).

[156] H. Okuno, *et al.*, Progress of RIBF accelerators, Progress of Theoretical and Experimental Physics **2012**, 03C002 (2012).

[157] T. Motobayashi *et al.*, Research with fast radioactive isotope beams at RIKEN, Progress of Theoretical and Experimental Physics **2012**, 03C001 (2012).

[158] T. Nakamura, *et al.*, Exotic nuclei explored at in-flight separators, Progress in Particle and Nuclear Physics **97**, 53 (2017).

[159] H. Sakurai, Nuclear physics with RI Beam Factory, Frontiers of Physics **13**, 132111 (2018).

[160] Y. Higurashi, *et al.*, Results of RIKEN superconducting electron cyclotron resonance ion source with 28 GHz, Review of Scientific Instruments **83**, 02A308 (2012).

[161] Y. Higurashi, *et al.*, Recent development of RIKEN 28 GHz superconducting electron cyclotron resonance ion source, Review of Scientific Instruments **85**, 02A953 (2014).

[162] K. Suda, *et al.*, Design and construction of drift tube linac cavities for RIKEN RI Beam Factory, Nuclear Instruments and Methods in Physics Research Section A: Accelerators, Spectrometers, Detectors and Associated Equipment **722**, 55 (2013).

[163] H. Okuno, *et al.*, Present status of and recent developments at RIKEN RI beam factory, Journal of Physics: Conference Series **1401**, 012005 (2020).

[164] H. Imao, *et al.*, Charge stripping of ^{238}U ion beam by helium gas stripper, Physical Review Special Topics - Accelerators and Beams **15**, 123501 (2012).

[165] H. Hasebe, *et al.*, Development of a rotating graphite carbon disk stripper, AIP Conference Proceedings **1962**, 030004 (2018).

[166] T. Kubo, Recent progress of in-flight separators and rare isotope beam production, Nuclear Instruments and Methods in Physics Research Section B: Beam Interactions with Materials and Atoms **376**, 102 (2016).

[167] Status of the calculated production cross section as well as measurements of that at RIBF are provided here., https://www.nishina.riken.jp/ribf/BigRIPS/intensity.html.

[168] J. Benlliure, *et al.*, Production of medium-mass neutron-rich nuclei in reactions induced by ^{136}Xe projectiles at 1 A GeV on a beryllium target, Physical Review C: Nuclear Physics **78**, 054605 (2008).

[169] B. Blank, *et al.*, New neutron-deficient isotopes from ^{78}Kr fragmentation, Physical Review C: Nuclear Physics **93**, 061301 (2016).

[170] K. Sümmerer, Improved empirical parametrization of fragmentation cross sections, Physical Review C **86**, 014601 (2012).

[171] M. Bernas, *et al.*, Discovery and cross-section measurement of 58 new fission products in projectile-fission of 750 · A MeV ^{238}U, Physics Letters B **415**, 111 (1997).

[172] J. Kurcewicz, *et al.*, Discovery and cross-section measurement of neutron-rich isotopes in the element range from neodymium to platinum with the FRS, Physics Letters B **717**, 371 (2012).

[173] Y. Shimizu, *et al.*, Observation of New Neutron-rich Isotopes among Fission Fragments from In-flight Fission of 345 MeV/nucleon ^{238}U: Search for New Isotopes Conducted Concurrently with Decay Measurement Campaigns, Journal of the Physical Society of Japan **87**, 014203 (2018).

[174] N. Fukuda, *et al.*, Identification of new neutron-rich isotopes in the rare-earth region produced by 345 MeV/nucleon 238U, Journal of the Physical Society of Japan **87**, 014202 (2018).

[175] T. Kubo, *et al.*, BigRIPS separator and ZeroDegree spectrometer at RIKEN RI Beam Factory, Progress of Theoretical and Experimental Physics **2012**, 03C003 (2012).

[176] J. Dufour, *et al.*, Projectile fragments isotopic separation: Application to the lise spectrometer at GANIL, Nuclear Instruments and Methods in Physics Research Section A: Accelerators, Spectrometers, Detectors and Associated Equipment **248**, 267 (1986).

[177] N. Fukuda, *et al.*, Identification and separation of radioactive isotope beams by the BigRIPS separator at the RIKEN RI Beam Factory, Nuclear Instruments and Methods in Physics Research Section B: Beam Interactions with Materials and Atoms **317**, 323 (2013).

[178] H. Kumagai, *et al.*, Delay-line PPAC for high-energy light ions, Nuclear Instruments and Methods in Physics Research Section A: Accelerators, Spectrometers, Detectors and Associated Equipment **470**, 562 (2001).

[179] H. Kumagai, *et al.*, Development of parallel plate avalanche counter (PPAC) for BigRIPS fragment separator, Nuclear Instruments and Methods in Physics Research Section B: Beam Interactions with Materials and Atoms **317**, 717 (2013).

[180] K. Kimura, *et al.*, High-rate particle identification of high-energy heavy ions using a tilted electrode gas ionization chamber, Nuclear Instruments and Methods in Physics Research Section A: Accelerators, Spectrometers, Detectors and Associated Equipment **538**, 608 (2005).

[181] H. Sato, *et al.*, Superconducting dipole magnet for SAMURAI spectrometer, IEEE Transactions on Applied Superconductivity **23**, 4500308 (2013).

[182] H. Otsu, *et al.*, SAMURAI in its operation phase for RIBF users, Nuclear Instruments and Methods in Physics Research Section B: Beam Interactions with Materials and Atoms **376**, 175 (2016).

[183] R. Shane, *et al.*, SπRIT: A time-projection chamber for symmetry-energy studies, Nuclear Instruments and Methods in Physics Research Section A: Accelerators, Spectrometers, Detectors and Associated Equipment **784**, 513 (2015).

[184] J. E. Barney, *Charged Pion Emission from ^{112}Sn+^{124}Sn and ^{124}Sn+^{112}Sn Reactions with the SπRIT Time Projection Chamber*, Ph.D. thesis, Michigan State University (2019).

[185] J. Barney, *et al.*, The SπRIT time projection chamber, Review of Scientific Instruments **92**, 063302 (2021).

[186] R. Veenhof, Garfield, recent developments, Nuclear Instruments and Methods in Physics Research Section A: Accelerators, Spectrometers, Detectors and Associated Equipment **419**, 726 (1998).

[187] S. Tangwancharoen, *et al.*, A gating grid driver for time projection chambers, Nuclear Instruments and Methods in Physics Research Section A: Accelerators, Spectrometers, Detectors and Associated Equipment **853**, 44 (2017).

[188] E. Pollacco, *et al.*, GET: A generic electronics system for TPCs and nuclear physics instrumentation, Nuclear Instruments and Methods in Physics Research Section A: Accelerators, Spectrometers, Detectors and Associated Equipment **887**, 81 (2018).

[189] T. Isobe, *et al.*, Application of the Generic Electronics for Time Projection Chamber (GET) readout system for heavy Radioactive isotope collision experiments, Nuclear Instruments and Methods in Physics Research Section A: Accelerators, Spectrometers, Detectors and Associated Equipment **899**, 43 (2018).

[190] X. Grave, *et al.*, in *14th IEEE-NPSS Real Time Conference, 2005.* (2005) pp. 5 pp.–.

[191] S. Callier, *et al.*, EASIROC, an easy & versatile ReadOut device for SiPM, Physics Procedia **37**, 1569 (2012).

[192] S. Agostinelli, *et al.*, Geant4—a simulation toolkit, Nuclear Instruments and Methods in Physics Research Section A: Accelerators, Spectrometers, Detectors and Associated Equipment **506**, 250 (2003).

[193] M. Bleicher, *et al.*, Relativistic hadron-hadron collisions in the ultra-relativistic quantum molecular dynamics model, Journal of Physics G: Nuclear and Particle Physics **25**, 1859 (1999).

[194] P. Lasko, *et al.*, KATANA – A charge-sensitive triggering system for the SπRIT experiment, Nuclear Instruments and Methods in Physics Research Section A: Accelerators, Spectrometers, Detectors and Associated Equipment **856**, 92 (2017).

[195] Y. Zhang, *et al.*, The Veto Collimator for the SπRIT-TPC, RIKEN Accelerator Progress Report **50**, 170 (2017).

[196] T. Kobayashi, *et al.*, SAMURAI spectrometer for RI beam experiments, Nuclear Instruments and Methods in Physics Research Section B: Beam Interactions with Materials and Atoms **317**, 294 (2013).

[197] I. Gašparić, *et al.*, NeuLAND demonstrator performance in EOS experiments, RIKEN Accelerator Progress Report **50**, 176 (2017).

[198] H. Baba, *et al.*, New data acquisition system for the RIKEN radioactive isotope beam factory, Nuclear Instruments and Methods in Physics Research Section A: Accelerators, Spectrometers, Detectors and Associated Equipment **616**, 65 (2010).

[199] H. Baba, *et al.*, Common trigger firmware for GTO, RIKEN Accelerator Progress Report **47**, 235 (2014).

[200] M. Kaneko, The ANAROOT-based software codes for analyzing RI beam-induced data of the BigRIPS detectors, https://github.com/SpiRIT-Collaboration/BeamAnalysis_S22.

[201] K. Makino *et al.*, COSY INFINITY Version 9, Nuclear Instruments and Methods in Physics Research Section A: Accelerators, Spectrometers, Detectors and Associated Equipment **558**, 346 (2006).

[202] O. Tarasov *et al.*, LISE++: Radioactive beam production with in-flight separators, Nuclear Instruments and Methods in Physics Research Section B: Beam Interactions with Materials and Atoms **266**, 4657 (2008).

[203] J. W. Lee, *et al.*, Charged particle track reconstruction with SπRIT time projection chamber, Nuclear Instruments and Methods in Physics Research Section A: Accelerators, Spectrometers, Detectors and Associated Equipment **965**, 163840 (2020).

[204] G. Jhang, *et al.*, Beam commissioning of the SπRIT time projection chamber, Journal of the Korean Physical Society **69**, 144 (2016).

[205] G. Jhang, *Performance of the SπRIT TPC for the Nuclear Physics Experiment at RIBF*, Ph.D. thesis, Korea University (2016).

[206] J. Estee, *et al.*, Extending the dynamic range of electronics in a Time Projection Chamber, Nuclear Instruments and Methods in Physics Research Section A: Accelerators, Spectrometers, Detectors and Associated Equipment **944**, 162509 (2019).

[207] C. Y. Tsang, *et al.*, Space charge effects in the SπRIT time projection chamber, Nuclear Instruments and Methods in Physics Research Section A: Accelerators, Spectrometers, Detectors and Associated Equipment **959**, 163477 (2020).

[208] R. Brun *et al.*, ROOT — An object oriented data analysis framework, Nuclear Instruments and Methods in Physics Research Section A: Accelerators, Spectrometers, Detectors and Associated Equipment **389**, 81 (1997).

[209] R. Frühwirth *et al.*, Robust circle reconstruction with the Riemann fit, Journal of Physics: Conference Series **1085**, 042004 (2018).

[210] J. Rauch *et al.*, GENFIT — a generic track-fitting toolkit, Journal of Physics: Conference Series **608**, 012042 (2015).

[211] W. Waltenberger, *et al.*, Adaptive vertex fitting, Journal of Physics G: Nuclear and Particle Physics **34**, N343 (2007).

[212] W. Waltenberger, RAVE—A detector-independent toolkit to reconstruct vertices, IEEE Transactions on Nuclear Science **58**, 434 (2011).

[213] Particle Data Group, *et al.*, Review of Particle Physics, Progress of Theoretical and Experimental Physics **2020**, 10.1093/ptep/ptaa104 (2020).

[214] C. Cavata, *et al.*, Determination of the impact parameter in relativistic nucleus-nucleus collisions, Physical Review C **42**, 1760 (1990).

[215] W. D. Myers, Geometric properties of leptodermous distributions with applications to nuclei, Nuclear Physics A **204**, 465 (1973).

[216] F. Cerutti, *et al.*, A semiclassical formula for the reaction cross-section of heavy ions, The European Physical Journal A - Hadrons and Nuclei **25**, 413 (2005).

[217] R. Kumar, *et al.*, Parameterization scheme for determining the reaction cross sections at intermediate beam energies for normal and exotic nuclei, Nuclear Physics A **849**, 182 (2011).

[218] M. Anderson, *et al.*, The STAR time projection chamber: A unique tool for studying high multiplicity events at RHIC, Nuclear Instruments and Methods in Physics Research Section A: Accelerators, Spectrometers, Detectors and Associated Equipment **499**, 659 (2003).

[219] E. Chabanat, *et al.*, A Skyrme parametrization from subnuclear to neutron star densities Part II. Nuclei far from stabilities, Nuclear Physics A **635**, 231 (1998).

[220] A. Ono, *et al.*, Nucleon flow and fragment flow in heavy ion reactions, Physical Review C **48**, 2946 (1993).